공학박사 학위논문

Effects of Carbon Nanotubes on Ultra-High Performance Concrete for Multi-Functional Applications

초고성능 콘크리트의 다기능 복합 응용을 위한

탄소나노튜브의 적용 및 영향 분석

2020 년 8 월

서울대학교 대학원

건축학과

정 명 준

Effects of Carbon Nanotubes on Ultra-High Performance Concrete for Multi-Functional Applications

지도 교수 홍 성 걸

이 논문을 공학박사 학위논문으로 제출함
2020 년 8 월

서울대학교 대학원
건축학과
정 명 준

정명준의 공학박사 학위논문을 인준함
2020 년 8 월

위 원 장 홍 근 (인)
부위원장 홍 성 걸 (인)
위 원 이 철 호 (인)
위 원 문 주 학 (인)
위 원 이 명 수 (인)

Abstract

This study aimed to develop multi-functional ultra-high performance concrete (UHPC) with excellent mechanical strength, electromagnetic interference (EMI) shielding effectiveness (SE), and damage sensing capabilities for applying structural health monitoring (SHM), in on-site production.

Carbon nanotubes (CNTs), selected as a key material to achieve the purpose of this study, were mixed with UHPC and investigated with regard to dispersion methods, mechanical properties, EMI SE, damage sensing, electrical curing (EC) and structural modifications with respect to CNT incorporation.

Ozone treatment was applied to CNTs as a dispersion method and its impact on dispersion of CNTs and hydration reaction of UHPC were investigated. The results reveals that oxygenic and carboxylic groups, formulated by ozone treatment, functionalized the surface of the CNTs and enveloped the cementitious grains, which increasing the degree of dispersion of CNTs and interfacial interaction between CNTs and UHPC particles. Ozone treatment provided multiple nucleation sites and double steric repulsion, accelerating hydration at early ages and improving compressive strength at later ages. Thus, the proposed ozone treatment can be an effective way to disperse CNTs in UHPC.

Dispersed CNT suspensions were fabricated using sonication and subsequent shear mixing with superplasticizer, a proposed method for dispersing high content of CNTs in UHPC. Then, the CNT suspensions were incorporated into UHPC to form UHPC/CNT composites and their mechanical properties were investigated with respect to the CNT content. The proposed dispersion method effectively dispersed CNTs

within both an aqueous solution and UHPC composite up to the critical incorporation concentration (CIC). In addition, it was found that CNT content below the CIC improve the mechanical properties of UHPC through pore filling, bridging, and calcium-silicate-hydrates (C-S-H) stiffening, whereas CNT content above CIC weakens the properties due to agglomeration of CNTs, suppression of hydration, and increase in air-voids.

A dispersed CNTs remarkably improved the electrical conductivity and resulting SE of UHPC up to the percolation threshold. Two testing methods for EMI SE (ASTM D4935-18 and IEEE-STD-299) verified the result and suggested that ASTM D4935-18 can only be used to evaluate a rough trend of SE, and IEEE-STD-299 using the samples with sufficient incident area size at least 1200 × 1200 mm^2 should be considered to accurately evaluate the EMI SE at actual structure level. In addition, a practical model to effectively estimate the SE of UHPC was proposed based on statistical analysis of the experimental results.

The addition of CNTs significantly decreased electrical resistivity of the UHPC, enabling EC at low voltages in the range of 19–23 V; improved mechanical properties via bridging, pore filling, and C-S-H stiffening effects; and influenced the deflection hardening behavior under flexural stress. Furthermore, the UHPC/CNT under compressive or flexural stress exhibited significant crack sensing capabilities due to the obtained low resistivity. A dramatic fractional change in resistivity (FCR) value of the UHPC/CNT composites can represent the failure under compression or first cracking under flexure. Therefore, it was verified that the UHPC/CNT can extend the applications of UHPC especially for on-site casting and structural crack sensors for UHPC-based structures.

Finally, the dispersed CNTs slightly interfered the hydration of the UHPC, but they significantly modified the structure of C-(A)-S-H to be denser, stiffer, and more complex than that of UHPC without CNTs

which have been evidenced by observed partial cross-linking in the C-(A)-S-H, reduced *d*-spacing and the higher fractal dimensions of solid system. Such behaviors were much more significant when EC was applied because the electrical field formed by EC activated ionic polarization and accelerated the chemical reaction among ions in the UHPC matrix, which led to a higher degree of hydration.

In conclusion, incorporating appropriate amount of CNTs into UHPC using the proposed dispersion methods can overcome the limitation of UHPC and produce multi-functional UHPC with EMI SE and crack sensing capabilities on-site using EC.

Keyword : Carbon Nanotubes (CNTs); Crack sensing; Electromagnetic interference (EMI) shielding; Electrical curing; Dispersion; Ultra-high performance concrete (UHPC)

Student Number : 2017-39383

Contents

List of Tables

List of Figures

List of Abbreviations

ACI	American Concrete Institute
AFGC	Association Française de Génie Civil
AFm	Al_2O_3-Fe_2O_3-mono phase, monosulphate
AFt	Ettringite
ASTM	American Society for Testing and Materials
BGD	Background
C-(A)-S-H	Calcium-aluminate-silicate-hydrates
CF	Carbon fiber
CH	Portlandite, $Ca(OH)_2$
CIC	Critical incorporation concentration
CNTs	Carbon nanotubes
C-S-H	Calcium-silicate-hydrates
CVD	Chemical vapor depositon
DOD	Degree of dispersion
DOH	Degree of hydration
DOR	Degree of reaction
DTG	Derivative of the thermogravimetric
EC	Electrical curing
EMI	Electromagnetic interference
EMP	Electromagnetic pulse
FRC	Fiber reinforced concrete
GF	Gauge factor
GGBGS	ground granulated blast-furnace slag
HPC	High performance concrete

HSC	High strength concrete
IEEE	Electrical and Electronics Standards
MCL	Mean chain length
MIP	Mercury intrusion porosimetry
MIS-STD	Military Standards
MWCNTs	Multi-wall CNTs
NBO	Non-bridging oxygen
NMR	Nuclear
NMR	Nuclear magnetic resonance
OAP	Onset of acceleration period
OPC	Ordinary Portland cement
QXRD	Quantitative X-ray diffraction
RH	Relative humidity
RPC	Reactive powder concrete
SANS	Small angle neutron scattering
SAXS	Small angle X-ray scattering
SC	Steam curing
SCMs	Supplementary cementitious materials
SE	Shielding effectiveness
SEM	Scanning Electron Microscope
SHM	Structural health monitoring
SWCNTs	Single-wall CNTs
TEM	Transverse electromagnetic
TG	Thermogravimetric
UHPC	Ultra-High Performance Concrete
UTM	Universal testing machine
vol.%	Volume percent
Wt.%	Weight percent
XRD	X-ray diffraction
XRF	X-ray fluorescence

Chapter 1. Introduction

1.1 Background

1.1.1 The latest issues in concrete technology

Concrete technology have been progressed significantly over the last 30 years. These developments have mostly focused on improving strength of concrete until 1990s. As a result, various concretes with excellent material performance such as high strength concrete (HSC), high performance concrete (HPC), ultra-high performance concrete (UHPC), reactive powder concrete (RPC) was introduced.

Since the beginning of 2000s, interest in hybrid concrete for multi-functional applications and various studies have been increasing. In particular, the importance of electromagnetic interference (EMI) shielding is becoming highly emphasized in the construction field because of the remarkable growth in the ubiquity of electronic devices and applications of radio communications. Long-term exposure to electromagnetic (EM) waves can directly affect the human body and promote the growth of tumor [1-4]. In addition, invasive powerful EMI such as an electromagnetic pulse (EMP) can cause the malfunction of electronic devices or jam and paralyze security facilities and important infrastructures such as dams, power plants, and military facilities. Thus, EMI shielding is not an option but a necessity in such areas. These facilities require not only radio wave shielding capability but also excellent physical protection to withstand vehicle or aircraft crashes, explosions, etc. For this reason, various works are in progress for developing cementitious materials with not only improved mechanical properties but also EMI shielding effectiveness (SE).

Another issue that is being significantly highlighted is structural health monitoring (SHM), which refers to the process of implementing a damage detection and characterization strategy for engineering structures. After extreme events, such as earthquakes or blast loading, SHM is used for rapid condition screening and aims to provide, in near real time, reliable information regarding the integrity of the structure. In general, SHM has been applied using commercial piezoelectric sensors and measuring stress and strain states of a structure. However, although it has been increasingly implemented in construction projects, sensor-based detection is often limited for various reasons, such as inability to locally assess the structural state and the uncertain coupling between the attached piezoelectric sensor and surface of the structure [5, 6]. Therefore, developing conductive cementitious materials as a crack sensor for SHM has been investigated.

1.1.2 Ultra High-Performance Concrete (UHPC)

UHPC was developed in the mid-1990s [7]. Owing to its superior material properties, including excellent durability, post-hardening behavior, and crack resistance with a high compressive strength, owing to the dense packing of particles with a low water to cement ratio (w/c), attempts to apply UHPC in construction projects have been increasing [8, 9].

However, UHPC, like most cementitious materials, cannot be obviously applied alone for EMI shielding due to very low electrical conductivity, which is in the range of 0.001–1 μS/m [10] because EMI shielding mainly results from the reflection or absorption of EM waves by means of a conductive material [11]. Application of damage sensing capability to UHPC is also limited and worth investigating because, most previous studies were based on cement paste and UHPC show completely different properties, such as the strength, strain hardening

and cracking behaviors. Therefore, to examine the feasibility of the adaptation of the self-sensor technique in SHM for UHPC structures, it is definitely necessary to develop suitable techniques considering various unique aspects of UHPC composites.

In UHPC production, the curing conditions play a crucial role in the hydration and resulting material performance of UHPC, which must achieve a target performance, such as compressive strength > 150 MPa defined in several international codes such as Association Française de Génie Civil (AFGC) and American Concrete Institute (ACI) committee 239 [12, 13]. To achieve this target performance, steam curing (SC) at temperatures of 60 or 90 ℃ for several days is generally required [14]. However, this requirement prevents the production of UHPC for on-site construction and needs large scale manufacturing facility, which can be only applicable in precast factory [15, 16]. In addition, although SC is a reliable and relatively easy-to-apply curing method, it has poor energy efficiency. Thus, UHPC is usually used in precast form or is designed by reducing its nominal strength. To overcome these limitations, it is desirable to develop a new curing method whereby the expected performance of UHPC can be developed on-site.

One approach is to solve this problem is electrical curing (EC), which is a relatively unexplored alternative in the construction industry. EC is a method using heat generated by means of the joule effect [6, 17-19]. Hardened concrete is not typically conductive, but it has a conductive characteristic until it reaches its final setting time. This is because a large amount of unreacted pore solution is available during this early period. Specifically, fresh concrete shows low electrical resistivity, while hardened concrete acts as an insulator because the internal water has been consumed by cement hydration, which significantly increases the electrical resistivity [20]. Therefore, because resistivity keeps increasing due to continuous water removal or consumption during main curing stage, a high power of more than 500

W is required to overcome the high resistivity of concrete; this makes it difficult to use the EC method in actual construction projects [19]. Thus, to apply an EC method to UHPC as an alternative to conventional SC, a new approach that could significantly decrease the resistivity of UHPC is prerequisite.

1.1.3 Carbon Nanotubes (CNTs)

Carbon nanotubes (CNTs), which were discovered independently by Iijima and Ichihashi [21] and Bethune et al. [22], are tubes made of carbon with diameters typically measured in nanometers. CNTs are one of the allotropes of carbon, intermediate between fullerene cages and flat graphene. This can be thought of as cutouts from a two-dimensional hexagonal lattice of carbon atoms rolled up along one of the Bravais lattice vectors of the hexagonal lattice to form a hollow cylinder. Based on the number of tubes, CNTs can be classified into single-wall CNTs (SWCNTs) and multi-wall CNTs (MWCNTs) consisting of nested SWCNTs, as illustrated in Fig. 1-1.

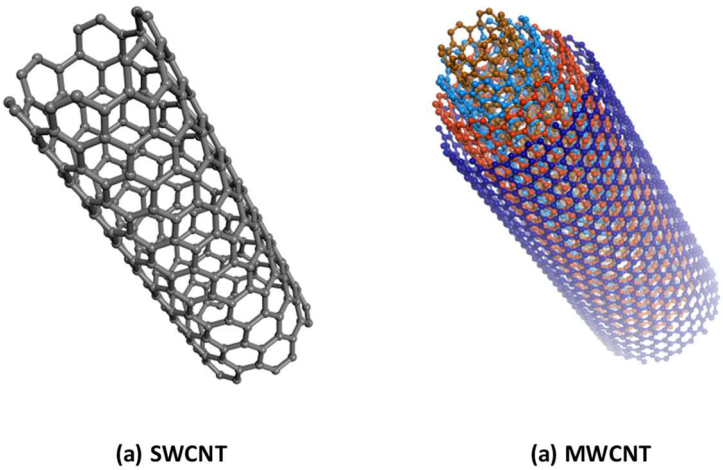

Fig. 1-1. Types of CNTs: (a) SWCNT, (b) MWCNT.

The development of CNTs has given various engineering fields a new avenue for realizing innovative materials because of their excellent mechanical, thermal, and electrical properties [23-25]. Among their many applications, CNTs can be used in construction engineering for nanoscale reinforcement to improve cementitious materials. Therefore, multiple studies have reported on the improved mechanical properties of cementitious materials reinforced with CNT [26-29]. In addition, CNTs exhibits an electrical conductivity more than 1000 times higher than that of copper, it can be used as effective conductive fillers to develop conductive cementitious materials for EMI shielding and SHM. A number of studies have shown that the electrical conductivity of cementitious materials improved with the addition of CNTs [24, 26, 30-37].

However, most previous studies have mainly focused on improving engineering properties or multifunctional behavior on the macro-scale level. The interaction mechanism between CNTs and cementitious materials (especially for the case of UHPC) have not been investigated comprehensively, especially the structural changes in micro- or meso-scale level. In addition, although there have been some successful applications of CNTs to cementitious binders, achieving both effective electrical conductivity and superior mechanical properties remains an engineering challenge. This is because dispersing CNTs in a structural binder requires a high solution ratio, which is detrimental to the development of mechanical strength in typical construction materials, due to their characteristics of hydrophobic nature, high specific surface areas, high aspect ratios, and strong Van der Waals forces [38]. In addition, it has been found that CNTs partially adsorb water molecules on its surfaces [39, 40]. Therefore, previous studies on cementitious composites with CNTs for EMI SE and SHM have reported limited compressive strength of 62 MPa with a w/c of 0.35 [41]. For this reason, previously proposed dispersion methods are not directly applicable to making UHPC more conductive because UHPC generally has a low w/c

of as low as 0.2 to achieve a high strength of over 150 MPa. Therefore, the engineering challenge of incorporating CNTs in UHPC is that CNTs leads to high water absorption, which decreases workability. Moreover, UHPC is composed of not only cement and fine aggregate but also various materials such as silica fume and silica powder. Thus, even if there is a way to uniformly disperse CNTs in a UHPC binder, it is not clear how the CNTs work within the complex matrix and what their impact is on the resulting electrical and mechanical properties.

Hence, for developing multi-functional UHPC with EMI SE and damage sensing capabilities and enabling EC to produce UHPC on-site, developing a desirable method to effectively disperse CNTs in UHPC and study of structural modification of UHPC at micro-, meso-, and macro-level according to incorporation of CNTs are required along with testing electrical performances.

1.1.4 Compatibility between UHPC and CNTs

UHPC is composed of micro- to millimeter-sized fine materials such as cement, silica fume, silica powder, and silica sand to increase the packing density (i.e., coarse aggregates are not included in UHPC). UHPC exhibits excellent mechanical properties, but there are some additional weaknesses besides requirement of SC. Firstly, UHPC is vulnerable to explosive spalling. Ironically, densified microstructure and pores of UHPC prevent water vapor from free transport and escapes in the matrix when exposed to elevated temperature. Therefore, if the pore pressure in the matrix accumulates to a threshold value exceeding their tensile strength, explosive spalling occurs. The other concern of UHPC is autogenous shrinkage. Autogenous shrinkage refers to reduction of apparent volume or length of cementitious matrix under seal and isothermal condition. UHPC typically has a low w/c less than 0.25, the internal water is insufficient to fully hydrate cementitious materials.

Thus, the occurrence probability of autogenous shrinkage may increase. In addition, silica fume in UHPC accelerate the consumption of water by filler effect and pozzolanic reaction, it causes further autogenous shrinkage. Autogenous shrinkage normally resulting microcracks in the matrix and decrease the durability of UHPC.

However, incorporation of CNTs into UHPC can alleviate the aforementioned problems. Physical role of CNTs on the microstructure of cementitious matrix is schematically presented in Fig. 1-2. In the beginning, CNTs can be effectively used for anti-spalling. Specifically, although dispersed CNTs partially absorb internal water, they can fill pores in the matrix and bridge between them. When the temperature elevates above 100 ℃, internal water absorbed on the surfaces of CNTs evaporates. If then, CNTs can act as pore paths connecting between pores. Thus they can alleviate and release of pore vapor pressure inside capillaries. In addition, incorporation of CNT into UHPC can remarkably decrease autogenous shrinkage. Well dispersed CNTs can physically interconnect the hydration products and fill the pores. Thus, densified pore solution and phases forming between CNTs could stiffen the matrix, which in turn could reduce the autogenous shrinkage. Fig. 1-3, the experimental result of autogenous shrinkage for UHPC with CNTs, shows how effective CNTs are for autogenous shrinkage.

Besides, CNTs can be used to improve the mechanical properties of UHPC by increasing packing density. Moreover, UHPC is relatively easy to improve their electrical performance using CNTs compared to normal concrete. This is because the finer composition and lower pores have less effect on the connection between CNTs in UHPC. On the other hand, coarse aggregate in normal concrete acts as an obstacle to the connection of CNTs, making it difficult to improve electrical properties.

However, no matter how good the compatibility between UHPC and CNTs is, if there is no way to effectively disperse CNTs in UHPC, the advantages of CNTs cannot be fully utilized.

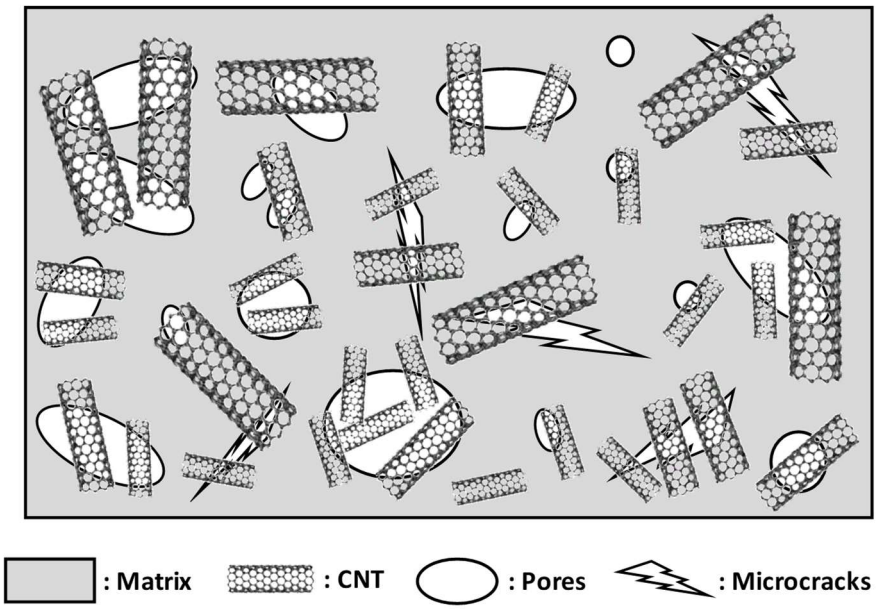

Fig. 1-2. Physical role of CNTs on the microstructure of cementitious matrix.

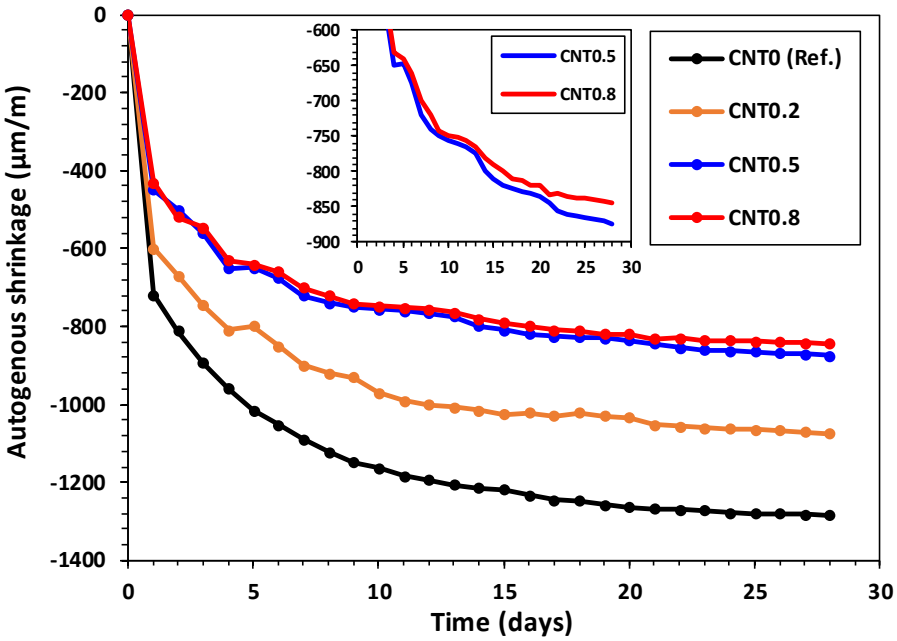

Fig. 1-3. Effects of CNTs on autogenous shrinkage for UHPC.

1.2 Objectives and structure of thesis

The objective of this study is develop a multi-functional UHPC that can be produced on-site while maintaining high strength as well as EMI SE and damage sensing capabilities by incorporating CNTs into UHPC using a new method to disperse CNTs can applicable to UHPC as schematically illustrated in Fig. 1-4.

This thesis consists of eight chapters. In Chapter 1, background, necessity, and purpose of this research were presented. Chapter 2 reviews the previous literature on CNT dispersion methods, EMI SE, and SHM techniques for the cementitious materials embedded with CNTs. In addition, information on materials used for UHPC production and experimental techniques frequently used in this study are briefly introduced. In Chapters 3 and 4, new methods to disperse CNTs to UHPC and effects of CNTs on mechanical performance of UHPC are investigated. Specifically, effect of ozone treatment on the dispersion of CNTs and the performance of UHPC is investigated in Chapter 3. In Chapter 4, Shear mixing with superplasticizer after sonication as an alternative to disperse CNTs into UHPC is introduced and the effects of dispersed CNTs by applying the method on the performance of UHPC is evaluated. Chapter 5 deal with UHPC embedded with CNTs in terms of EMI SE. In addition, an effective way to test SE of UHPC at actual structural level and a practical model to effectively estimate EMI SE are proposed. In Chapter 6, CNTs were incorporated into UHPC mainly for two objectives of the potential application of EC for UHPC production on-site and the implementation of crack sensing ability in UHPC structure. Chapter 7 discuss the effect of incorporation of CNTs on the structural modifications of UHPC at multi-scale levels such as micro-, meso-, and macro-level. Finally, in Chapter 8, the advantages, feasibility, and practically of the developed multi-functional UHPC are discussed, along with a summary of this study.

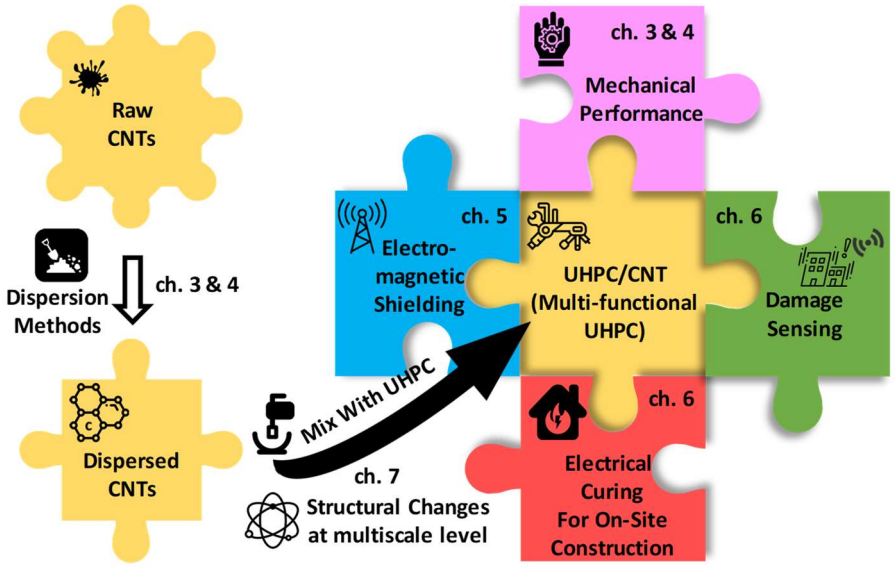

Fig. 1-4. Schematic illustration of research objectives.

Chapter 2. Preliminary Study

2.1 Literature review

2.1.1 Methods to disperse CNTs

CNTs, exhibiting excellent mechanical, thermal, and electrical performances, have been increasingly used in cementitious materials for improving their mechanical properties, or for developing multi-functional cementitious materials with EMI shielding and self-sensing capabilities [27, 30, 31, 42, 43]. However, the dispersion of CNTs is still a critical issue, which determines the overall properties of the cementitious materials with embedded CNTs. Especially, achieving desirable dispersion of CNTs is difficult due to its characteristics such as high aspect ratios, high specific surface areas, and strong Van der Waals forces [44].

To improve the dispersion of CNTs, sonication process with a polycarboxylate-based surfactant has been widely used [38, 45-48] (Fig. 2-1a). However, this method generally requires specialized equipment, and can damage the structure of CNTs by causing the dislocation of carbon atoms, formation of amorphous carbon, and shortening the carbon chain lengths. This results in a decrease in their aspect ratio, and hampers the cohesion between the tubes and the host matrix [49, 50]. In addition, the determination of optimal sonication energy that balances desirable dispersion with minimal induced damage is very difficult. Furthermore, it has been reported that the surfactant applied during sonication can act as an air entraining agent, generating entrapped pores in the cementitious matrix and ultimately degrading the mechanical properties of the cement composites [51]. Besides, as the sonication

progressed, the high specific surface area of CNTs increased, which leads to high water absorption resulting decrease in the workability and increase in the entrapped pores in the cementitious matrix [39, 40]. Therefore, previous studies have reported inconsistent and even contradictory results pertaining to the effects of CNTs on the properties of cementitious materials [52].

An alternative method to disperse CNTs is plasma oxidation, which can functionalize CNTs without damage [53-55] (Fig. 2-1b). This method can covalently attach chemical groups on the surfaces of the CNTs, resulting in enhanced dispersion of the latter. However, the process requires the application of high power from a microwave generator. Further, the entire process is complicated and time consuming, involving the following steps: modification of CNTs → fabrication of CNT suspension using surfactants or via sonication → mixing of CNTs with cementitious materials → curing. In addition, chemical pre-treatment is not environmentally favorable and can cause negative impacts on the fresh and hardened cementitious material [38].

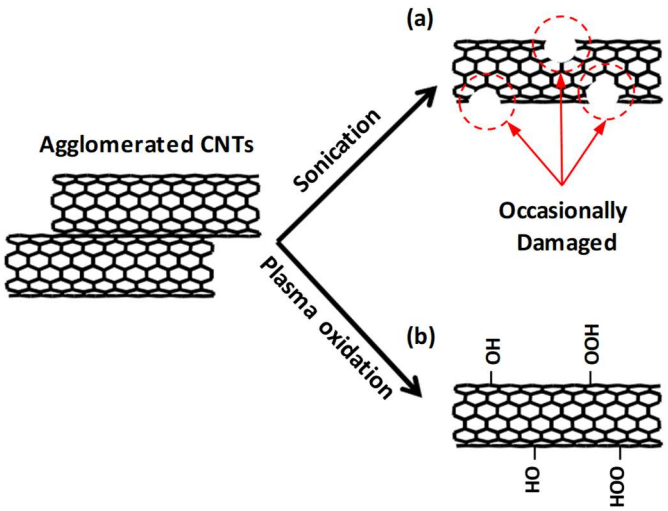

Fig. 2-1. Typical CNT dispersion methods: (a) sonication, (b) plasma oxidation.

Attaining improved interfacial interaction between CNTs and hydration products, which can lead to uniform distribution of CNTs in cementitious materials [56], is another major challenge. Typically, since hydration products such as calcium-silicate-hydrates (C-S-H), ettringite, and portlandite ($Ca(OH)_2$, CH) have similar or larger size than CNTs, only a few CNTs can be embedded in such hydration products [36]. Thus, if the degree of distribution of CNTs is low, these would not be able to effectively reinforce the hydration products; a large portion of CNTs (i.e., agglomerated CNTs) would acts as pores and cracks, weakening the mechanical properties of the cementitious matrix.

Hence, to overcome the aforementioned limitations, developing a new method in applicable to UHPC is required for better dispersion of CNTs in solution and to attain enhanced interfacial interaction among various components in UHPC.

2.1.2 Cementitious materials incorporated with CNTs for applying EMI shielding

There are several standard methods for measuring electromagnetic interference (EMI) shielding effectiveness (SE), such as American Society for Testing and Materials (ASTM) D4935-18, ASTM E1851-15, Military Standards (MIL-STD) 188-125-1, and Institute of Electrical and Electronics standard (IEEE-STD) 299 [57-60]. These methods can be classified into small sample testing and large sample testing according to the required geometry of the sample. ASTM D4935-18 can be regarded as being representative of small sample testing, and the other methods can be considered to be large-sample testing.

Multiple studies are in progress for developing cementitious materials with EMI SE. Most previous studies improved the EMI SE of cementitious materials by using conductive fillers such as carbon materials, steel fibers, nickel powder, and steel slag. In particular,

carbon materials such as CNTs, graphene, and carbon black have been reported to be effective conductive fillers for EMI shielding because of their extraordinary electrical conductivity.

Previous research on EMI SE properties of cement-based materials embedded with CNTs is summarized as follows. Nam et al. reported EMI SE results for mortars with various amounts of MWCNT (0–1.5 wt.%) at frequencies of 45 MHz to 18 GHz. The SE of a mortar with 1.5 wt.% MWCNT was 2.6 dB at a frequency of 2 GHz [61]. They also analyzed the influence of the CNT dispersion on the SE of cementitious binders (i.e., cement mixed with silica fume) mixed with CNTs and maximized the enhancement at 0.6 wt.% CNT and 20 wt.% silica fume [62]. Singh et al. found that a cement matrix with 15 wt.% MWCNT had a SE more than 27 dB at frequencies in the range of 8.2–12.4 GHz [63]. Wang et al. investigated the EM wave absorption properties of a MWCNT–mortar composite with varying CNT contents at frequencies of 2–8 GHz and 8–18 GHz. They reported that a mortar with 0.6 wt.% MWCNT had a SE of 28 dB at a frequency of 2.9 GHz, while a mortar with 0.9 wt.% MWCNT had a SE of 10 dB at 7.1 GHz [64]. Experiments and simulations showed that the EMI SE of a 15 cm thick mortar with 3 wt.% MWCNT was more than 50 dB at frequencies of 0.75–1.12 GHz [65]. Several other studies have reported similar results on the application of carbon materials to develop conductive cementitious materials for EMI shielding [41, 66-70].

Although there have been some successful results on EMI SE of cement-based materials with CNTs, the reported compressive strength along with the EMI SE was limited to be less than 62 MPa. This is because a high w/c of more than 0.35 was applied to prevent the flow rate from decreasing due to incorporation of CNTs. In addition, most previous studies were based on cement paste and mortar. Thus, it is difficult to extend the previous results directly to UHPC, generally has a low w/c of as low as 0.2 to achieve a high strength of over 150 MPa.

Moreover, UHPC is composed of not only cement and fine aggregate but also various materials such as silica fume and silica powder, it is not clear how the CNTs work within the complex matrix and what their impact is on the resulting electrical and mechanical properties.

Most previous research tested the EMI SE based on small sample testing, such as ASTM D4935-18, or a similar method, using a coaxial transverse electromagnetic (TEM) cell because the samples are easy to fabricate and simple to testing, and reducing the required amount of labor, resources, time, etc. However, this method is not appropriate for cement-based composites [65] because fabricating a homogeneously small less than diameter of 13.3 mm and thin sample with a thickness of 25 μm (i.e., the required dimension according to ASTM D4935-18) is impossible. In addition, if EMI SE testing is conducted on a sample that is several millimeters thick, the EMI SE could be overestimated because the gap between the coaxial TEM cells increases with the thickness of sample. Thus, even if accurate calibration is confirmed, the total transmission signal cannot be directly received through the sample, and some portions of signal may leak through the gap. Moreover, it is difficult to assume that the EMI SE obtained from small sample testing can be representative of that in actual structure level. Hence, small sample testing should only be used to roughly estimate the effect of different components on the EMI SE of cementitious materials and large sample testing should be considered.

IEEE-STD-299 is a representative large sample testing method that can indicate the SE of an actual structure. This method requires that the incident area of the sample should be equal to or greater than 2.0×2.0 m^2. However, it is difficult to fabricate test samples satisfying the required dimensions. Nevertheless, there is no previous research that has been performed to determine the requirement of the sample size or incident area, and the effect of the small size of the incident area on the EMI SE.

Hence, investigating the effect of CNTs on EMI SE of UHPC at actual scale level, while maintaining the superb compressive strength of 150 MPa, is necessary. In addition, the mechanism of EMI SE between UHPC and CNTs should be considered along with the effect of incident area size on EMI SE.

2.1.3 Cementitious materials embedded with CNTs for applying SHM techniques

Structural health monitoring (SHM) refers to the diagnosis of the condition of structural members that make up the entire structure in near real time by using piezoresistive sensors as illustrated in Fig. 2-2. Conventionally used sensors, such as strain gauges, accelerometers, and fiber optic sensors are often limited due to drawbacks of the uncertain coupling between sensors and surface of the structures, point-based sensing characteristics, and the possibility of artificial defects.

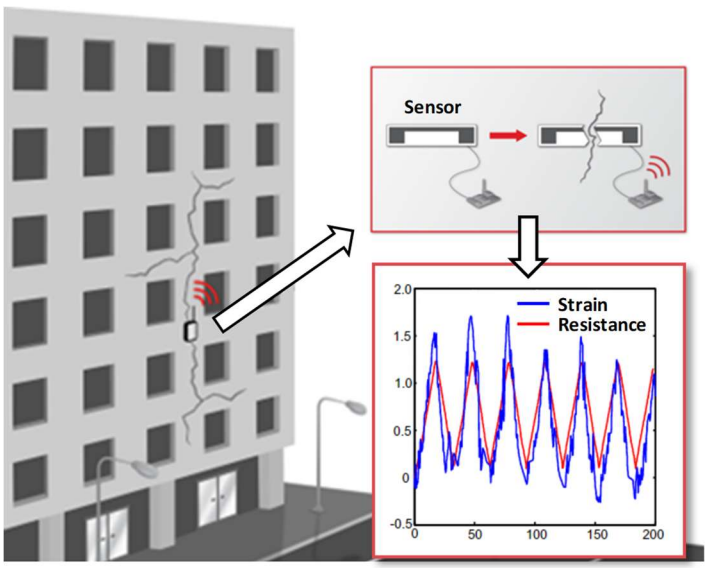

Fig. 2-2. Schematic illustration of SHM.

Conductive cement-based composites are considered a promising sensing material for SHM due to the piezoresistivity, which refers to a change in electrical resistance of a material in response to external load. Thus, attempts to make cementitious materials conductive using CNTs for applying SHM have been increasing. Azhari and Banthia performed on the piezoresistive properties of cement with carbon fiber (CF) and CNTs under compression and it was found that cement composites with CF/CNTs showed better piezoresistivity than that of cement composites with just CNTs [71]. Nam et al. investigated the piezoresistivity of cementitious binders mixed with MWCNTs subjected to compressive loading [72]. They also evaluated the relationship between the content of MWCNT and the piezoresistive sensitivity of the composites. Lee et al. reported that the cement composites incorporated with 0.1 wt.% of CF and 0.5 wt.% of CNTs exhibited similar piezoresistivity to that containing 1 wt.% of CNTs [73]. It was found that cement paste with 1 wt.% of MWCNT showed better piezoresistivity than that embedded with 1 wt.% of graphene nanofiber or graphene during compressive strength and split tensile strength test. Meanwhile, few studies on the sensing capability under flexural stress with the use of CNT embedded cement-based materials. Saafi introduced an in situ cement-CNT sensor which can evaluate the stress, damage, and cracking under flexural stress [74]. There are many other studies on developing conductive cement-based composites using CNTs [5, 75-77], but most of them used cement paste and mortar as base materials. Thus, the previous studies could be inapplicable to UHPC exhibiting completely different mechanical behaviors, such as exhibiting high compressive strength caused by dense packing with a low w/c, strain hardening, and multiple cracking behavior, which are not observed in ordinary cement paste and mortar.

Hence, it is necessary to investigate the effect of incorporation of CNTs on piezoresistivity of UHPC under both compressive and flexural stresses.

2.1.4 Electrical curing (EC) of cementitious materials

As aforementioned in Chapter 1, UHPC generally requires steam curing (SC) at temperatures of 60 or 90 ℃ for several days to achieve high compressive strength > 150 MPa. However, application of SC to field construction is limited, so UHPC is typically used in precast type.

Electrical curing (EC), which is a very powerful technique that can be applied to accelerate the curing process as evidenced in various experimental studies [15, 35, 78, 79]. Fresh concrete containing a large amount of water in the matrix behaves as a semiconductor due to the low electrical resistivity. Therefore, an applied voltage and resulting current generate heat by means of the joule effect, which have been reported as an efficient way to cure concrete materials at early ages [17, 18]. In contrast, hardened concrete acts as an insulator owing to the removal of internal water via the hydration reaction and evaporation process [20], which substantially increases the electrical resistivity. Consequently, because of the increased electrical resistance due to water consumption during curing process, a high amount of power: more than 500 W is typically required to overcome the high resistivity [16] which makes the use of this method in actual construction projects even more difficult [19].

Several studies investigated incorporation of conductive filler such as steel fibers, and CNTs into cementitious materials as an alternative way to decrease resistance and enables EC. Cecini et al. fabricated concrete samples mixed with 0.45 and 0.9 vol.% of steel fibers and electrically cured them at maximum voltage of 250 V. The result confirmed the feasibility of electrical curing for fiber reinforced concrete (FRC) production [15]. It was reported that FRC with 1 vol.% of steel fibers showed an eight-fold reduction of electrical resistance compared to plain concrete and enabled EC by applying 31–87 V/m [15]. Kim et al. reported that cementitious binder with 0.6 wt.% of CNTs showed the electrical resistivity of 560 Ω·m and the temperature

of the sample increased to 50 ℃ under EC at 4–7 W [78].

However, none of the previous studies compared EC and SC under nearly identical conditions, nor did they considered the possibilities of applying EC on UHPC. In addition, the previously reported resistance and applied electrical power are very high and insufficient to enable EC on-site. Electrical resistance of UHPC could be higher than that of cement paste and mortar due to low w/c. The high power applied the structure during curing can cause potential hazards, such as electric shock. Hence, to produce UHPC on-site, it is necessary to investigate a desirable method of incorporating conductive fillers, such as steel fibers, CNTs, or both, to improve electrical conductivity of UHPC sufficient to apply EC at low voltages.

2.2 Materials used in this study

The raw materials for the fabrication of UHPC were Type I ordinary Portland cement (OPC, Union Cement Co., Ltd., Korea), silica fume (Grade 940U, Elkem, Norway), silica powder (S-SIL 10, SAC, Korea, mean particle size of 4.2 μm), and silica sand (Saeron Co., Ltd., Korea, with particle diameter in the range of 0.2–0.3 mm) and steel fibers (smooth type with a length of 13 mm). OPC and silica fume were used as binders, and silica sand and silica powder were used as fine aggregate and physical filler, respectively. The chemical composition of cementitious materials was examined via X-ray fluorescence (XRF) and is listed in Table 2-1 . In addition, the mineralogical compositions of OPC as determined by quantitative X-ray diffraction (QXRD) analysis with Rietveld refinement are listed in Table 2-2. Rietveld analysis was conducted by refining the scale factor, peak asymmetry, zero shift, displacement, and unit cell parameters with a manually fixed background [80]. Note that around 20 % of limestone powder was originally included in the OPC for higher flowability.

Table 2-1. Chemical composition of cementitious materials (%).

Chemical composition	SiO_2	Al_2O_3	Fe_2O_3	MgO	CaO	K_2O	SO_3	SrO	LOI[1]	Total
OPC	21.40	4.63	0.36	1.27	65.8	0.13	2.89	0.076	3.4	99.95
Silica fume	96.90	0.29	0.15	0.18	1.54	0.64	-	-	0.02	99.72
Silica powder	97.70	0.49	0.05	0.21	1.37	0.02			0.02	99.86

[1] Loss of ignition

Table 2-2. Mineralogical composition of OPC (%).

Alite (mono-clinic)	Alite (tri-clinic)	β-Belite	γ-Belite	Aluminate	Amorphous	Anhydrite	Calcite	Dolomite	Gypsum
46.79	6.94	2.19	1.38	0.88	6.38	0.61	21.38	12.36	1.09

2.3 Basics of microstructural analysis used in this study

2.3.1 X-ray diffraction (XRD)

X-ray diffraction (XRD) is one of the most prominent analytical techniques in the characterization of crystalline, fine-grained materials, such as cements, in which the crystalline structure causes a beam of incident X-rays to diffract into many specific directions. By measuring the angles and intensities of these diffracted beams, a crystallographer can produce a three-dimensional picture of the density of electrons within the crystal. From this electron density, the mean positions of the atoms in the crystal can be determined, as well as their chemical bonds, their crystallographic disorder, and various other information.

Crystals are regular arrays of atoms, and X-rays can be considered waves of electromagnetic radiation. In general, atoms scatter X-ray waves, primarily through the atoms' electrons. An X-ray striking an electron produces secondary spherical waves emanating from the electron. This phenomenon is known as elastic scattering, and the electron (or lighthouse) is known as the scatterer. A regular array of scatterers produces a regular array of spherical waves. Although these waves cancel one another out in most directions via destructive interference, they add constructively in a few specific directions, determined by Bragg's law:

$$2d \sin\theta = n\lambda, \tag{2.1}$$

where d is the spacing between diffracting planes, θ is the incident angle, n is any integer, and λ is the wavelength of the beam.

Specifically, as illustrated in Fig. 2-3, if scatterers are arranged symmetrically with a separation d, these spherical waves will be in sync (add constructively) only in directions where their path-length

difference $2d\sin\theta$ equal an integer multiple of the λ. In that case, part of the incoming beam is deflected by an angle 2θ producing a reflection spot in the diffraction pattern. Using this diffraction pattern, microstructure of cementitious materials can be evaluated. An example of XRD pattern for cement is presented in Fig. 2-4.

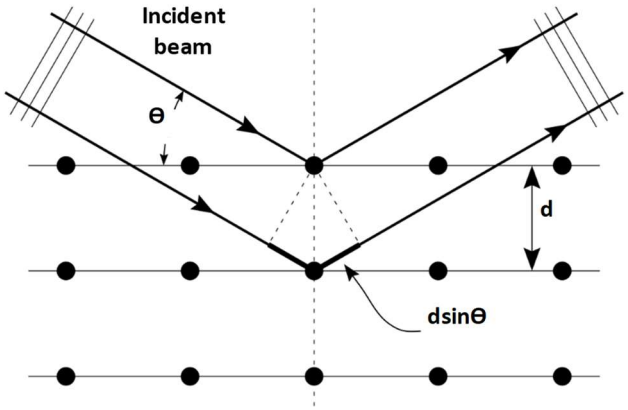

Fig. 2-3. X-ray diffraction.

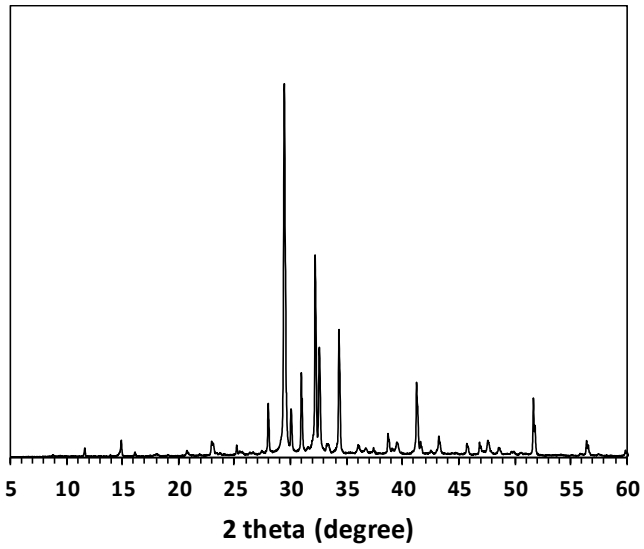

Fig. 2-4. An example of XRD pattern for anhydrous OPC.

2.3.2 Thermogravimetric (TG) analysis

Thermogravimetric analysis (TGA) is a widely used technique in the cement science. Measuring bound water and portlandite content by TGA are often used to follow the reaction of OPC or to evaluate the reactivity of supplementary cementitious materials (SCMs), such as fly ash, silica fume, and ground granulated blast-furnace slag (GGBFS). TGA is able to identify amorphous hydrates, such as calcium-silicate-hydrates (C-S-H) or monosulphate (Al_2O_3-Fe_2O_3-mono phase, AFm), and can be used complementary.

Minerals and hydration products can undergo several thermal reactions such as dehydration, dihydroxylation, decarbonation, phase transition, and decomposition. These reactions are attributed to weight changes or release of heat. The temperature ranges at which these processes occur are specified. When conducting TG, the sample is heated and the weight loss is recorded. Differentiation of the TG data enables a better identification of consecutive weight losses. Example of TG and DTG curves for a cement is shown in figure.

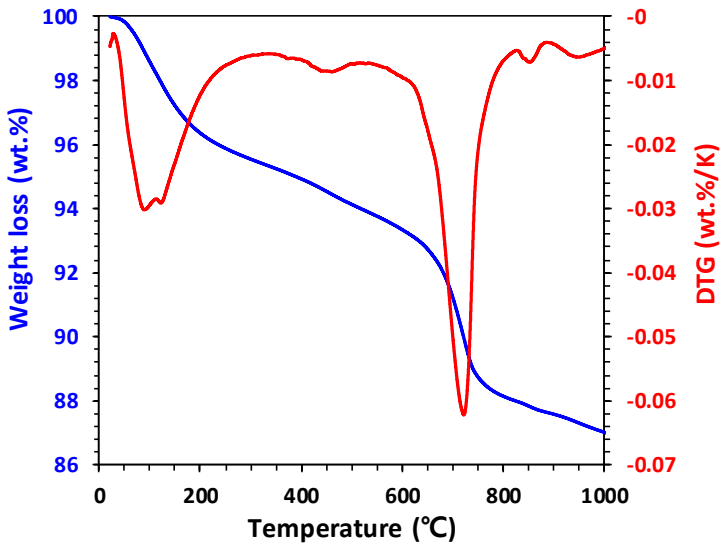

Fig. 2-5. An example of TG/DTG curves for OPC.

2.3.3 Solid-state ^{29}Si nuclear magnetic resonance (NMR)

Solid-state nuclear magnetic resonance (NMR) spectroscopy is a critical research technique for the characterization and structural analysis of cement-based materials and has been increasingly employed. A main strength of this method is nuclear-spin selectivity, where one nuclear-spin isotope of the NMR periodic table (eg., ^{1}H, ^{11}B, ^{19}F, ^{27}Al and ^{29}Si) is identified at the time, which often results in rather simple but informative spectra for complex multiphase systems, such as cementitious materials [81]. In addition, the resonances owing to these spin nuclei are very sensitive to local structural modifications and dynamic effects, which allows investigate crystalline phases as well as amorphous components, such as C-S-H. Therefore, NMR effectively supports a lot of other microstructural analysis.

The principle of NMR is as follows. All nucleons (i.e., neutrons and protons), composing any atomic nucleus, have the intrinsic quantum property of spin, an intrinsic angular momentum analogous to the classical angular momentum of a spinning sphere. In the absence of an external magnetic field, the nuclear spins are randomly aligned. If a nucleus is placed in a magnetic field, an induced magnetic field is generated, in which the nuclear spins are aligned in the same or opposite directions as the external magnetic field. When aligned in the same direction as the external magnetic field, the energy level is lowered, and when aligned in the opposite direction, the energy level is increased. The degree of energy increasing or decreasing from the existing energy level is the same. At this time, if the frequency which level of radio wave is provided as energy, the spin of the nucleus receives the energy and can change the spin state in the opposite direction to the external magnetic field. Since the intensity of the nuclear spin of each atom in the compound is different, the absorption frequency is different even when a magnetic field with same intensity is applied. Thus, it is possible to infer which atom exists by measuring the

frequency absorbed via the NMR. The most popular analysis in cement science is ^{29}Si NMR, which analyzes a Si-29 atom through spin resonance of a silicon-29 atom. An example of ^{29}Si NMR results for the anhydrous cement is presented in Fig. 2-6.

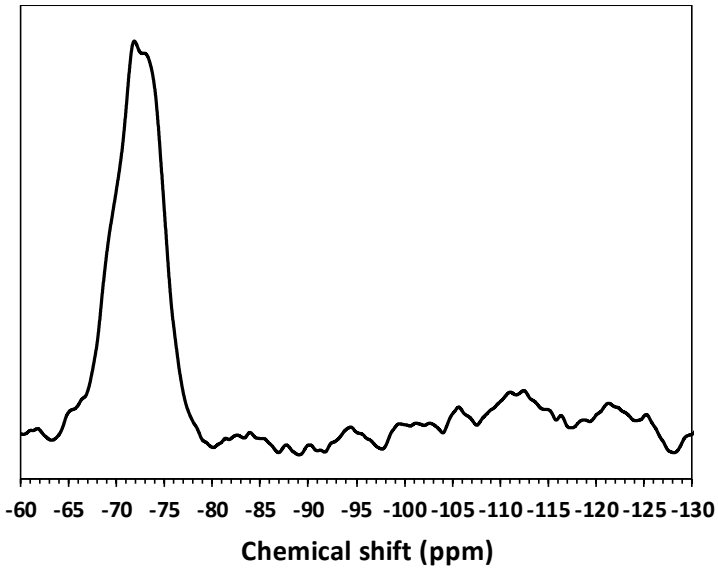

Fig. 2-6. An example of solid-state ^{29}Si NMR for OPC.

2.3.4 Isothermal calorimetry

Isothermal calorimetry, measuring heat emission rate, is one of the most common method to study the hydration of cementitious materials. Isothermal calorimetry quantifies cement hydration kinetics by measuring the heat emission rate in a small sample using a heat flow sensor as heat is conducted to a heat sink that is placed in a thermostated environment. To reduce the noise in the measurement, the reference sample with the same heat capacity but without any heat production is generally required. The typical result from 3 days of isothermal calorimetry for the hydration of cement is presented in Fig.

2-7. For the heat flow curve, the cement hydration can be classified into different period, such as initial (A), induction (B), accelerating (C), and decelerating (D). For the cumulative heat curve, the heat per gram of cement produced during 1 or 3 days of hydration is a standardized measure of the reactivity of cements based on ASTM C1702. The data begins from approximately zero heat and time and there is an initial significant increase in heat when water and cement start to react. Then, after the induction period, the cumulative heat rapidly increases in the accelerating period. After that, the slope of the curve decreases and converges close to approximately zero. Under the assumption that the degree of hydration is a function only of the heat flow, it is possible to qualitatively evaluate the degree and speed of hydration of cementitious materials using the calorimetry. In addition, heat of hydration can be transformed approximately into degree of hydration if the hydration enthalpies of the cement clinker phases and the phase composition of a OPC are obtained. However, in this study, this quantitative method was not performed because it requires a more accurate calculation of the kinetic reactions of the clinker phases and the accuracy is not high.

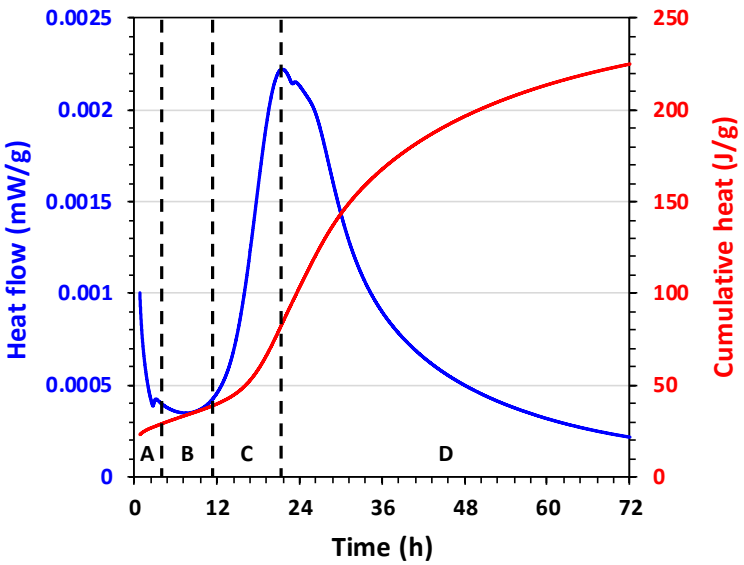

Fig. 2-7. Typical result from 3 days of measurement of isothermal calorimetry.

2.3.5 Mercury intrusion porosimetry (MIP)

Cementitious materials have a lot of multiple size of pores from the micron to the nanoscale. Four main categories of pores are often quoted. The first category is the entrapped and entrained air voids. They are the largest pores in a cement matrix with sizes in the range of micrometers to millimeters and result from imperfect placing. The second and third categories are the macrospores and mesopores, respectively, which are called the capillary pores. They are regarded as the remaining spaces which are not occupied by hydration products or unreacted cement grains. The volume fraction of capillary pores decreases with hydration as cement reacts progressively with capillary water to form hydration products. Thus, the size of capillary pores decreases from initially micrometers to nanometers in well-hydrated cement. The fourth category is generally denominated as the gel pores, which are regarded intrinsic porosity having sizes of nanometer within C-S-H .

Few methods are available to evaluate the complex pore structure of hydrated cementitious materials. One of the most widely applied techniques is mercury intrusion porosimetry (MIP) which can determine various quantifiable characteristics of a porous nature of cementitious materials, such as pore diameter, total pore volume, surface area, and bulk and absolute densities. This method involves the intrusion of a non-wetting liquid (i.e., mercury) at high pressure in to a material through the use of a porosimetry. The pore size can be determined based on the external pressure required to force the liquid into a pore against the opposing force of the liquid's surface tension. A force balance equation known as Washburn's equation under the assumption that the shape of pore is cylindrical is as follow:

$$P_M - P_G = -\frac{4\sigma\cos\theta}{D_P}, \tag{2.2}$$

where P_M is the pressure of mercury, P_G is the pressure of gas, σ is the surface tension of mercury, θ is the contact angle of intrusion mercury, and D_P is the pore diameter. Since the technique is usually conducted within a vacuum state, the initial gas pressure is zero. The contact angle of mercury with cementitious materials is in the range of 130–140 °. The surface tension of mercury under vacuum is approximately 480 dynes/cm at 20 ℃. Thus, the pore diameter can be calculated at a given pressure. As pressure increases, so does the cumulative pore volume. From the cumulative pore volume, one can find the pressure and pore diameter where 50% of the total volume has been added to give the median pore diameter.

An example of MIP results for hydrated cement is shown is Fig. 2-8. By applying preceding approach, the pore structure of hydrated cement can be evaluated in relation to mechanical strength by using the obtained MIP results, such as porosity, ratio of pores for each category, and bulk density.

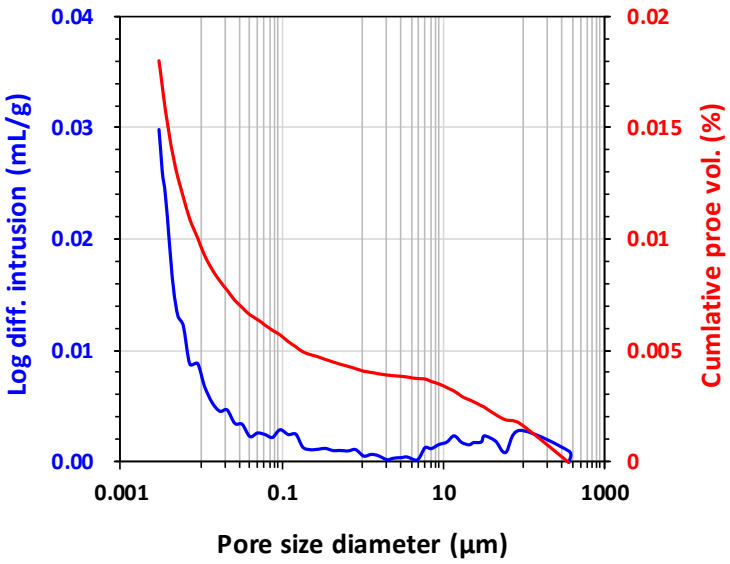

Fig. 2-8. An example of MIP results for the hydrated cement.

2.3.6 Small angle X-ray scattering (SAXS)

Small angle X-ray scattering (SAXS) is a small angle scattering technique by which nanoscale density differences in a sample can be quantified. This indicates that it can evaluate particle size distributions at nanoscale, define the size and shape of macromolecules, determine pore sizes, characteristic distances of partially ordered materials, etc. This can be achieved by analyzing the data, recorded at a small angle (generally 0.1 - 5°, thus the "Small-angle" in its name), for the elastic scattering behavior of X-rays when incident to material. It belongs to the family of small-angle scattering (SAS) techniques along with small-angle neutron scattering (SANS), and is typically done using X-rays.

The basic scheme of a SAXS experiment is illustrated in Fig. 2-9. In a SAXS experiment, when a X-ray source with a wave length λ incident to the sample, a small fraction of X-rays is scattered by the sample and is recorded by the detector. It is considered that scattering is occurred in a particulate system where particles of density ρ_p are dispersed in an uniform solid matrix with a density ρ_m. At this time, the incident beam having a wave vector $\overrightarrow{k_i}$, and the scattered beam with a wave vector $\overrightarrow{k_s}$ make the angle of 2θ with the direction of the transmitted beam. Then, the scattering vector $\vec{q}$ can be calculated as follows:

$$\vec{q} = \overrightarrow{k_i} - \overrightarrow{k_s} = \frac{4\pi \sin\theta}{\lambda}. \tag{2.3}$$

Here, the scattering amplitude *A(q)* is defined by the Fourier transform of the excess scattering length density $\rho(r)$:

$$A(q) \equiv \int_v \rho(r) e^{-iqr} d^3 r, \tag{2.4}$$

where v is the total volume irradiated by the beam, $\rho(r)$ is defined by $\Delta\rho = \rho_m - \rho_p$, r is the object positions. The scattering amplitude is typically converted to radially averaged one-dimensional curves *I(q)*. The low q range of these curves give information on the large distances in the particle. These ranges in a typical X-ray experiment correspond to the physical scattering angles below a few angles, thus the method is called small-angle scattering [82].

Fig. 2-10 shows the schematic illustration of typical log-log SAXS plot for the perfectly fractal structure in term of the transition of q. For very small q (i.e., length scales larger than the biggest inhomogeneities of the sample), the *I(q)* is high and constant. Scattering experiments at higher q range can yield information about the radius gyration (R_g), resolving the biggest structure yielding. At slightly high q, > $1/R_g$, the *I(q)* starts to drop and the slope of the plot (D) can be interpreted as fractal dimension. Here the scales (i.e., -D) are in the range of 2–4. At very high q range produce the Porod scaling of q^{-4} and gives information about the surface structure of the primary particles with a radius of r. The molecular and atomic structure of the samples can be evaluated in this region. However, the order of these regions can be changed according to characteristics of materials. For example, the hydrated cementitious materials are not a perfectly fractal structure, so the Porod region appears in the lower range of q in the log-log SAXS plot.

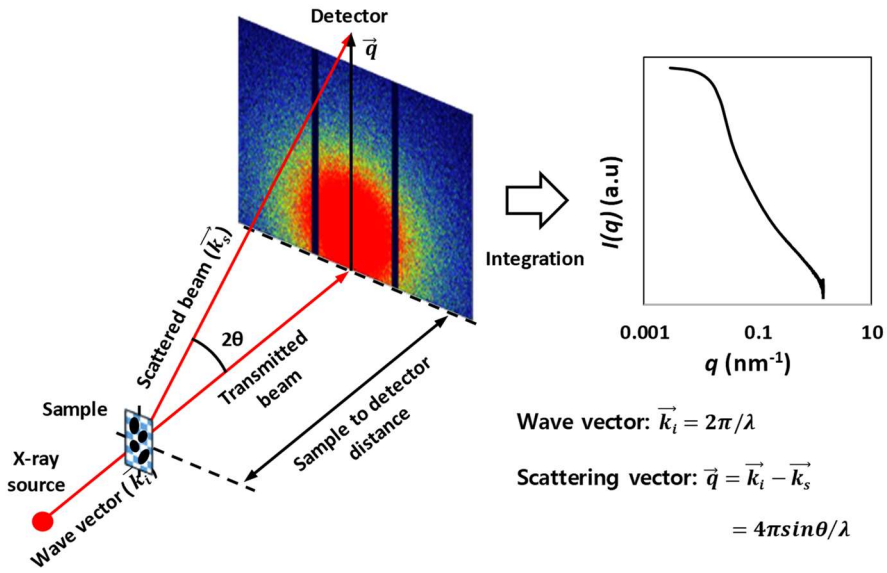

Fig. 2-9. Schematic representation of a SAXS.

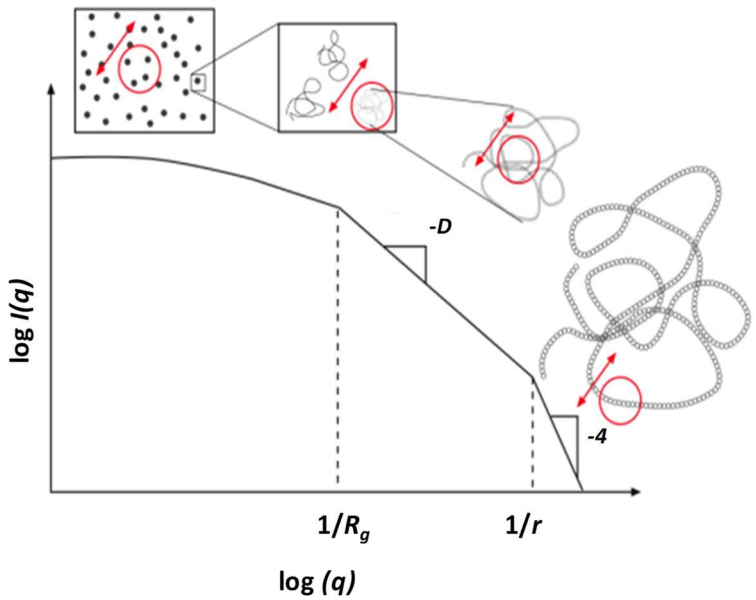

Fig. 2-10. Schematic illustration of typical log-log SAXS plot in terms of scattering vector scale.

Chapter 3. Ozone Treatment for the Dispersion of CNTs and Hydration Acceleration of UHPC

This chapter aimed at investigating the effects of ozone treatment on the dispersion of CNTs in suspension and the resulting influence on the hydration characteristics of UHPC. Small angle X-ray scattering was used to quantitatively evaluate the degree of dispersion of CNTs in UHPC. It was confirmed that the ozone treatment functionalized the CNTs by formulating oxygenic and carboxylic groups on the surfaces of CNTs. In addition, the surface of the cementitious materials was enveloped with the chemical groups present on the CNTs. Thus, the degree of dispersion of CNTs enhanced in both aqueous solution and UHPC. Ozone treatment did not significantly modify the general hydration of UHPC. Instead, it provided multiple nucleation sites and double steric repulsion thorough the improved degree of dispersion of CNTs that resulted in accelerated hydration at early ages, as well as improved compressive strength of the composites at later ages.

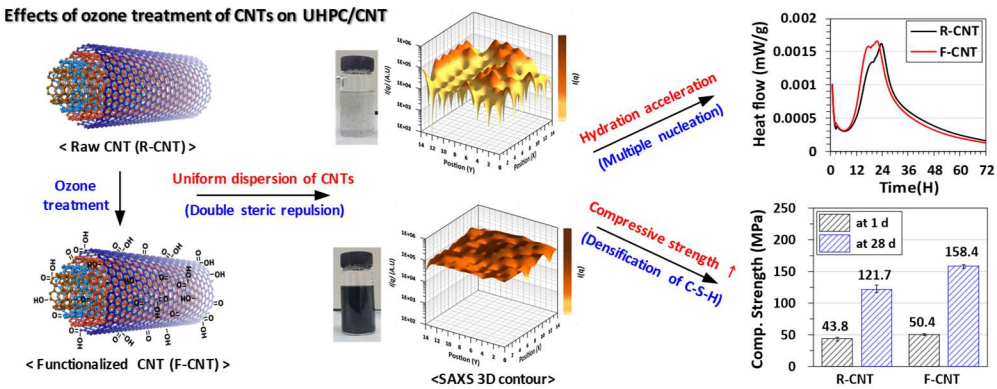

Fig. 3-1. Graphical abstract of chapter 3.

3.1 Introduction

This chapter covered ozone treatment as a new and improved method for better dispersion of CNTs in aqueous solution without damage and to attain enhanced interfacial interaction among various components in UHPC. The degree of dispersion of CNTs in aqueous suspension and solid matrix was successfully evaluated via microscopic, laser diffraction, zeta potential, and spatially-resolved small angle X-ray scattering (SAXS) experiments. Furthermore, microstructural analyses were performed to elucidate the effect of ozone treatment on various material properties of UHPC with regard to flowability, acceleration of hydration reaction, mineralogical changes, and mechanical properties.

3.2 Experimental Details

3.2.1 Properties of CNTs

In this study, commercially available multi-wall CNT powders (LUCAN BT1003, LG Chem., Ltd., Korea) produced via chemical vapor deposition (CVD) method were used and their properties are listed in Table 3-1. The particle size distribution and zeta potential measured using a laser scattering particle size analyzer (LA 960, HORIBA, Japan) and nano-particle analyzer (sz-100, HORIBA, Japan) are presented in Fig. 3-2 and Fig. 3-3, respectively. The mean particle size, zeta potential, and mobility were 501.6 μm, -2.0 mV, and -0.0016 mm^2/Vs, respectively. These result indicate that before dispersion, the raw CNTs were strongly attracted each other and became agglomerated considering their originally synthetized size properties (Table 3-1) due to its characteristics such as high aspect ratios, high specific surface areas, and strong Van der Waals forces.

Table 3-1. Properties of multi-wall CNTs.

Avg. diameter (nm)	Avg. length (μm)	Bulk density (g/cm^3)	Purity (wt.%)	Specific surface area (m^2/g)
13	12	0.12	96	186

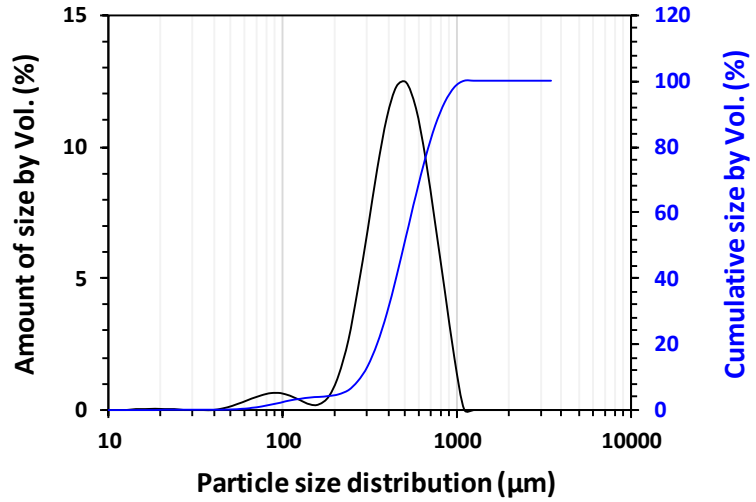

Fig. 3-2. Particle size distribution of raw CNTs.

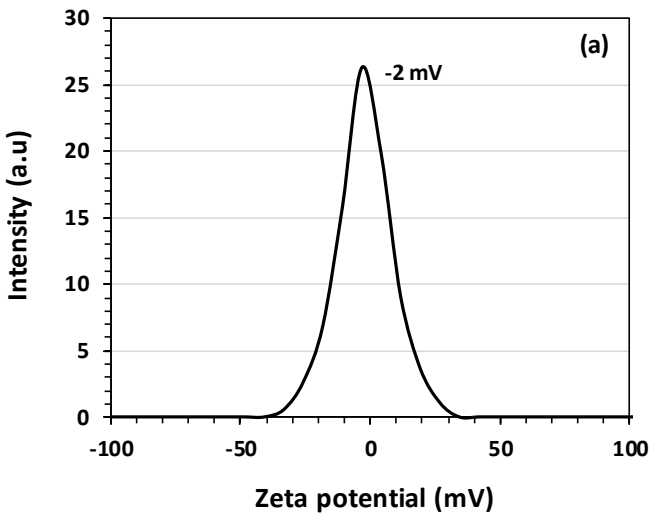

Fig. 3-3. Zeta potential (a) and electrophoretic mobility (b) of raw CNTs.

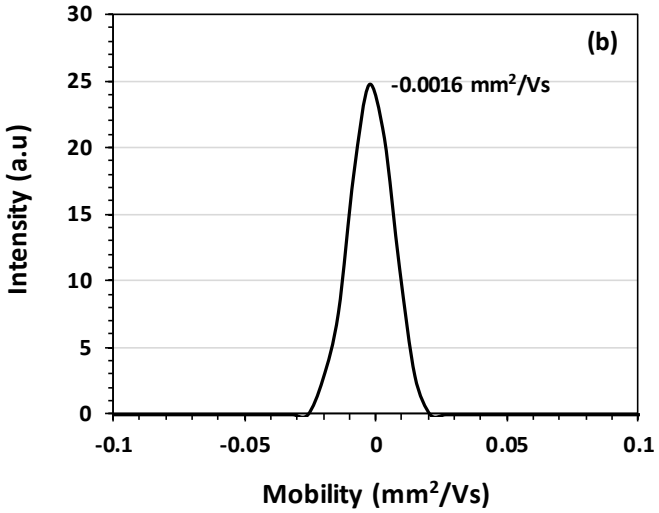

Fig. 3-3. *(Continued)* Zeta potential (a) and electrophoretic mobility (b) of raw CNTs.

3.2.2 Mixture proportions and sample preparation

Table 3-2 presents the mixture proportions. The water to cement ratio (w/c) was kept at 0.23. The water used in the reference sample was replaced by ozone water CNT0-O_3 produced via ozone treatment. In addition, 0.1 wt.% of CNTs was mixed with the reference UHPC mixture to form a UHPC/CNT in two ways: without applying ozone treatment (CNT0.1-P) and with the application of ozone treatment (CNT0.1-O_3).

Table 3-2. Mixture proportions (wt.% of cement).

Sample	w/c	OPC	Silica fume	Silica powder	Silica sand	Super-plasticizer	CNTs	Ozone treatment
CNT0 (Ref.)	0.23	1	0.25	0.35	1.1	0.05	-	×
CNT0-O_3							-	O
CNT0.1-P							0.001	×
CNT0.1-O_3							0.001	O

The samples for isothermal calorimetry, X-ray diffraction (XRD), and thermogravimetric (TG) analyses were synthesized without silica sand, whereas the samples for scanning electron microscopy (SEM), SAXS, and compressive strength test were fabricated following the proportions detailed in Table 3-2.

Sample preparation comprised of four steps: (a) fabrication of CNT suspension; (b) mixing of the dry pre-mixture with the CNT suspension; (c) sample casting; and (d) curing.

First, a CNT suspension was fabricated via ozone treatment (Fig. 3-4). Distilled water was added into the vessel of portable ozone generator with a polycarboxylic acid-based superplasticizer. Then, CNTs were added in the vessel and activated the plasma for 10 min to generate ozone in aqueous suspension. During ozone treatment, the suspension was circulated using a bubble generator installed under the vessel to attain uniform dispersion of CNTs. The highest ozone concentration (after ozone treatment) in the suspension measured by DOZ30 (Clean instrument, China) was approximately 0.1 ppm. In case of CNT0-O_3, the same procedure followed albeit without the addition of CNTs. For CNT0.1-P, a CNT suspension was fabricated by mixing water, superplasticizer, and CNTs by hand stirring for 10 min (step a).

Once the CNT suspension was prepared, a dry pre-mixture was fabricated by blending the cementitious materials homogeneously using a Hobart mixer for 5 min. Then, the dry pre-mixture was mixed with the CNT suspension for 5 min. Thereafter, the synthesized fresh mixtures were placed in molds (step b).

Cubic samples with volumes of 50 × 50 × 50 mm^3 were prepared to measure the compressive strength. In addition, samples for SEM and SAXS analyses were fabricated using a cylindrical mold with a height of 1.5 mm and a diameter of 25 mm (step c).

The samples were cured at a temperature of 20 ℃ and at a relative humidity (RH) of 99 % in a sealed chamber for 24 h; they were further cured under air-drying conditions in a chamber at 20 ℃ and at RH of 60 % until the subsequent tests (step d).

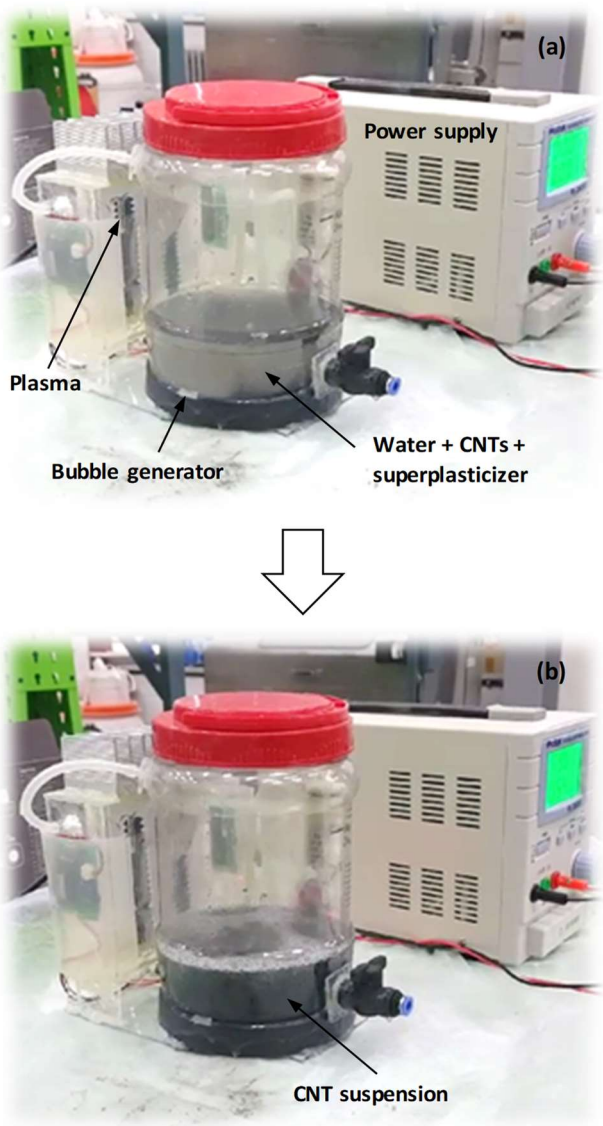

Fig. 3-4. Fabrication of CNT suspension via ozone treatment: (a) before, (b) after.

3.2.3 Test methods

To evaluate the effect of ozone treatment on the dispersion of CNTs in the aqueous phase, morphology of the CNTs in the suspension was examined under a light microscope (DM1750M, Leica, Germany) during fabrication of the CNT suspension. In addition, particle size and zeta potential analyses were performed using the LA-960 and sz-100, respectively. The experiments were performed 10 min after the complete fabrication of CNT suspension (i.e., the experiments were conducted after the CNT suspension was completely stabilized) to avoid the possibility of CNT movement in the suspension negatively affecting on the test results.

The effect of ozone treatment on the dispersion of CNTs in hardened UHPC was evaluated in terms of the fluidity, SEM, and spatially-resolved SAXS analyses. The fluidity of fresh mixtures was measured using a flow table according to American society for testing and materials (ASTM) C1856 [83]. A mold with inner diameter of the upper and lower openings being 70 mm and 100 mm, respectively, was used. The SEM (JSM-7800F Prime, JEOL Ltd., Japan) and SAXS (XEUSS2.0, Xenocs, France) analyses were performed using samples for which the hydration was terminated at 28 d. The SAXS analysis was performed in the q (scattering vector = 4π sin [θ] / λ, where λ denotes the incident wavelength of the X-ray and θ represents the scattering angle) range of 0.001–0.8 $Å^{-1}$. The X-ray source was operated at 50 kV/0.6 mA with CuKα (λ = 1.5418 Å) and sample-to-detector distance was 270 mm. A total of 64 points were analyzed within a 16 × 16 mm^2 square on the surface of each sample, at intervals of 2 mm (Fig. 3-5). The step size and exposure time for each point were 0.002336 Å and 60 s, respectively.

To investigate the effect of ozone treatment and CNTs on the acceleration of hydration reaction of UHPC at early ages, isothermal calorimetry was measured for 72 h using a TAM Air system (TA

instruments, USA). The hydration heat of 10 g fresh mixture was measured under isothermal conditions at 20 ℃. The obtained heat flow and cumulative heat were normalized by the weight of the binder. Then, the onset of the acceleration period (OAP) was derived from the calorimetric curve in two steps by modifying the methods previously reported in literature [84, 85] as illustrated in Fig. 3-6. First, minimum heat flow during the dormant period was determined. Second, a linear regression for the acceleration period in the heat flow range of 0.0005–0.001 mW/g was estimated. Then, the hydration time at the intersection point of the minimum heat flow and the linear regression during the induction period marked the beginning of the acceleration period.

XRD and TG experiments were performed using samples with hydration stoppage at 1 d and 28 d of curing. The XRD analysis was performed using a D2 Phaser (Bruker, Germany) with CuKα (λ = 1.5418 Å) radiation at 30 kV and 10 mA, a step size of 0.02027 ° and 2 s per step were employed over a 2θ range of 5–50°. The International Centre for Diffraction Data (ICDD) PDF database was utilized for phase identification. TG analysis was conducted using a TA instrument Q500 (Bruker, Germany) under a N_2 condition at a heating rate of 10 K/min up to 1050 ℃. The first derivative of the TG curve (DTG) was derived to identify the weight loss of several hydration products.

Compressive strength of the samples was measured at 1 d and 28 d according to ASTM C109 [28]. A displacement-controlled universal testing machine (UTM) was used with a load cell capacity of 2000 tons by applying a loading rate of 0.02 mm/s. The strength was calculated as follows and determined as the average of the strength of three samples.

$$\text{Compressive strength (MPa)} = P / A, \tag{3.1}$$

where P is the maximum load (N) and A is the surface area (mm^2).

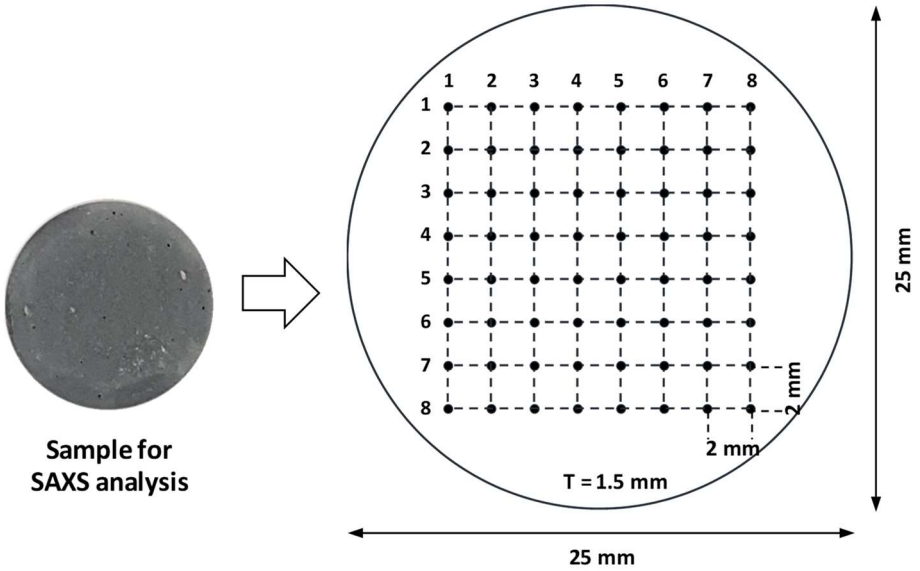

Fig. 3-5. 64 points in a sample for the spatially-resolved SAXS analysis.

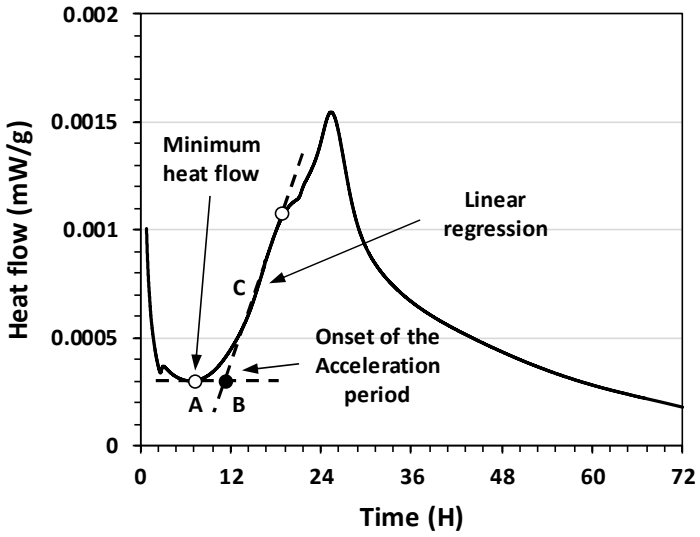

Fig. 3-6. Typical hydration heat flow of cementitious material and calculation method used to define the onset of the acceleration.

3.3 Results and Discussion

3.3.1 Effect of ozone treatment on dispersion of CNTs

3.3.1.1 Effect of ozone treatment on dispersion of CNTs in aqueous

Fig. 3-7 shows the CNT suspension fabricated with and without ozone treatment. It is clear that the degree of dispersion (DOD) of CNTs between samples is substantially different. For the suspension produced without applying ozone treatment (CNT0.1-P), the CNTs were not well-dispersed despite the addition of 5 wt.% of super plasticizer was incorporated. On the contrary, for the CNT suspension produced by ozone treatment (CNT0.1-O_3), no visible sedimentation was observed even after 10 min. Similarly, on a microscopic level, it was found that the CNTs in the suspension CNT0.1-P were not well-dispersed during the development of the CNT suspension. On the contrary, it was observed that the CNTs in the suspension CNT0.1-O_3 were significantly dispersed as the ozone treatment progressed (Fig. 3-8).

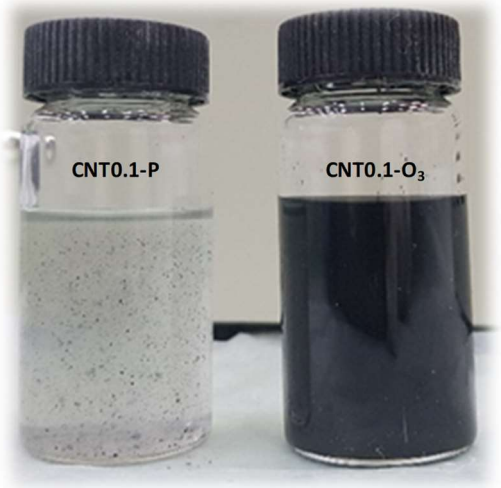

Fig. 3-7. CNT suspensions without ozone treatment (CNT0.1-P) and with ozone treatment (CNT0.1-O_3).

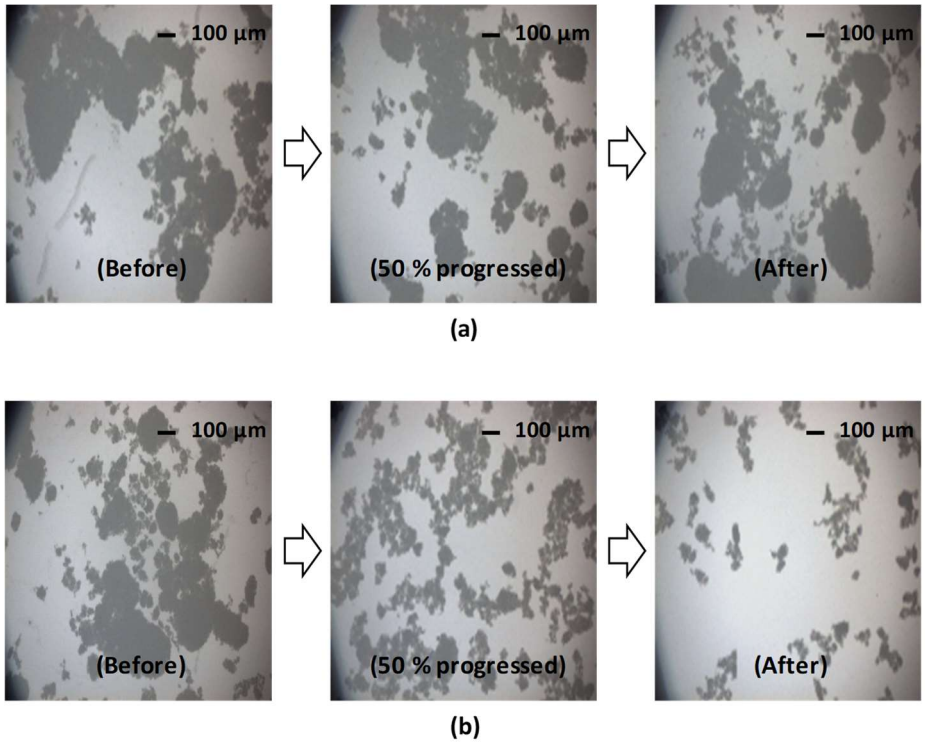

Fig. 3-8. Morphology of the CNTs in an aqueous during fabrication of CNT suspension: (a) CNT0.1-P, (b) CNT0.1-O_3.

The DOD and stability of CNTs in suspension were quantitatively analyzed using laser diffraction and zeta potential measurements (Fig. 3-9 and Fig. 3-10). For the CNT suspension CNT0.1-P, the obtained particle size, zeta potential, and mobility were 428.6 μm, -2.9 mV and -0.2 mm^2/Vs, respectively. These results indicate that the CNTs were still strongly agglomerated considering the particle size of the raw CNTs, though the particle size was slightly reduced. In addition, low magnitude of zeta potential and mobility values represent that attractive forces between CNTs could exceed the electrostatic repulsion. Thus, it confirmed that CNTs could not effectively dispersed in aqueous without applying specific dispersion method. In contrast, for the CNT suspension CNT0.1-O_3, the mean particle size significantly reduced to

116.2 μm with a reduction rate of 77.1 %. In addition, the magnitude of zeta potential and mobility remarkably improved to -22.3 mV and -1.7 mm^2/Vs, which corresponds to values 7.7 and 8.5 times higher, respectively. This is because the carboxylic groups of superplasticizer and oxygenic groups of ozone water could be effectively attached to the surfaces of the CNTs through the ozone treatment. Specifically, the oxygen atom produced via ozone oxidation, which is a heteroatom with significant electronegative characteristics than carbon, altered the electronic properties of the CNTs and behaved as an intermediate between carboxylic groups and CNTs [22]. As a result, the CNTs were functionalized and the chemical groups with negative charges attached on the surfaces of CNTs dispersed the CNTs through electrostatic repulsion and prevented them from agglomerating in an aqueous solution through steric stabilization. Hence, it can be concluded that even with a low level of ozone treatment can effectively disperse CNTs in an aqueous solution without damage.

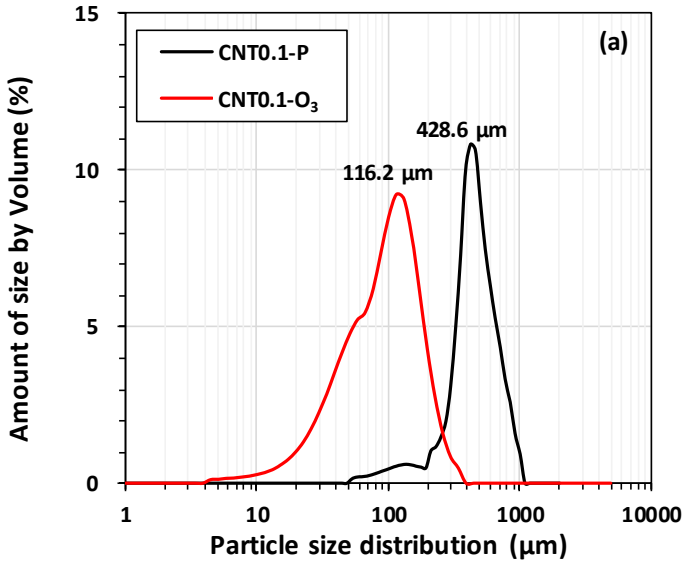

Fig. 3-9. Particle size distribution of the CNT suspensions: (a) amount of size by vol.%, (b) cumulative size by vol.%.

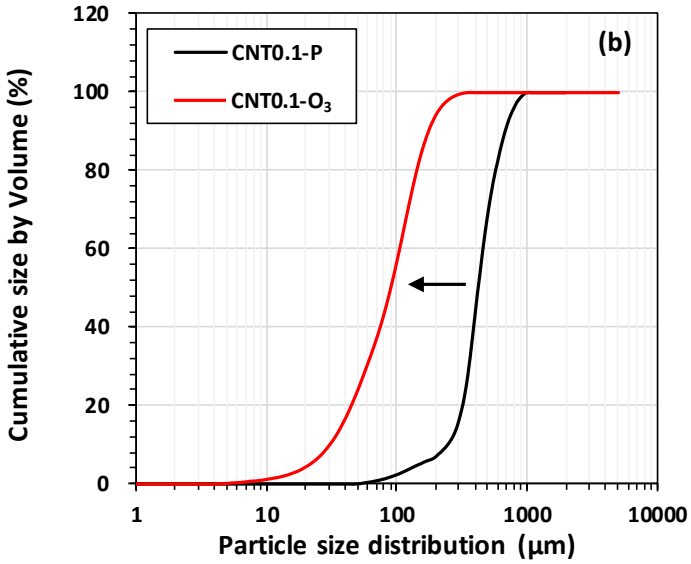

Fig. 3-9. *(Continued)* Particle size distribution of the CNT suspensions: (a) amount of size by vol.%, (b) cumulative size by vol.%.

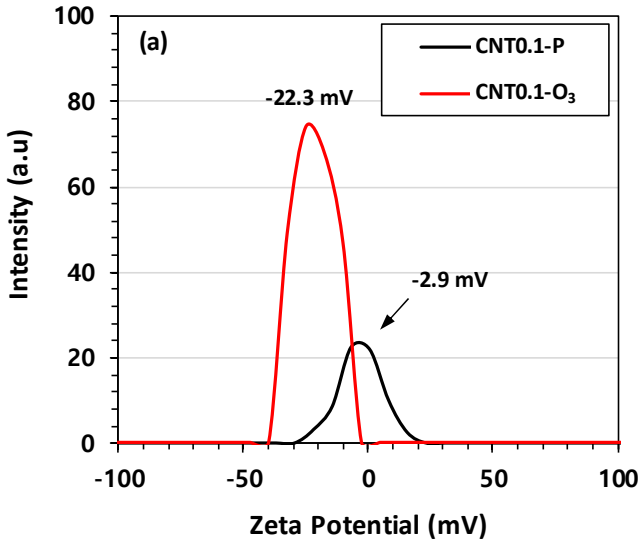

Fig. 3-10. Zeta potential (a) and electrophoretic mobility (b) of the CNT suspensions.

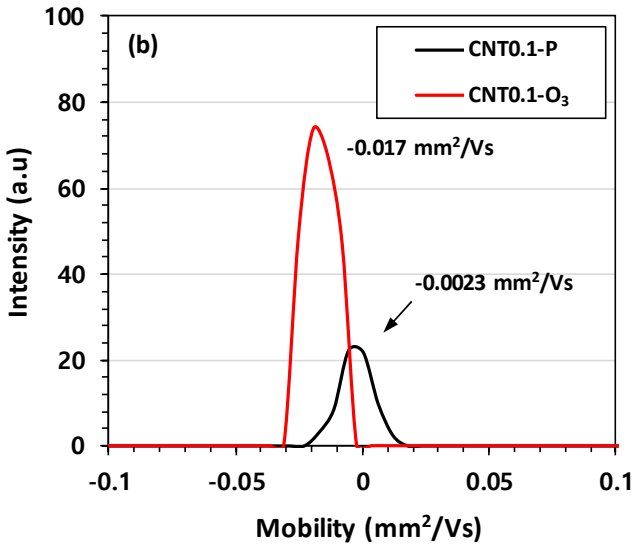

Fig. 3-10. *(Continued)* Zeta potential (a) and electrophoretic mobility (b) of the CNT suspensions.

3.3.1.2 Effect of ozone treatment on dispersion of CNTs in UHPC

Fig. 3-11 shows the fluidity of the fresh mixtures. The fluidity of the CNT0 (Ref.) and CNT0-O_3 were almost identical in the range of 23.3–23.5 cm. This indicates that the ozone treatment did not affect the fluidity of the UHPC, in the cases where no CNTs were added. The fluidity of the CNT0.1-P significantly reduced to 20.1 cm, with a decrease of 13.8 %. This is due to the characteristics of the CNTs: high aspect ratio, high specific surface areas, and strong Van der Waals forces. In addition, incorporating fibers into cementitious materials generally reduces flow regardless of the type of fiber [86]. However, the fluidity of the CNT0.1-O_3 increased to 22.9 cm, though the flow value was slightly lower than that of the reference sample. This is because the oxygenic and carboxylic groups formed on the surfaces of the CNTs exhibited the steric repulsion as demonstrated in Fig. 3-10. In addition, they also envelop the surfaces of cementitious materials via intermolecular interactions during mixing. This strong steric repulsion

effect pushes the cementitious materials and CNTs each other [87]. This double steric repulsion effect resulted in the increase of fluidity.

Fig. 3-12 shows the morphologies of the CNTs in the UHPC. For the CNT0.1-P, it was generally difficult to find CNTs, and the found CNTs were heavily agglomerated (Fig. 3-12a). There were no signs of uniform distribution of CNTs throughout the sample. Thick clumps of CNT agglomerates were found and the hydration products of the UHPC did not incorporate these CNTs. On the other hand, the ozone treatment provided reasonably uniform dispersion and distribution of CNTs within the hydration products of CNT0.1-O_3 (Fig. 3-12b).

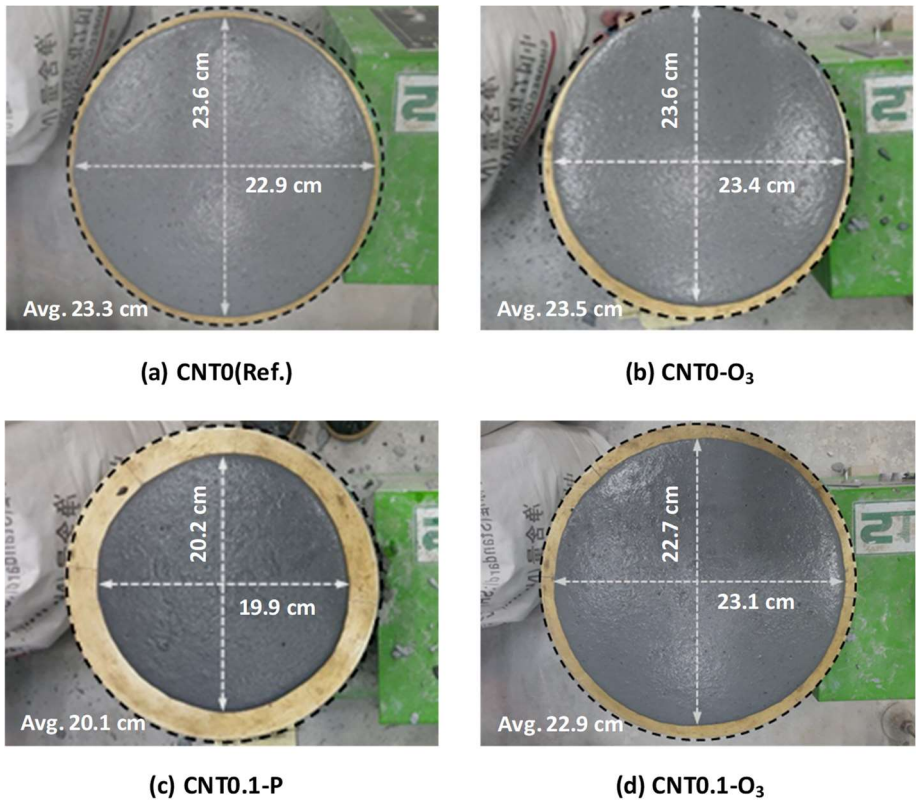

Fig. 3-11. Fluidity of the fresh mixtures: (a) CNT0 (Ref.), (b) CNT0-O3, (c) CNT0.1-P, and (d) CNT0.1-O_3.

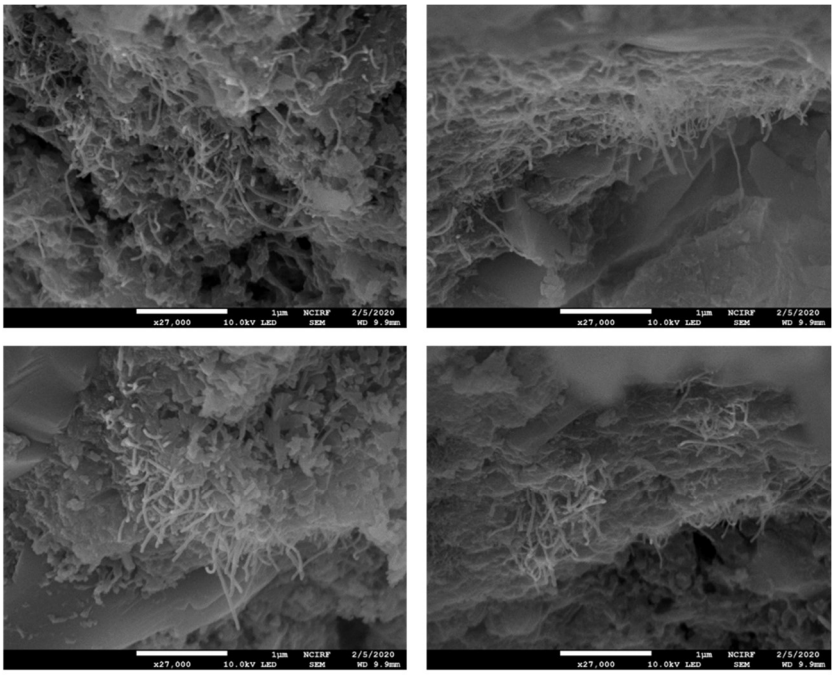

(a) CNT0.1-P

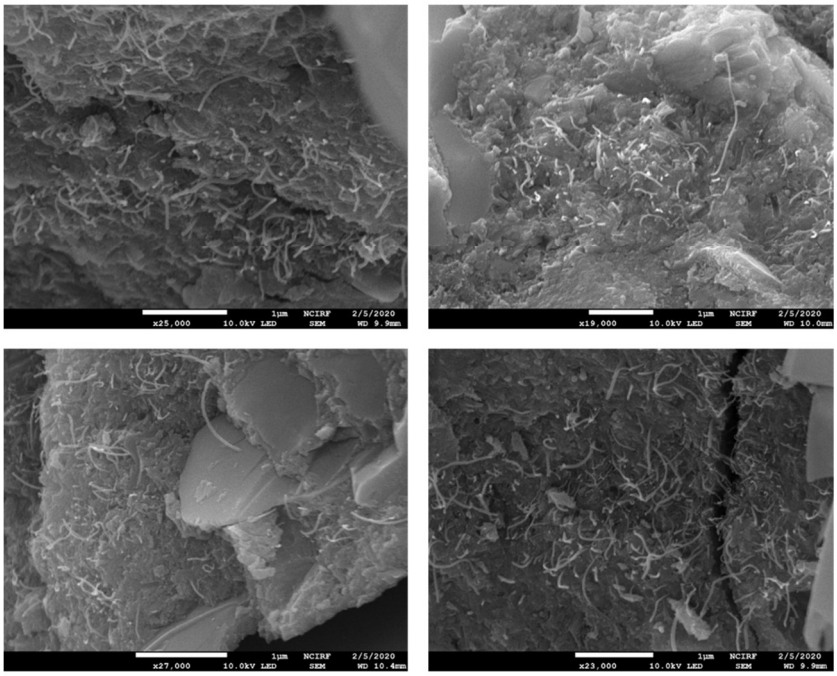

(b) CNT0.1-O_3

Fig. 3-12. SEM images of the samples at 28 d: (a) CNT0.1-P, (b) CNT0.1-O_3.

In addition, the DOD of CNTs in the UHPC was successfully evaluated using spatially-resolved SAXS analysis. Because CNTs are strong field emitters with high current density owing to extraordinary electrical properties, the intensity of the SAXS plot measured at the point of the UHPC embedded with CNTs would be much higher than that of the plain UHPC.

Fig. 3-13 show a total of 64 SAXS plots measured at the different spots in each sample. For the reference sample, the SAXS patterns were almost identical. Therefore, the CNT0 (Ref.) can be regarded as uniformly fabricated. However, the SAXS plots for the CNT0.1-P shows substantial variation depending on the pre-defined measurement locations (Fig. 3-5). This is due to that the CNTs were not evenly distributed throughout the sample. Specifically, the intensities at the points of high CNT concentration were high, whereas that of the points of low CNT concentration were low (i.e., the intensities were similar to those of the reference sample). In case of the point where the CNTs were concentrated, there is a sign that CNTs were strongly agglomerated because large number of CNTs in a given volume of UHPC shorten the relative distance between CNTs, which lead to strengthening the Van der Waals forces. On the contrary, it can be observed that all the SAXS plots for the CNT0.1-O_3 showed similar patterns with much higher and more uniform intensities in comparison to the of the CNT0 (Ref.) and CNT0.1-P samples, respectively. This experimental result provides a strong quantitative indication of higher DOD in the CNT0.1-O_3 sample.

The SAXS plots were converted to a 3D contour plot for visually evaluating the DOD of the CNTs by measuring the samples according to X and Y coordinates, with the intensity corresponding to a q value of 0.0014 $Å^{-1}$, which exhibited the highest intensity in the SAXS plots, along the Z axis. It is confirmed that the CNTs were poorly distributed and highly agglomerated in the CNT0.1-P, whereas they were uniformly distributed in the CNT0.1-O_3 due to the ozone treatment.

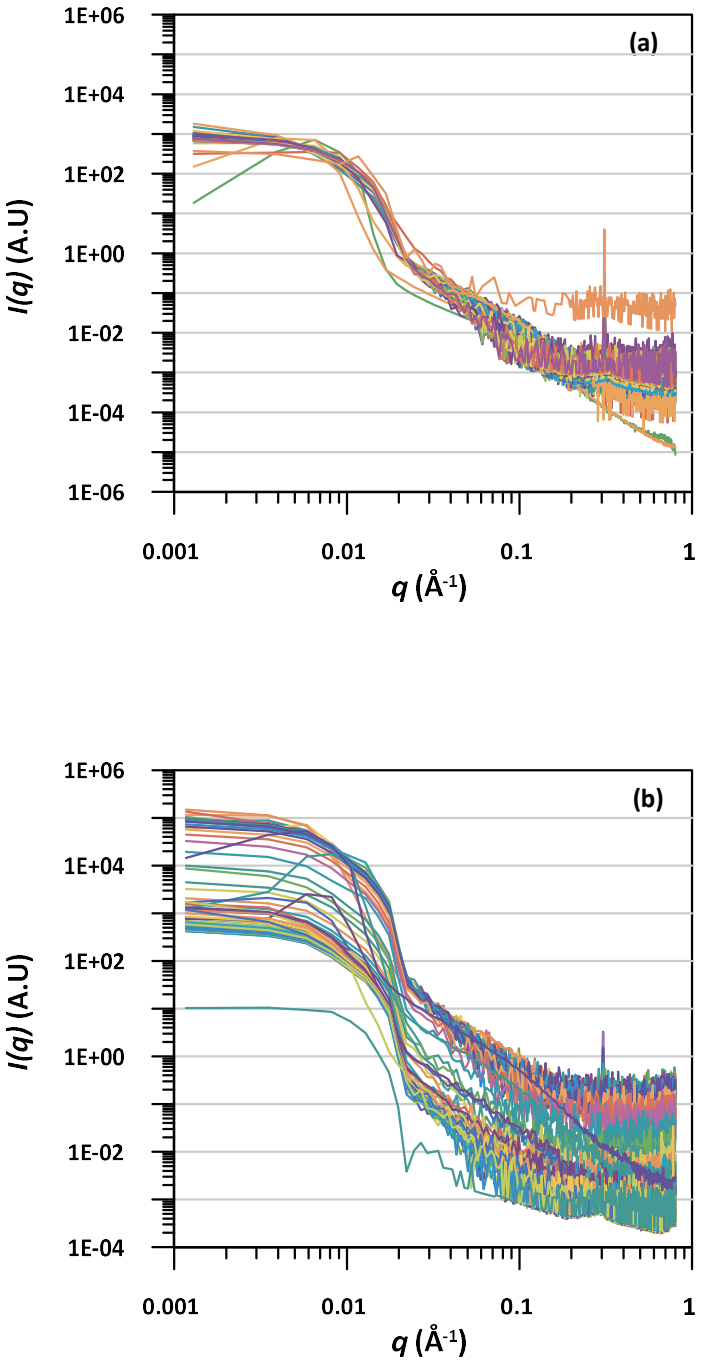

Fig. 3-13. A total of 64 SAXS curves measured at each sample: (a) CNT0 (Ref.), (b) CNT0.1-P, and (c) CNT0.1-O_3.

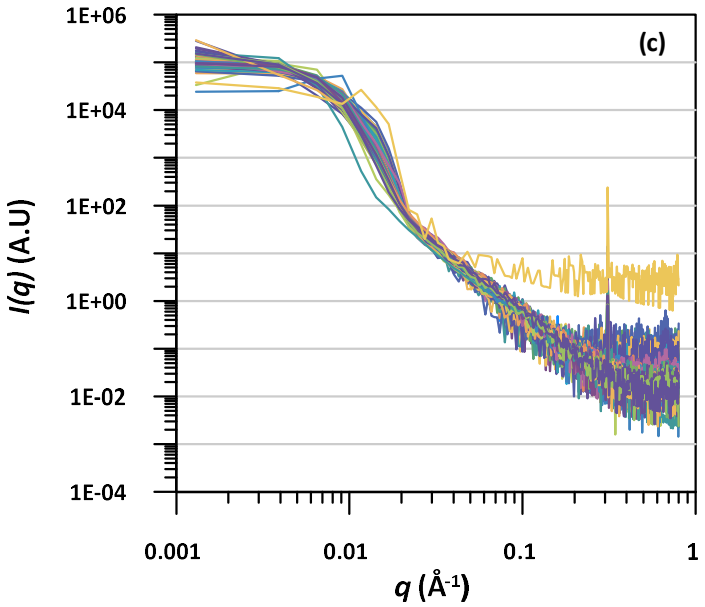

Fig. 3-13. *(Continued)* A total of 64 SAXS curves measured at each sample: (a) CNT0 (Ref.), (b) CNT0.1-P, and (c) CNT0.1-O_3.

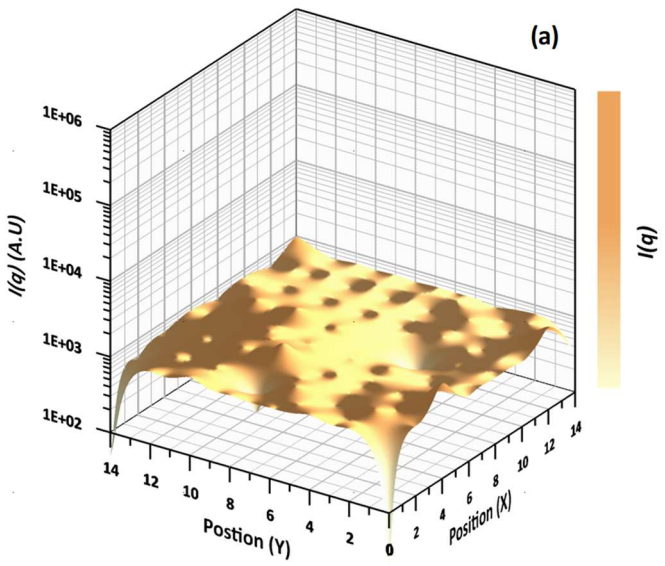

Fig. 3-14. SAXS 3D contour of the samples by making the measured point of sample to X and Y coordinates and the intensity at 0.0014 $Å^{-1}$ of q to Z coordinates: (a) CNT0 (Ref.), (b) CNT0.1-P, and (c) CNT0.1-O_3.

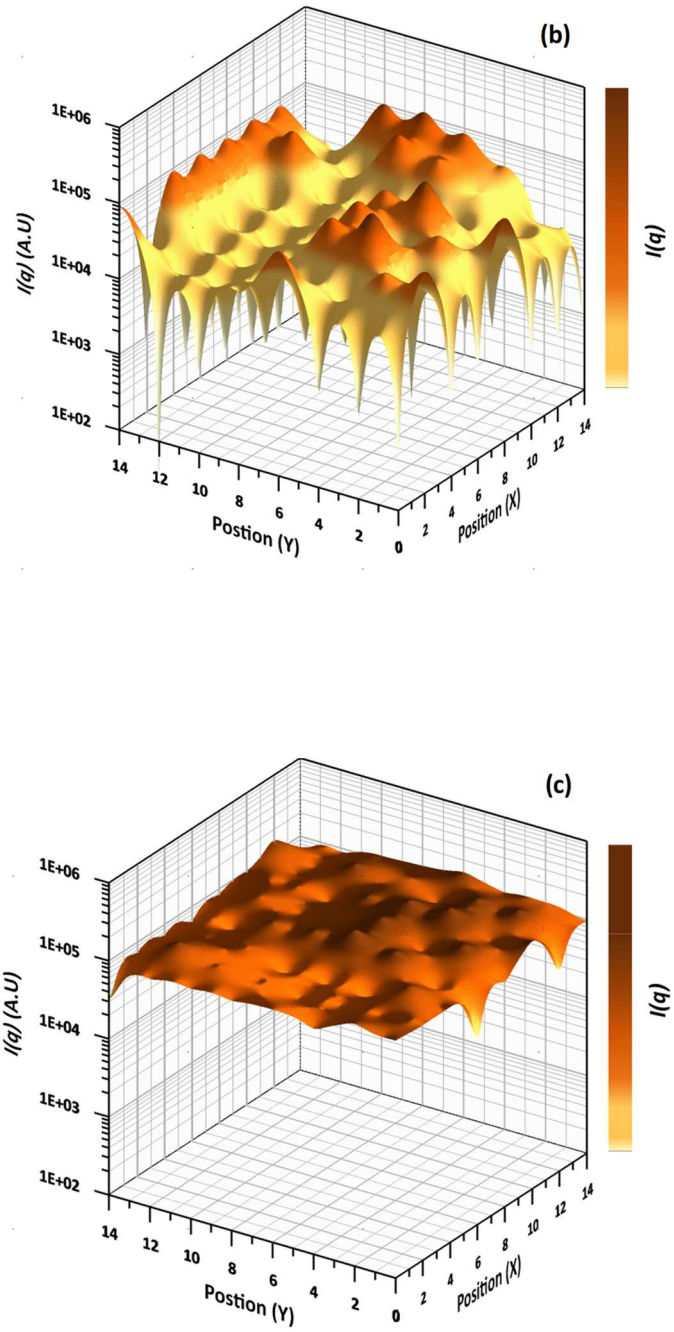

Fig. 3-14. *(Continued)* SAXS 3D contour of the samples by making the measured point of sample to X and Y coordinates and the intensity at 0.0014 $Å^{-1}$ of q to Z coordinates: (a) CNT0 (Ref.), (b) CNT0.1-P, and (c) CNT0.1-O_3.

In summary, the low concentration of ozone treatment led to the attachment of oxygenic and carboxylic chemical groups on the surfaces of the CNTs. This leads to increase of the steric repulsion forces of the CNTs and prevents them from agglomerating in the aqueous solution. In addition, the chemical groups are not only attached on the CNTs but also enveloped the surfaces of cementitious materials, exhibiting a strong steric repulsion effect and leading to a uniform distribution of CNTs in the UHPC. The increased uniformity of the UHPC/CNT composites was successfully evaluated using spatially-resolved SAXS measurements.

3.3.2 Effect of ozone treatment on hydration of UHPC composite

3.3.2.1 Hydration reaction at early ages

The results of isothermal calorimetric and the characteristic values from heat flow curves are presented in Fig. 3-15 and Table 3-3, respectively. The heat flow of all the samples showed a relatively longer induction period caused by a high dosage of superplasticizer and a second peak due to the incorporation of a large amount of amorphous silica [88]. The curve patterns and characteristic values for the reference sample and CNT0-O_3 were similar. This demonstrates that the ozone treatment does not affect both the main hydration reaction of UHPC and its fluidity. However, with the addition of CNTs, the OAP was shifted to an earlier time and the slope became steeper with increased magnitude regardless of ozone treatment. In addition, the magnitude increments of the second peak (indicating hydration of aluminate, C_3A) was higher than that of first peak (indicating hydration of alite, C_3S). This indicates that CNTs acted as nucleation sites for both cement clinkers of C_3S and C_3A, resulting in the acceleration of the hydration reaction [89]. Such behavior was more remarkable when the ozone treatment was applied; dispersed CNTs with smaller

agglomerate size via ozone treatment were distributed on a much finer scale. It enhanced the nucleation effect, further accelerating the hydration reaction [90]. Thus, it can be concluded that ozone treatment itself does not modify the main hydration reaction of UHPC but can accelerate the hydration of UHPC/CNT at early ages by causing better dispersion of CNTs (i.e., acting as multiple nucleating agents).

Table 3-3. Characteristic values from heat flow curve of the samples.

Sample	Minimum heat flow (mW/g)	Onset of acceleration period (h)	Slope (mW/g/h)
CNT0 (Ref.)	0.0003	10.88	0.000097
CNT0-O_3	0.00029	10.93	0.00009
CNT0.1-P	0.0003	10.39	0.00014
CNT0.1-O_3	0.00031	9.54	0.00017

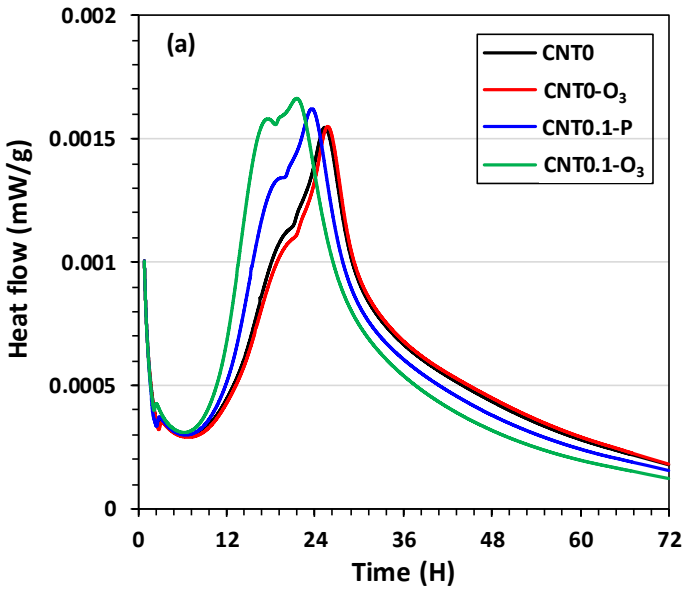

Fig. 3-15. Heat flow (a) and cumulative heat (b) of the samples.

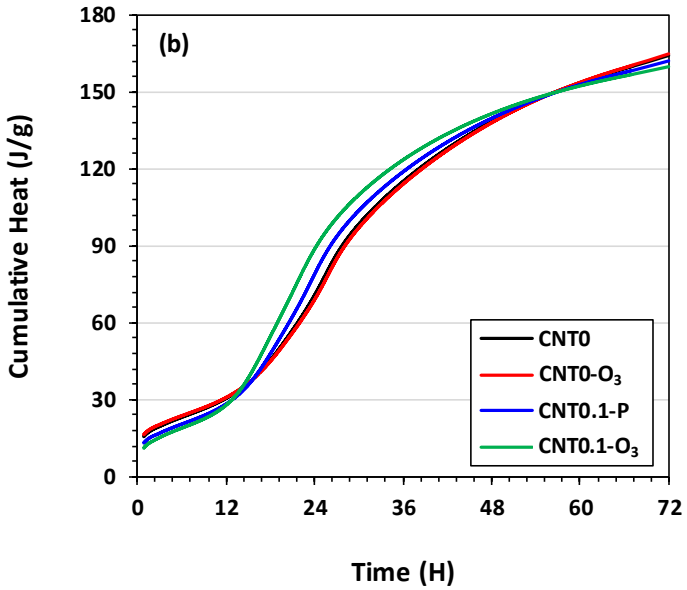

Fig. 3-15. *(Continued)* Heat flow (a) and cumulative heat (b) of the samples.

3.3.2.2 X-ray diffraction

Fig. 3-16a shows the XRD patterns of the raw materials (i.e., OPC, silica fume and silica powder). Major crystalline phases in the anhydrous OPC were belite (C_2S), C_3S, C_3A, and gypsum. In addition, calcite ($CaCO_3$, ISCD# 98-022-1912) was observed at 23.1°, 29.2°, 35.9°, 43.1°, 47.5° and 48.5 °. A diffused band in the range of 15–30° in the silica fume corresponds to amorphous silica. In the silica powder, the peaks corresponding to quartz (SiO_2, ISCD# 98-008-3849) were observed at 21.0°, 26.5°, 36.5°, 39.5° 40.0°, 42.5°, 45.8°, and 50.1° respectively.

The XRD patterns of the samples are presented in Fig. 3-16b–c. The products of the samples produced by main hydration reaction were calcium-silicate-hydrate (C-S-H), portlandite ($Ca(OH)_2$, CH, ISCD # 98-005-1411), and ettringite (ISCD # 98-015-5395). The intensity peaks corresponding to the silica powder and quartz did not show

noticeable change in all the samples because most of them had the characteristics of inert fillers unless they are exposed to 150 ℃ or higher temperature [81, 91]. It was observed that there was no significant difference between the XRD patterns of the reference sample and CNT0-O_3 regardless of the curing period. This also supports the previous observation that the ozone water did not affect the main hydration reaction of the UHPC.

In the XRD patterns of the samples at 1 d (Fig. 3-16b), the peak associated with gypsum was slightly decreased in both the reference sample and CNT0-O_3, as compared to that of anhydrous OPC, while the peak almost vanished in both CNT0.1-P and CNT0.1-O_3. In addition, for the samples containing CNTs, the intensity of the peaks corresponding to ettringite and portlandite significantly increased, whereas that of the peaks indicating clinkers (especially, C_3S and C_3A) remarkably decreased. Such behavior was much more significant when the ozone treatment was applied (i.e., in the case when dispersed CNTs were incorporated into UHPC). This confirms that CNTs accelerated the hydration of UHPC at early ages by nucleating the sites of hydration products (produced from C_3S and C_3A), which is the same reasons mentioned in section 3.3.2.1; this effect was enhanced following the ozone treatment.

In the XRD patterns of the samples at 28 d (Fig. 3-16c), the peak corresponding to portlandite almost disappeared for all the samples because of the pozzolanic reaction. Thus, it is shown that the predominant reaction during the early ages was the hydration of clinker phase (C_2S, C_3S, and C_3A), while the pozzolanic reaction of amorphous silica begins at a later stage [88]. A qualitative comparison of the degree of hydration (DOH) among the samples was difficult in the case of XRD patterns; however, the DOH of the CNT0.1-P appeared to be lower because the peaks corresponding to clinkers were slightly higher than those of the others.

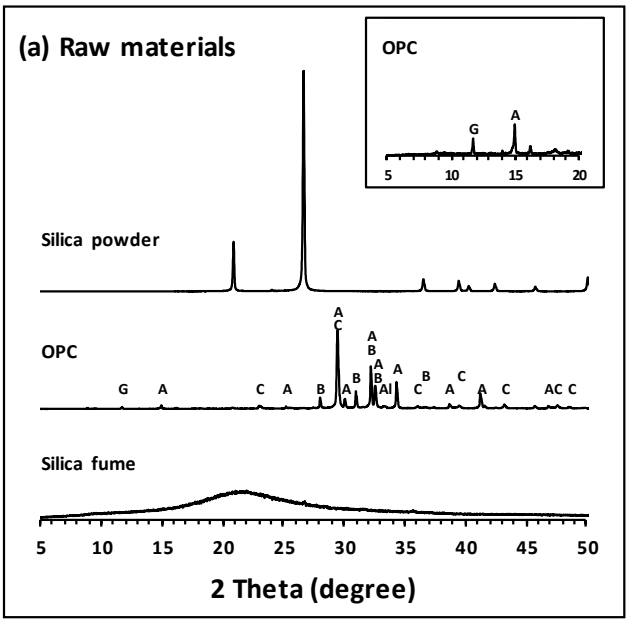

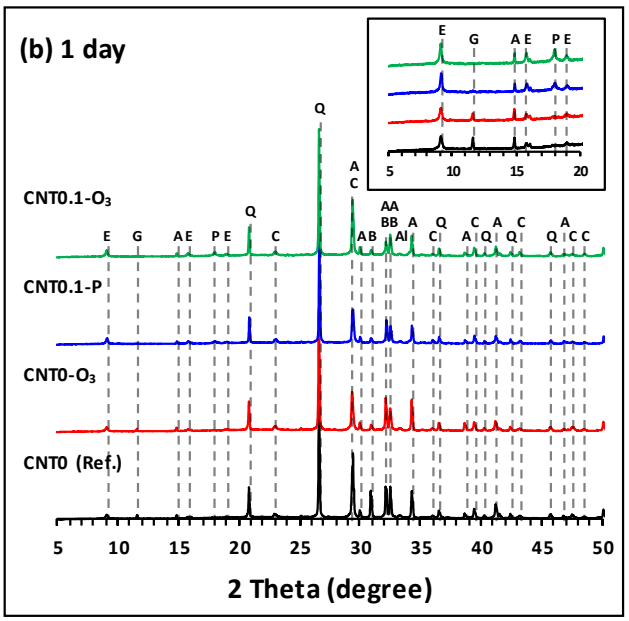

Fig. 3-16. XRD patterns of the samples: (a) raw materials, (b) at 1 d, and (c) at 28 d (A : alite; Al : aluminate; B : belite; C : calcite; E : ettringite; G : gypsum; P : portlandite; Q : quartz).

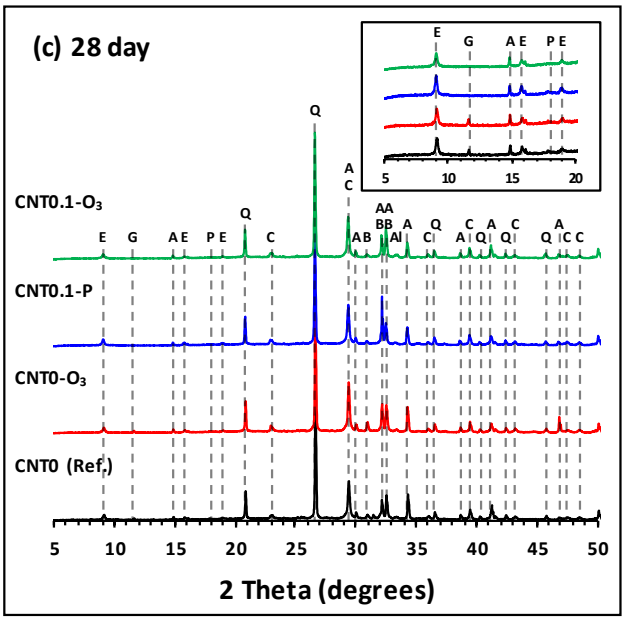

Fig. 3-16. *(Continued)* XRD patterns of the samples: (a) raw materials, (b) at 1 d, and (c) at 28 d (A : alite; Al : aluminate; B : belite; C : calcite; E : ettringite; G : gypsum; P : portlandite; Q : quartz).

3.3.2.3 Thermogravimetric analysis

Fig. 3-17a shows the TG and DTG curves of the samples at 1 d. The DTG curves of all the samples showed a weight loss at a temperature of approximately 100 ℃ due to the evaporation of free water, physically bound water, and dehydration of ettringite and C-S-H. The weight loss at this region can also result from the presence of third aluminate hydrate (TAH) species which decomposes at 70–90 ℃. The weight loss at a temperature of 140 ℃ indicates the dehydration of the Al_2O_3–Fe_2O_3-mono (AFm) phase [91]. The peak centered at 420 ℃ was attributed to the dihydroxylation of portlandite, while the peak in the range of 640–760 ℃ was associated with the decarbonation of calcite [81]. The TG and DTG curves of the reference sample and CNT0-O_3 were almost identical. For the CNT0.1-O_3, the peak

intensities corresponding to the decomposition of ettringite and portlandite were much higher than those of the reference sample. Fig. 3-18 shows the portlandite content of the samples calculated using a tangential method along with normalization by weight loss at 600 ℃ [81] for quantitative comparison. The amount of portlandite produced by the hydration of alite and belite in the reference sample and CNT0-O_3 was as low as 0.1 %. On the contrary, the portlandite content remarkably increased in the samples containing CNTs. The portlandite content of the CNT0.1-P was calculated as 0.21 %, which enhanced 210 % higher than that of the reference sample. In addition, the CNT0.1-O_3 had the highest portlandite content of 0.65 %, which was 650 % higher than that of the reference sample. This result was consistent with those of isothermal calorimetry and XRD analyses, and well explained how the dispersed CNTs produced by ozone treatment further enhanced the nucleation effect and accelerated the hydration reaction (especially C_3S) of the UHPC at early ages.

The TG and DTG curves of the samples at 28 d are presented in Fig. 3-17b. The TG and DTG curves for the reference sample and CNT0-O_3 were similar. This result support and reaffirm previous experimental results that the ozone treatment does not affect both early and long-term hydration of the UHPC. The peak corresponding to the decomposition of portlandite almost vanished for all the samples owing to the pozzolanic reaction (See Fig. 3-18.). In addition, the peak at 100 ℃ (i.e., the decomposition of ettringite) was reduced, while the peak at 140 ℃ (i.e., decomposition of AFm phase) was notably observed. It was presumed that ettringite decomposed to AFm due to the low amount of gypsum [92]. However, the peaks representing the dehydration of ettringite and C-S-H in the CNT0.1-P were much lower than those of other samples, which indicates that the DOH of CNT0.1-P was the lowest. This is because the agglomerated CNTs covered the surfaces of the cement clinkers and hindered the hydration reaction as shown in Fig. 3-12 [36].

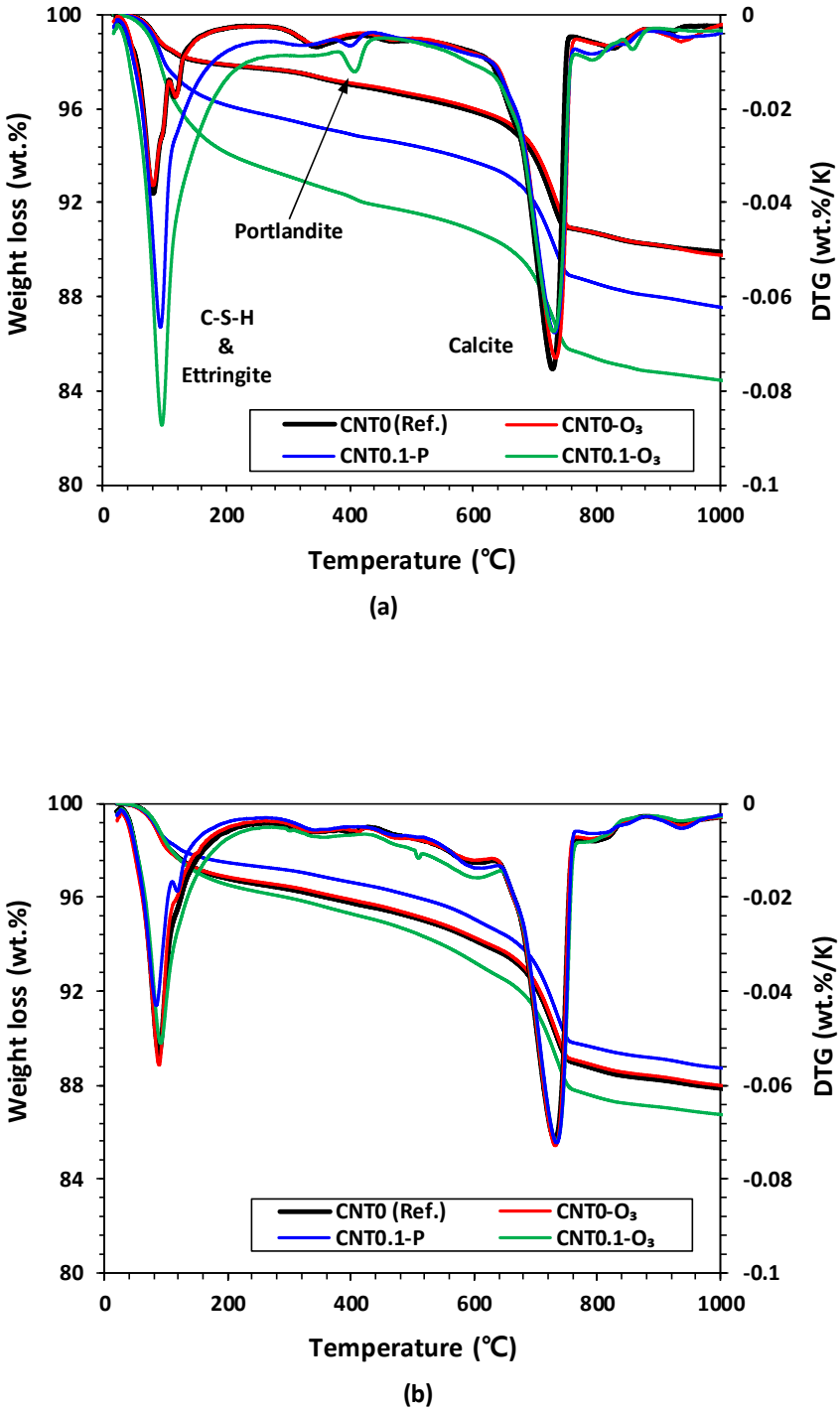

Fig. 3-17. TG and DTG curves of the samples: (a) at 1 d, (b) at 28 d.

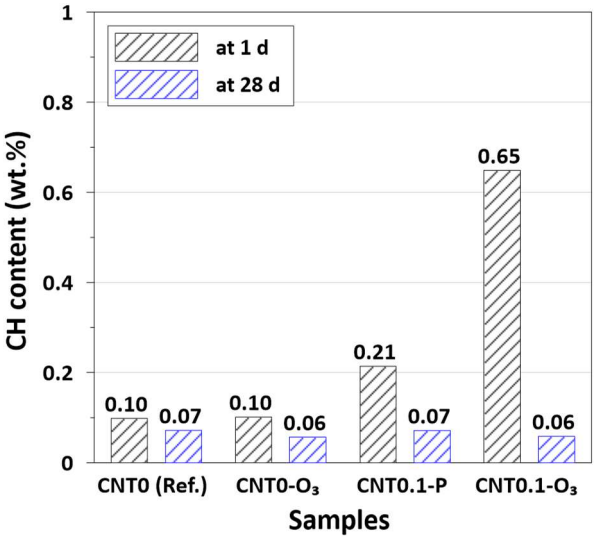

Fig. 3-18. Portlandite (CH) content of the samples.

3.3.2.4 Compressive strength

Fig. 3-19 showcases the compressive strength of the samples at 1 and 28 d. The compressive strength of the reference sample and CNT0-O_3 at both 1 and 28 d was similar in the range of 37–38 MPa at 1 d and 144–146 MPa at 28 d, which clearly indicates that the ozone treatment does not affect the hydration of UHPC without CNTs. For the CNT0.1-P, the compressive strength at 1 d was 43.8 MPa where the 13.5 % of increment is due to the nucleation effect via the incorporation of CNTs while the strength at 28 d decreased to 121.7 MPa. This is because the agglomerated CNTs not only hindered the hydration reaction but also acted as pores and cracks, leading to decrease in compressive strength [36]. In contrast, the CNT0.1-O_3 showed the highest compressive strength of 50.4 MPa at 1d and 158.4 MPa at 28 d, which increased at rates of 0.6 and 9.8 %, respectively, as compared to those of the reference sample. This is attributed to the dispersed CNTs via ozone treatment; not only did they further accelerate the hydration of the UHPC but also made the C-S-H denser. Specifically, massive surface

areas provided by well-dispersed CNTs to cement hydrates can conceivably occur in a well-packed format that would contribute to the formation of denser C-S-H with higher stiffness [26]. In addition, uniformly distributed and dispersed CNTs anchored the adjacent hydrated particles as shown in the SEM images (Fig. 3-12); this increased the compressive strength.

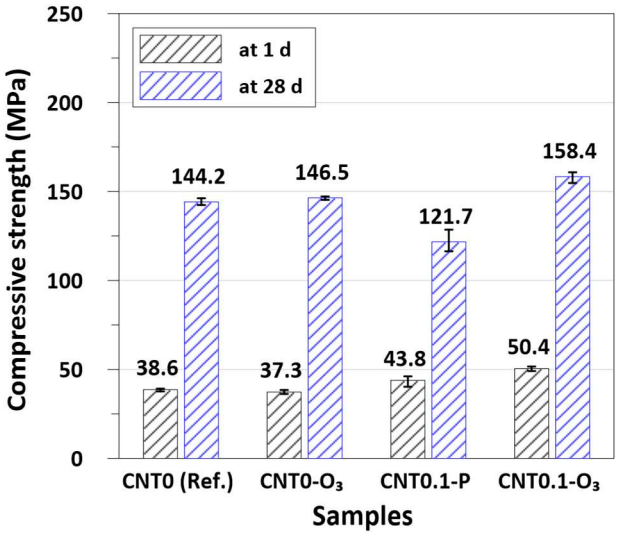

Fig. 3-19. Compressive strength of the samples.

In summary, the ozone treatment did not modify the main hydration characteristics of the UHPC. Incorporation of CNTs even without applying the dispersion method slightly accelerated the hydration of the UHPC at early ages by providing nucleating sites for hydration of clinker phases. This lead to an increase of the initial compressive strength, whereas long-term strength decreased due to the agglomerated CNTs, which hindered the later hydration reaction and acted as pores in the hardened matrix. However, in the case of incorporating well-dispersed CNTs via ozone treatment in the UHPC, much finer scales of dispersed CNTs not only further accelerated the

hydration of the UHPC at early ages by providing multiple nucleation effects, but also improved the long-term compressive strength owing to the formation of denser C-S-H and the anchoring effect.

3.4 Conclusions

In this chapter, effects of ozone treatment on the dispersion of CNTs in suspension and its influence on the material properties of the hardened UHPC/CNT composites were investigated for the first time. A 0.1 wt.% proportion of CNTs was successfully incorporated into the UHPC mixture through ozone treatment. Enhanced dispersion of CNTs in suspension and the UHPC/CNT solid system was quantitatively confirmed via laser diffraction and spatially-resolved SAXS measurements, respectively. Based on XRD, TG, and SEM experiments conducted, the following conclusions can be drawn along with a schematic diagram to summarize the effect of ozone treatment on the UHPC/CNT system (Fig. 3-20).

Ozone treatment is an effective method that can not only prevent CNT damaging, which is one of the weakness of sonication, but also simply disperse CNTs within both aqueous solution and UHPC even without using specific equipment required for plasma oxidation.

Ozone treatment even with a low concentration of 0.1 ppm, successfully disperses CNTs in aqueous solution by attaching oxygenic and carboxylic chemical groups on the surfaces of CNTs. It also uniformly distributes the dispersed CNTs in UHPC by enveloping the surfaces of cementitious materials with the chemical groups having negative charges. It increases the flowability of the UHPC/CNT composite because of the double steric repulsion effect.

Ozone treatment does not affect both early and long-term

hydration of UHPC. Instead, when applied with the incorporation of CNTs, it substantially provided multiple nucleation sites by better dispersed CNTs, which resulted in the acceleration of the hydration of UHPC/CNT at early ages. In addition, the CNTs dispersed via ozone treatment enhanced flowability and formed denser and stiffer C-S-H by anchoring adjacent hydration products. This effect eventually improved the compressive strength at later ages.

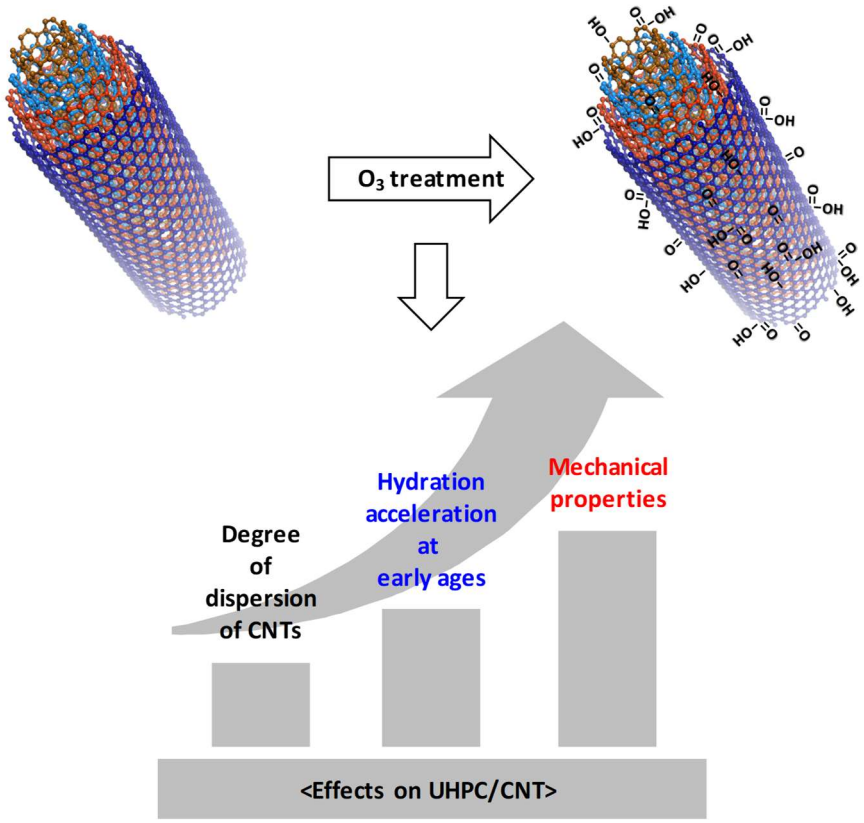

Fig. 3-20. Effects of ozone treatment on dispersion of CNTs and hydration of UHPC/CNT.

Chapter 4. Effect of CNTs on Mechanical Properties of UHPC

In this chapter, the effects of incorporation of CNTs on UHPC was investigated with regard to the dispersion of CNTs and mechanical properties. Dispersed CNT suspensions (0–2.0 wt.%) were prepared by ultra-sonication and subsequent shear mixing with superplasticizer to achieve the high flowability of UHPC fresh mixture. The proposed dispersion method was effective to disperse CNTs within both an aqueous solution and UHPC composite up to the critical incorporation concentration (CIC). Conducted experiments revealed that CNT content below the CIC improve the mechanical properties of UHPC through pore filling, bridging, and densification of C-S-H structure, whereas CNT content above CIC weakens the properties due to agglomeration of CNTs, suppression of hydration, and increase in air-voids.

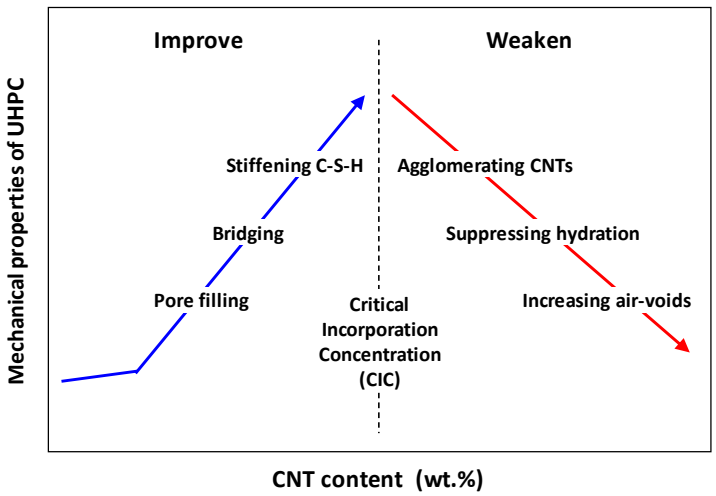

Fig. 4-1. Graphical abstract of chapter 4.

4.1 Introduction

This chapter covered the effect of CNTs on mechanical properties of UHPC. UHPC composites with six different contents of dispersed CNTs were manufactured. SEM, mercury intrusion porosimetry (MIP), and mechanical tests were conducted to determine how the dispersed CNTs affect the material properties of UHPC according to CNT content.

4.2 Experimental Details

4.2.1 Properties of CNTs

Multi-wall CNT powders (K-Nanos-P, Kumho inc., Korea) produced via CVD method were used and there properties are listed in Table 4-1.

Table 4-1. Properties of CNTs.

Avg. diameter (nm)	Avg. length (μm)	Bulk density (g/m^3)	Purity (wt.%)	Specific surface area (m^2/g)
10–20	10–70	100,000–150,000	> 95	165–205

4.2.2 Mixture proportions and sample preparation

Table 4-2 shows the mixture proportions. CNTs were incorporated into the base UHPC mixture at six different dosages: (0, 0.2, 0.5, 0.8, 1.0 and 2.0 wt.% relative to the cement). The weight ratios of the water and polycarboxylate superplasticizer (SP) were kept constant at 0.23 and 0.04, respectively, except for the sample with 2.0 wt.% CNT. For sample CNT2.0, w/c of 0.28 was applied so that the flow value was equal to that of sample CNT1.0. This was to prevent a false setting from the rapid decrease of flow with the high CNT dosage.

Table 4-2. Mixture proportions (wt.% of cement).

Sample	w/c	OPC	Silica fume	Silica powder	Silica sand	Super plasticizer	CNTs
CNT0 (Ref.)	0.23	1	0.25	0.35	1.1	0.04	0
CNT0.2							0.002
CNT0.5							0.005
CNT0.8							0.008
CNT1.0							0.01
CNT2.0	0.28						0.02

The following equipment was prepared to manufacture samples: an ultrasonic processor (VCX 750, Sonics Inc.), shear mixer (L5M-A, Silverson Inc.), Hobart mixer, jacketed beaker with a capacity of 2 liters, and chiller (Fig. 4-2).

Fig. 4-2. Equipment to fabricate samples.

Fig. 4-3 presents the sample preparation process, which consisted of four steps: (a) fabrication of the dispersed CNT suspension, (b) mixing of the UHPC dry pre-mixture with the solution, (c) casting, and (d) curing.

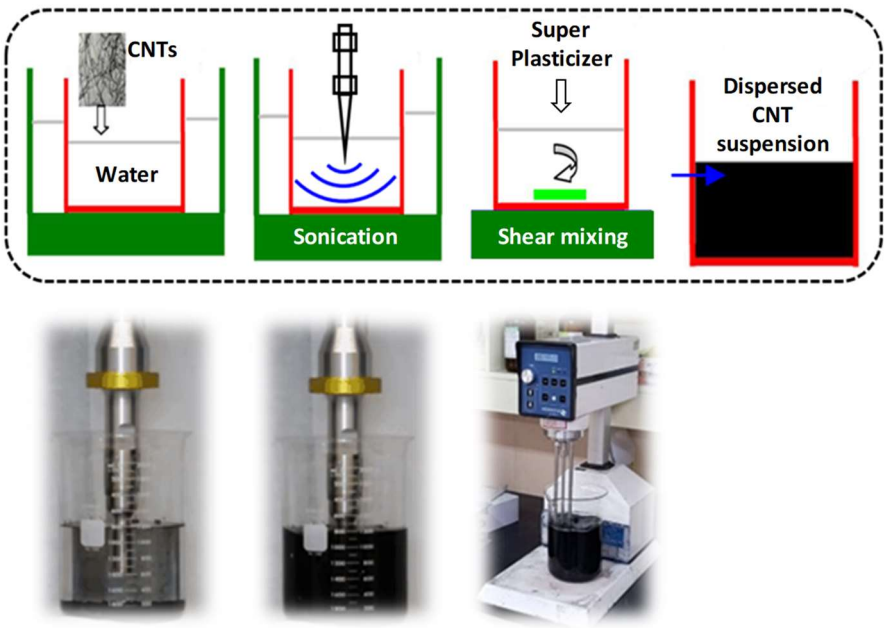

Fig. 4-3. Sample preparation process.

First, the dispersed CNT suspension was fabricated by sonication and subsequent shear mixing with the SP (Fig. 4-3a). Sonication with polycarboxylate superplasticizer is one of the most commonly used techniques for achieving a desirable level of dispersion of CNTs within both an aqueous solution and cementitious composite [87, 93, 94]. However, this method could be inapplicable to UHPC with a low w/c. This is because the specific surface area of CNTs is large; as the dispersion progresses, some of the water and SP adsorb on the CNTs. This results in a rapid decrease in the flow [87], which leads to a false setting. Thus, in this study, CNTs were dispersed by sonication first then shear mixing with superplasticizer. Specifically, CNTs were sonicated in distilled water without incorporation of SP through the use of an ultrasonic processor with a 25 mm diameter cylindrical boost probe. The sonicator was operated at an output power of 600 W (amplitude of 80 %) to deliver energy at a rate of 35000–36000 J/min. During sonication, the temperature of the vessel was maintained at 7 ℃ to prevent potential overloading of the equipment and deterioration of dispersion efficiency due to heat generation. In addition, the solution was circulated with a pump for uniform dispersion. After sonication was completed, SP was added into the solution and shear mixed for 5 min. With this method, the flow was increased compared to previously reported methods [32]. Because the surface of the CNTs had already adsorbed sufficient water, the amount of later adsorption of the superplasticizer on the CNTs was negligible. The dispersion progressed until the average particle size of the CNTs reached about 10–30 μm in which particle size analysis performed immediately after finishing dispersion.

After the dispersed CNT suspension was prepared, a UHPC dry pre-mixture was fabricated through the homogeneously blending of Portland cement, silica fume, silica powder, and silica sand. The pre-mixture was then added into the dispersed CNT suspension and mixed for 5 min with a Hobart mixer (Fig. 4-3b). For CNT0 (Ref.), water and

SP were used instead of the dispersed CNT suspension. Then, fresh mixture was poured into molds for casting samples (Fig. 4-3c).

Cubic samples with a volume of 50 × 50 × 50 mm^3 were fabricated for the measurements of the electrical conductivity and compressive strength.

Once a fresh mixture casted, the surface was immediately covered with a plastic sheet to prevent sudden moisture evaporation, and the samples were cured for 24 h at 20 ℃. Then, the molds were removed, and the samples were steam-cured at 90 ℃ for 48 h. Subsequently, the samples were kept at 20 ℃ for 25 days, for a total curing period of 28 days (Fig. 4-3d).

4.2.3 Test methods

The CNT particle size distributions in the aqueous suspension were analyzed using a laser diffraction particle size analyzer (Bluewave, Microtrac, USA) to evaluate the degree of dispersion of CNTs in different amounts of CNTs.

SEM analysis was carried out with a FE-SEM (JSM-6700, JEOL Ltd. Japan) to analyze the morphology of the dispersed CNTs in the hardened UHPC matrix. During the SEM analysis, energy dispersive spectroscopy (EDS) spectra were examined to distinguish CNTs from needle-shaped hydration products, which have similar shapes with CNTs such as ettringite, by verifying the chemical compositions. Thin sections (approximately 2 mm) of samples with hydration stopped at 28 d were used.

The compressive strength of the UHPC/CNT composites was measured in accordance with ASTM C109 using the Eq. (3.1). A UTM with a load cell capacity of 2000 tons was used by applying a loading

rate of 0.02 mm/s. Six samples for each mix proportion were tested and the average value of four samples excluding the largest and smallest values was taken as the representative compressive strength. The elastic modulus was calculated using following equations according to ASTM C469 and BS-1881 part 121:

$$E_c = (\sigma_s - \sigma_c)/(\varepsilon_s - \varepsilon_c), \tag{4.1}$$

For ASTM C469 : $\sigma_s = 0.4 f_c^{'}$, $\varepsilon_c = 50\mu\varepsilon$

BS-1881 Part 121 : $\sigma_s = 0.3 f_c^{'}$, $\sigma_s = 0.5$ MPa

where f_c' is the ultimate compressive strength and ε is the strain.

Mercury intrusion porosimetry (MIP) testing was performed using an AutoPore IV 9500 (manufactured by Micromeritics Instrument Corp., USA) to investigate the porosity and pore size distribution of the UHPC/CNT composites. The samples cured for 28 d were cut into small pieces (approximately 5 × 5 × 5 mm^3 cubes), and the hydration reaction was stopped. A pressure range of 0–420.58 MPa (0.1–61,000 psia) was employed during the intrusion and extrusion of mercury. The testing parameters were set to a surface tension of 485 dynes/cm and a mercury contact angle of 130 °.

4.3 Results and Discussion

4.3.1 Degree of dispersion of CNTs

4.3.1.1 Dispersion of CNTs in aqueous

The CNT particle size in the aqueous solution was analyzed through a laser diffraction equipment (Bluewave, Microtrac, USA) to

evaluate the dispersion of different amounts of CNTs. Fig. 4-4 shows the particle size distributions of CNTs in the aqueous solution before and after dispersion (i.e., sonication and shear mixing procedures). The results are averaged of three experimental results for each sample. The mix proportions containing CNTs after dispersion had similar particle size distributions, and their mean volume diameter (MVD) was in the range of 13.93–29.01 μm (Fig. 4-4a–b). The average MVD value after dispersion of 22.75 μm was 38 times smaller than that before dispersion (i.e., MVD of 506.87 μm) (Fig. 4-4c–d). Considering the size properties listed in Table 4-1, it can be safely assumed that CNT bundles in the aqueous solution were dispersed well by the proposed method. Thus, a dispersed CNT suspension with a similar dispersion degree (i.e., similar MVD value) was used to manufacture the listed samples.

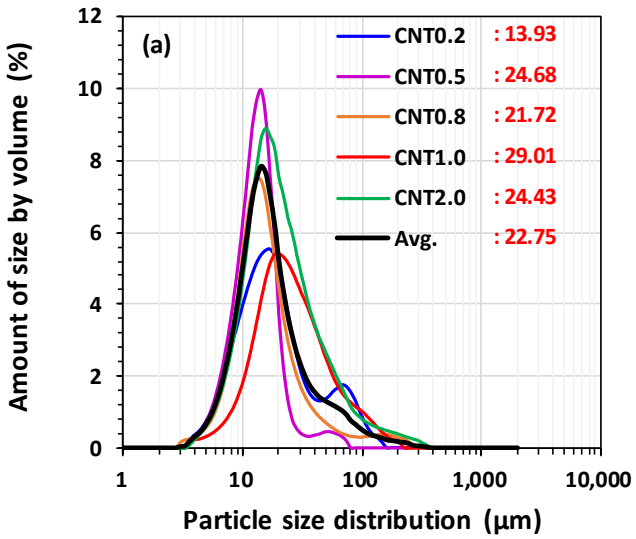

Fig. 4-4. Particle size distribution of CNTs in aqueous solution (red number next to legend indicates the measured mean volume diameter of CNTs): (a–b) amount size by vol. (%) and cumulative size by vol. (%) after dispersion, (c–d) comparison before and after dispersion.

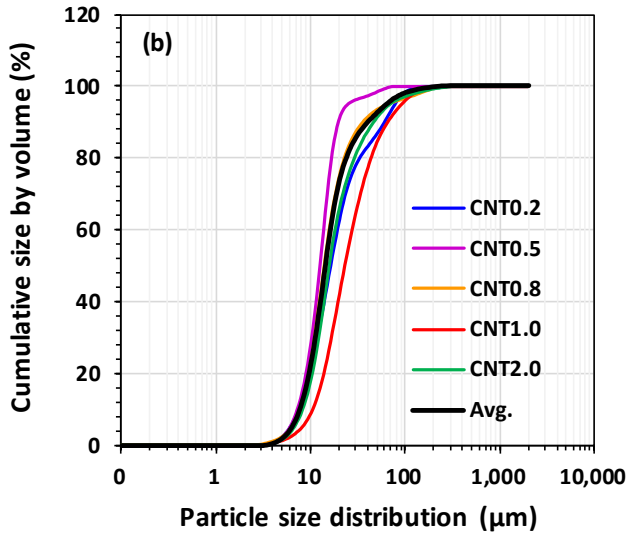

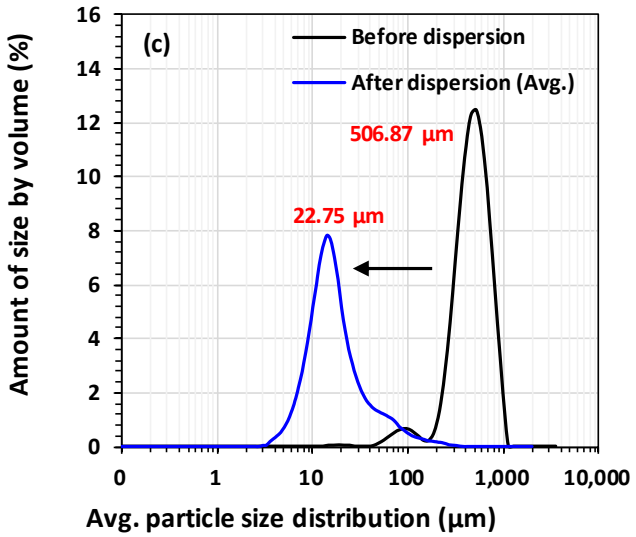

Fig. 4-4. *(Continued)* Particle size distribution of CNTs in aqueous solution (red number next to legend indicates the measured mean volume diameter of CNTs): (a–b) amount size by vol. (%) and cumulative size by vol. (%) after dispersion, (c–d) comparison before and after dispersion.

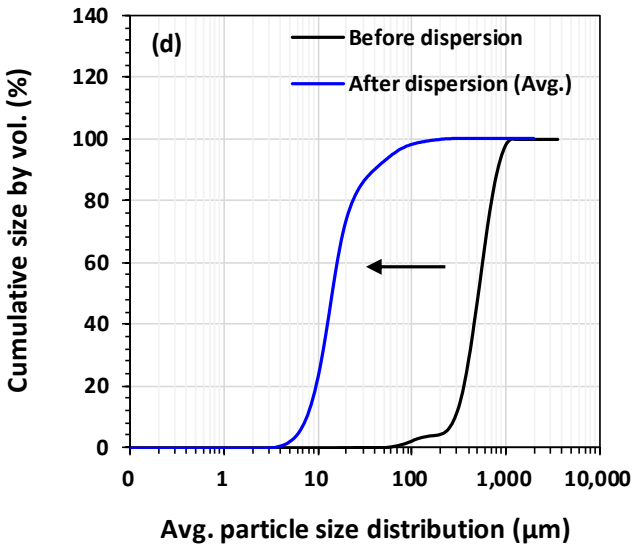

Fig. 4-4. *(Continued)* Particle size distribution of CNTs in aqueous solution (red number next to legend indicates the measured mean volume diameter of CNTs): (a–b) amount size by vol. (%) and cumulative size by vol. (%) after dispersion, (c–d) comparison before and after dispersion.

4.3.1.2 Dispersion of CNTs in UHPC

Fig. 4-5 shows the morphology of dispersed CNTs in the UHPC matrix. CNTs distributed as individual fibers with a length of less than 1 µm were observed to be abundant in the UHPC matrix. This analysis qualitatively demonstrates that the proposed dispersion method used in this study (i.e., subsequent shear mixing with superplasticizer after sonication) effectively disperses CNTs in both the aqueous solution and cementitious composite while a low w/c ratio was maintained for UHPC production. The average length of the CNTs was shorter than that based on the results of the particle size analysis (Fig. 4-4). This is because the CNTs were additionally mechanically dispersed by the silica fume particles, which have similar particle sizes with those of CNTs, during mixing. Incorporating an appropriate amount of silica fume has been shown to effectively disperse CNTs in cementitious

composites [36]. In particular, in a SEM image taken of a fragment after the compressive strength test, a large amount of CNT fibers was observed between the crack surfaces (Fig. 4-5c). However, as the CNT content was increased to 0.8 wt.% or more, significant differences in the morphologies of the CNTs were found. Agglomerated CNT bundles were often observed on the surface of unhydrated cement or in the hydration products (Fig. 4-5d–e). This may be because the additional amount of CNTs exceeded the critical incorporation concentration (CIC). Excessive addition of CNTs in a given volume of UHPC shortens the relative distance between CNT fibers; this strengthens the Van der Waals forces, which leads to agglomeration of CNTs in the UHPC matrix. In addition, the rapid decrease in the flow with an increase in the CNT content can disturb the uniform dispersion in the UHPC matrix. Based on the morphological study of the UHPC–CNT composites, the CIC could be proposed between the CNT content of 0.8 and 1.0 wt.% (i.e., mean value of 0.9 wt.%) in this study.

In summary, it was verified that shear mixing with superplasticizer after sonication can be an effective way to disperse CNTs within both an aqueous solution and UHPC matrix. However, if the incorporated CNT content in a given volume of the UHPC matrix is close to the CIC, CNTs could be partly agglomerated.

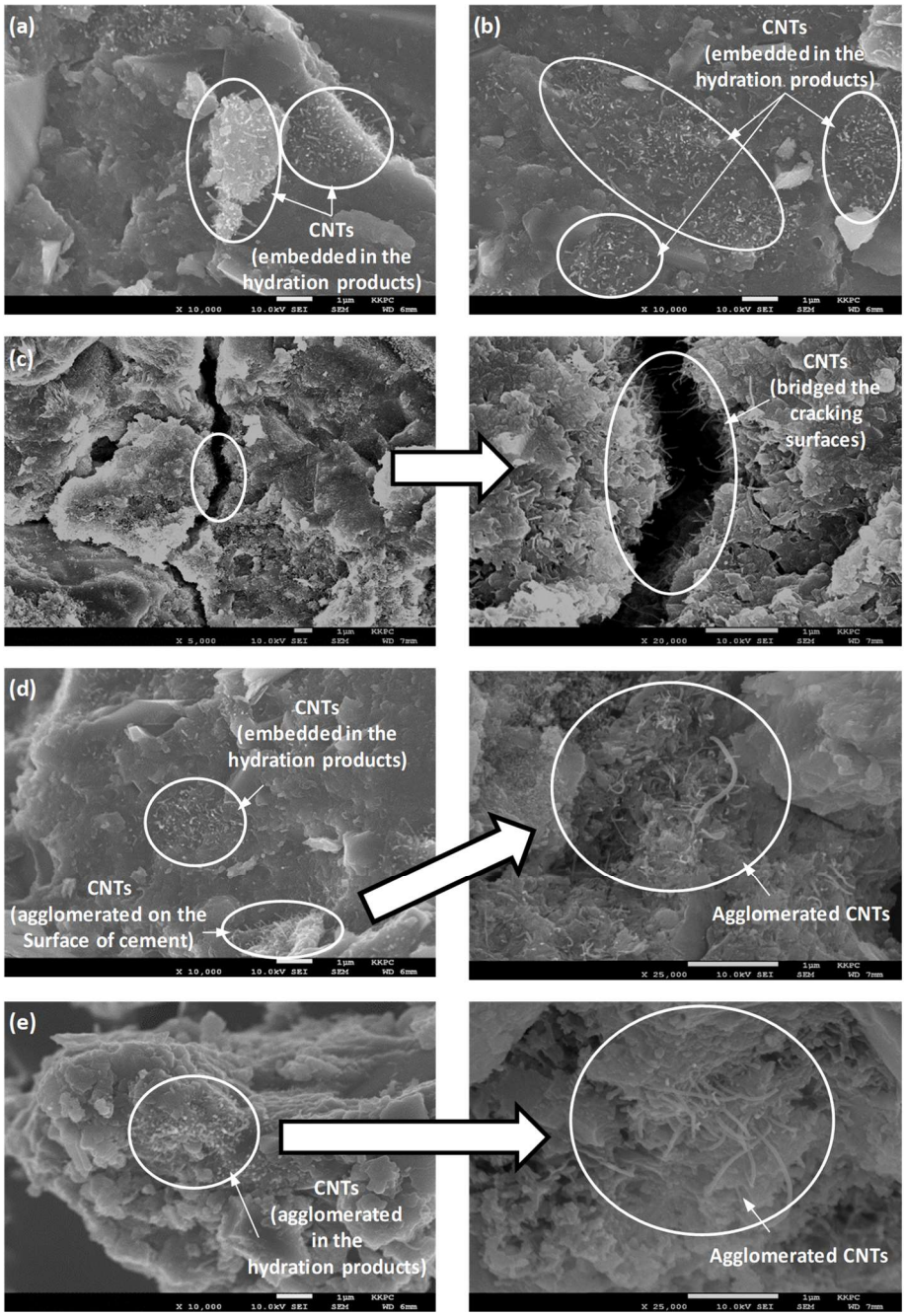

Fig. 4-5. SEM images of the UHPC/CNT composites: (a) CNT0.2, (b–c) CNT0.5, (d) CNT0.8 and (e) CNT1.0.

4.3.2 Effect of CNTs on Mechanical properties of UHPC

4.3.2.1 Compressive strength and elastic modulus

Note that the mechanical test was not conducted for the sample CNT2.0 due to the different w/c. Fig. 4-6 summarizes the compressive stress–strain curves of the samples and their compressive strength and elastic modulus (Appendix A-1). All samples satisfied the strength requirement for UHPC (i.e., compressive strength > 150 MPa). The CNT0 (Ref.) had a compressive strength of 178.6 MPa, and its elastic modulus was 49.1 GPa by ASTM and 52.1 GPa by BS code. The mechanical properties of sample CNT0.2 did not significantly differ from those of the reference sample, whereas sample CNT0.5 exhibited a 5.5 % improvement in the compressive strength and approximately 12.0 % improvement in the elastic modulus. However, as the CNT content approached or went above the CIC, both the compressive strength and elastic modulus decreased, although, the elastic modulus remained higher than that of the reference sample. For sample of CNT0.8, the compressive strength was 177.1 MPa, which is similar to that of CNT0 (Ref.), but the elastic modulus was 6.4–7 % higher.

The effect of dispersed CNTs on the mechanical properties of UHPC can be explained based on the morphology of the samples. First, well-dispersed CNTs provide a massive surface area for the precipitation of cement hydrates. This could conceivably occur in a well-packed format that would contribute to the formation of denser C–S–H agglomerates with high stiffness [26], as shown in Fig. 4-5. In addition, embedded CNTs in the hydration product phase bridge the adjacent hydrated particles, which is called the bridging effect (Fig. 4-5c) [38]. Therefore, the compressive strength and elastic modulus improve. However, when the CNT content close to the CIC (i.e., 0.8–1.0 wt.%), the CNTs become clumped (Fig. 4-5d–e). They, act as pores or cracks and covers the surface of the component, which hinders the development of uniform hydration [36]. This decreases the mechanical properties.

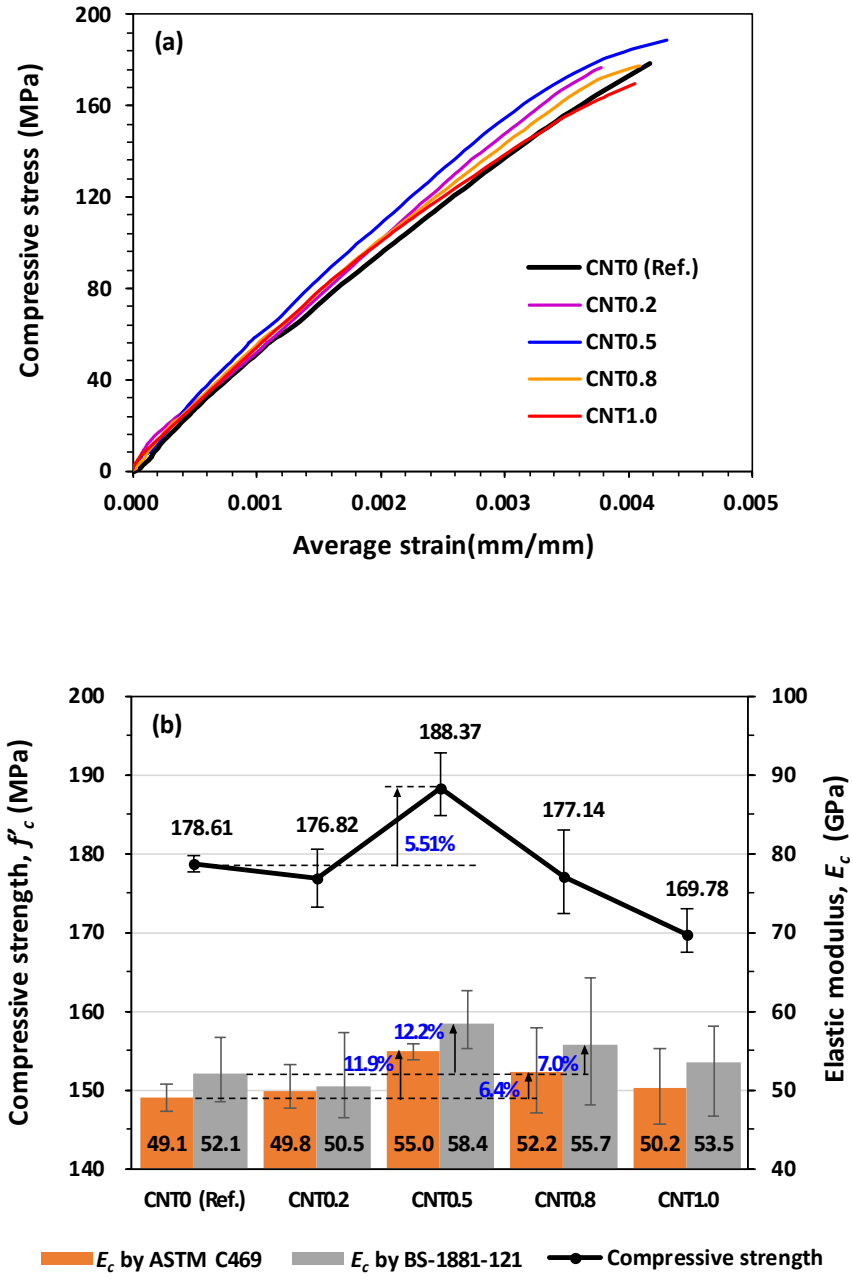

Fig. 4-6. Compressive strength and elastic modulus of the UHPC/CNT composites: (a) compressive stress-average strain curves and (b) summary of the compressive strength and elastic modulus.

4.3.2.2 Poromechanical properties

Fig. 4-7 and Fig. 4-8 show the pore size distribution and porosity, respectively, divided into four ranges based on the pore diameter of the samples. The pore structure of the UHPC changed completely as the CNT content increased. The total porosity of the UHPC samples containing CNTs significantly decreased regardless of the CNT content compared to that of the reference sample (Fig. 4-8). In particular, the proportion of the mesopores (4.5–25 nm) were remarkably reduced with the addition of CNTs by the pore filling effect. However, the proportion of the entrained or entrapped air bubbles typically formed at 100–1000 μm significantly increased as the CNT content increased because of the lower flowability. Generally, incorporating fibers into cementitious materials reduces flow regardless of the type of fiber and a low fluidity for a fresh concrete mixture leads to more air voids being included in the hardened matrix [77].

The poromechanical properties of the samples can be correlated with the compressive strength. As shown in Fig. 4-7a and Fig. 4-8, the total porosity and proportion of mesopores for sample CNT0.5 decreased remarkably because of the pore filling effect, which improved the compressive strength. On the other hand, the pore volume distribution of sample CNT0.2 was similar to that of the reference sample, so the compressive strength was not improved significantly. As the CNT content approached the CIC, although the total porosity and proportion of mesopores decreased, the proportion of air voids became much larger than that of the reference sample, which decreased the compressive strength. In the case of samples CNT0.8 and CNT1.0, the relative pore volume in the matrix increased because the hydration reaction was suppressed by an excessive amount of CNTs, which increased the cumulative mercury intrusion (Fig. 4-7b). This result demonstrates the correlation between the CIC and poromechanical properties.

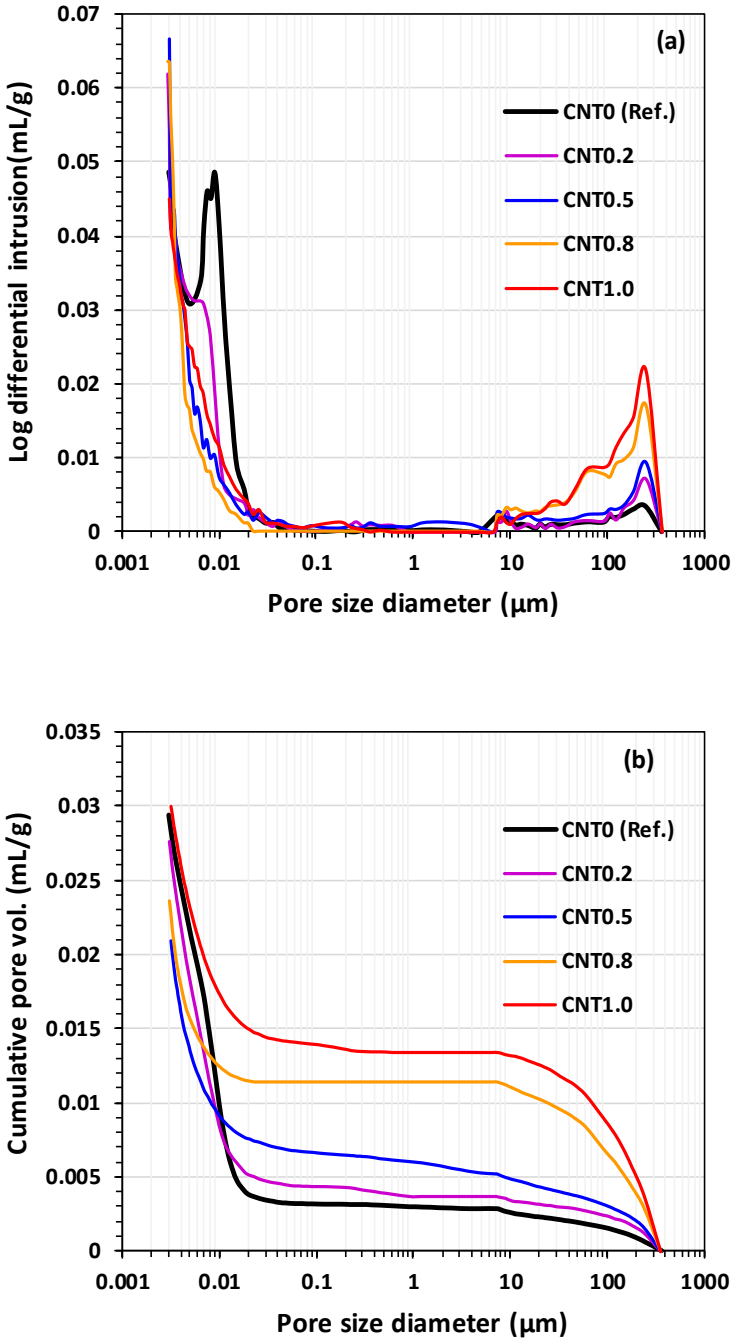

Fig. 4-7. Pore size distribution of the UHPC/CNT composites at 28 d: (a) log differential intrusion and (b) cumulative pore volume.

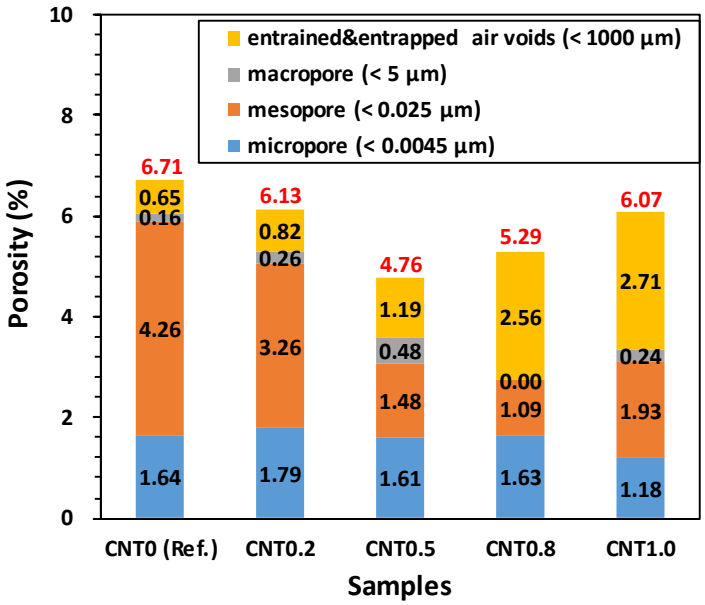

Fig. 4-8. Pore volume distribution of the UHPC-CNT composite at 28 d (red number on the bars indicate the total porosity).

In summary, incorporation of dispersed CNTs into UHPC can significantly improve the mechanical properties up to the CIC because of the pore filling effect, bridging effect, and formation of a hydration product (C-S-H) with denser and higher stiffness. However, excessive incorporation of CNT content beyond the CIC is rather ineffective for improving the mechanical properties because of the agglomeration of CNTs that act as crack and pores, suppression of hydration, and increase of air voids in the matrix.

4.4 Conclusions

In this chapter, UHPC/CNT composites were considered with regard to the dispersion method and mechanical properties. UHPC composites with six different CNT dosages (0, 0.2, 0.5, 0.8, 1.0, and 2.0

wt.%) were designed. First, the method to disperse the CNTs in both an aqueous solution and UHPC matrix was proposed to achieve a high fluidity of UHPC fresh mixture. Then, the degree of dispersion of CNTs were evaluated through particle size and SEM analyses. In addition, fundamental mechanical properties were investigated through a compressive strength test, measurement of the elastic modulus, and MIP test to determine the effect of CNTs on UHPC. The following conclusion were drawn along with a schematic diagram to summarize the effect of CNTs on the UHPC/CNT system.

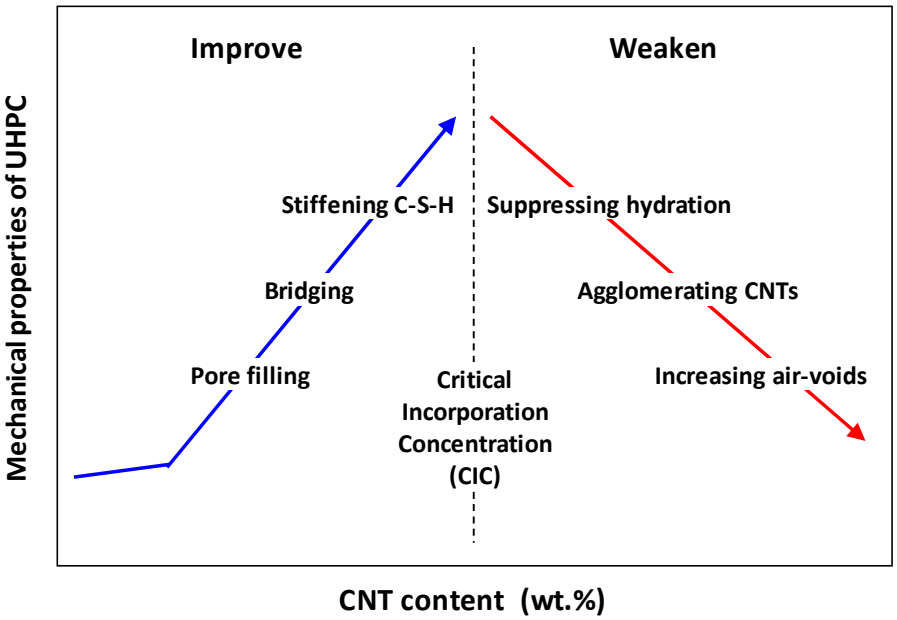

Fig. 4-9. Effect of CNTs on mechanical properties of UHPC.

Sonication and subsequent shear mixing with superplasticizer can be an effective way to disperse CNTs both in an aqueous solution and to manufacture UHPC/CNT composites while enhancing sufficient flow. However, if the incorporation of dispersed CNTs is increased to the CIC, CNTs could be partially agglomerated.

Dispersed CNTs can improve the mechanical properties of UHPC below the CIC owing to the pore filling, bridging, and C-S-H stiffening effects. However, when an excessive amount of CNTs close to the CIC is incorporated, agglomerated CNTs act as pores or cracks and suppress the hydration by covering the cement clinkers, which weakens the mechanical properties. There is the direct correlation among the CNT dispersion, CIC, and mechanical properties.

Chapter 5. Role of CNTs in the Electromagnetic Shielding Effectiveness of UHPC

In this chapter, the effects of incorporation of CNTs on UHPC was investigated in terms of electromagnetic interference (EMI) shielding effectiveness (SE) for the first time. Dispersed CNTs remarkably improved the electrical conductivity and resulting SE of UHPC up to the percolation threshold. Two testing methods for SE of cementitious materials (ASTM D4935-18 and IEEE-STD-299) verified the result and suggested that ASTM D4935-18 can only be used to evaluate a rough trend of SE, and IEEE-STD-299 using the samples with sufficient incident area size at least 1200 × 1200 mm^2 should be considered to accurately evaluate the SE at the actual structural level. Otherwise, the SE could be overestimated and distorted in the magnetic field due to the opening effect. According to a statistical analysis of the experimental results, a practical model to effectively estimate the SE of cementitious materials was proposed.

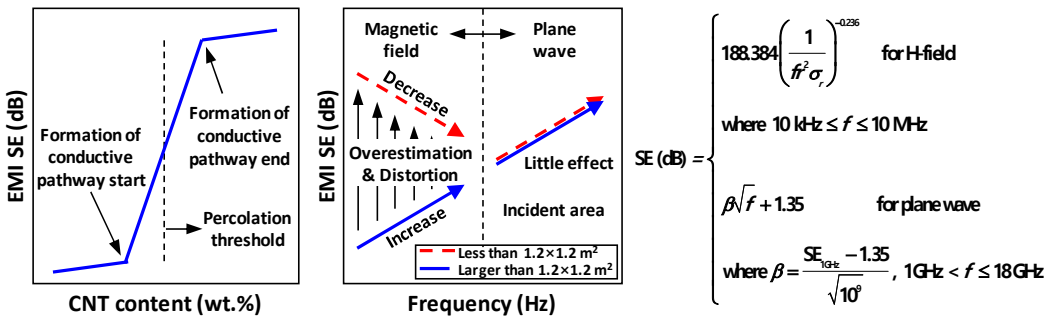

Fig. 5-1. Graphical abstract of chapter 5.

5.1 Introduction

In this chapter, followed by the study in chapter 4, effects of CNTs on UHPC was investigated in terms of electromagnetic interference (EMI) shielding effectiveness (SE), which refers to absorption or reflection of electromagnetic (EM) waves, for the first time. Two different methods of EMI SE testing were considered: ASTM D4935-18 (Coaxial TEM-cell method represented by small sample testing) and Institute of Electrical and Electronics standard 299 (IEEE-STD-299, representative method for large sample testing which can provide SE that is sufficiently representative for the actual structure). The results were interpreted according to electromagnetic compatibility (EMC) theory. Based on the experimental data and analysis, an effective way to test SE for cementitious materials and a practical model to estimate the SE were proposed.

5.2 Experimental Details

5.2.1 Mixture proportions and sample preparation

In this study, the properties of CNTs, mixture proportions, and the process of sample preparation were same as aforementioned in section 4.2 (i.e., six different contents of CNT suspensions (0, 0.2, 0.5, 0.8, 1.0, and 2.0 wt.%), were fabricated via sonication and subsequent shear mixing with superplasticizer. Then, they were mixed with the reference UHPC mixture and cured at 90 ℃ for 2 d and subsequently at 20 ℃ for 25 d.).

The geometries of the test samples are presented in Fig. 5-2. Cubic samples with a volume of 50 × 50 × 50 mm^3 were fabricated for the measurements of the electrical conductivity. Two copper plates with dimensions of 20 × 20 × 0.4 mm^3 were embedded into the samples as

electrodes. The contact area of each copper plate to the composite was coated with silver paint to minimize the surface resistivity and avoid electrode corrosion during the curing [31, 37].

The samples for EMI SE testing based on ASTM D4935-18 were manufactured according to the required dimensions except for the thickness. These included a reference sample and load sample with a thickness of 3 mm. The reference sample for calibration was disc-shaped; it comprised a circle with a diameter of 33 mm inside a ring with an outer diameter of 133.1 mm and inner diameter of 76.2 mm. The load sample for SE measurement was in the shape of a circle with a diameter of 133.1 mm.

The samples for EMI SE testing according to IEEE-STD-299 were in the form of two different square panels with a thickness of 200 mm, which is a typical building wall depth. The samples had different areas: 350 × 350 mm^2 and 1250 × 1250 mm^2, respectively. The incident area of these test samples were smaller owing to the test setting: 300 × 300 mm^2 and 1200 × 1200 mm^2, respectively.

The moisture in the samples, which can provide ionic conduction, was completely removed by oven drying at 60 ℃ for 2 d prior to testing to identify the sole effect of electronic conduction by CNTs on the results.

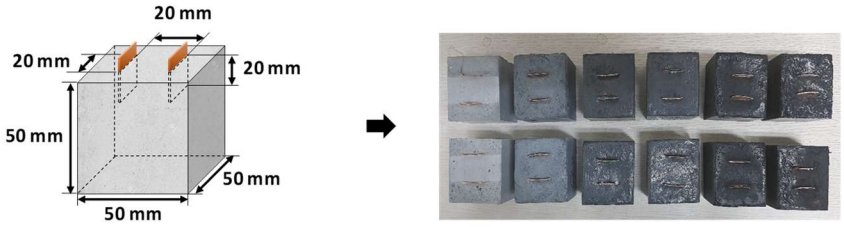

(a) Cubic sample used for electrical conductivity testing

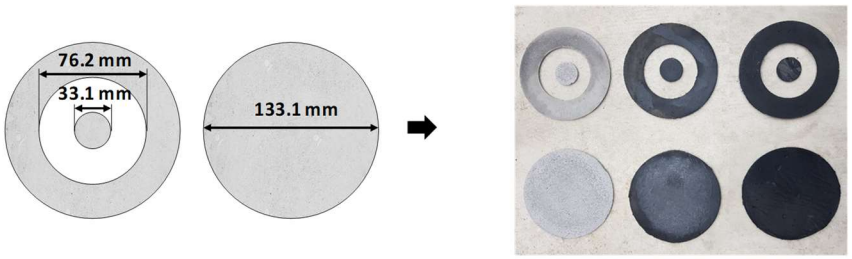

(b) Samples for SE testing based on ASTM D4935-18

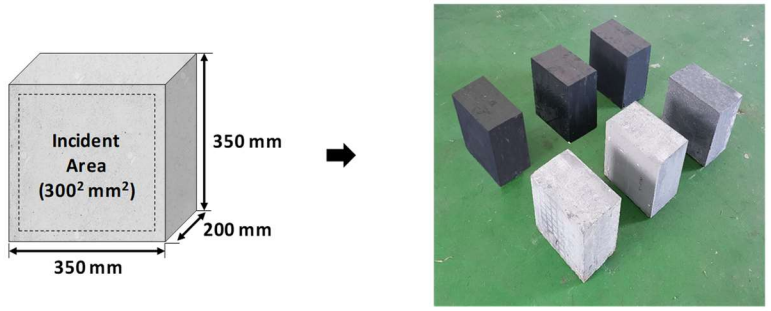

(c) Samples for SE testing based on IEEE-STD-299 (1)

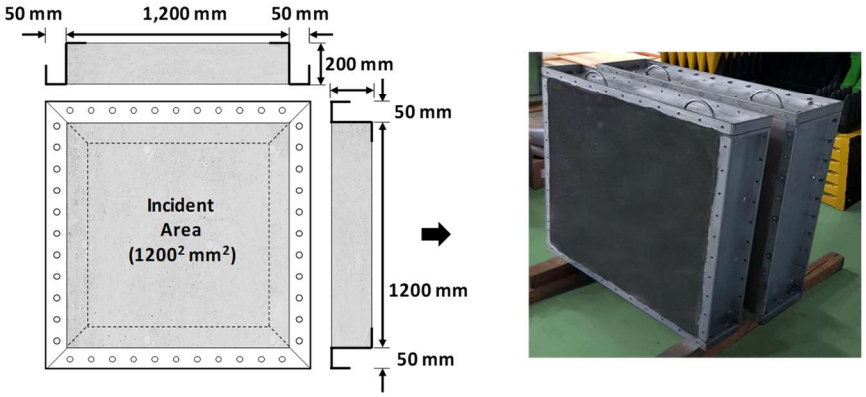

(d) Samples for SE testing based on IEEE-STD-299 (2)

Fig. 5-2. Geometry of the samples.

5.2.2 Test methods

The electrical resistance of the samples was measured through the four-wire method using an LCR meter (LCR-6100, GW INSTEK, Taiwan) as shown in Fig. 5-3. For each mix proportion, six samples were tested at a frequency of 10 kHz, and the average value of four samples excluding the largest and smallest values was taken as the representative electrical resistance. The electrical conductivity, which is the reciprocal of the electrical resistivity, was then calculated using the following equation.

$$\sigma\ (\mathrm{S/m}) = \frac{1}{\rho} = \frac{L}{RA}, \tag{5.1}$$

where σ is the electrical conductivity (S/m), ρ is the electrical resistivity (Ω·m), R is the electrical resistance (Ω), A is the cross-sectional area of the composite between the electrodes (m^2), and L is the distance between the electrodes (m).

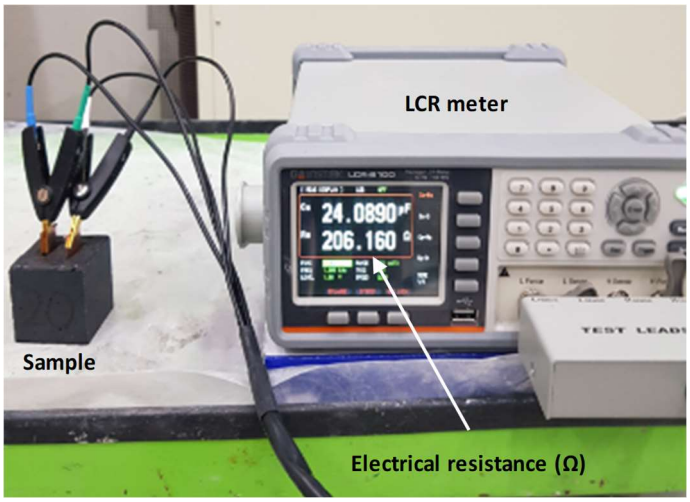

Fig. 5-3. Measurement of electrical resistance.

EMI SE testing based on ASTM D4935-18 was performed in the frequency range of 30 MHz–1.5 GHz with a step size of 7.35 MHz [57]. The detailed procedure is presented in Fig. 5-4. A coaxial TEM cell with a discontinuous inner conductor and flanged outer conductor, and a network analyzer (KEYSIGHT PNA series, E8364B, USA) were prepared (Fig. 5-4a). Before the testing, silver paint was applied to both the inner and outer edges of the samples to ensure complete electrical contact and prevent leaking of signal.

Once the preparation of the sample and equipment was completed, the samples were placed on the holder of the TEM cell (Fig. 5-4b and d) and the equipment was connected. Each time the ancillary equipment was connected, the signal of the reference sample was checked to ensure that the measurement system is in proper working order. The dynamic range (DR) of the system were checked by comparing the maximum signal level obtained with a reference sample to the minimum signal level obtained when using a load sample to control the sensitivity of the system and define the detectable level of output signal. Then, EM waves were generated at the range of interested frequency, and it was transmitted through the samples placed between the flanges of the coaxial TEM cell. Subsequently, the power levels of the signals for the reference and load sample were measured using a spectrum analyzer (Fig. 5-4c and e). The EMI SE (in decibels, dB) of the samples was calculated from the following ratio:

$$\mathrm{SE\,(dB)} = 10\log\left(\frac{P_i}{P_t}\right), \tag{5.2}$$

where P_i and P_t are the amounts of electromagnetic power measured from the reference (free space in IEEE-STD-299) and load sample, respectively. Three samples were tested and their average value was determined.

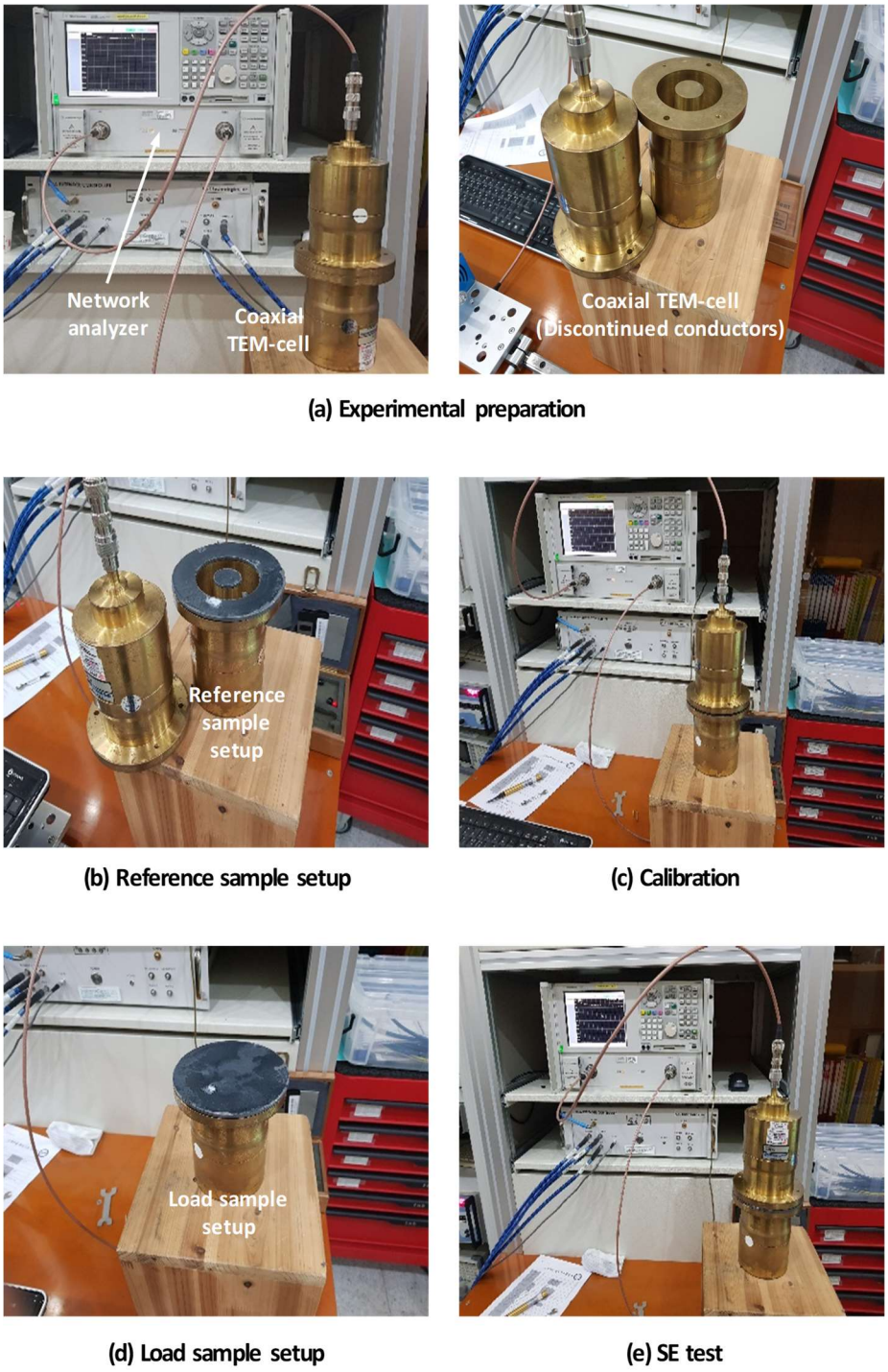

Fig. 5-4. EMI SE testing procedure based on ASTM D4935-18.

The EMI SE testing based on IEEE-STD-299 was performed in the frequency range 10 kHz–18 GHz [60]. A shielded chamber made of steel and zinc with a volume of 2400 × 2400 × 2400 mm^3 with an opening, a spectrum analyzer (8563E, HP, USA), a signal generator (SMB100A, ROHDE&SCHWARZ, Germany), and antenna kits were used in the testing.

Fig. 5-5 and Fig. 5-6 present the schematic illustration of EMI SE instrumentation system and details of the procedure for the EMI SE test, respectively. It starts with a free-space calibration (Fig. 5-6a). The calibration values at the frequency of interest (P_i) were taken as the zero point to set for the receiver, which showed the difference from the nominal value in the readout. Once the calibration was completed, a test sample was mounted on the opening of the chamber (Fig. 5-6b). Conductive gaskets were affixed to the gap between the chamber and the edge of the sample to ensure the complete electrical contact and prevent the leaking of EM waves. After mount sample on, the transmitting antenna was set up outside the chamber, and the receiving antenna was placed inside the chamber. Both antennas were installed perpendicular to the geometric center of the sample. The distances between the antennas and sample are listed in Table 5-1. After the experimental setup was completed, a signal was generated at the frequency of interest and transmitted with the transmitting antenna. Then, the power level of the signal detected by the receiving antenna (P_t) that passed through the sample was measured using a spectrum analyzer (Fig. 5-6c).

Twelve frequencies (i.e., 10 kHz, 100 kHz, 1 MHz, 10 MHz, 30 MHz, 100 MHz, 1 GHz, 1.5 GHz, 5 GHz, 10 GHz, 15 GHz, 18 GHz) were selected as frequencies of interest. To measure the SE, loop antennas were used in the low frequency range (10 kHz–10 MHz), bi-conical antennas were used in the transition and resonant ranges (10 MHz–100 MHz). In addition, in the high frequency range (100 MHz–

18 GHz), log periodic (LP) antennas were between 100 MHz–1 GHz, and horn antennas were used in the range of 1–18 GHz.

The EMI SE test was performed three times for each sample at each frequency of interest, and the average value of the results was taken as a representative SE of the UHPC/CNT composites.

Table 5-1. Distance between antennas and samples

Ant. type			Loop	LP / Bi-conical / Horn
Distance (m)	Calibration (between Antennas)		0.6	2
	Testing (from sample)	Transmitting	0.3	1.7
		Receiving	0.3	0.3

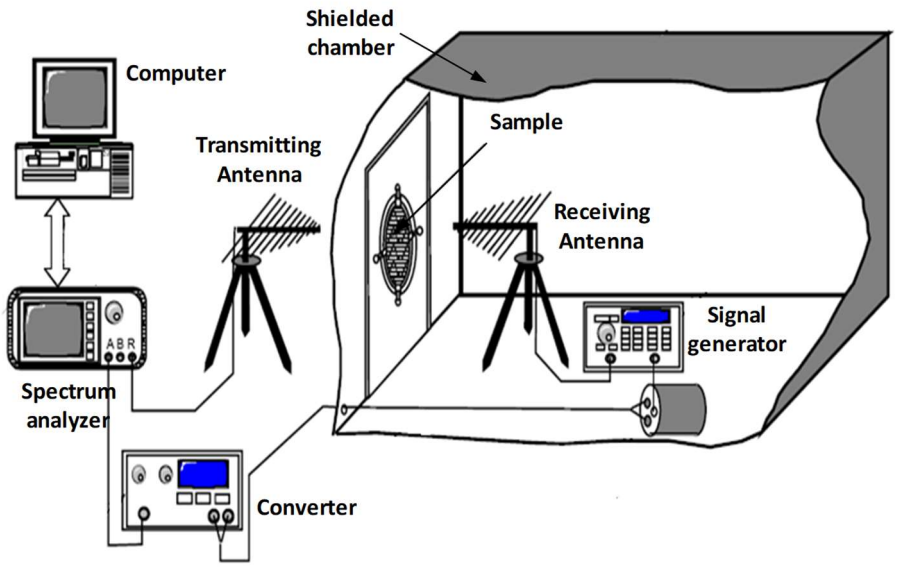

Fig. 5-5. Schematic illustration of SE instrumentation system.

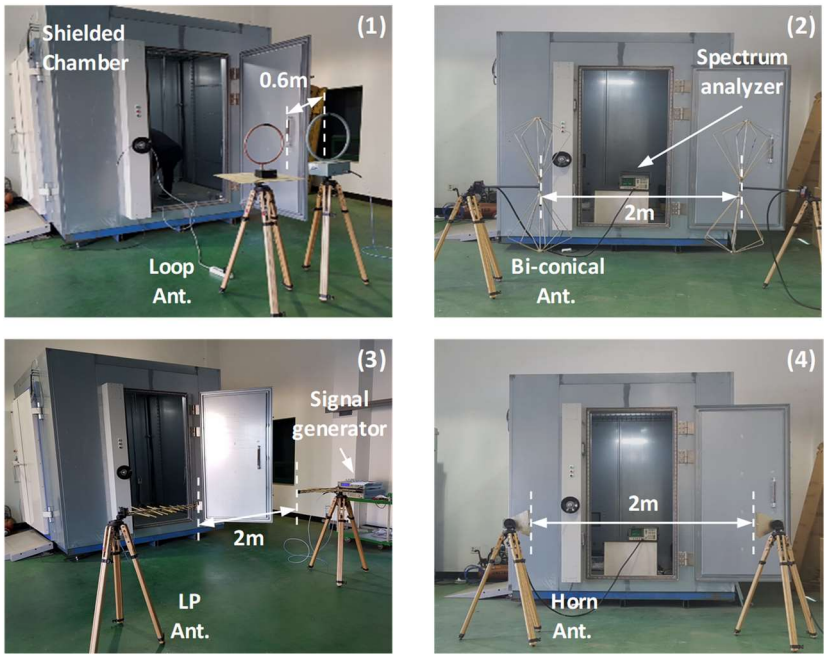

(a) Free space calibration : (1) Loop Ant., (2) Bi-conical Ant., (3) LP Ant., (4) Horn Ant.

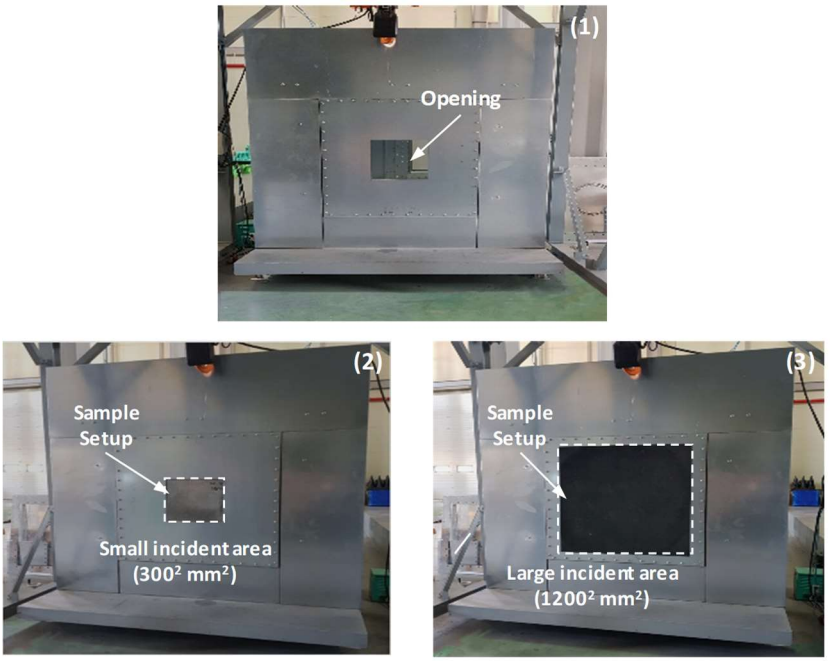

(b) Sample setup: (1) Opening, (2-3) after set sample up

Fig. 5-6. EMI SE testing procedure based on IEEE-STD-299.

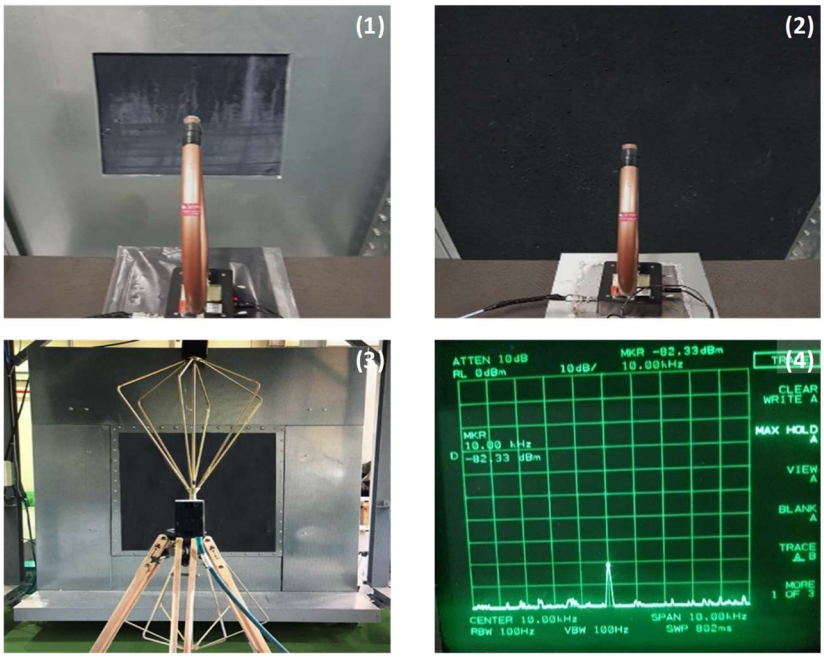

(c) Antenna setup and SE test: (1-3) Antenna setup, (4) SE test result

Fig. 5-6. *(Continued)* EMI SE testing procedure based on IEEE-STD-299.

5.3 Results and Discussion

5.3.1 Electrical resistivity and conductivity

Fig. 5-7a shows the electrical resistivity of the samples, obtained by converting measured electrical resistance of the samples (Appendix A-2), using Eq. (5.1) with respect to the CNT content. The electrical resistivity decreased significantly with an increase in the CNT content up to 1.0 wt.% (Fig. 5-7a). The obtained resistivity of the reference sample (i.e., at a CNT content of 0 wt.%) was 121173.3 Ω·m. It was significantly reduced to 4.8 Ω·m with 1.0 wt.% CNTs. This indicates that most CNTs were uniformly distributed throughout the composites via the proposed dispersion method in Chapter 4. If the degree of dispersion of CNTs is poor, the slope of the resistivity would gradually

decrease with increasing CNT content, and exhibit a modest increment. However, the electrical resistivity of the CNT2.0 was similar to that of CNT1.0. To analyze this behavior in detail, the electrical resistivity of the samples was converted to electrical conductivity.

Fig. 5-7b shows the electrical conductivity of the samples. The electrical conductivity improved with the CNT content. When the CNT content was less than 0.8 wt.%, the conductivity improved slightly, whereas a dramatic improvement in the conductivity was observed in the range of 0.8–1.0 wt.%. The conductivity obtained at a CNT content of 0 wt.% was 0.008 mS/m, but it sharply improved to 209.8 mS/m with 1.0 wt.% of CNT. However, at a CNT content of 2.0 wt.%, despite being double the content of 1.0 wt.%, the conductivity did not improve significantly, the conductivity of the CNT2.0 was only 224.0 mS/m. This is due to the percolation threshold, which is the ratio at which a conductive pathway is obtained through the connection of adjacent conductive fibers. A schematic diagram for the percolation threshold is shown in Fig. 5-8. The electrical resistivity of the samples decreased with increasing dispersed CNT fibers uniformly distributed in the UHPC matrix, and eventually the CNT fibers constructed the strong conductive pathway by completely connecting adjacent fibers at the percolation threshold, resulting in a significant improvement in conductivity. Thus, increasing the CNT content beyond the percolation threshold did not significantly improve the conductivity because the conductive pathway was already constructed at the percolation threshold. In this study, the mean CNT content when the conductivity sharply improved was 0.9 wt.%. Namely, the formation of the conductive pathway started at a CNT content of 0.5 wt.% and ended at 1.0 wt.%. Therefore, the CNT content of 0.9 wt.% can be regarded as the percolation threshold; this is the same as the previously obtained CIC value in Section 4.3. This demonstrates the correlation between the CIC and percolation threshold.

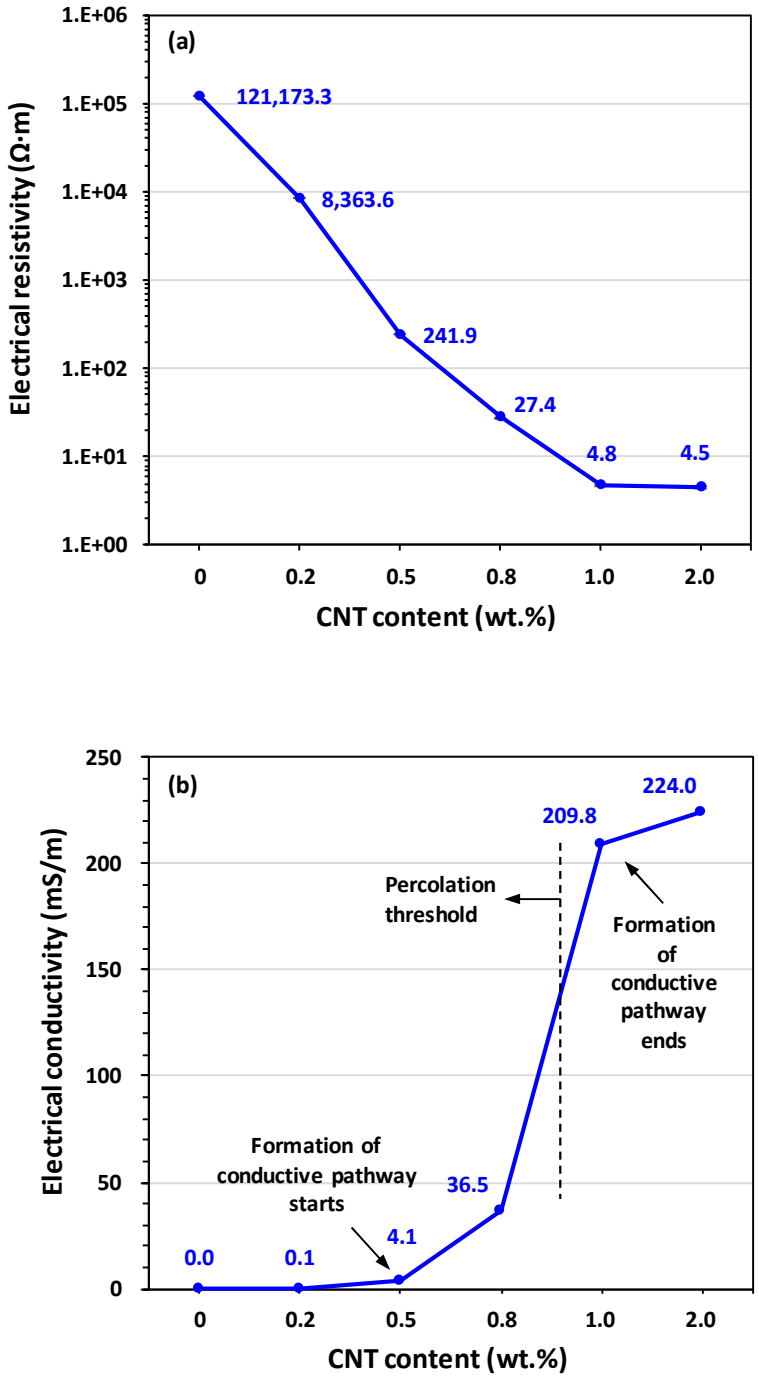

Fig. 5-7. Electrical (a) resistivity and (b) conductivity of the samples with respect to CNT content.

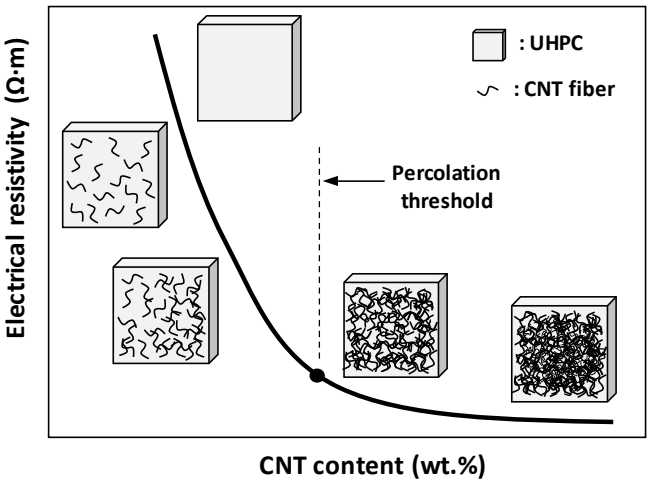

Fig. 5-8. Schematic variation of electrical resistivity of UHPC with respect to CNT content.

5.3.2 Basics of EMC theory

In this section, basics of EMC theory was outlined for better understanding on the discussion of EMI SE results in the following section. Table 4 presents the notations for the properties of EMI SE used in this chapter.

According to the law of conservation of energy, when incident energy is passing through a material, some of the energy is reflected off the surface of the material and is absorbed into the interior; this is converted to heat energy. The remaining energy is transmitted through the material, some of which is reflected again on the opposite surface of the material. Therefore, the SE that generated when EM waves pass through a material is theoretically the sum of the absorption loss (SE_A), reflection loss (SE_R), and multiple refection loss (SE_M) as shown in Fig. 5-9. Thus, Eq. (5.2) can be also expressed as follows:

$$SE\,(dB) = SE_A + SE_R + SE_M \tag{5.3}$$

Table 5-2. Notations for EMI SE properties.

Notation	Meaning	Unit	Remark
K	impedance ratio		
c	velocity of light	m/s	3.0×10^{8}
f	frequency	Hz	
l	maximum linear dimension of opening	m	
r	distance from antenna to sample	m	
t	thickness of sample	m	
ε_o	space permittivity	F/m	8.85×10^{-12}
ε_r	relative permittivity		
μ_o	space permeability	H/m	4.0×10^{-7}
μ_r	relative permeability		
λ	wavelength (c/f)	m	
σ_o	conductivity of copper	S/m	5.82×10^{7}
σ_r	relative conductivity		
δ	skin depth	m	

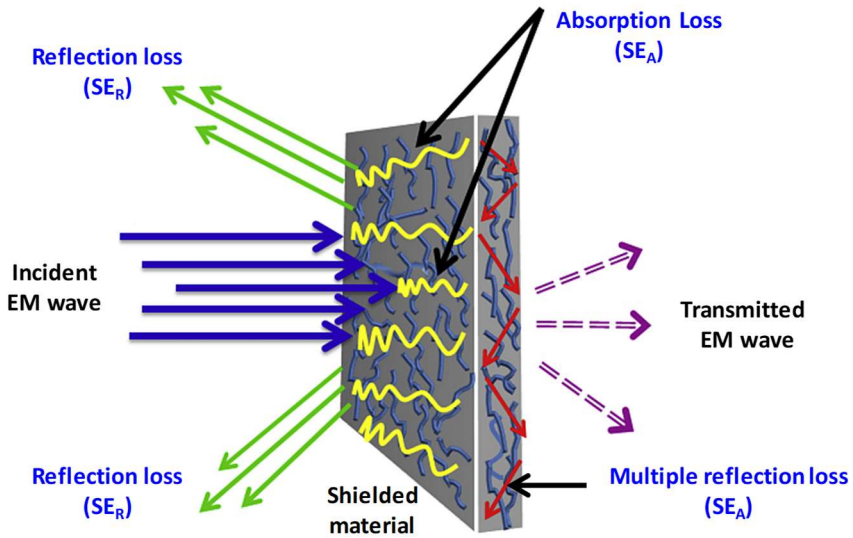

Fig. 5-9. Schematic representation of EMI shielding mechanism [95].

For SE_A, thickness of material (t) is one of important parameter because the amplitude of an EM wave decreases exponentially passes as it passes through a material as illustrated in Fig. 5-10. The thickness required for the EM wave to be shielded to $1/e$ or 37 % of its original value (i.e., amplitude of incident wave) is defined as the skin depth (δ).

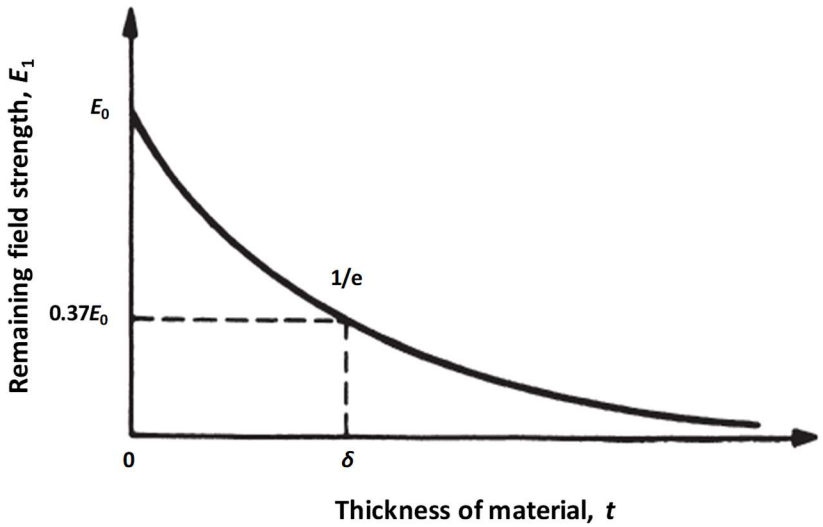

Fig. 5-10. Amplitude of an EM wave that decreases exponentially as it passes through a material.

SE_R occurs owing to the impedance mismatch between the wave impedance (Z_w) and the intrinsic impedance of the material (Z_m). Z_w, which is ratio of the electric field (E-field) to the magnetic field (H-field), is well defined in the near field and for far field at a distance from the source (r), and is normalized by $\lambda/2\pi$, as shown in Fig. 5-11. In the near field, Z_w is defined by the characteristics of the source and the distance from the source to where the field is observed. If the source has high current and low voltage ($E/H < 377\ \Omega$), the near field is predominantly magnetic. Conversely, if the source has the low current

and high voltage (E/H > 377 Ω), the near field is predominantly electric. For a predominantly H-field, as the distance from the source increases, E-field attenuates at a rate of $(1/r)^2$, whereas the H-field attenuates at a rate of $(1/r)^3$. Thus, the Z_w increases with distance and asymptotically approaches the impedance of free space in the far field. On the contrary, for a predominantly E-field, as the distance from the source increases, E-field attenuates at a rate of $(1/r)^3$, whereas the H-field attenuates at a rate of $(1/r)^2$. Therefore, the Z_w decreases with distance and approaches that of free space at a distance of $\lambda/2\pi$. However, in the far field, they combine to form a plane wave with an impedance of 377 Ω equal to the impedance of the material (e.g., $E/H = Z_m$ = 377 Ω). The region around $\lambda/2\pi$ is the transition region between the near and far fields. Hence, SE_R should be considered separately according to the characteristics of Z_w for each field. Given that the SE of the E-field is always higher than that of the H-field, it is not mentioned in general. Therefore, the SE associated with the E-field is not discussed in this study.

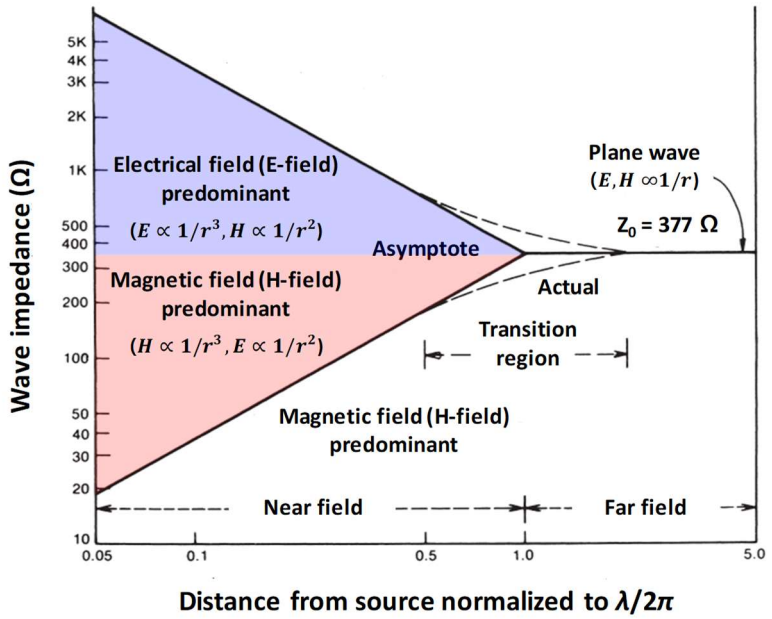

Fig. 5-11. Wave impedance depending on the distance from the source.

The impedance of each corresponding frequency region can be calculated as follows:

$$Z_w(\Omega) = k\sqrt{\frac{\mu_o}{\varepsilon_o}} \cong 120\pi k,$$
$$\text{where } k = \begin{cases} \dfrac{2\pi k}{\lambda} & \text{for H-field} \\ 1 & \text{for plane wave} \end{cases} \tag{5.4}$$

$$Z_m(\Omega) = \sqrt{\frac{\mu_o}{\varepsilon_o \varepsilon_r}} \quad \text{for dielectric.} \tag{5.5}$$

According to EMC theory, each SE component can be calculated as follows depending on the frequency region [96]:

$$SE_A\ (\text{dB}) = 8.689\left(\frac{t}{\delta}\right) = 131.4t\sqrt{f\mu_r\sigma_r} \tag{5.6}$$

$$SE_R\ (\text{dB}) = \begin{cases} 20\log\dfrac{(1+K)^2}{4K} & \text{in general,} \quad (5.7a) \\ 14.6 - 10\log\left(\dfrac{\mu_r}{fr^2\sigma_r}\right) & \text{for H-field } (SE_R^H), \quad (5.7b) \\ 168 - 10\log\left(\dfrac{f\mu_r}{\sigma_r}\right) & \text{for plane wave } (SE_R^P), \quad (5.7c) \end{cases}$$

$$SE_M\ (\text{dB}) = 20\log\left[1 - \left(\frac{K-1}{K+1}\right)^2 e^{-2rt}\right] \tag{5.8}$$

SE_M term can be neglected when SE_A has more than 10 dB or in the case of a relatively thick material. This is because EM waves are absorbed by passing through the material several times each time it is reflected multiple times by the boundary of the material, weaken the magnitude of SE_M [96, 97].

It can be seen from the Eqs. (5.4–5.7) that electrical conductivity, frequency of incident wave, permeability, and thickness of material are the important parameters for defining EMI SE. However, the preceding equations are valid only for solid (uniform) material (e.g., metal) without an opening. In the opposite case (i.e., solid material with an opening), EMI SE considerably decreases through the opening. Thus, the following equation (which describes the "opening effect, SE_o") should be considered to calculate the SE according to the theory of slot antenna.

$$SE_o\ (\mathrm{dB}) = 20\log\left(\frac{\lambda}{2l}\right) = 20\log\left(\frac{c}{2fl}\right). \tag{5.9}$$

As shown in Eq. (5.9), SE_o depends on the maximum linear dimension of opening (l). Eq. (5.9) can only be used when the l is less than half of the wavelength (λ) because maximum radiation from a slot antenna occurs when its l is equal to $\lambda/2$.

Fig. 5-12 shows a general trend of the SE for materials without and with an opening. For materials without an opening, SE_A increases with the frequency regardless of the frequency region. SE_R increases with the frequency in the H-field, while decreases with increasing frequency in the plane wave. In determining the SE, SE_A term is dominant in the H-field, whereas SE_R term is dominant in the plane wave. For materials with an opening, the magnitude of SE_o exponentially decreases with increasing frequency.

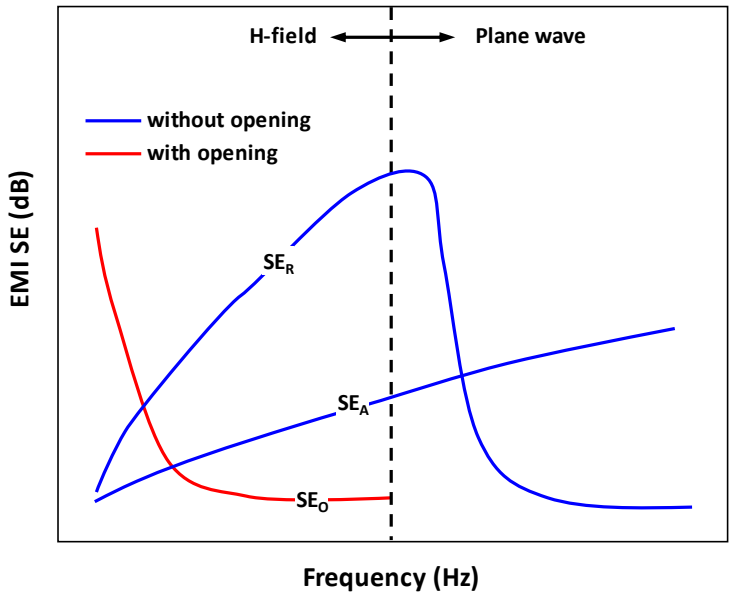

Fig. 5-12. General trend of SE for a material without or with an opening.

5.3.3 EMI SE results based on two different SE testing method

Fig. 5-13 presents the EMI SE testing results of the samples based on ASTM-D4935-18. The SE of the CNT0 (Ref.) was close to 0 dB in all frequency bands. This indicates that UHPC has no EMI shielding capability. However, with the addition of the CNTs, the SE not only improved at the same frequency but also linearly increased with the frequency. In particular, the SE noticeably improved from the CNT content of 0.5 wt.%, at which the conductivity significantly developed and indicated the beginning of the formation of a conductive pathway. The SE of the samples CNT0.5 and CNT0.8 was measured as 3.7 and 7.5 dB at 30 MHz, and 10.6 and 16.6 dB at 1.5 GHz, respectively. The SE of the samples CNT1.0 and CNT2.0, which had similar electrical conductivity, was almost identical in all the frequency bands. They had approximately 18 and 25 dB at 30 MHz and 1.5 GHz, respectively. This demonstrates that electrical conductivity is the key parameter for the SE and that there is the direct correlation between them.

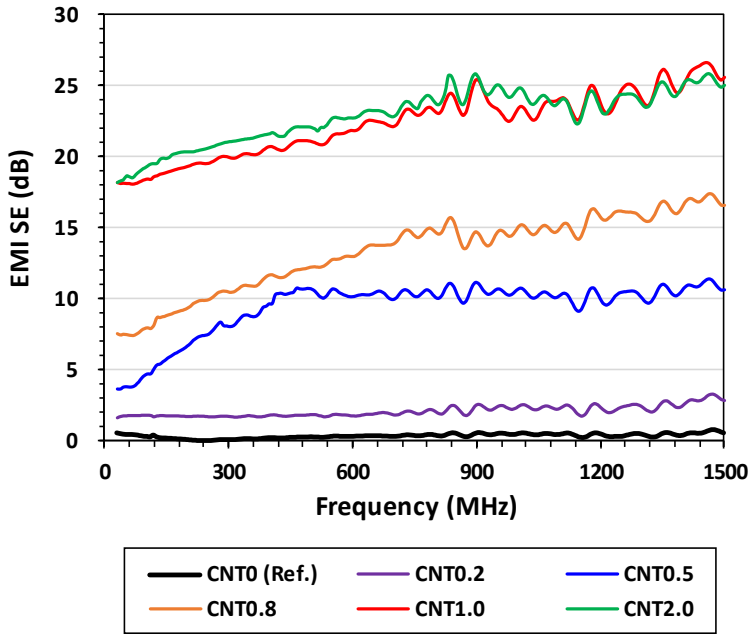

Fig. 5-13. EMI SE testing results based on ASTM D4935-18.

This result can be validated by employing the EMC theory. First, the samples used in this experiment were relatively thick (3 mm) compared to the required dimension (25 μm). In addition, similar to most cementitious materials, UHPC is a dielectric that experiences very little loss compared to metals. Thus, the SE_M term can be neglected. Second, the experimental frequency bands can be regarded as the H-field because the distance from the signal to the sample (r; assumed to be 0.003 m, i.e., the thickness of the sample) was much less than $\lambda/2\pi$. In the H-field, both SE_A and SE_R increase as the electrical conductivity and frequency increase, but the SE_R term is dominant as indicated in Eqs. (5.6–7a) and Fig. 5-12. In addition, the relative permeability (μ_r) of the samples can be assumed to be constant (i.e., close to 1) because both the cementitious materials and CNTs are not magnetic [68]. Hence, the SE of the reference sample was close to zero due to poor electrical conductivity. In other word, the SE of the samples containing CNTs improved because the electrical conductivity enhanced as the CNT

content increased. Furthermore, the SE increased linearly with the frequency because the measured frequency bands were in the H-field. However, the magnitude of the SE for CNT2.0 was not significantly improved in comparison with that of CNT1.0 because they had similar electrical conductivity.

Fig. 5-14 shows the EMI SE testing results of the samples with a small incident area of 300 × 300 mm^2 conducted according to IEEE-STD-299 in the range of 10 kHz–1.5GHz. According to EMC theory and the experimental conditions (e.g., distances from the transmitting antenna to the sample), the experimental frequency ranges can be classified into three regions: the H-field (below 10 MHz), transition and resonant region (from 10 MHz to 100MHz), and plane wave (above 100 MHz). The SE of the samples improved at the same frequency with the addition of CNTs compared to that of the reference sample. In particular, the SE noticeably increased above a CNT content of 0.5 wt.%, at which the conductivity significantly developed. In addition, the SE of samples CNT1.0 and CNT2.0 was almost identical for the entire measured frequency range. These were the same trends observed for the SE testing results based on ASTM D4935-18 and confirmed that the electrical conductivity is a major parameter for the SE. However, two interesting differences were observed. Firstly, the magnitude of the SE was significantly different. The SE of all samples was noticeably higher than the SE obtained from ASTM D4935-18 method in all frequency bands. In particular, the SE of the reference samples, which had no SE (close to 0 dB) in the testing result based on ASTM D4935-18, was higher than 25 dB at frequencies below 1 GHz. In addition, as the frequency increased above 30 MHz, the SE of the samples, which had increased in the ASTM D4935-18 method, decreased. Hence, the SE of the cementitious material (especially UHPC) seems to vary depending on the testing method. The result based on the IEEE-STD-299 are discussed in detail in the following section with the SE testing result of the samples with a large incident area.

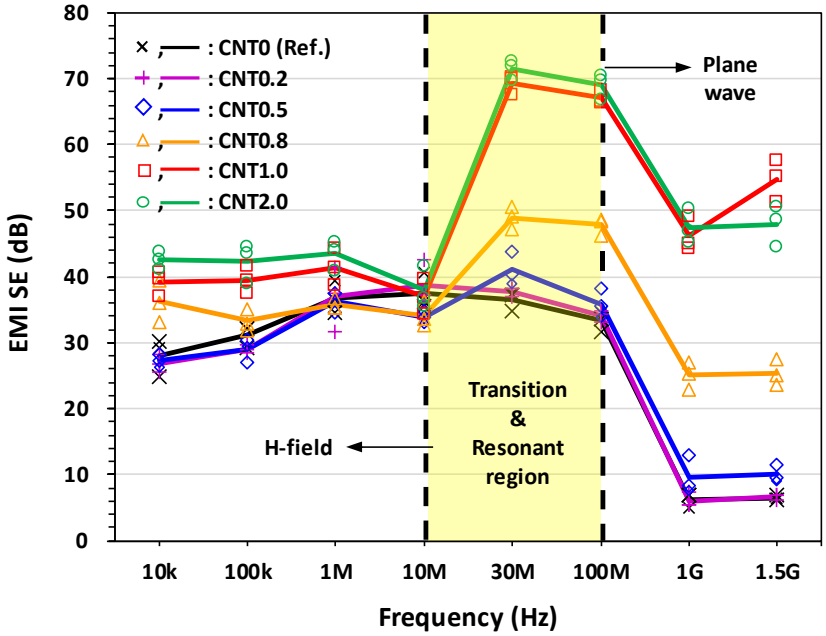

Fig. 5-14. EMI SE testing results of the samples with a small incident area based on IEEE-STD-299 the range of 10 kHz–1.5GHz (symbols and lines represent the experimental values and their average values, respectively).

5.3.4 Effects of incident area size on EMI SE

The EMI SE testing results based on IEEE-STD-299 in the range of 10 kHz–18GHz obtained from the samples with two different incident areas (i.e., a small incident area of 300 × 300 mm^2 and a large incident area of 1200 × 1200 mm^2) are presented in Fig. 5-15. SE at frequencies of 30 MHz and 1.5GHz was excluded because the 30 MHz was in the transition and resonant region and the SE at 1.5 GHz was similar to that at 1 GHz. The standard deviation of the SE test results for each sample was less than 5 dB, indicating that the SE test was performed appropriately. For all the samples, the SE improved as the CNT content increased in all frequency bands regardless of the size of the incident area. In addition, the SE was similar between samples CNT1.0 and CNT2.0 for the entire measured frequency range.

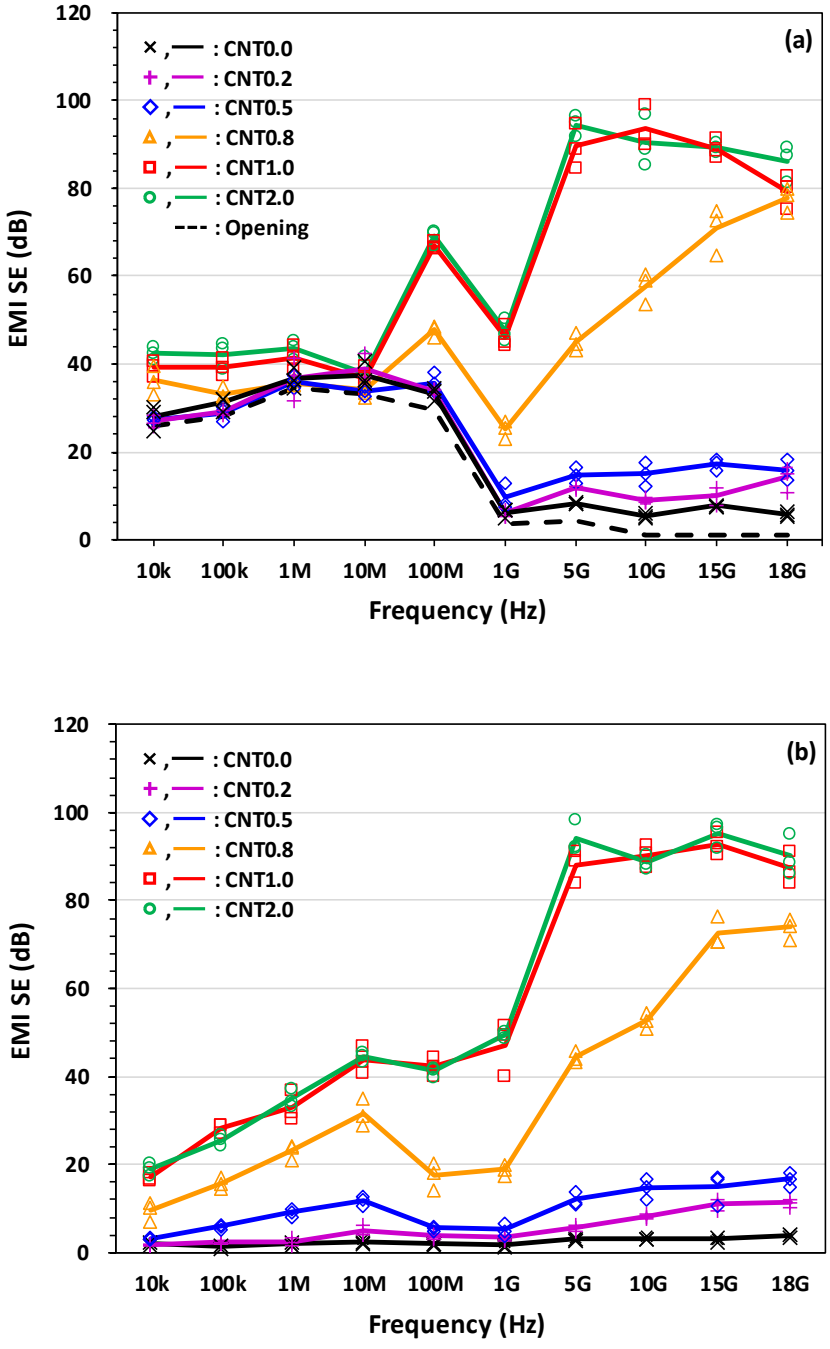

Fig. 5-15. EMI SE testing results of the samples with different incident areas based on IEEE-STD-299: (a) 300 × 300 mm^2, (b) 1200 × 1200 mm^2 (symbols and lines represent the experimental values and average values, respectively).

One interesting observation from the experimental results was that the SE could be overestimated when a small sample with a relatively small incident area was used, owing to collateral shielding by a region of the shielded chamber in the vicinity of the opening. The SE values obtained for small and large incident areas were almost identical at frequencies above 1 GHz. Meanwhile, for the small incident area (Fig. 5-15a), the SE measured at frequencies below 1 GHz was more than twice that of the samples with large incident area (Fig. 5-15b), although the samples were fabricated with the same batch mixtures and curing conditions. In particular, the reference sample had an SE value of 28.11 dB at 10 kHz, which appears to be a very high considering that it has very low electrical conductivity, which is the dominant parameter for SE. This was assumed to be that the electrical dimension of the opening, which had the same size as the small incident area, was smaller than the transmitted λ as described in Fig. 5-16.

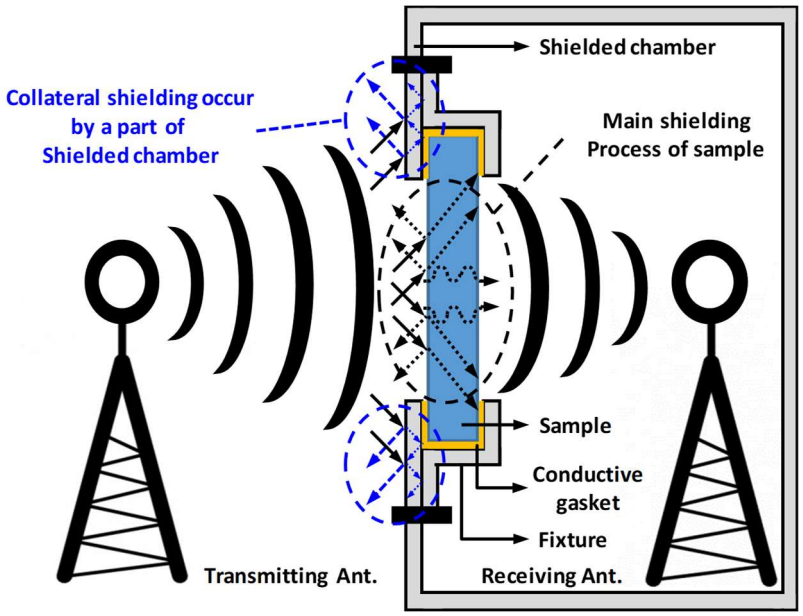

Fig. 5-16. Collateral shielding by a region of the shielded chamber because of the insufficient size of incident area.

Specifically, the transmitted EM waves were not completely incident to the mounted sample, but some was collaterally shielded by a region of the shielded chamber in the vicinity of the opening. Thus, the receiving antenna received only a small part of the signal that should have been received. This resulting that the SE was measured to be high as if the reference sample had a SE. To validate this assumption, the SE of the opening (i.e., without a sample being mounted) was tested. The SE measured only with an opening was nearly the same as that of the reference sample below 1 GHz, where as it was close to 0 dB at above 1 GHz (black dotted line in Fig. 5-15a). This indicates that as the transmitted λ decreased with an increase in the frequency up to 1 GHz, SE_C decreased, and eventually, it disappeared at above 1 GHz because the value of λ became so small that the incoming EM waves were completely incident on the samples regardless of the dimension of opening (i.e., size of incident area). Therefore, to evaluate the SE of the samples itself ($SE_{effective}$, SE_{eff}), it is more effective to subtract the SE of the opening ($SE_{opening}$) from the SE measured based on conventional method (i.e., IEEE-STD-299) to eliminate the potential contribution of collateral shielding despite the calibration as follows:

$$SE_{eff}\ (dB) = SE - SE_{opening} = SE_A + SE_R + SE_M \tag{5.10}$$

This approach was applied to the SE test results (given in Fig. 5-15), and the results are presented in Fig. 5-17. The reference sample exhibited low SE values close to 0 dB for all frequency bands regardless of the size of the incident area, which was the consistent with the result of coaxial TEM cell testing method. In addition, the SE of the samples containing CNTs for the small incident area at 10 kHz was reduced to values that are similar to those for the large incident area. These results validate the assumption that the SE can be overestimated if it is tested using a sample with a relatively small incident area.

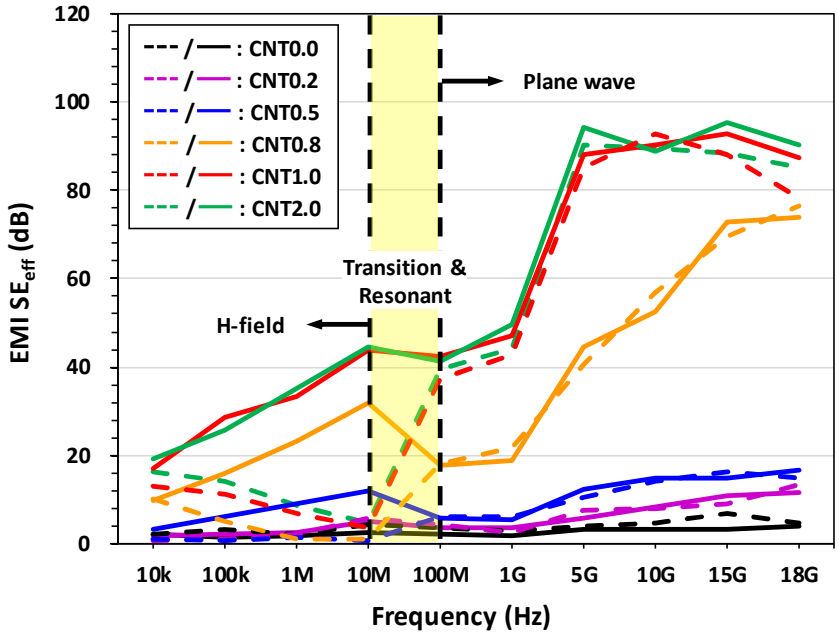

Fig. 5-17. EMI SE testing results with collateral shielding eliminated (SE_{eff}, dotted and solid lines represent the results for the 300 × 300 mm^2 and 1200 × 1200 mm^2 incident areas, respectively).

Another observation was that a small incident area can result in a distorted SE in the H-field owing to the opening effect (SE_o), whereas it has little effect for a plane wave. In the H-field (i.e., frequency range of 10 kHz–10 MHz), the SE_{eff} of the samples with a large incident area increased, which was consistent with not only the result of coaxial TEM cell testing method but also the trend according to EMC theory. However, the SE_{eff} of the samples with a small incident area decreased in the H-field. It is presumed that this result was also attributed to the dimensions of the opening. Fig. 5-18 shows the effect of a shield discontinuity by the type of material. The incident EM field induces a current into the material, and this current then generates an additional field on the opposites side. This new field cancels or reflects the original field in some regions of space, specifically the region on the opposite surface of the material from the incident surface. For this

cancellation to occur, the induced shield current must be allowed to flow undisturbed in the manner in which it is induced. If an opening forces the induced current to flow in a different path, then the generated field will not completely cancel or reflect the original field, and the SE will be reduced. Forcing the current to detour more cause the SE to further decrease. UHPC, which is similar to most cementitious materials, has multiple size pores ranging from the nanometers to millimeters. The pores in the material can act as micro-opening. Therefore, it is more appropriate to consider UHPC as a porous material with micro-openings rather than a uniform material. In addition, it has very low electrical conductivity, which results in a low SE close to 0 dB. Thus, the UHPC matrix can be regarded as a single opening that can cause a shield discontinuity from the viewpoint of electromagnetics. In the case of the samples with CNTs, only the UHPC matrix reinforced with CNTs acts as a shield, and the other parts (i.e., the UHPC matrix without CNTs and pores) acts as an opening. Hence, Eq. (5.9) allows the SE of a material with an opening (i.e., corresponding to the effect of the UHPC matrix without CNTs) should be considered in addition to the Eqs. (5.6–5.7b) for the materials SE of materials without an opening (i.e., corresponding to the effect of CNTs in the UHPC matrix).

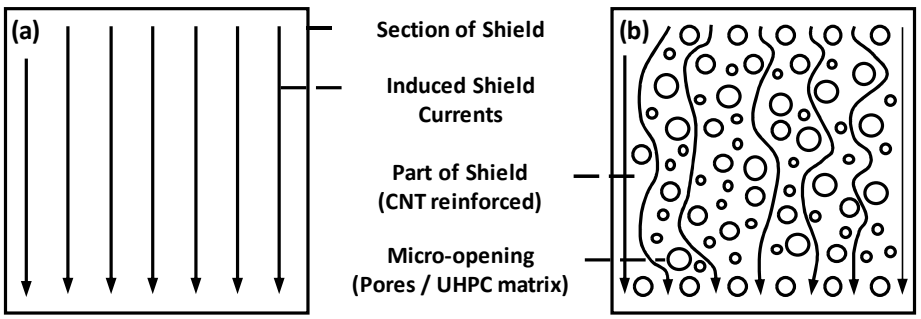

Fig. 5-18. Effect of shield discontinuity on a magnetically induced shield current: (a) uniform material and (b) porous material.

Based on this assumption, the new SE_{eff} in an H-field (SE_{eff}^{H*}) considering the opening effect can be expressed as follows:

$$SE_{eff}^{H*}\,(dB) = SE_{eff}^{H} + SE_o = SE_A + SE_R^H + \cancel{SE_M} + SE_o, \tag{5.11}$$

SE_M can be ignored because the UHPC is dialectic and the thickness of the samples was relatively thick, as discussed in Section 5.3.3.

Let SE_{eff}^{H*} at a given frequency (f_1) be $SE_{eff\_1}^{H*}$. Then, that at a certain frequency (f_2), $SE_{eff\_2}^{H*}$, can be written as

$$SE_{eff\_2}^{H*} = SE_{eff\_1}^{H*} + dSE_{eff}^{H*}, \tag{5.12}$$

where dSE_{eff}^{H*} is the differential increment and can be calculated as follows:

$$dSE_{eff}^{H*} = \frac{d}{df}(SE_A + SE_R^H + SE_o)df, \tag{5.13}$$

By substituting Eqs. (5-6), (5-7b), and (5-9) into Eq. (5.13), Eq. (5.14) can be derived.

$$dSE_{eff}^{H*} = \frac{d}{df}\left[131.4\sqrt{f\mu_r\sigma_r} + 14.6 - 10\log\left(\frac{\mu_r}{fr^2\sigma_r}\right) + 20\log\left(\frac{c}{2fl}\right)\right]df \tag{5.14}$$

By differentiating Eq. (5.14) with respect to the frequency (f), dSE_{eff}^{H*} can be calculated as follows:

$$
\begin{aligned}
&d\mathrm{SE}_{\mathrm{eff}}^{\mathrm{H}*} \\
&= \left(\frac{65.7t\sqrt{\mu_r\sigma_r}}{\sqrt{f}} + \frac{10}{\ln 10}\frac{fr^2\sigma_r}{\mu_r} - \frac{20}{\ln 10}\frac{2fl}{c}\frac{c}{2f^2l} \right) df \\
&= \left(\frac{65.7t\sqrt{\mu_r\sigma_r}}{\sqrt{f}} + \frac{10}{f}\frac{1}{\ln 10} - \frac{20}{f}\frac{1}{\ln 10} \right) df \\
&\approx \left(-\frac{10}{f}\frac{1}{\ln 10} \right) df, \qquad \text{where } \frac{65.7t\sqrt{\mu_r\sigma_r}}{\sqrt{f}} \approx 0
\end{aligned}
\tag{5.15}
$$

Given that the contribution of SE_A in the H-field is small and the calculated dSE_A is close to 0 dB based on the experimental conditions, it can be considered as negligible.

It should be noticed again that as the frequency increases in the H-field, both SE_A and SE_R increase whereas SE_o decreases. However, a negative increment has been derived; this is noteworthy because it means that the rate of increase in SE_R is smaller than the rate of decrease in SE_o. Thus, $SE_{\mathrm{eff}}^{\mathrm{H}*}$ decreases gradually instead of increasing. $dSE_{\mathrm{eff}}^{\mathrm{H}*}$ can be calculated to be approximately -3.91 dB regardless of frequency based on Eqs. (5.14–15). Because the SE was measured at 10 frequency intervals from 10 kHz to 1 GHz, df corresponded to $9f_1$ ($f_2 - f_1 = 10f_1 - f_1 = 9f_1$). Thus, the SE in the H-field decreased with the corresponding increment as the frequency by a factor of 10. Good agreement between the SE reduction rates of the experimental results and derived result of -3.9 dB was observed, as shown in Fig. 5-19 (the results for specimens CNT0–CNT0.5 are not presented because they had low SE of less than 2 dB within the error range). However, this tendency was not observed in the SE result for the large incident area samples. This is possibly because the opening effect was removed by increasing the dimension of the incident area. SE_o decreases with an increase in l, as indicated by Eq. (5.9).

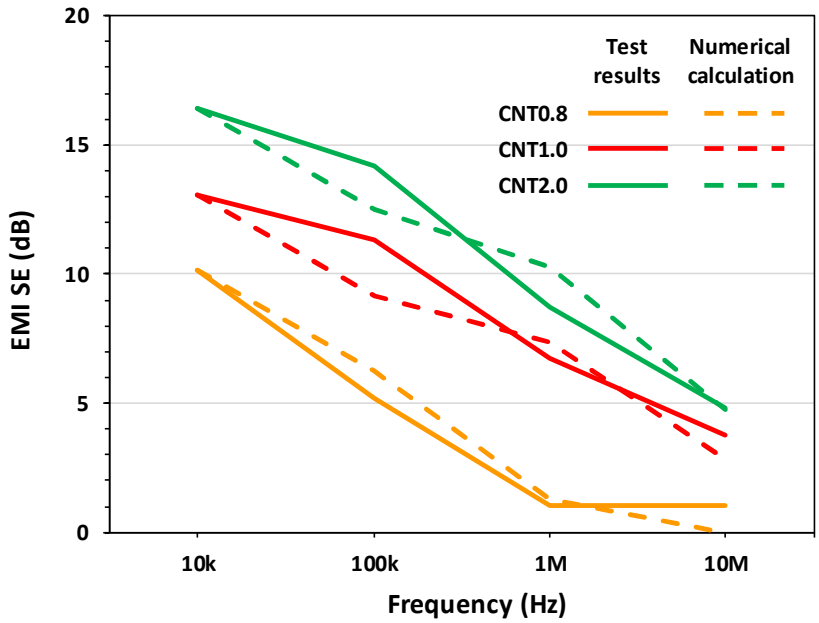

Fig. 5-19. Comparison between the SE reduction rates for the experimental results and numerical calculation.

The SE for a plane wave was hardly affected by the opening effect. Note again that Eq. (5.9) can be used only when the value of l is less than $\lambda/2$, and SE_o decreases with increasing the frequency. The l value of the samples with a small incident area was approximately 425 mm ($\sqrt{2}$ × 300 mm) which is larger than 150 mm, corresponding to $\lambda/2$ at 1 GHz (the lowest experimental frequency in the plane wave region). Thus, Eq. (5.9) cannot be used for a plane wave. Specifically, the SE_o decreased with increasing frequency, and it eventually disappeared in the plane wave region. Note that the SE values obtained for small and large incident areas were almost identical at above 1 GHz. This demonstrates that the effect of the opening on SE for a plane wave was small regardless of the size of the incident area. However, if the SE test is performed using a sample with l smaller than 150 mm, the SE for a plane wave could be distorted owing to the opening effect, but the effect is not significant.

In the case where the SE was measured for a large incident area, it temporarily decreased in the frequency range of 10–100 MHz, which is defined as the transition and resonant region. This is because resonance occurred in this region. Resonance occurs when $l = \lambda/2$. Given that the l value of the large incident area was approximately 1700 mm ($\sqrt{2}$ × 1200 mm), the resonant frequency corresponding to $\lambda/2$ was calculated as 88 MHz. Thus, the resonance occurred at a resonant frequency of approximately 88 MHz, resulting in an SE reduction.

Based on preceding analysis, it can be concluded that the EMI SE obtained from samples with a large incident area can represent the actual UHPC structure. The SE of the reference sample was below 3 dB in all frequency bands, whereas the CNT1.0 had the SE of 17.16 dB at 10 kHz (H-field) and 47.14 dB at 1 GHz (plane wave), which are increase of 8.58 and 23.57 times, respectively. This result is completely different from that of the coaxial TEM cell testing. Thus, ASTM D4935-18 should only be used to roughly estimate the effect of different component on the SE of cementitious material, large sample testing method using samples with a sufficient incident area should be required to evaluate the SE of cementitious materials for actual application.

In summary (Fig. 5-20), the SE results for small and large incident areas are correlated with the frequency region. When testing the SE of UHPC/CNT composites according to IEEE-STD-299 in the H-field, samples should be fabricated to have an incident area of at least 1200 × 1200 mm^2 to eliminate the aperture effect. Otherwise, the SE could be overestimated and distorted. However, the SE for a plane wave is hardly affected by the aperture effect to be sufficient to represent the SE for the actual structure regardless of the size of the incident area. This finding can be applied to not only UHPC/CNT composites, but also cementitious materials such as cement paste, mortar, and concrete, because they have similar electrical resistivity.

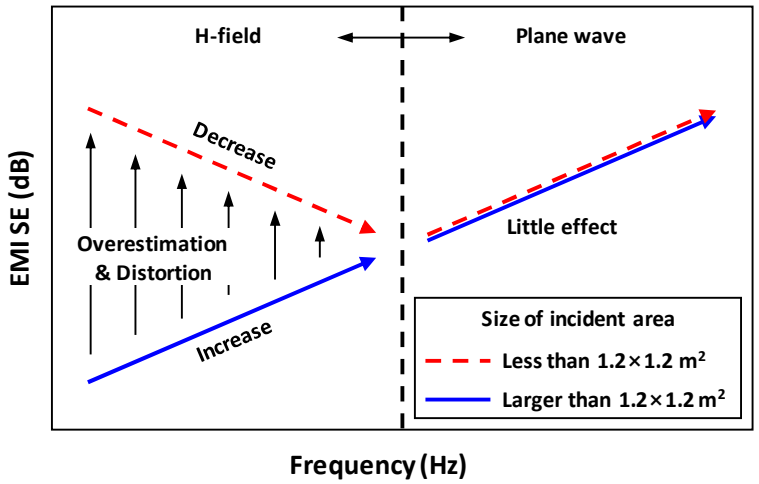

Fig. 5-20. Effect of incident area size on EMI SE of cementitious composite materials (especially UHPC/CNT).

5.3.5 Modelling to practically estimate SE of UHPC

In this section, a practical model to effectively estimate the SE for cementitious materials was proposed. Fig. 5-21 shows the comparison of SE results between the experimental data and numerical calculation via Eqs. (5.6–7) and it is found that there were significant differences. However, the SE trend of the experimental data became similar to that of numerical calculation with increasing CNT content. This is because the equations were derived for metals, which have good electrical properties, while cementitious materials have poor electrical properties. Thus, the SE of numerical calculation for the reference sample was very inaccurate, but with the addition of CNTs, although the accuracy of the SE was still poor, the samples with CNTs showed similar SE trend to that of numerical calculation by having characteristic of conductor. For this reason, many researchers have attempted to develop a model to predict the SE of cementitious materials [98-101]. However, these previous models require information on variables that are difficult to measure such as μ_r, ε_r, and the moisture content to estimate SE. Therefore, they have limited use in practical situations.

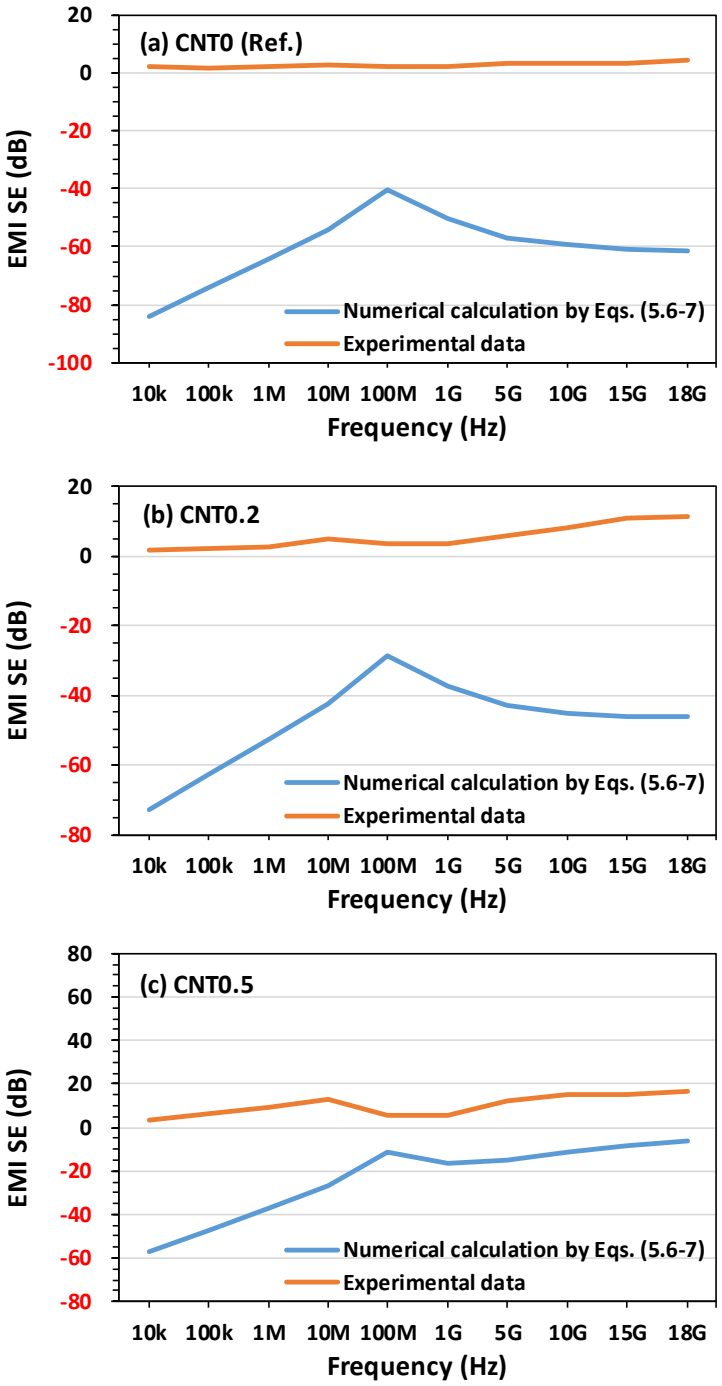

Fig. 5-21. Comparison of SE results between experimental data and numerical calculation via Eqs. (5.6–7).

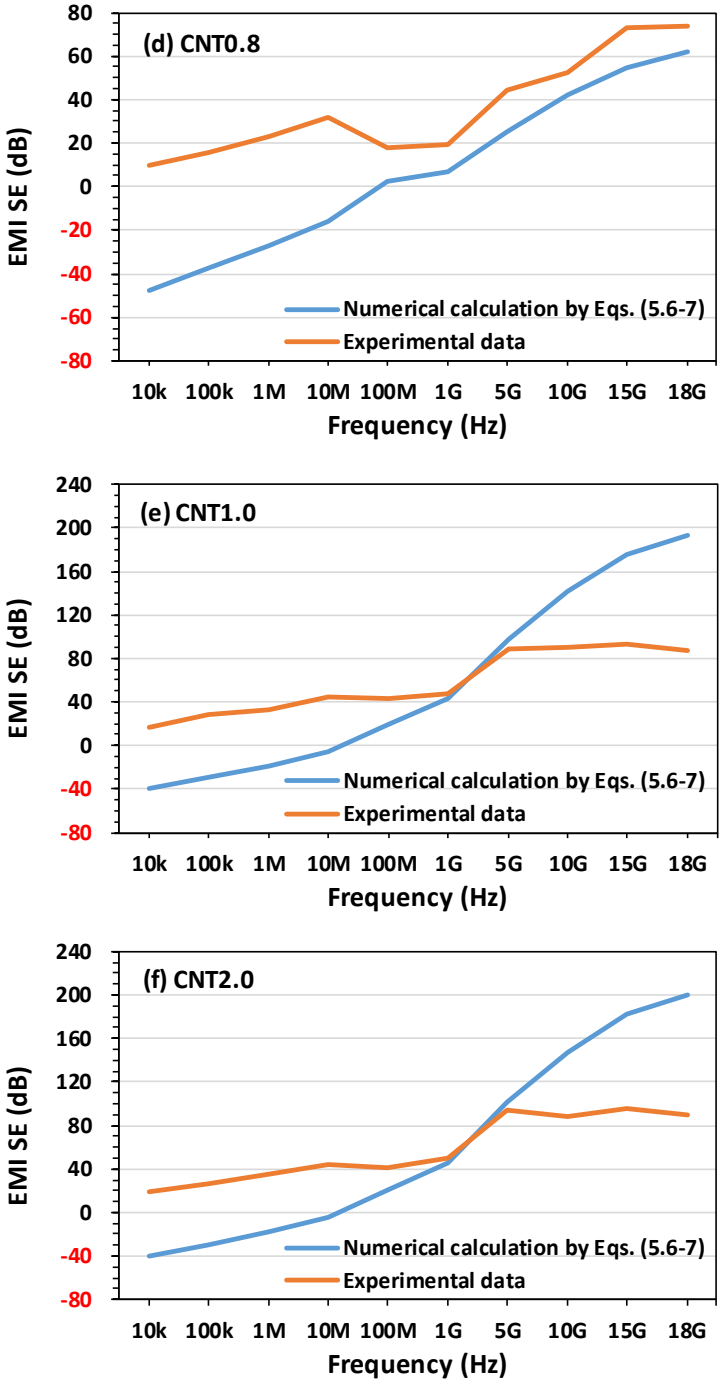

Fig. 5-21. *(Continued)* Comparison of SE results between experimental data and numerical calculation via Eqs. (5.6–7).

Hence, a practical model to approximately estimate the SE of UHPC/CNT composites in terms of simple properties that are easy to measure, such as σ_r, r, t, and the frequency of interest f, is proposed according to the experimental results. The proposed model consists of equations for calculating the EMI SE in the H-field and for a plane wave, respectively, as follows:

$$\text{SE (dB)} = \begin{cases} 188.384\left(\dfrac{1}{fr^2\sigma_r}\right)^{-0.236} & \text{for H-field} \quad (5.16a) \\ \text{where } 10\text{ kHz} \le f \le 10\text{ MHz} & \\ \beta\sqrt{f} + 1.35 & \text{for plane wave} \quad (5.16b) \\ \text{where } \beta = \dfrac{\text{SE}_{1\text{GHz}} - 1.35}{\sqrt{10^9}},\ 1\text{ GHz} < f \le 18\text{ GHz} & \end{cases}$$

To construct the model, it is first assumed that the μ_r and ε_r of the UHPC composites are 1 and 4.94, respectively [102], regardless of the CNT content. This assumption is made because the CNTs are not magnetic materials and cannot improve μ_r [68]. Moreover, a carbon filler, e.g., CNTs, can significantly affect the relative conductivity σ_r, whereas it has little effect on the relative permittivity ε_r [65, 98, 103].

Initially, a regression model was employed to estimate the SE in the H-field according to the experimental results. In the H-field, SE_R can be regarded as the SE because SE_R is the key factor for determining the SE, and the contribution of SE_A is negligible. Therefore, Eq. (5.7b) was revised as Eq. (5.16a) by performing regression analysis using the software SPSS Statistics 25.0. shows the results of the regression analysis for $\text{SE}_\text{M}^\text{H}$. The experimental data are scattered around the line plotted by the regression equation (5.16a). In Table 5-3, which is a summary of the

regression analysis, the value of significance (Sig.) is less than 0.001. Accordingly, it is considered that there is a significant relationship between the independent variables (f, r^2, and σ_r) and the dependent variable (SE_M^H) in the model. In addition, because the coefficient of determination (R^2) is 0.826, it can be considered that this model implies that there is an 82.6 % variability in the dependent variable. In statistics, a regression model in which R^2 is greater than 0.7, and a Sig. less than 0.001 is regarded as significant enough to be applied as an estimation model. Thus, (5.16a) can be applied to estimate the SE in the H-field.

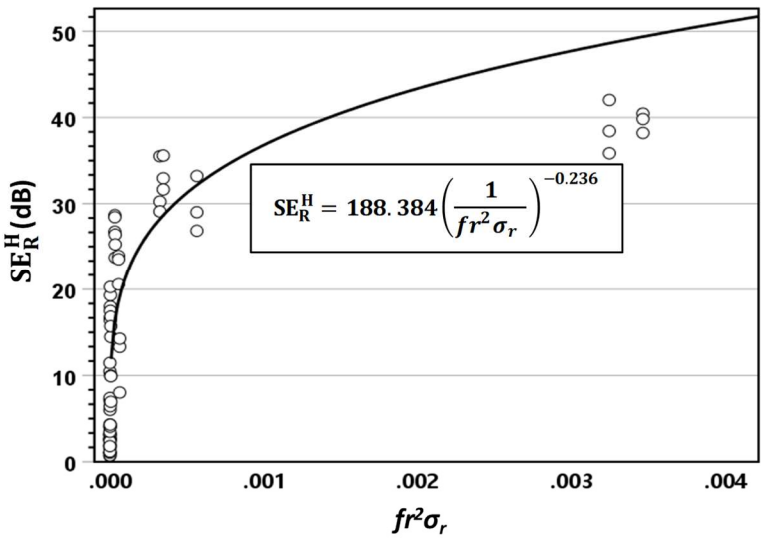

Fig. 5-22. Results of the regression analysis for SE_R^H.

Table 5-3. Summary of the regression analysis for SE_R^H.

Equation type	Model summary					Parameter estimates	
	R^2	F	Dof1	Dof2	Sig.	Constant	b1
Power	**0.826**	332.84	1	70	**0.000**	188.384	-0.236

When a plane wave passes through a material, its amplitude is attenuated exponentially as a function of the skin depth (δ) [104]. The δ can be calculated as follows [105]:

$$\delta(\mathrm{m}) = \frac{0.066}{\sqrt{f \mu_r \sigma_r}}. \tag{5.17}$$

SE_A can also be calculated by substituting Eq. (5.17) into Eq. (5.6).

Fig. 5-23 shows the δ of the samples and copper calculated using Eq. (5.17). The δ of the samples was very thick in the plane wave, whereas that of the copper was very thin. However, as the CNT content increased, the δ of the samples decreased via the decrease in resistivity. Therefore, the samples containing CNTs cannot be regarded as a conductor as copper, but it can be regarded as lossy dielectric material, where the incident plane wave is partially reflected causing SE_R, while the remainder penetrates and is attenuated resulting in SE_A.

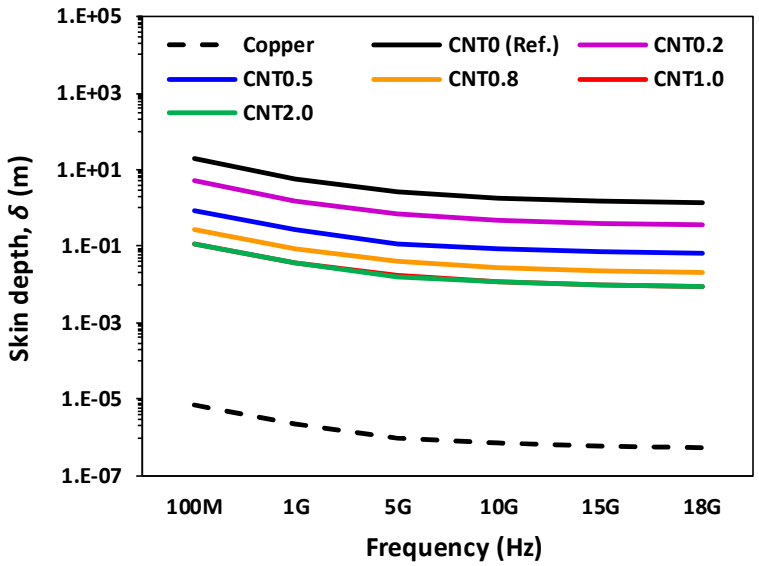

Fig. 5-23. Skin depth (δ) of the samples and copper.

Hence, Eq. (5.16b) is derived using the following procedure. First, the impedance ratio (K) is calculated using Eqs. (5.4) and (5.5) to determine the contribution of SE_R to the SE for a plane wave (SE_R^P). It is expressed as follows:

$$K = \frac{Z_m}{Z_w} = \sqrt{\left(\frac{\mu_o}{\varepsilon_o \varepsilon_r}\right) / \left(\frac{\mu_o}{\varepsilon_o}\right)} = \sqrt{\frac{1}{\varepsilon_r}} \tag{5.18}$$

Then, SE_R^P is calculated as 1.35 dB regardless of the frequency by substituting Eq. (5.18) into Eq. (5.7a). This indicates that for a plane wave, the contribution of SE_R is very small, and the major factor determining the SE is SE_A.

To derive the appropriate equation to calculate SE_A for a plane wave, the experimental SE value measured at 1 GHz (SE_{1GHz}) was used as the reference. Theoretically, a frequency corresponding to a plane wave starts at 28.09 MHz, but this frequency is within the resonant and transition region. Hence, it is not appropriate as the reference frequency to estimate SE at high frequencies for a plane wave. In addition, because the δ of the samples calculated at 100 MHz (Fig. 5-24) was thicker than the thickness of the samples (0.2 m), it cannot be considered that sufficient A has been occurred at 100 MHz. However, the δ at 1 GHz was smaller than the thickness of the samples, except samples CNT0 (Ref.) and CNT0.2, where SE were close to 0 dB so that A can be considered to be occurred enough at 1 GHz. Thus, SE_{1GHz}, i.e., the first measured SE value in the plane wave outside of the resonant and transition region, was selected as the reference. It is reasonable that an SE_A at 1 GHz ($SE_{A\ at\ 1GHz}$) can be calculated by subtracting SE_R^P from SE_{1GHz}. Then, $SE_{A\ at\ 1GHz}$ is equated with Eq. (5.6) as follows:

$$SE_{A\ at\ 1GHz} = SE_{1GHz} - SE_R^P = 131.4t\sqrt{f\mu_r\sigma_r}, \tag{5.19a}$$

Let $131.4t\sqrt{\mu_r\sigma_r}$ be equal to β. Then, the constant β is obtained as follows:

$$\beta = \frac{\mathrm{SE}_{\text{A at 1GHz}}}{\sqrt{f}} = \frac{\mathrm{SE}_{\text{1GHz}} - \mathrm{SE}_{\mathrm{R}}^{\mathrm{P}}}{\sqrt{10^9}\ \text{(i.e., 1GHz)}}, \tag{5.19b}$$

β is directly calculated from Eq. (5.19b). The value increases with the CNTs content owing to the improvement of the electrical conductivity, and the slope is similar to that of the conductivity (Fig. 5-7b), as shown in Fig. 5-24. Therefore, the $\mathrm{SE_A}$ at other frequencies ($\mathrm{SE_A'}$) can be expressed as follows:

$$\mathrm{SE_A'} = \beta\sqrt{f} \tag{5.19c}$$

Consequently, the equation for the SE for a plane wave can be derived as Eq. (5.16b) by combining Eq. (5.19c) with the $\mathrm{SE_R^P}$ value of 1.35.

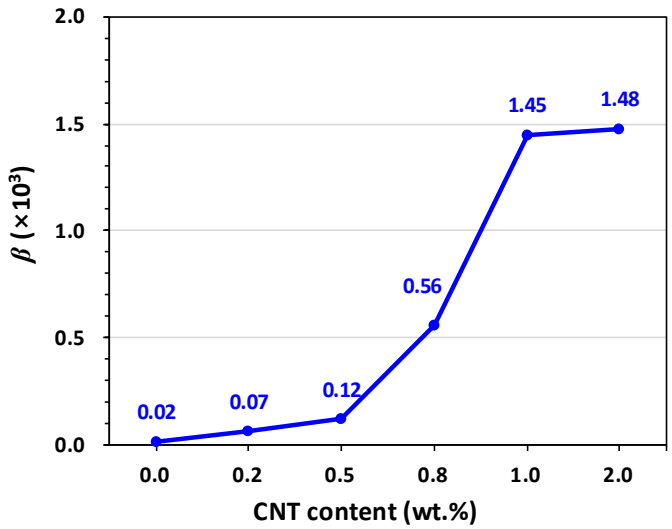

Fig. 5-24. Calculated value of β with respect to the CNT content.

The SE at frequencies between 10 MHz and 1 GHz can be calculated via a linear interpolation using the calculated SE value at 10 MHz and the experimental value of SE_{1GHz}.

To validate the suitability of the proposed model, the estimated SE by applying the preceding approach were compared to the experimental SE results. Specifically, the SE in the H-field was calculated by substituting the frequency (10 kHz–10 MHz), sample-to-transmitting antenna distance (0.3 m), and relative conductivity of the samples (Fig. 5-7) into f, r, and σ_r in Eq. (5.16a). Then, the SE for a plane wave was calculated by substituting the β, obtained from Eq. (5.19b), and the frequency (1–18 GHz) into Eq. (5.16b). Subsequently, the SE in the transition and resonant region (10–100 MHz) were calculated via a linear interpolation. The comparison of the SE results is shown in Fig. 5-25, indicating good agreement. Most of the calculated SE is caused by SE_R in the H-field and by SE_A for a plane wave. It should be noticed again that this is because in the H-field, the δ is calculated as very thick, as indicated in Eq. (5.17), so the incident EM waves are not attenuated well (i.e., SE_A hardly occurred), whereas SE_R increases with the frequency, as indicated in Eq. (5.7b). However, for a plane wave, the δ decreases as frequency increases, so SE_A increases, but SE_R decreases as evident in Eq. (5.7c), and its contribution is small based on the result of calculation using Eq. (5.7a).

Every SE result measured at 100 MHz was smaller than the value obtained via numerical calculations by the proposed model. This is because the frequency was in the transition and resonant region, as previously mentioned. However, the measured SE values for samples CNT1.0 and CNT2.0 at above 1 GHz were lower than those obtained via the numerical calculations. This is possibly because the transmitted signal power used in the experiment was weak. If a sufficiently high-power signal could be used to measure the SE up to 200 dB, it is expected that the SE will be similar to that of the calculated SE.

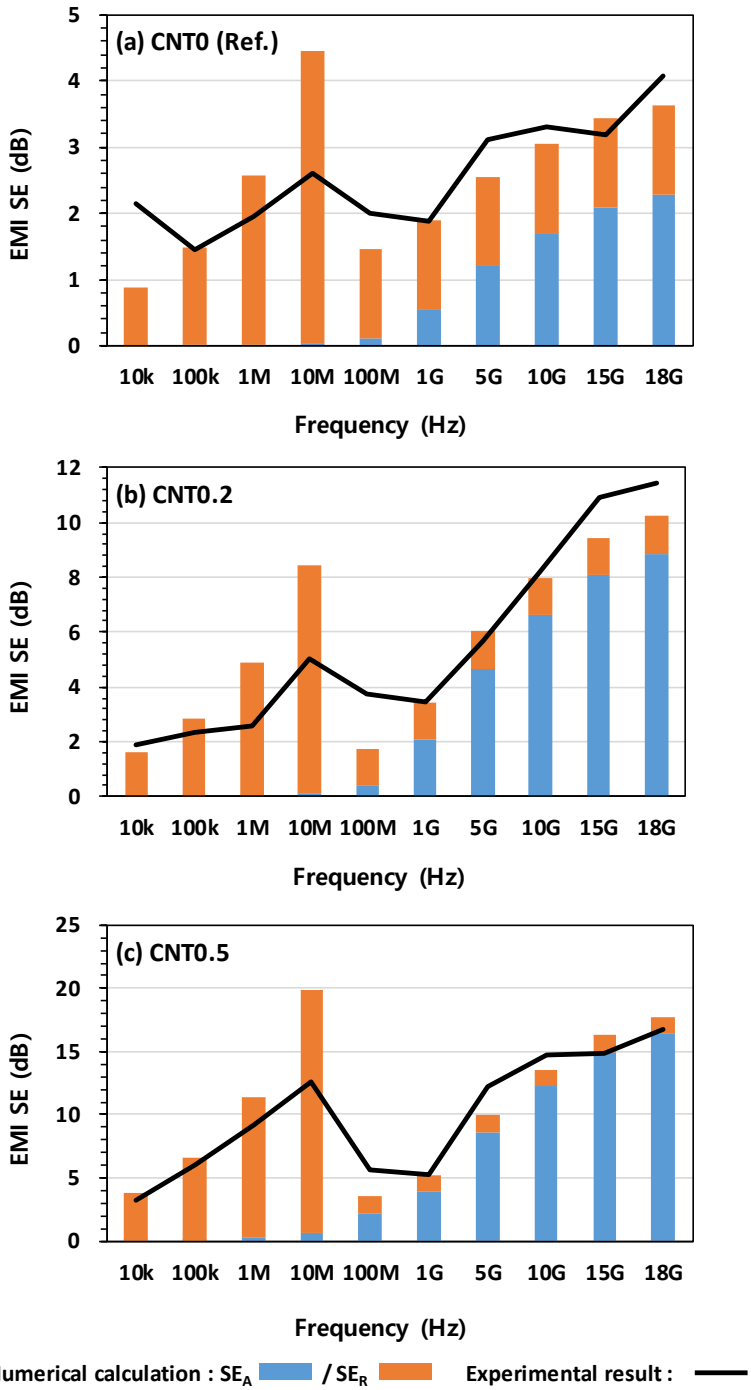

Fig. 5-25. Comparison of SE results between experimental data and numerical calculation using the proposed model.

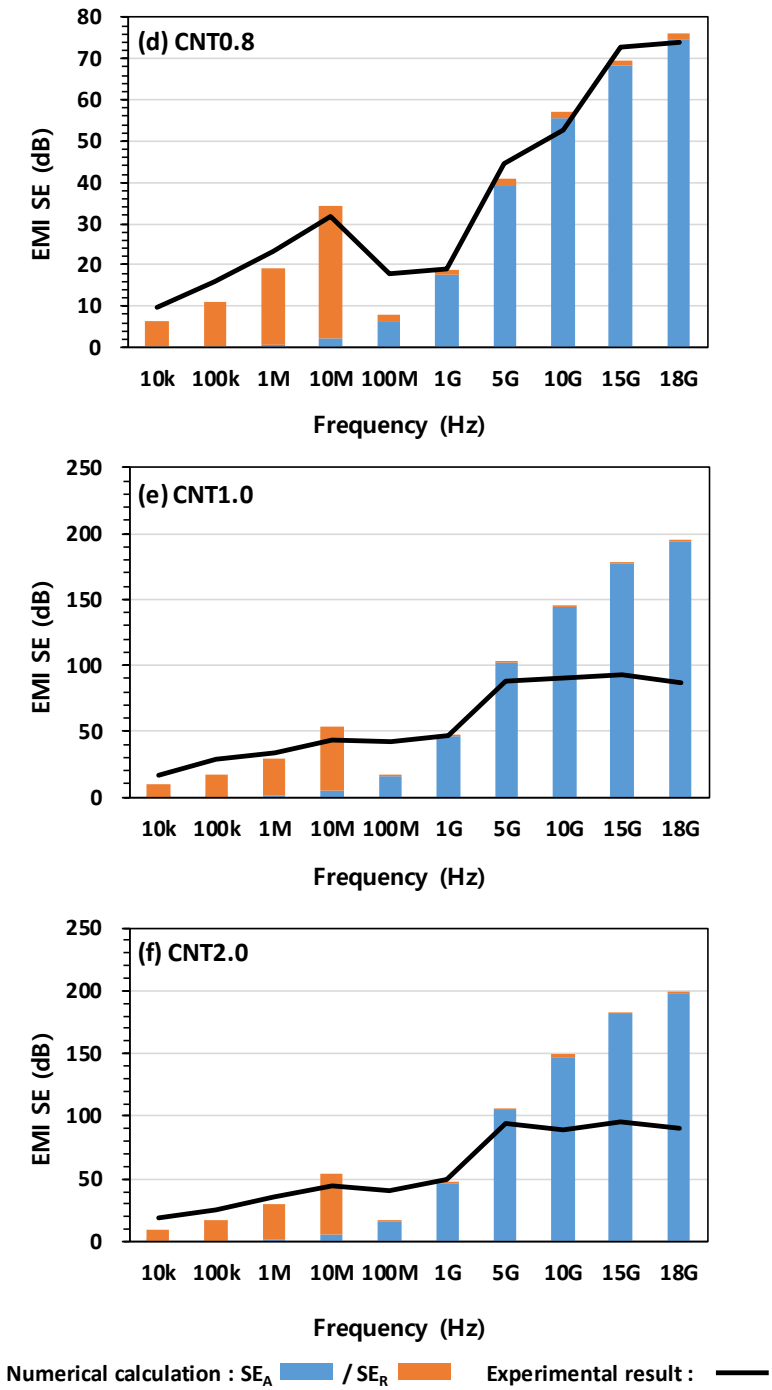

Fig. 5-25. *(Continued)* Comparison of SE results between experimental data and numerical calculation using the proposed model.

In summary, the proposed model can be used to practically estimate the SE of a UHPC/CNT composite. The SE in the H-field with respect to the frequency of interest can be estimated by measuring only the values of r, t, and σ_r. In addition, using the experimental value of SE_{1GHz}, the SE of higher frequencies can be predicted without performing further experiments. Therefore, this can reduce the necessary amounts of labor, time, resources, etc. The proposed model can be employed to estimate the SE for most cementitious materials because their electrical resistivity range is within the database range of the model. However, it is necessary to accumulate data and to modify the equations continuously based on the results of additional experiments to establish more robust model.

5.4 Conclusions

In this chapter, the EMI SE of UHPC/CNT composites were experimentally investigated for the first time. UHPC composites with six different CNT amounts (0, 0.2, 0.5, 0.8, 1.0, and 2.0 wt.%) were designed. Then, the EMI SE was examined through measurement of the electrical conductivity and SE. Two types of SE testing methods were considered, and the results were analyzed according to EMC theory. The following conclusions were drawn:

1) Dispersed CNTs can significantly improve the electrical conductivity of UHPC up to the percolation threshold owing to the formation of conductive pathway in the matrix. However, incorporation of CNTs beyond the percolation threshold does not develop the conductivity because the conductive pathway is already constructed at the percolation threshold.

2) The EMI SE of UHPC improve with the CNT content up to the percolation threshold regardless of the testing method because

of the improved electrical conductivity. This demonstrates that the close correlation between the electrical conductivity (or resistivity) and the SE. However, large sample testing should be required to evaluate the SE for actual structure level.

3) To obtain reliable SE results for UHPC based on IEEE-STD-299, which is a representative large sample testing, samples should be fabricated to have a sufficiently large incident area. If a sample with a relatively small incident area is used, the SE in the H-field is probably overestimated and distorted owing to the effect of the opening. However, the SE for a plane wave is hardly affected by the dimension of the incident area. This observation can be used to update the existing guides of IEEE-STD-299.

4) The proposed model by statistical analysis can be used to estimate the SE for cementitious materials, particularly UHPC/CNT composites. It is sufficiently practical to use onsite. However, to improve the accuracy of the model, more appropriate data should be collected via further experiments and analyses, including the effect of CNTs on the permittivity of the composites.

Chapter 6. Electrically Cured UHPC with CNTs for Field Casting and Crack Self-sensing

In this chapter, the effects of CNTs on UHPC were investigated in terms of electrical curing, mechanical properties, and crack sensing. The addition of CNTs significantly decreased electrical resistivity of the UHPC, allowing electrical curing at low voltages; improved mechanical properties via bridging, pore filling, and C-S-H stiffening effects; and influenced the deflection hardening behavior under flexural stress. Furthermore, the UHPC/CNT composites under compressive or flexural stress exhibited significant crack sensing capabilities due to the obtained low electrical resistivity. A dramatic fractional change in the resistivity (FCR) of the UHPC/CNT composites can represent the failure under compression or first cracking under flexure. Therefore, it was experimentally verified that the UHPC/CNT composites can extend the applications of UHPC materials especially for on-site casting and structural crack sensors for UHPC-based structures.

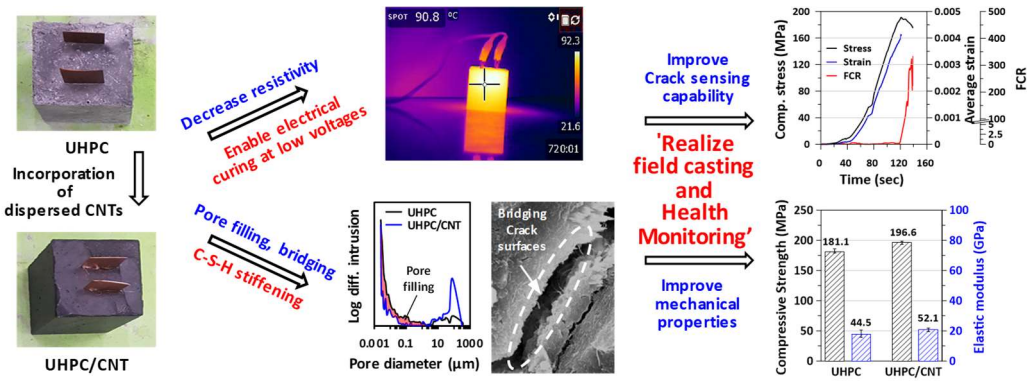

Fig. 6-1. Graphical abstract of chapter 6.

6.1 Introduction

In this chapter, dispersed CNTs were incorporated in UHPC to fabricate a UHPC/CNT composite mainly for two objectives: the potential application of electrical curing (EC) as an alternative to steam curing (SC) for UHPC production and the implementation of crack sensing ability in UHPC structure. This new composite can solve the practical problem of the incapacity to obtain a high compressive strength that is > 150 MPa by on-site casting, and provide a new possibility of producing a suitable UHPC-based crack sensor for structural health monitoring (SHM). This study is organized as follows: First, the applicability of EC is discussed based on a comparison of curing methods, namely, SC and EC. These were evaluated by measuring the electrical resistivity and internal temperature of the composite during both types of curing. Then, the influence of CNTs on the mechanical properties of the UHPC is detailed based on an examination of the results of compressive and flexural strength tests along with several microstructural investigations. Finally, the crack sensing potentials of both UHPC and UHPC/CNT are described based on measurements of the FCR during mechanical tests.

6.2 Experimental Details

6.2.1 Properties of CNTs

Sonication is a widely used technique for the desirable dispersion of CNTs, but it is not ideal for manufacturing large quantity and has not been reported for cement-based sensor production [106]. Thus, in this study, a commercial pre-dispersed multi-wall CNT suspension (K-Nanos-D, Kumho Inc., Korea) was used in place of sonicated CNTs considering practical application (i.e., manufacture of UHPC on-site).

The dispersed CNT suspension consisted of 50 g of multi-wall CNTs dispersed in 1 L of distilled water by a small amount of polycarboxylic acid-based surfactant (< 5 g) used as a dispersant. The properties of the CNTs are listed in Table 3. In addition, the results of the particle size distribution and zeta potential analyses for the CNTs measured by a laser scattering particle size distribution analyzer (LA-960, HORIBA, Japan) and nano-particle analyzer (sz-100, HORIBA, Japan) are presented in Fig. 6-2 and Fig. 6-3, respectively. The mean particle size, zeta potential, and mobility value were 0.452 μm and -49.8 mV, and respectively.

Table 6-1. Properties of the pre-dispersed multi-wall CNT suspension.

Avg. diameter (nm)	Avg. length (μm)	Bulk density (g/m^3)	Purity (wt.%)	Specific surface area (m^2/g)
1–8	0.1–5	150,000	> 95	180

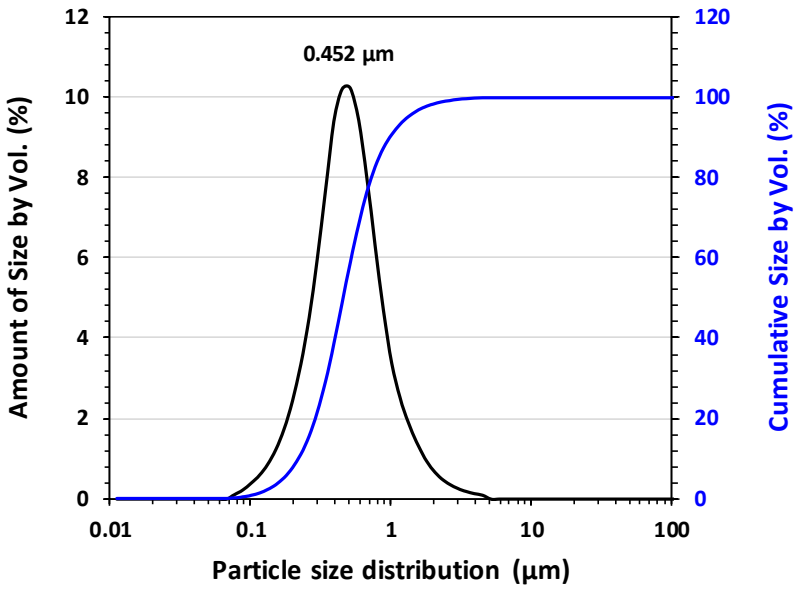

Fig. 6-2. Particle size distribution of dispersed CNT suspension.

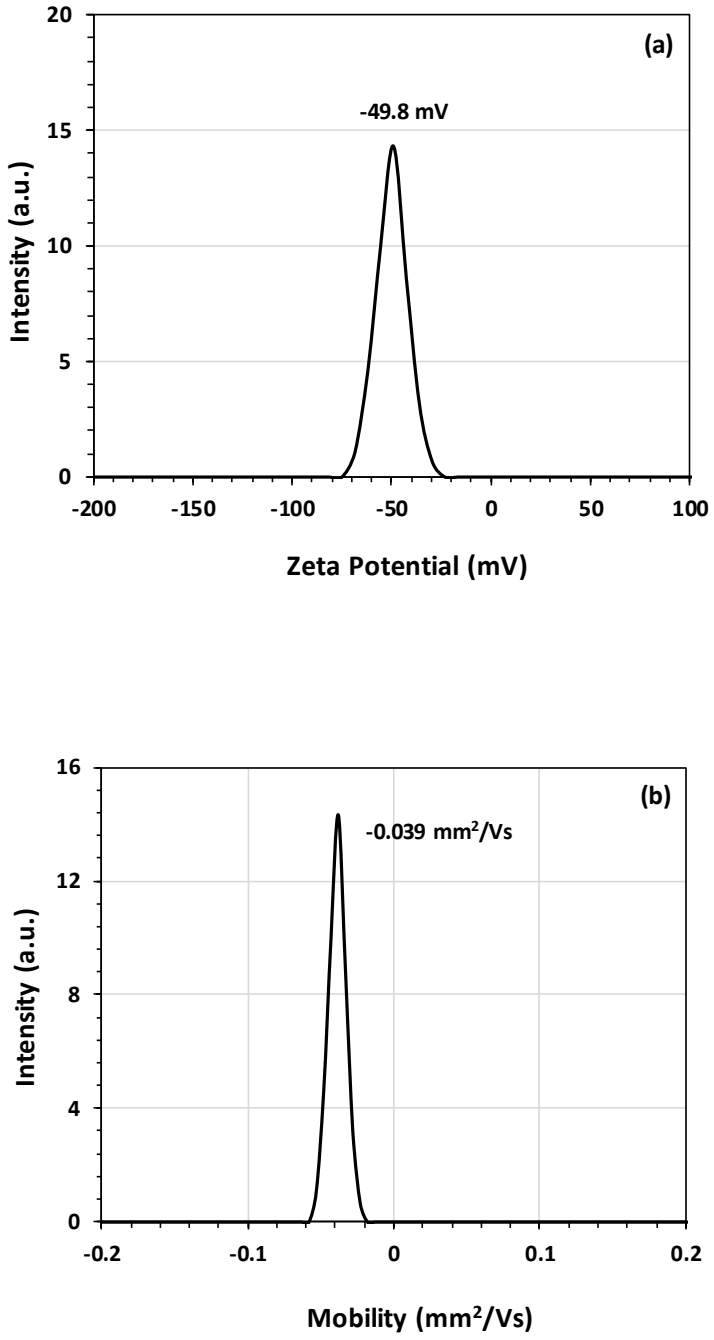

Fig. 6-3. Zeta potential (a) and electrophoretic mobility (b) of the dispersed CNT suspension.

6.2.2 Mixture proportions and sample preparation

The mixture proportions are listed in Table 2. The w/c was maintained at 0.24. Initially, OPC, silica fume, silica powder, and silica sand were homogeneously blended using a Hobart mixer for 5 min. The dry pre-mixture was then added into the water with polycarboxylate superplasticizer and mixed for 10 min to fabricate the UHPC. A dispersed CNT suspension was applied to manufacture UHPC/CNT composites. Upon the conversion of the dry mixture to a fresh mixture (after approximately 3 min of mixing), steel fibers were incorporated.

The fresh mixture was cast into 50 × 50 × 50 mm^3 cubic molds and 40 × 40 × 160 mm^3 prismatic molds, which were then tamped to ensure uniform compaction. In addition, two copper plates with dimensions of 20 × 20 × 0.4 mm^3 for the cubic samples and 10 × 10 × 0.4 mm^3 for the prismatic samples were embedded as electrodes to measure the changes in electrical resistivity [107] during the curing process and mechanical tests. The area of each copper plate where it contacted the samples was coated with silver paint to improve electrical contact between them [108-110]. A thermocouple was embedded between the electrodes in the cubic samples to measure the internal temperature during the curing process. In contrast, three thermo-couples were installed in the prismatic samples based on the location of the electrodes: one was inserted between the electrodes (center) and two were embedded out of the plane of each electrode (left and right). The geometry of the samples is illustrated in Fig. 6-4.

The surfaces of the cast fresh mixtures were immediately covered with a plastic sheet to prevent moisture evaporation after which the samples were cured for 24 h at 20 ℃ and RH of 60 %. Then, the molds were removed and the samples were cured using either SC at 90 ℃ and RH of 95 % or EC at low voltages of 19–23 V and RH of 95 % for a period of 48 h. Subsequently, the samples were held at 20 ℃ and RH of 60 % for 25 d, for a total curing period of 28 d.

Table 6-2. Mixture proportions (wt.% of cement).

Sample	Water	CNT suspension	OPC	Silica fume	Silica powder	Silica sand	Super-plasticizer	Steel fibers	Curing method
UHPC-SC	0.24	-	1	0.25	0.35	1.1	0.05	2 (vol.%)	SC
UHPC-EC									EC
UHPC/CNT-SC	-	0.24							SC
UHPC/CNT-EC									EC

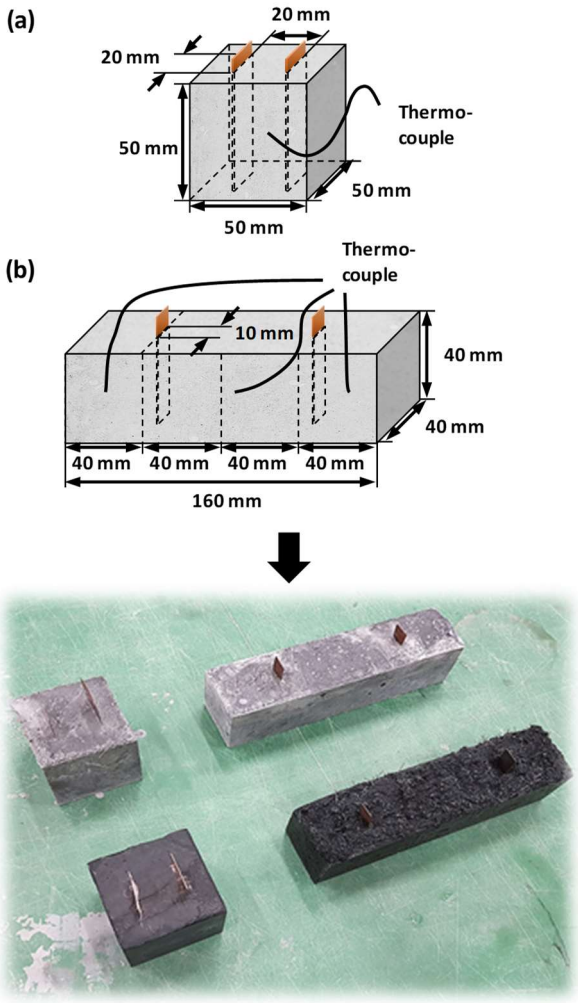

Fig. 6-4. Geometry of the samples: (a) cubic sample, (b) prismatic sample.

6.2.3 Test methods

The fluidity of the fresh mixtures was measured using a flow table according to ASTM C1437 [111]. The standard test method for UHPC is detailed in ASTM C1856; however, the test method for hydraulic mortar was adopted to enable a direct comparison for the samples in which the fluidity was altered by the addition of CNTs [112]. The mold on the flow table had upper and lower inner diameters of 70 and 100 mm, respectively, and the mold was tapped 25 times in 15 s.

The electrical resistance of the samples was measured every 5 min via the four-probe method using an LCR meter (LCR-6100, GW INSTEK, Taiwan) and programmable power supply (MK 6205P, MKPOWER, Korea) during the SC and EC cycles, respectively. The measured electrical resistance was converted into electrical resistivity using the Eq. (5.1). The temperature of the samples was synchronously measured every 5 min by a thermocouple linked to a data logger (TDS-303, Tokyo Measuring Instruments Lab., Japan).

SEM analysis was conducted using a JSM-6700 (JEOL Ltd., Japan) to analyze the morphology of the dispersed CNTs in the UHPC matrix. Fragments from the compressive strength tests were used as SEM samples. During the SEM analysis, EDS was examined to distinguish the CNTs from needle-shaped cement hydration products.

MIP analysis was conducted to evaluate the effects of CNTs on modification of pore structure for UHPC using an Autopore VI 9500 (Micromeritics, USA). Samples hydration stopped at 28 d and cut into approximately $5 \times 5 \times 5$ mm^3 were used for the test.

The compressive strength and flexural strength tests were conducted using a displacement-controlled UTM with a capacity of 2000 tons based on ASTM C109 and ASTM C348, respectively. The loading rates of 0.02 mm/s and 0.002 mm/s were applied to compressive

strength and flexural strength tests, respectively. Two strain gauges linked to the data logger and attached to the surface of each side of the cubic samples were used to measure the strain under compressive load, and the elastic modulus was calculated according to ASTM C469 as shown in Eq. (4.1). Flexural strength was determined as follows:

$$\text{Flexural strength (MPa)} : 0.0028P \tag{6.1}$$

where P is the total maximum load (N).

When the samples were under load during mechanical tests, the change in electrical resistivity was synchronously measured using the LCR meter and recorded in a computer to evaluate the crack sensing capability (Fig. 6-5). Then, the FCR induced by loading was calculated as follows:

$$\text{FCR} = \frac{\Delta\rho}{\rho_0} \times 100\ (\%),\ (\Delta\rho = \rho - \rho_0), \tag{6.2}$$

where ρ is the electrical resistivity of the samples under load and ρ_0 is the initial electrical resistivity without loading.

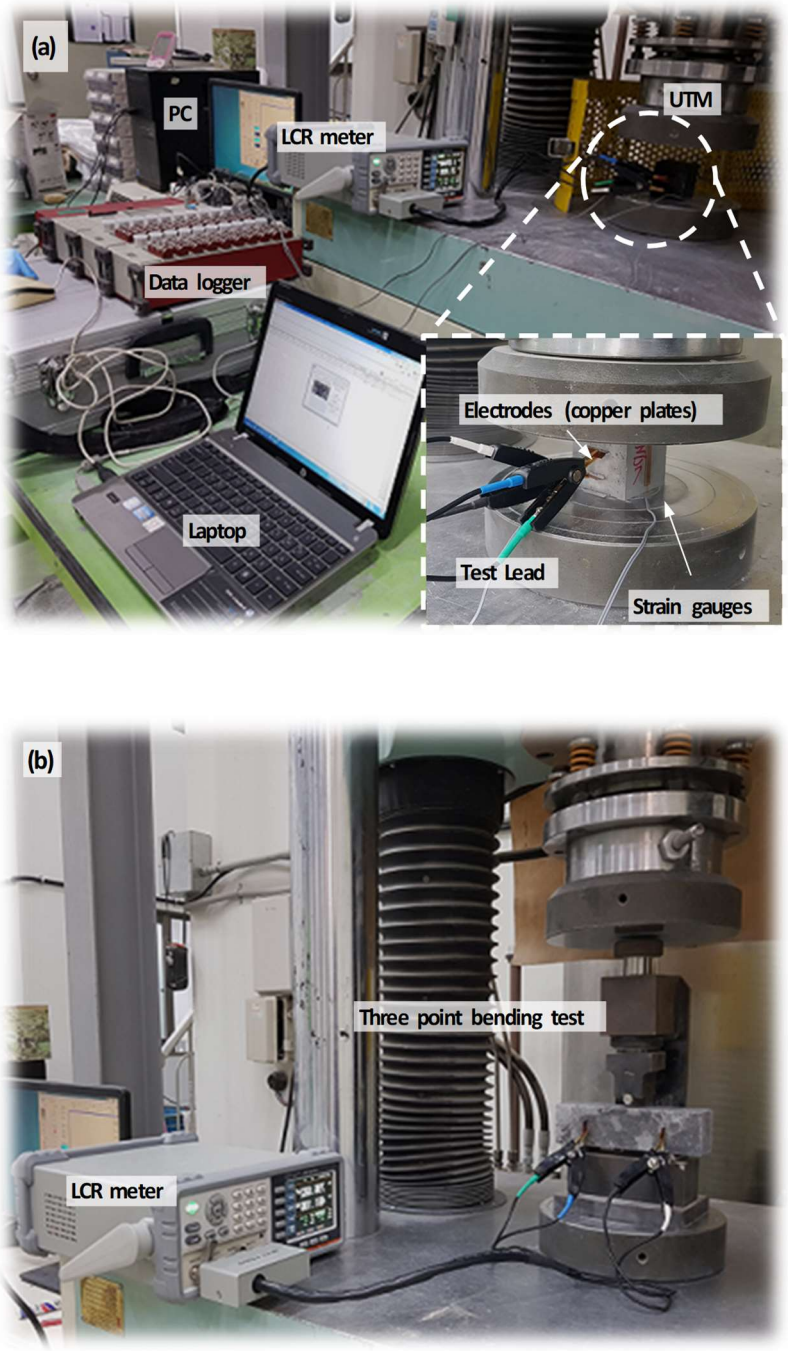

Fig. 6-5. Experimental setup for measuring FCR during mechanical tests: (a) compressive strength test, (b) flexural strength test.

6.3 Results and Discussion

6.3.1 Flowability

The flow table test results are presented in Fig. 6-6. The flow of the UHPC was measured at 23.7 cm; however, the flow of the UHPC/CNT was noticeably lower as 16.7 cm, which was about 30 % less than that of the UHPC. This is attributed to water absorbing characteristics of the CNTs such as a high aspect ratio, high specific surface area, and strong Van der Waals forces [31]. In general, the UHPC did not require tamping when molding the fresh mixtures due to its high self-compacting capability provided by the high flow (Fig. 6-6a). However, the tamping procedure was necessary for the UHPC/CNT because of the low flow value (Fig. 6-6b). Otherwise, if the sample was not sufficiently compacted, a large amount of air could be trapped in the matrix, negatively affecting the mechanical strength.

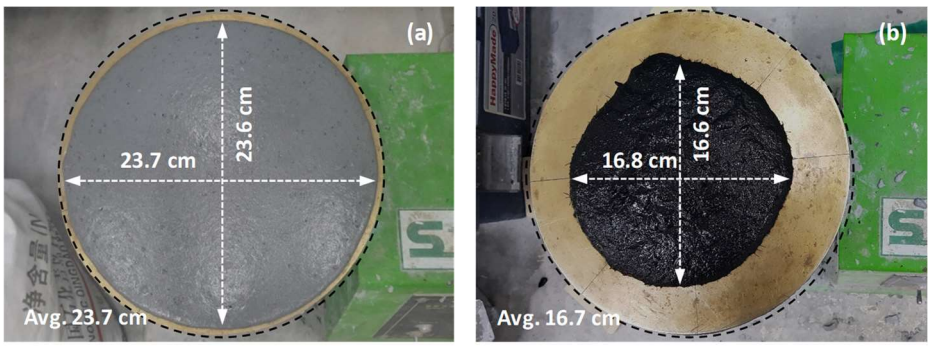

Fig. 6-6. Flow table test results: (a) UHPC, (b) UHPC/CNT.

6.3.2 Change in temperature and electrical resistivity during curing

The change in the temperature and electrical resistivity of the cubic samples during curing are shown in Fig. 6-7. For the UHPC (Fig. 6-7a–b), the electrical resistivity was approximately 6.3–7.6 Ω·m before curing, but it sharply increased after 2 d of curing to 306.5 Ω·m

under SC and 40 Ω·m under EC, respectively, even though 2 vol.% of conductive steel fibers had been incorporated. In particular, under EC with a low voltage of 19 V (Fig. 6-7b), the temperature of the samples initially increased gradually to 38 ℃ (over about 1 h), but as the resistivity increased over time (i.e., as hydration reaction progressed), the temperature did not increase further. Instead, it converged to 26 ℃. In contrast, for the UHPC/CNT (Fig. 6-7c–d), the electrical resistivity did not change significantly and remained in the range of 0.6–0.8 Ω·m during curing regardless of the curing method. In addition, even with a low voltage of 19 V, it shows a promising result that the internal temperature of the samples increased to approximately 90 ℃ within 2 h. This temperature was maintained until the samples were fully cured, as shown in Figs. 6-7d and 8, verifying the high efficiency of EC for UHPC/CNT composites.

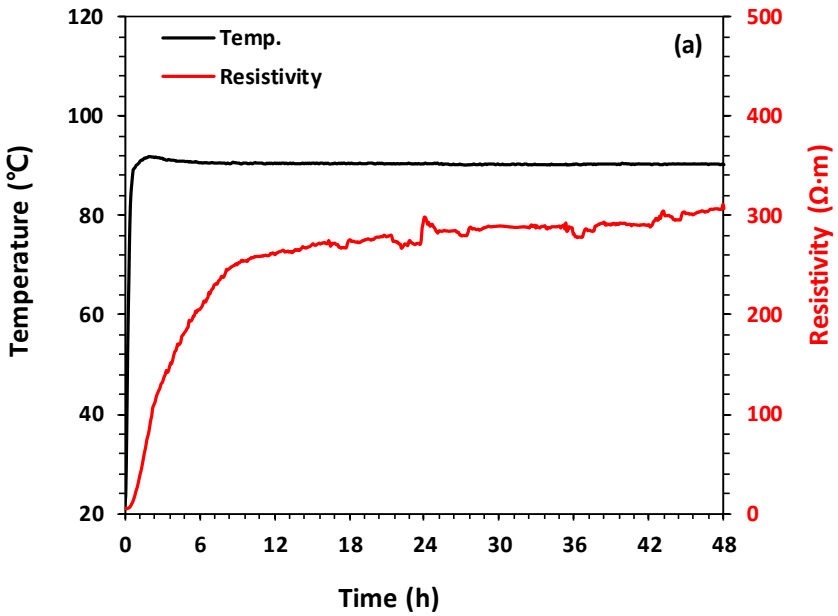

Fig. 6-7. Changes in temperature and electrical resistivity for cubic samples during curing: (a) UHPC-SC, (b) UHPC-EC, (c) UHPC/CNT-SC, and (d) UHPC/CNT-EC.

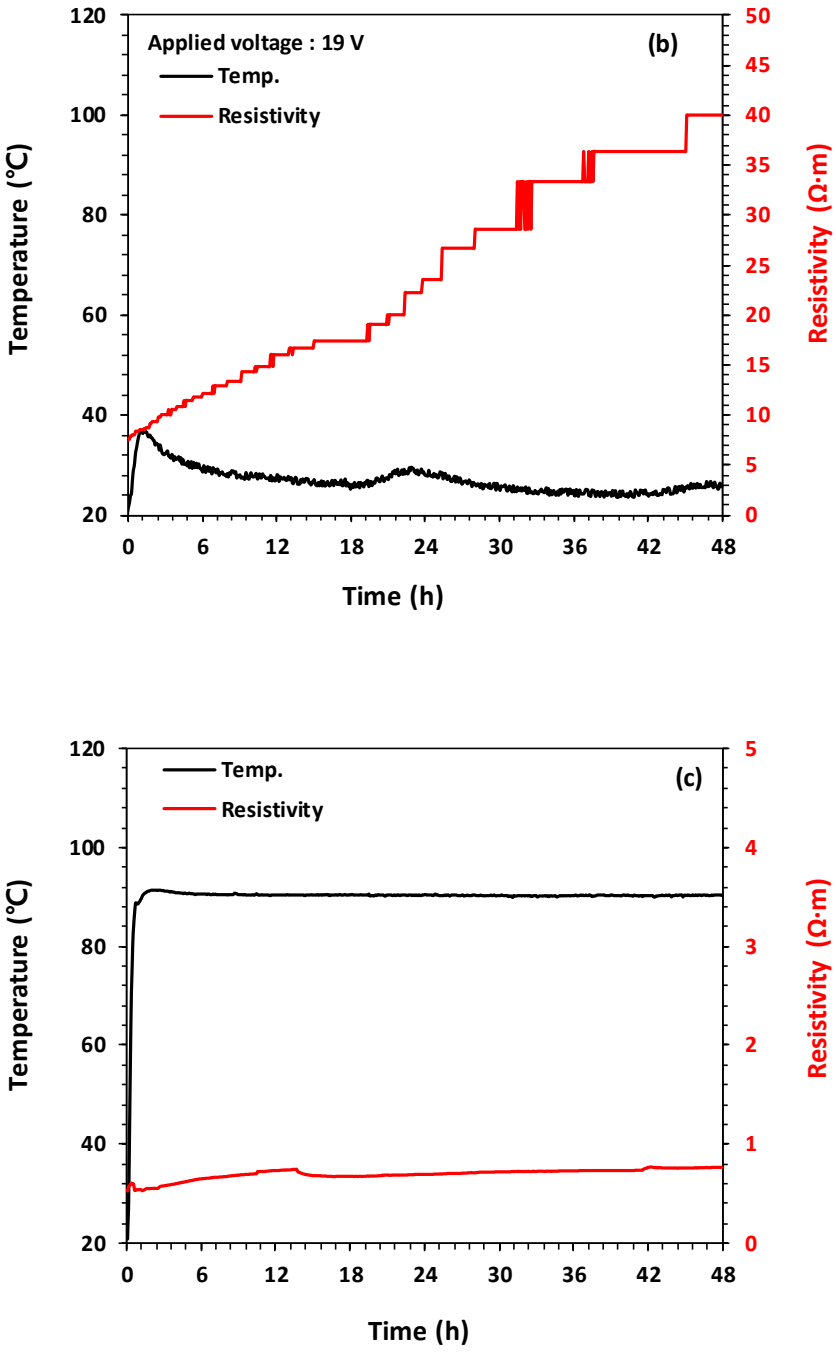

Fig. 6-7. *(Continued)* Changes in temperature and electrical resistivity for cubic samples during curing: (a) UHPC-SC, (b) UHPC-EC, (c) UHPC/CNT-SC, and (d) UHPC/CNT-EC.

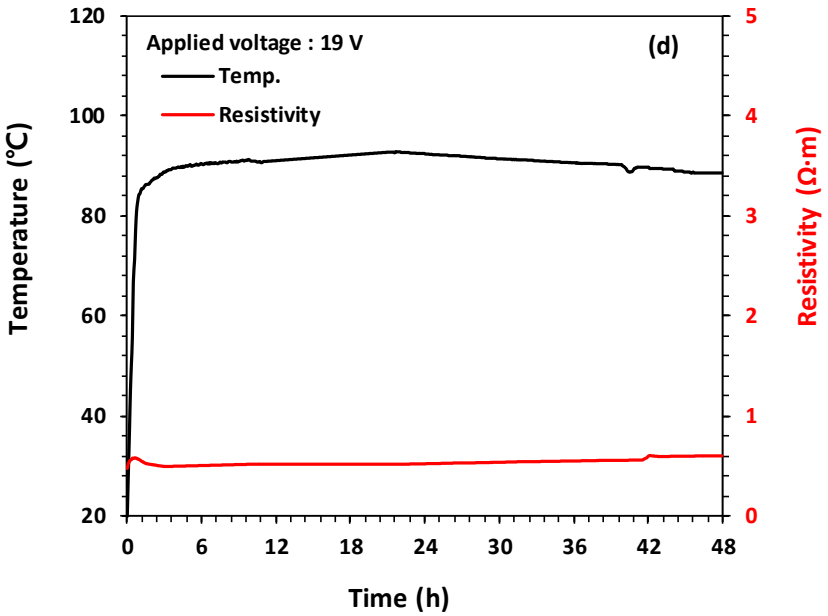

Fig. 6-7. *(Continued)* Changes in temperature and electrical resistivity for cubic samples during curing: (a) UHPC-SC, (b) UHPC-EC, (c) UHPC/CNT-SC, and (d) UHPC/CNT-EC.

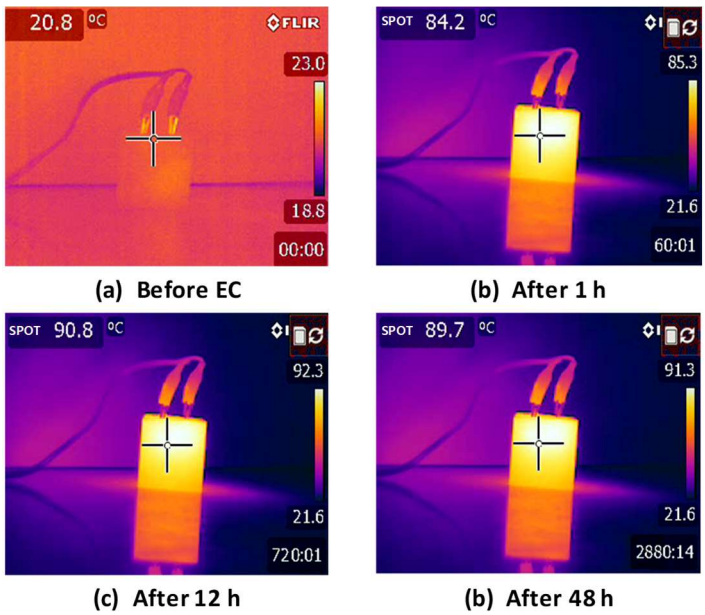

Fig. 6-8. Thermo-graphic images of the UHPC/CNT-EC during curing.

As shown in Fig. 6-9, the results for the prismatic samples were similar to those of the cubic samples. The resistivity of the UHPC was initially 2.5–5.4 Ω·m, but dramatically increased during 2 d of curing to 552.2 Ω·m under SC and 50 Ω·m under EC. For UHPC-EC, the low voltage of 23 V was insufficient to increase the temperature of the samples to 90 ℃ because of the high resistivity (Fig. 6-9b). In contrast, for the UHPC/CNT, there was little variation in the electrical resistivity, which ranged from 0.27–0.46 Ω·m during curing irrespective of the curing method. In particular, for UHPC/CNT-EC, even with a low voltage of 23 V, the temperature of the samples increased to almost 90 ℃ within 3h and remained at that level until the completion of curing (Fig. 6-9d). However, the temperature varied by up to 8 ℃ depending on the location in the sample. The temperature in the middle of the sample rose the fastest and remained the highest whereas the temperature of the right side of the sample where the anode (+) was applied rose rapidly and remained at the level close to that of the center of the sample. However, the temperature of the left side of the sample where the cathode (–) was applied remained in the range of 81–85 ℃.

The large variation in the measured electrical resistivity between the UHPC and UHPC/CNT samples was attributed to the change in the dominant electrical conduction mechanism in the UHPC matrix incorporated with the CNTs. In general, electrical conduction can be classified as either ionic or electronic [113]. Ionic conduction is caused by the motion of the ionic charge whereas electronic conduction occurs due to the movement of electrons in response to an electric field. The increase in the number of charges transferred can cause an increase in temperature [114]. The significant variation in the measured electrical resistivity for the UHPC during curing showed that ionic conduction was the dominant conduction mechanism for the UHPC, even with the addition of steel fibers. Specifically, the UHPC matrix was surrounded by water prior to the initiation of curing, and the ions in the water (i.e., pore solution) could carry current between the steel fibers. Thus, the

electrical resistivity was initially low and a conductive pathway in the matrix was constructed. However, as the curing progressed, the ionic feature of the pore solution and ions in the matrix decreased because of the hydration reaction and evaporation, thus weakening the strength of the conductive pathways between steel fibers (Fig. 6-10a). As a result, the resistivity increased significantly and low voltages of 19–23 V were not enough to increase the temperature of the samples. Therefore, it is insufficient for EC. In contrast, for the UHPC/CNT, the conduction mechanism changed from ionic to electronic when the CNTs were incorporated. Specifically, the dispersed CNTs that were uniformly distributed throughout the matrix formed strong conductive pathways along which the electrons could move rapidly by building connections with the steel fibers regardless of the water content in the matrix (Fig. 6-10b). Thus, the CNT content used in this study can be regarded as close to percolation threshold. For this reason, the initial resistivity was considerably lower than that of the UHPC. In addition, the reduction in the number of ions in water as the curing progressed had little effect on the degree of the electrical resistivity of the matrix. Thus, the resistivity remained unchanged during curing. Furthermore, even with low voltages of 19–23 V, the temperature of the matrix could be increased to approximately 90 ℃ and enabled EC that could produce a similar effect to SC, but in a much more energetically efficient way. For the prismatic sample, it was found that the differences in the rates of temperature increase and the variation in the maximum temperatures at various points in the sample were attributable to the direction of current that flowed from the anode (+) to the cathode (–).

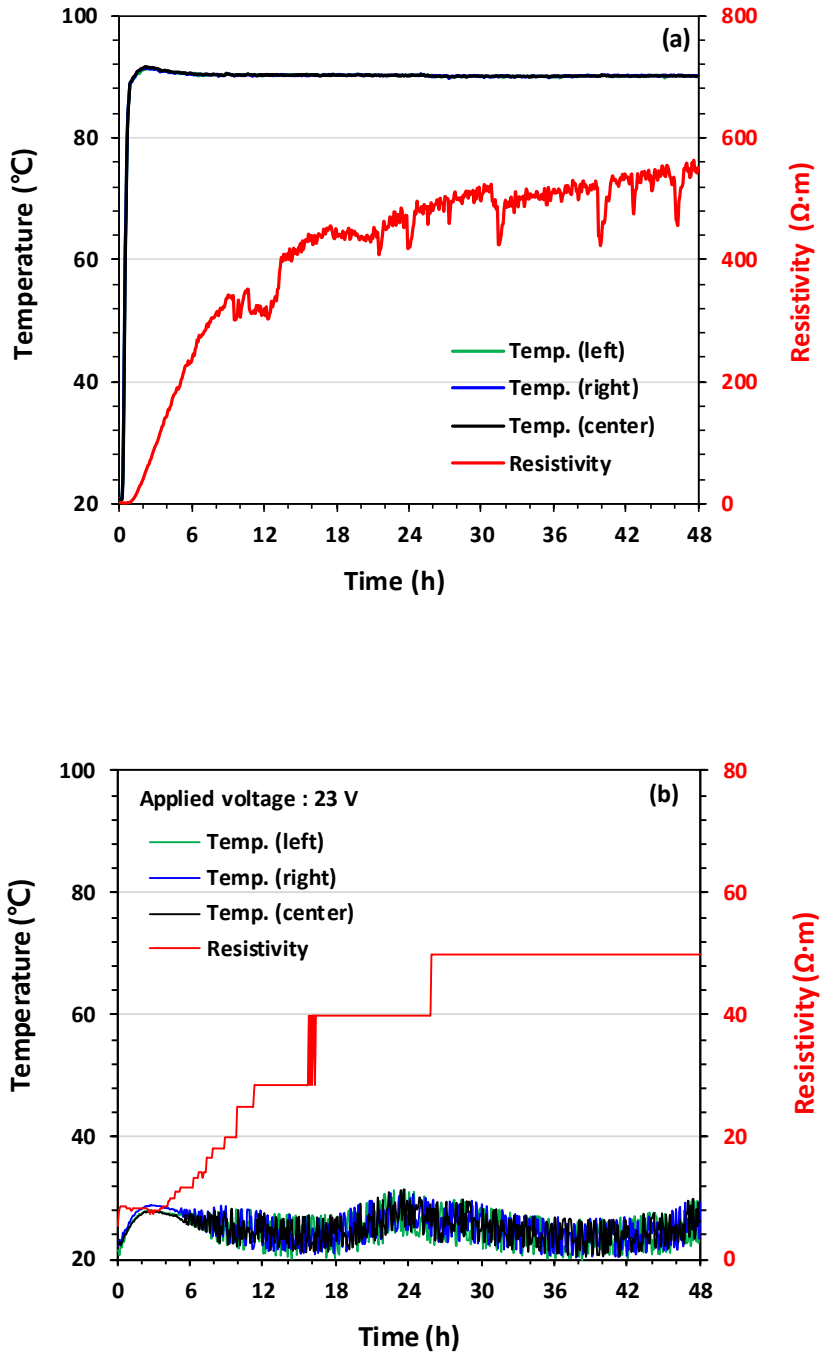

Fig. 6-9. Changes in temperature and electrical resistivity for prismatic samples during curing: (a) UHPC-SC, (b) UHPC-EC, (c) UHPC/CNT-SC, and (d) UHPC/CNT-EC.

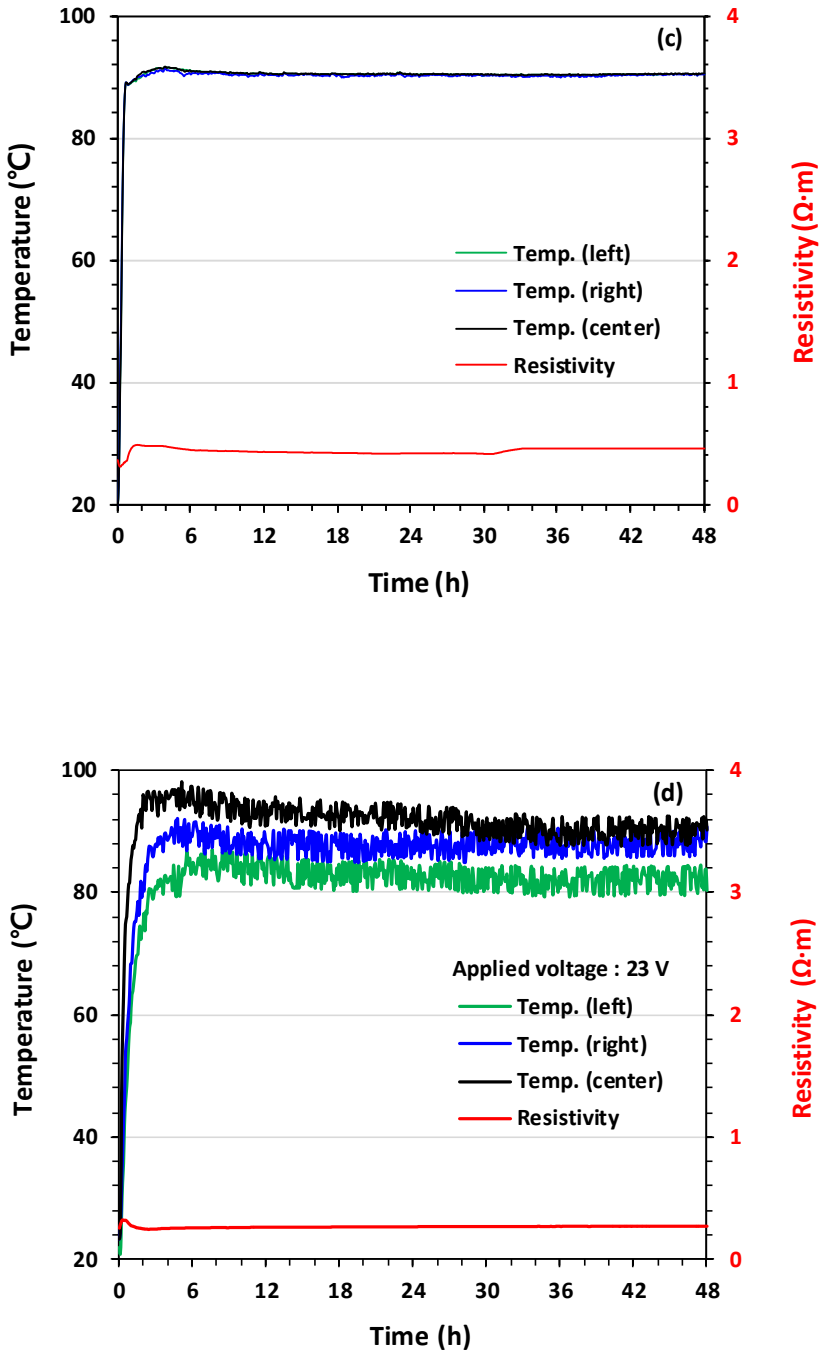

Fig. 6-9 *(Continued)* Changes in temperature and electrical resistivity for prismatic samples during curing: (a) UHPC-SC, (b) UHPC-EC, (c) UHPC/CNT-SC, and (d) UHPC/CNT-EC.

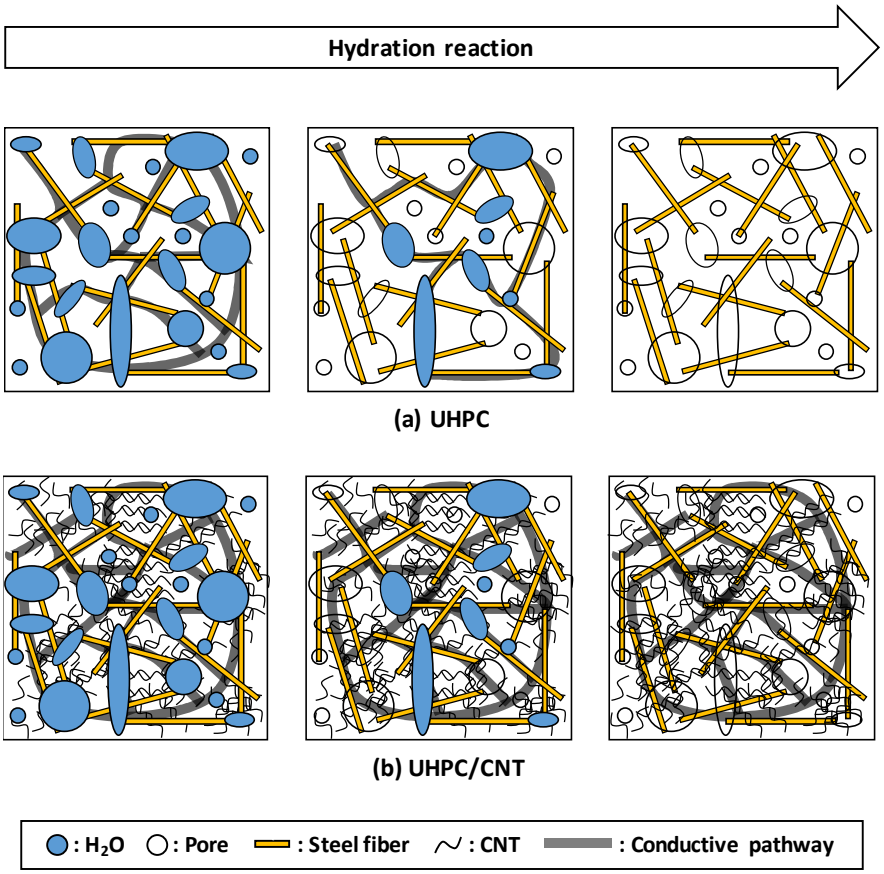

Fig. 6-10. Schematic variation of electrical conduction in UHPC composites during curing: (a) UHPC, (b) UHPC/CNT.

6.3.3 Morphology of the CNTs in the UHPC

The morphology of the CNTs in the UHPC matrix is presented in Fig. 6-11. For all the UHPC/CNT samples, most of CNTs were distributed as single fibers shorter than 1 μm and embedded in the hydration product regardless of the curing method (Fig. 6-11c–d). In addition, some of the CNT fibers were clearly connected to each other (Fig. 6-11a–b). In particular, in the SEM images taken around the cracks in the matrix, a large number of CNT fibers can be observed between the surfaces of the cracks (Fig. 6-11e–f).

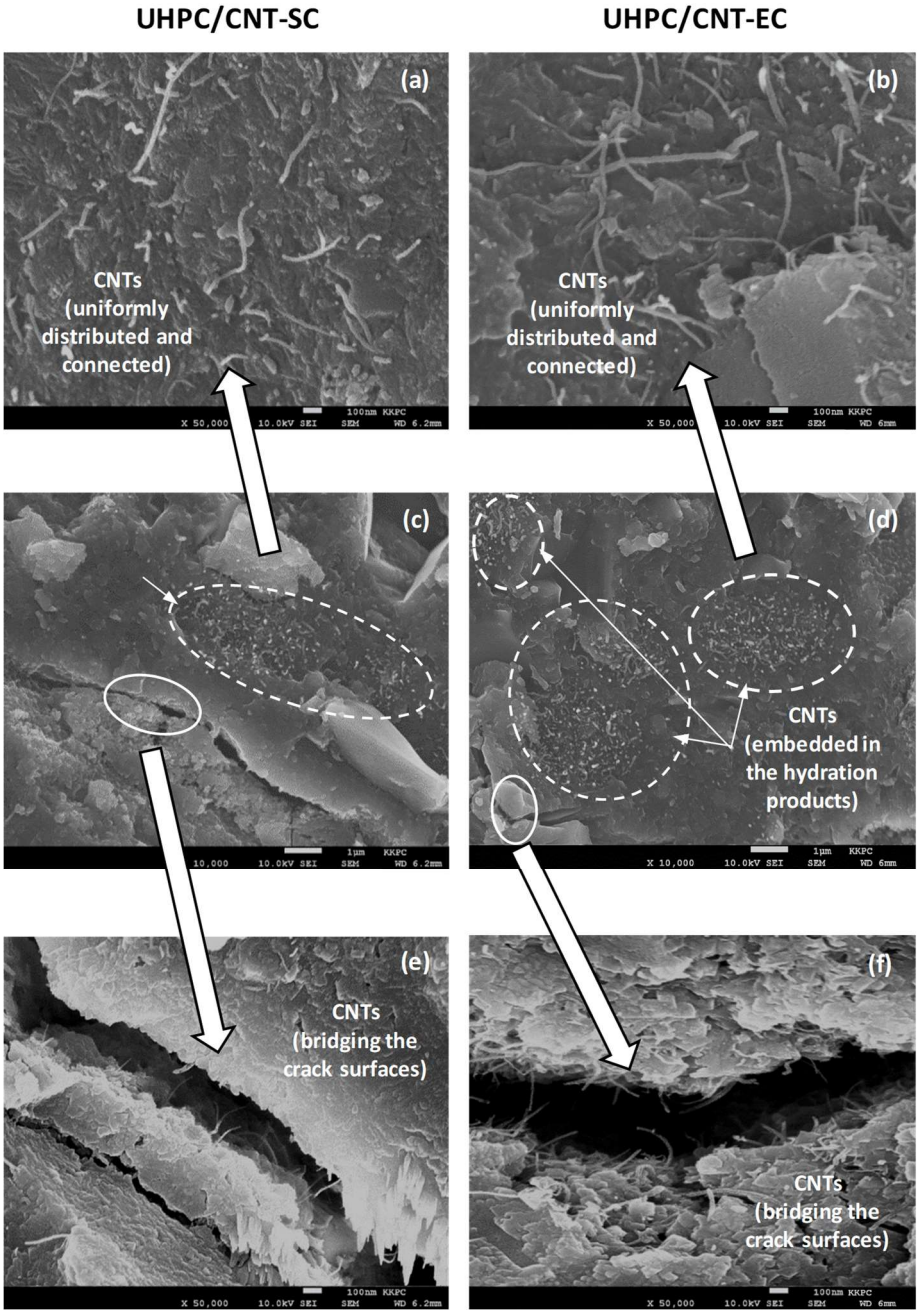

Fig. 6-11. SEM images of the UHPC/CNT composites: (a, c, e) UHPC/CNT-SC, (b, d, f) UHPC/CNT-EC.

These morphological analysis can provide strong evidence of the effective mechanism whereby the UHPC/CNT can be produced by the EC. Specifically, the CNT fibers constructed a strong conductive pathway by connecting adjacent CNT fibers and steel fibers. This allowed an electric field to form in the strong conductive pathway and the resulting temperature increased up to 90 ℃ due to the active motion of electrons, thereby enabling EC.

6.3.4 Poromechanical properties

Note that the following tests were not conducted for the UHPC-EC sample because effective curing could not be achieved by the EC (i.e., obtained internal temperature was lower than 90 ℃), which prevented a direct comparison of the performance with other samples.

The pore size distribution and porosity are shown in Figs. 6-12 and 13, respectively, and were divided into four ranges based on the pore diameter of the samples [115, 116]. The total porosity of the reference sample (UHPC-SC) was 5.99 %; however, the pore structure of the UHPC changed significantly after CNTs were incorporated. The total porosity of the UHPC/CNT significantly decreased regardless of the curing method. Those of the UHPC/CNT-SC and UHPC/CNT-EC were 4.19 % and 3.99 %, respectively, which were 30 % and 33.4 % less than that without the CNT (UHPC-SC). In particular, the number of macropores (0.025–5 μm), mesopores (4.5–25 nm), and micropores (< 4.5 nm) significantly decreased because those pores became filled with the CNTs when the particle sizes were in the range of the pore sizes, as indicated in Fig. 6-2. However, the amount of entrained and entrapped air that formed at 100–1000 μm increased remarkably due to the lower fluidity (Fig. 6-6) as it was well reported that a low fluidity in a fresh concrete mixture increases the number of air voids in the hardened matrix [117, 118].

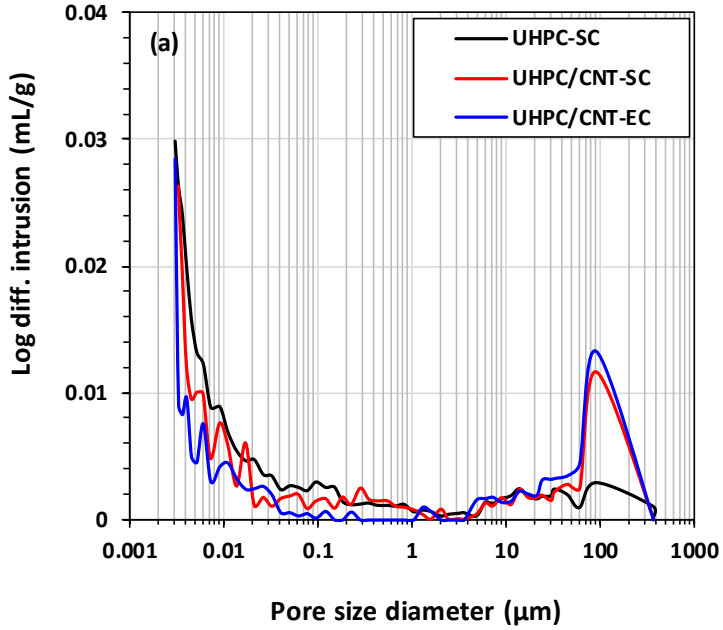

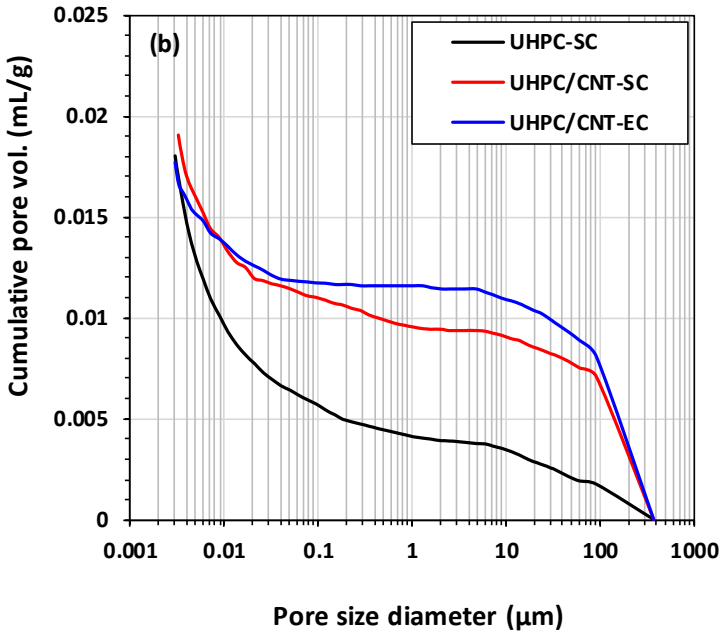

Fig. 6-12. Pore size distribution of the samples at 28 d: (a) log differential intrusion and (b) cumulative pore volume.

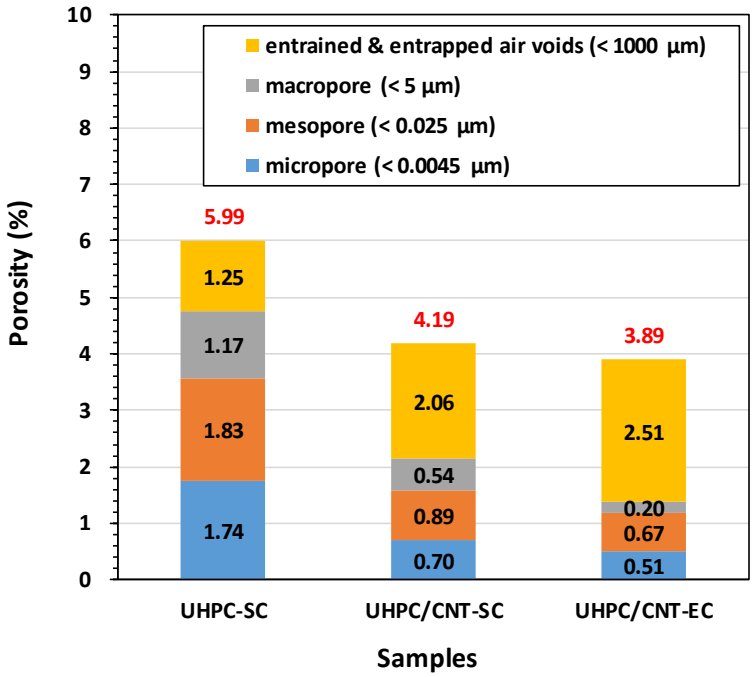

Fig. 6-13. Pore volume distribution of the samples at 28 d (the red numbers on the bars indicate the total porosity).

6.3.5 Compressive strength, elastic modulus, and FCR

In general, the compressive strength and elastic modulus of UHPC are > 180 MPa and in the range of 40–50 GPa, respectively, as confirmed in Chapter 4 [119]. The compressive strength test results are presented in Fig. 6-14 and all samples satisfied the minimum strength requirement of > 150 MPa. In addition, the compressive strength and elastic modulus were higher than 180 MPa and 40 GPa, respectively. In particular, UHPC/CNT showed a higher compressive strength and elastic modulus than those of UHPC. The highest compressive strength of 196.6 MPa and elastic modulus of 52.1 GPa were obtained for the UHPC/CNT-EC sample, which were about 8.6 % and 17.1 % higher than those of UHPC-SC (181.1 MPa and 44.5 GPa, respectively).

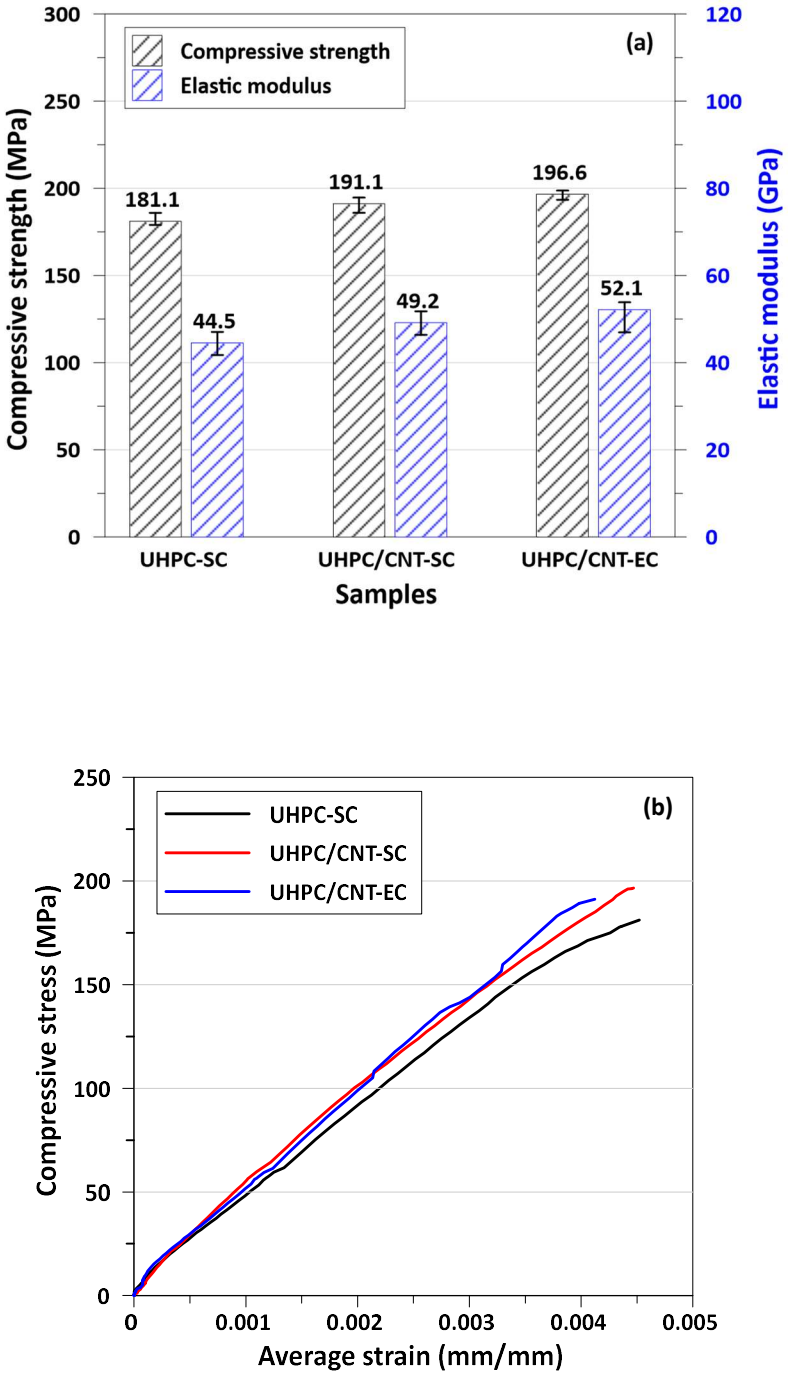

Fig. 6-14. Compressive strength and elastic modulus of the samples: (a) summary of the results, (b) stress-strain curves.

The increases in the compressive strength and elastic modulus were due to the CNTs, which strengthened the hydration product and meso-structural change accompanying with acceleration effect [27]. Specifically, the dispersed CNTs provided a massive surface area for the precipitation of cement hydrates. This could conceivably occur in a well-packed format that would contribute to the formation of denser C-S-H agglomerates with high stiffness [26], as shown in Fig. 6-11a–d. In addition, the CNTs increased the density of the UHPC matrix by filling the macro–micro pores although this increased the proportion of mesopores (Figs. 6-11–12). Furthermore, Fig. 6-11e–f show evidence of the bridging effect, in which the embedded CNTs in the hydration product phase bridged the adjacent hydrated particles [38].

The compressive stress, strain, and FCR behaviors of the samples with respect to time are shown in Fig. 6-15. In previous studies, the compressive behavior of ordinary cement paste with CNTs could be simulated by evaluating the FCR with increasing compressive load (piezoresistivity) because some of the CNTs embedded in the cement-based matrix become connected under compression and form a conductive pathway, leading to a decrease in the electrical resistance [34, 71]. However, it was difficult to use piezoresistive sensing to simulate the compressive stress and strain response of both the UHPC and UHPC/CNT based on the measured FCR as all samples exhibited quite linear compressive stress versus strain behaviors up to the ultimate compressive stress (σ_{cu}) and strain, whereas the value of the FCR changed only slightly until approximately 70% of the σ_{cu} load. This was attributed to the limited mobility of both the steel fibers and CNTs due to the dense microstructures of the UHPC and UHPC/CNT matrices produced by the dense packing of particles with a low w/c. For example, the low porosity of the UHPC based composites (Fig. 6-13) indicates the dense matrix. Thus, it can be concluded that it is not possible to monitor the compressive stress and strain states using the FCR in either the UHPC or UHPC/CNT.

However, beyond 70 % of the σ_{cu}, the FCR exhibited a completely different pattern depending on the existence of CNTs in the UHPC. The FCR of the UHPC increased slightly until the yield point with increasing loading, but the value was lower than 0.64. This result was limited to determining the durability of the UHPC regardless of the yield point. However, for the UHPC/CNT, the FCR of all samples remained close to zero regardless of the curing method until σ_{cu} was reached and then increased sharply up to 300–400, which made it feasible to decide whether the samples were cracked or not. This is owing to the strength of the formulated conductive pathway in the UHPC matrix.

A schematic illustration of the UHPC and UHPC/CNT matrices before and after cracking was presented in Fig. 11. The strength of the conductive pathway for the UHPC was already very weak at the end of SC or EC because the steel fibers became disconnected due to the hydration reaction and evaporation of water. Therefore, the initial electrical resistivity (ρ_0) was very high, which led to a small variation in the FCR following the Eq. (6.2). In addition, when cracks formed in the matrix near the σ_{cu}, most of the steel fibers bridged the cracks, although some were pulled out or failed. Thus, the increment in the electrical resistivity ($\Delta\rho$) before and after cracking was low (Fig. 6-16a). In contrast, for the UHPC/CNT, ρ_0 was very low from the beginning of the test because the CNTs and steel fibers were intricately connected and provided a strong conductive pathway in the matrix. Futhermore, since the initiation of microcracks was delayed to σ_{cu}, there was little variation in the FCR until σ_{cu} was reached. However, once cracks formed in the matrix, the conductive pathway collapsed when the CNTs became disconnected, as shown in Fig. 7e–f, and the electrical resistivity increased significantly. Therefore, a low value of ρ_0 and a high value of $\Delta\rho$ before and after cracking at the σ_{cu} point resulted in significant changes in FCR (Fig. 6-16b).

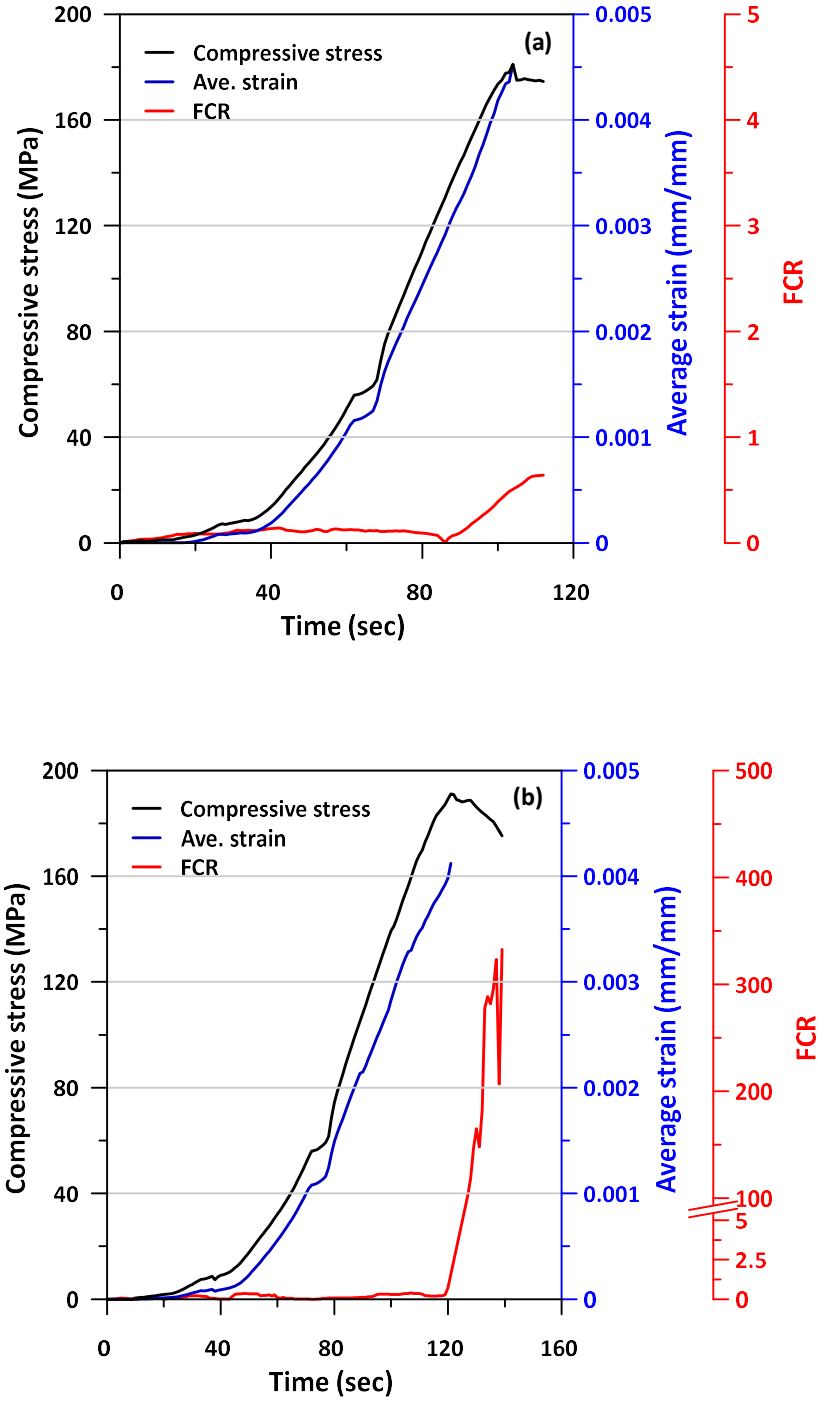

Fig. 6-15. Compressive stress-time, strain-time, and FCR-time behaviors: (a) UHPC-SC, (b) UHPC/CNT-SC, and (c) UHPC/CNT-EC.

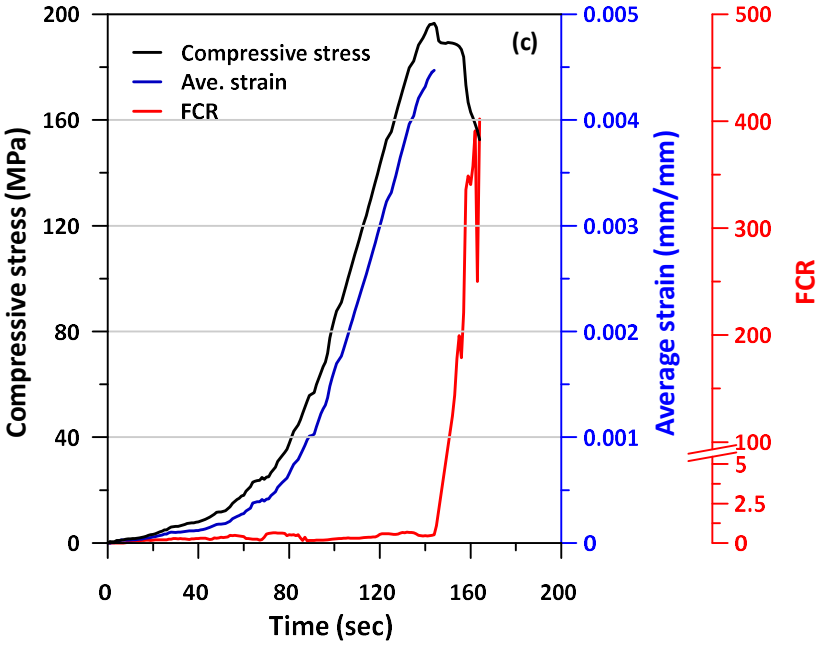

Fig. 6-15. *(Continued)* Compressive stress-time, strain-time, and FCR-time behaviors: (a) UHPC-SC, (b) UHPC/CNT-SC, and (c) UHPC/CNT-EC.

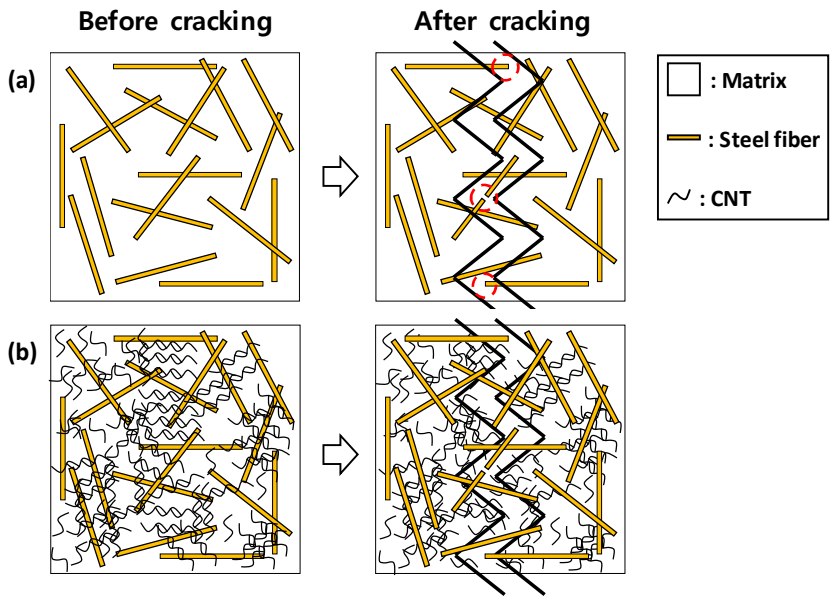

Fig. 6-16. A schematic illustration of the matrix before and after cracking: (a) UHPC, (b) UHPC/CNT.

To verify the potential of UHPC/CNT crack-sensor, the gauge factor (GF), which is the ratio of the FCR to the longitudinal strain of the sample, was calculated at the point of σ_{cu} to evaluate the crack sensing capability of the UHPC and UHPC/CNT under compression as follows:

$$\mathrm{GF} = \frac{\Delta\rho / \rho_0}{\varepsilon} = \frac{\mathrm{FCR}}{\varepsilon}, \tag{6.3}$$

where ε is the longitudinal strain of the sample.

The GF of the UHPC-SC was calculated as 113.3 whereas those of the UHPC/CNT-SC and UHPC/CNT-EC were calculated as 3610.7 and 4111.1, respectively, which were 31.9 and 36.3 times higher (Fig. 6-17). Hence, it can be concluded that the FCR values of the UHPC/CNT can be used for cracking and failure detection under compression, whereas those of the UHPC without CNTs are not applicable.

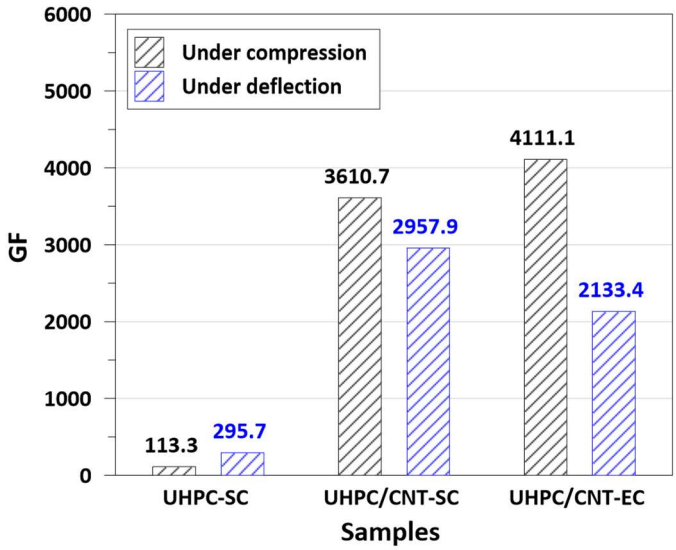

Fig. 6-17. GF of the samples under compression and deflection.

6.3.6 Flexural strength and FCR

The results of the flexural strength test are shown in Fig. 6-18. The trend in these results is identical to that observed in the compressive strength tests (i.e., the flexural strength of the UHPC/CNT was higher than that of the UHPC). The lowest flexural strength of 30.5 MPa was obtained for the UHPC-SC, while the highest flexural strength of 34.4 MPa was obtained for the UHPC/CNT-EC. The relative increase in the strength of the UHPC/CNT_SC and UHPC/CNT-EC samples were 9.6 % and 12.9 %, respectively.

The general flexural stress–strain curves of UHPC and the flexural stress and FCR behaviors of the samples with respect to time are shown in Fig. 6-19 and Fig. 6-20, respectively. The flexural stress–time response curves of all samples were similar to the general flexural stress–strain curves for the UHPC except for approximately 180–300 s from the beginning of the loading where the load did not significantly increase due to the displacement control. Thus, the response curves were classified into three zones: a linear elastic zone (I), a deflection hardening zone (II), and a crack opening zone (III). The flexural stress increased almost linearly until the first cracking stress (σ_{fc}) was reached in zone (I). After this point, the flexural stress in zone (II) gradually increased compared with that in the elastic zone (I) until the stress reached the maximum post cracking stress (σ_{pc}). After this point, the stress gradually decreased as the crack width increased, which is called crack localization, in zone (III) [119].

The σ_{fc} for all samples was similar and in the range of 28–30 MPa. This is because the effect of nano–micro scale fibers on the first cracking stress was small [75, 120]. However, in the deflection hardening zone (II), the UHPC/CNT exhibited significantly improved strain hardening behavior regardless of the curing method in comparison with that of the UHPC. In addition, beyond the σ_{pc}, the

stress decreased slightly for the UHPC/CNT whereas that of the UHPC decreased relatively more rapidly. This indicates that the CNTs with a high aspect ratio favorably affected the strain hardening and multiple cracking behavior due to the bridging effect as shown in Fig. 6-11e–f. Fibers smaller than micro size increase the strain hardening and post cracking behavior rather than increasing the first cracking stress in the UHPC [120].

As was the case under compression, the FCR of the UHPC could not be used to accurately estimate the flexural state or crack sensing timing under deflection. The FCR of the UHPC increased slightly to 0.65 as the stress increased until the σ_{pc} was exceeded, then abruptly increased in the crack opening zone (III). However, the value of the FCR was still below 1.5, which was not large enough to use for the crack sensing. In addition, the point at which the first crack occurred did not match the point at which the FCR rapidly increased. Therefore, it was difficult to recognize the point of first cracking and whether the sample had yielded or not. In contrast, the measurement of the FCR enabled the detection of cracking in the UHPC/CNT. The FCR of the UHPC/CNT was close to zero until the σ_{fc} was reached regardless of the curing method. However, after first cracking, the FCR rapidly increased up to about 25 and fluctuated wildly. In addition, the FCR gradually increased and fluctuated as the crack width increased. Thus, it is possible to determine whether the samples had cracked or not based on the obtained FCR data. These results were explained via the reasons previously mentioned in Section 6.3.2. In addition, since the multiple cracks gradually progressed from the bottom to the top of sample, the disconnection between the CNTs also progressed slowly. Therefore, the FCR significantly increased at the point of first crack because some of the CNTs became disconnected and then began to fluctuate as this increased.

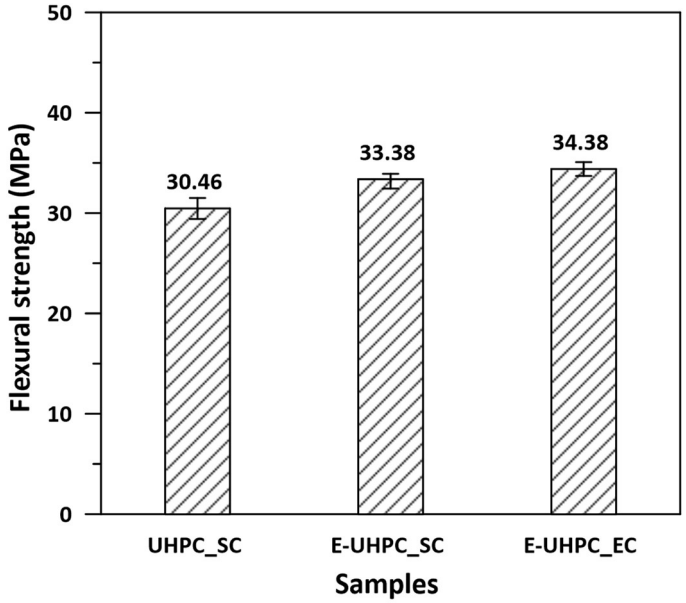

Fig. 6-18. Flexural strength of the samples.

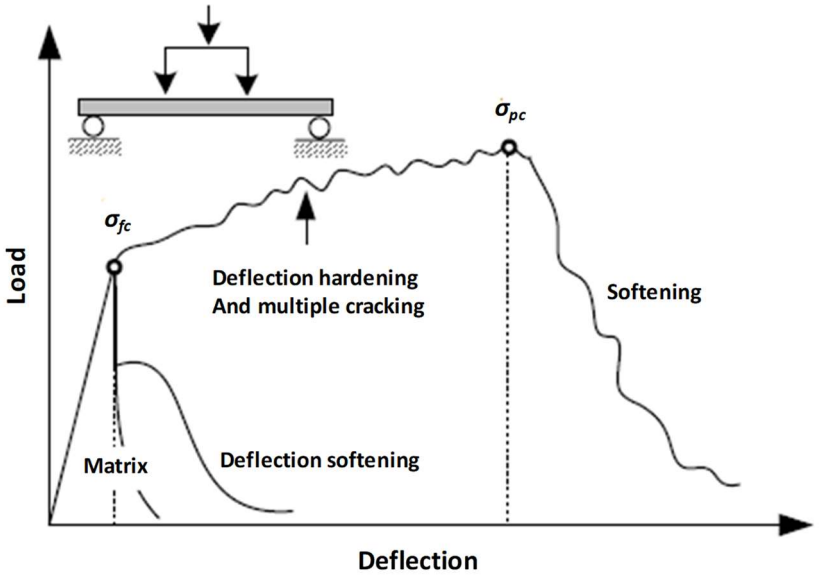

Fig. 6-19. General flexural stress–strain curves of UHPC

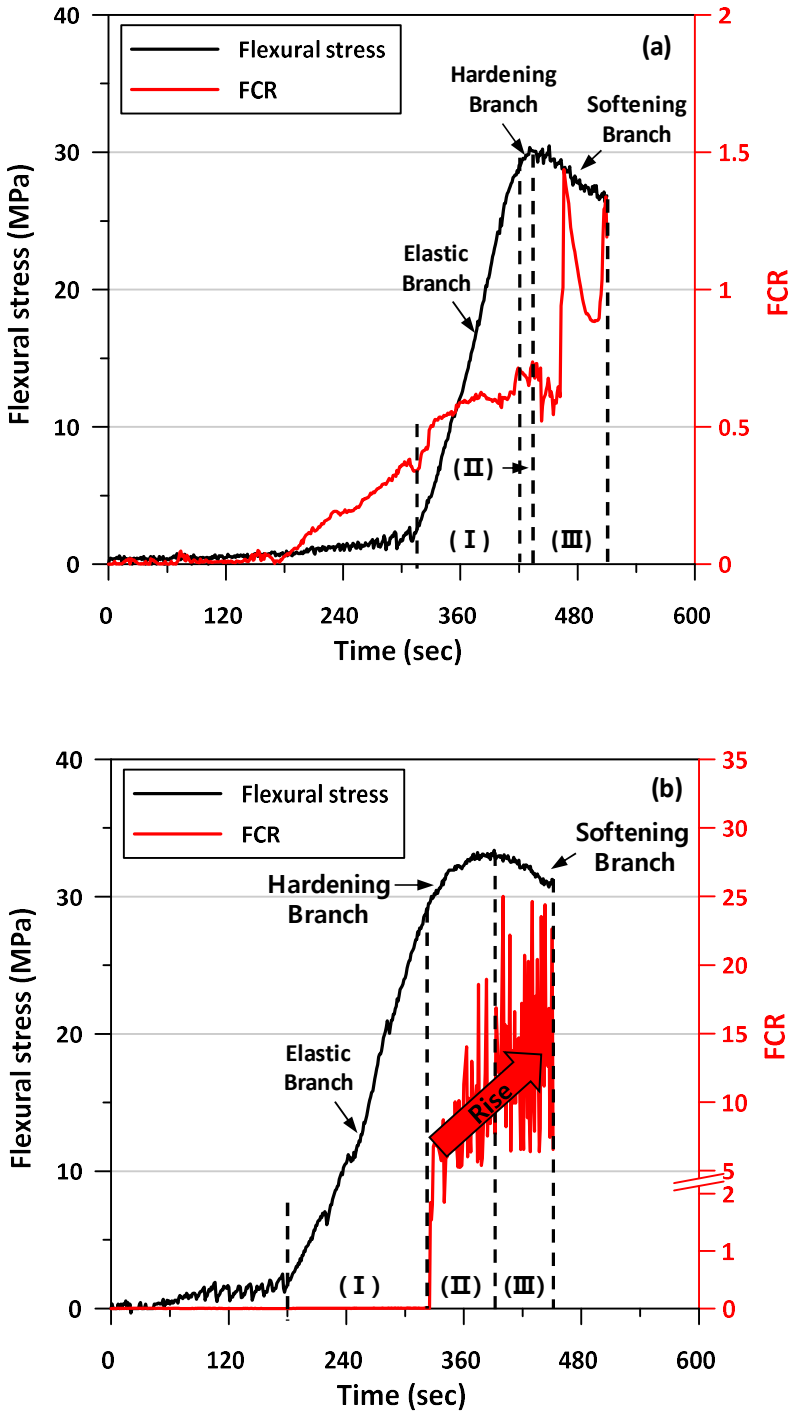

Fig. 6-20. Flexural stress and FCR behaviors with respect to time: (a) UHPC-SC, (b) UHPC/CNT-SC, and (c) UHPC/CNT-EC.

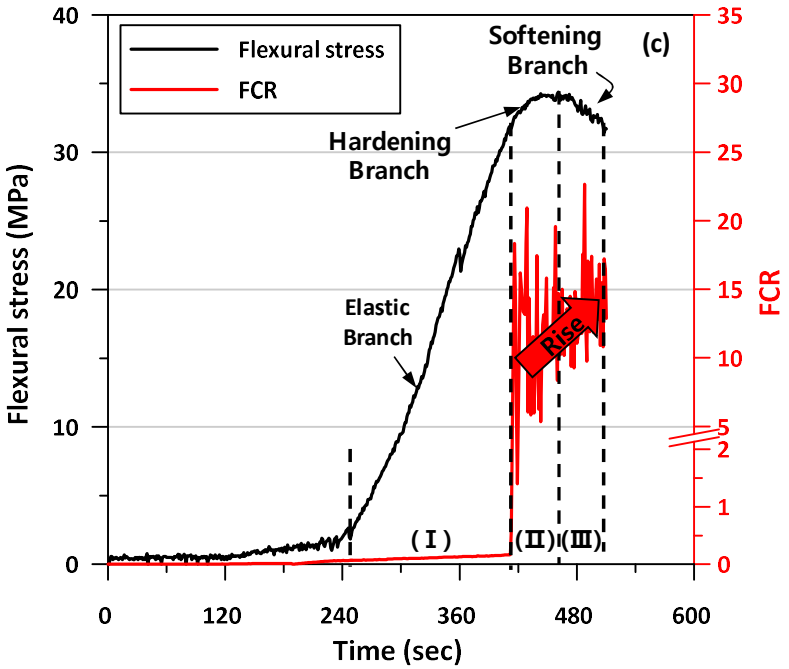

Fig. 6-20. *(Continued)* Flexural stress and FCR behaviors with respect to time: (a) UHPC-SC, (b) UHPC/CNT-SC, and (c) UHPC/CNT-EC.

The GF was calculated at the point of the first crack to evaluate the crack sensing capability of the UHPC and UHPC/CNT under deflection as Eq. (6.3). Note that the ε of the samples was not measured under the flexural strength test; however, since the stress–time response based on displacement control was quite linear until the σ_{fc} was reached, ε could be calculated as follows:

$$\varepsilon = -\frac{My}{EI}, \tag{6.4}$$

where M is the flexural moment (kNm), y is the distance from the sample to the tension surface (m), E is the elastic modulus (GPa), and I is the moment of inertia of the cross-section (m^4) of the sample.

The GF of the UHPC-SC was calculated as 295.7, whereas those of the UHPC/CNT-SC and UHPC/CNT-EC were calculated as 2957.9 and 2133.4, respectively, which were approximately 10.0 and 7.2 times higher (Fig. 6-17). Thus, it can be confrmed from the GF value that the crack sensing capability of the developed UHPC/CNT under deflection improved enough to determine the yielding point.

6.4 Conclusions

Application of UHPC in field construction is limited owing to the particular requirements of SC. In this chapter, incorporation of CNTs in UHPC was reported for practical manufacture of UHPC via EC as well as multi-functionality as crack sensible structural material. In the designed experiment, a pre-dispersed CNT suspension was selected for the UHPC base and two types of curing (SC and EC) were applied. This was followed by the examination of the mechanical properties of the UHPC/CNT composites under both compression and flexure conditions and microstructure analyses were conducted. Lastly, the feasibility of using the composites as crack sensor was assessed. The following conclusions can be drawn from the experimental results with schematic diagram of effects of CNT on UHPC (Fig. 6-21):

1) Incorporation of dispersed CNTs significantly decreased the electrical resistivity of the UHPC by forming connections along with added the steel fibers. This resulted in the construction of a strong conductive pathway in the whole material that was not affected by the water content (i.e., degree of hydration of UHPC). As a result, the electrical resistivity of the UHPC/CNT maintained unchanged during curing process, enabling EC with significantly low voltages of 19–23 V.

2) The mechanical properties of the UHPC/CNT were improved due to the generation of denser and stiffer C-S-H that caused bridging and pore filling effects. Furthermore, the EC applied UHPC/CNT has better performance which was explained by the electric field, formed during curing condition, efficiently activated the ionic polarization which is resulting in accelerated hydration of the UHPC/CNT composite.

3) The piezoresistive sensing of stress under compression and flexure was limited for both UHPC and UHPC/CNT due to the dense packing of particles in the matrix with a low w/c. However, the crack sensing capability (i.e., not stress sensing capability) of the UHPC significantly improved with the addition of CNTs which enables potential SHM application. The GF of the UHPC was 113.3 under compression and 295.7 under deflection. In contrast, that of the UHPC/CNT improved to 4111.1 under compression and 2133.4 under deflection.

Based on these results, the production of UHPC structures in field construction by applying EC on UHPC/CNT composites is feasible. This is possible because the resistivity of a material is not affected by its geometry [20] and the temperature of the actual structure can be effectively increased with even a low voltage. In this way, the proposed approach uses significantly less energy than that required for traditional UHPC production to accelerate curing and achieve target performance. Lastly, it was found that the UHPC/CNT composites could be also used as a SHM structural sensor with high crack sensing capability.

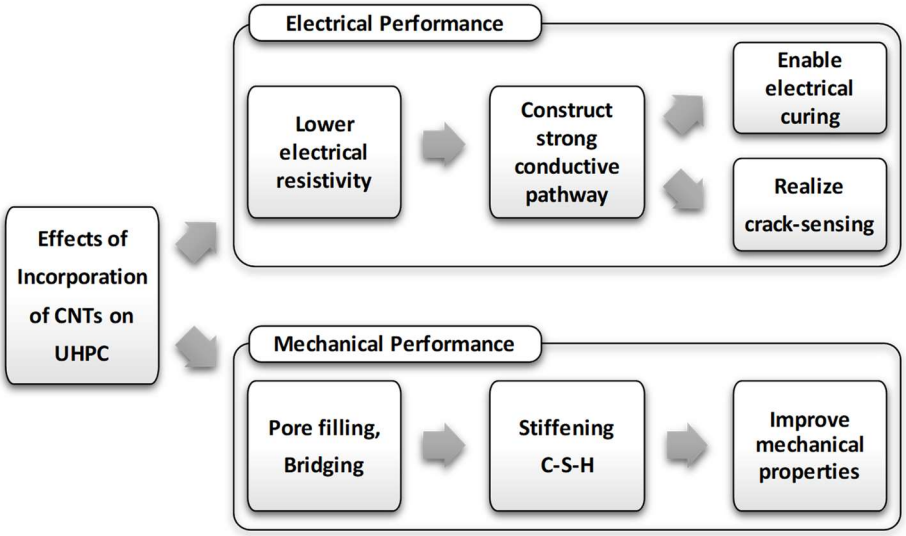

Fig. 6-21. Effects of incorporation of CNTs on UHPC in terms of electrical curing for field casting, and crack sensing for structural health monitoring.

Chapter 7. Micro- and Meso-Structural Changes of UHPC by CNTs

This chapter, followed by chapter 6, deals with the effects of CNTs, which was rarely reported in previous studies, on the structural changes of cementitious materials (especially for the case of UHPC) in micro- and meso-scale level as well as the feasibility of electrical curing. The added CNTs slightly hindered the hydration reaction of the UHPC, but it significantly modified the structure of C-(A)-S-H to be denser, stiffer, and more complex which have been evidenced by observed partial cross-linking in the C-(A)-S-H, reduced *d*-spacing and the higher fractal dimensions of solid system. This behavior was much more significant when EC was applied because the electrical field formed by EC activated ionic polarization and accelerated the chemical reaction among ions, resulting in a higher degree of hydration.

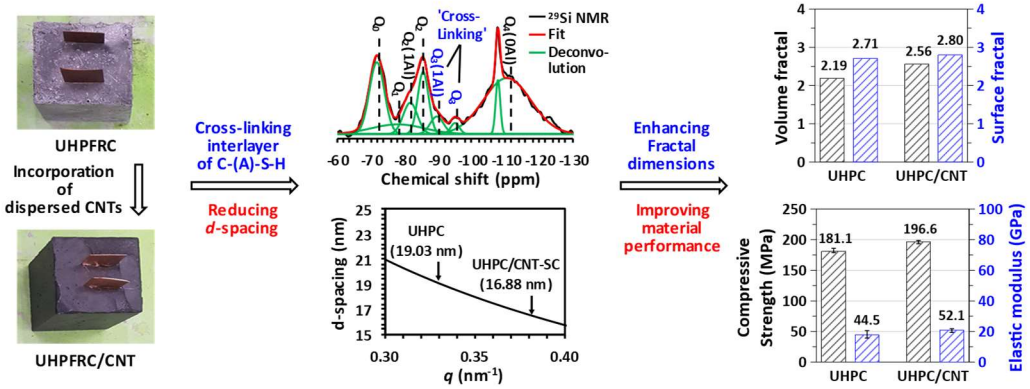

Fig. 7-1. Graphical abstract of chapter 7.

7.1 Introduction

The interaction mechanism between CNTs and cementitious materials (especially for the case of UHPC) have not been investigated comprehensively, especially the structural changes in micro- and meso-scale level.

Hence, in this chapter, followed by the study in chapter 6, effects of CNTs on micro- and meso-structural modifications of UHPC were investigated with respect to curing conditions based on examinations of XRD, TG, solid-state ^{29}Si nuclear magnetic resonance (NMR), and SAXS analyses.

7.2 Experimental Details

7.2.1 Mixture proportions and sample preparation

In this study, the properties of CNTs, mixture proportions, and the process of sample preparation were same as aforementioned in section 6.2 (i.e., UHPC/CNT composites were fabricated by mixing the UHPC dry pre-mixtures with 0.24 wt.% of distilled water or commercially available pre-dispersed CNT suspensions. Then, the samples were cured for a period of 48 h by applying two different curing methods: SC at 90 ℃ with RH = 95 % and EC at low voltages of 19–23 V and RH = 95 %).

Separate samples without steel fibers were prepared for analyses of the hydration reaction and the microstructure of the samples. In addition, samples for XRD, TG, and SAXS analyses were synthesized without silica sand, while the samples for solid-state ^{29}Si NMR analysis were manufactured with silica sand.

7.2.2 Test methods

The samples for the XRD, TG, solid-state ^{29}Si NMR, and SAXS analyses were prepared by applying hydration stoppage at 28 d using isopropanol and diethyl-ether. The samples were then mechanically ground.

The XRD analysis was performed using a D2 Phaser (Bruker, Germany) with CuKα (λ = 1.5418 Å) radiation at 30 kV and 10 mA, and a step size of 0.01° and 1 s per step were employed over a 2θ range of 5–50°. The International Centre for Diffraction Data (ICDD) database was used for phase identification.

TG analysis was conducted using a TA Instrument Q500 (Bruker, Germany) under an N_2 environment at a heating rate of 10 K/min up to 1,050 °C. The first derivative of the TG curve (DTG) was derived to identify the weight loss of several hydration products.

Solid-state ^{29}Si NMR spectra was acquired using an Advance III HD (Bruker, Germany) at 119.182 MHz. The NMR spectra were obtained using a 5 mm HX CPMAS probe and a 5 mm zirconia rotor by employing a spinning speed of 10.0 kHz, a pulse width of 2.2 μs, and a relaxation delay of 22 s. The ^{29}Si chemical shifts were referenced to an external sample of tetrakis (trimethylsilyl) silane at -135.5 ppm with respect to tetramethylsilane (TMS) at 0 ppm and aqueous $AlCl_3$ at 0 ppm, respectively.

The SAXS analysis was performed in the q (scattering vector = $4\pi\sin[\theta] / \lambda$) range of 0.0028–1.4 nm^{-1} using a XEUSS2.0 (Xenocs, France). The X-ray source was operated at 50 kV/0.6 mA with CuKα, and the sample-to-detector distance was 2500 mm. The step size and exposure time were 0.0028 nm^{-1} and 60 s, respectively. Obtained 2D SAXS data were converted to 1D data by azimuthal integration using Foxtrat 3.4.9 software.

7.3 Results

7.3.1 X-ray diffraction

Fig. 7-2a shows the XRD patterns of the used raw materials (i.e., OPC, silica fume, and silica powder). The major crystalline phases in the anhydrous OPC were alite (C_3S), belite (C_2S), aluminate (C_3A), and ferrite (C_4AF). In addition, calcite ($CaCO_3$, ISCD#98 002 1912) was found at 23.1°, 29.2°, 35.9°, 43.1°, 47.5° and 48.5 ° in the OPC. A diffused band in the range of 15–30° in the silica fume corresponds to amorphous silica. In the silica powder, the peaks corresponding to quartz (SiO_2, ISCD# 98-008-3849) were observed at 21.0°, 26.5°, 36.5°, 39.5° 40.0°, 42.5°, 45.8°, and 50.1° respectively.

The XRD patterns of the samples cured at 28 d are presented in Fig. 7-2b–d. The peaks corresponding to the calcite were similar among the samples. In addition, the quartz peaks from silica powder were not noticeably changed for all samples. This result indicates the inertness of used crystalline silica powder in UHPC which was reported as intact unless it is exposed to 150 ℃ or higher temperatures [121]. The peaks associated with ettringite and portlandite in the range of 5–25° almost vanished for all the samples due to high temperature curing at 90 ℃ and the pozzolanic reaction, respectively (Fig. 7-2c). It is known that when cementitious materials are exposed to temperatures above 70 ℃, ettringite starts to decompose. However, in the range of 25–50° (Fig. 7-2d), the intensities of the peaks corresponding to clinkers (especially C_3S and C_2S) were relatively lower in the reference sample of UHPC-SC in comparison to those of the UHPC/CNT-SC and UHPC/CNT-EC. This clearly implied that the degree of hydration (DOH) of the reference sample (UHPC-SC) was relatively higher than that of UHPC/CNT and that a significant amount of the OPC remained unreacted in the samples containing CNTs.

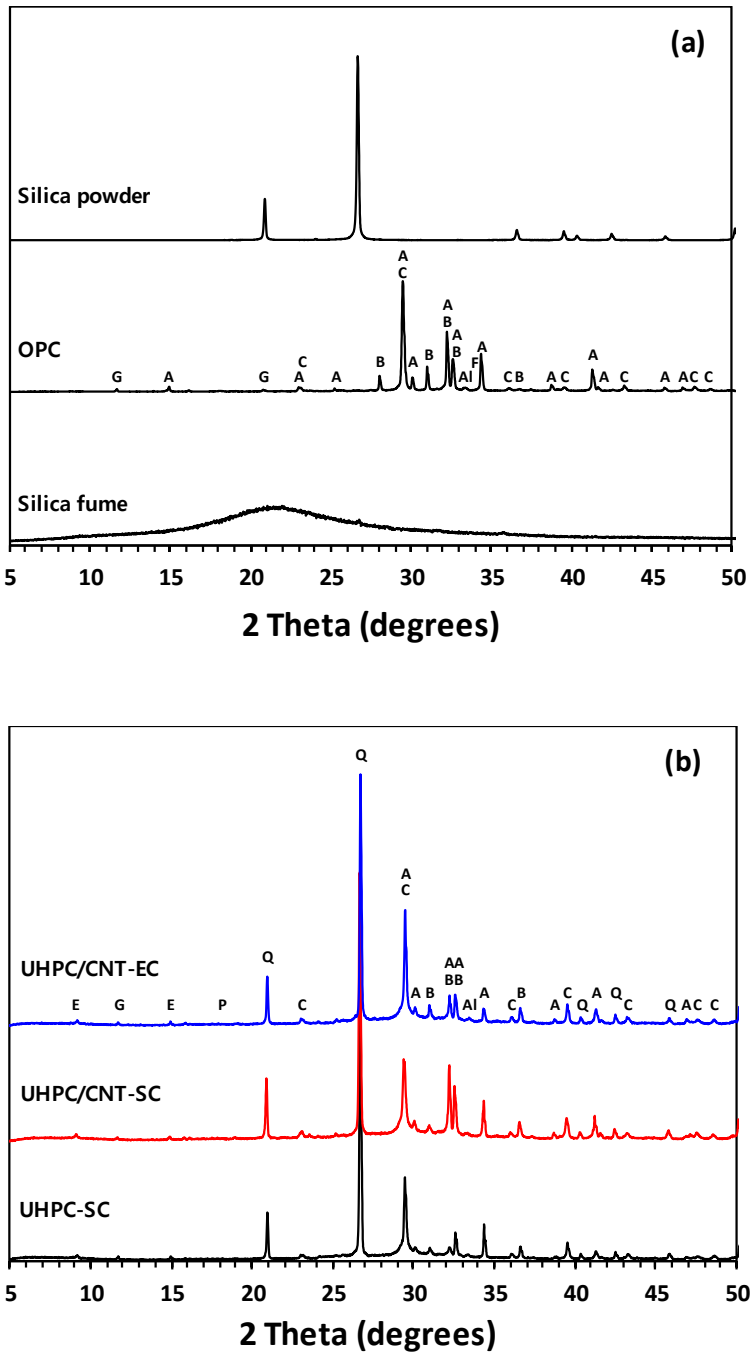

Fig. 7-2. XRD patterns: (a) raw materials, (b–d) samples at 28 d (A: alite, Al: aluminate, B: belite, C: calcite, E: ettringite, F: ferrite, G: gypsum, P: portlandite, Q: quartz).

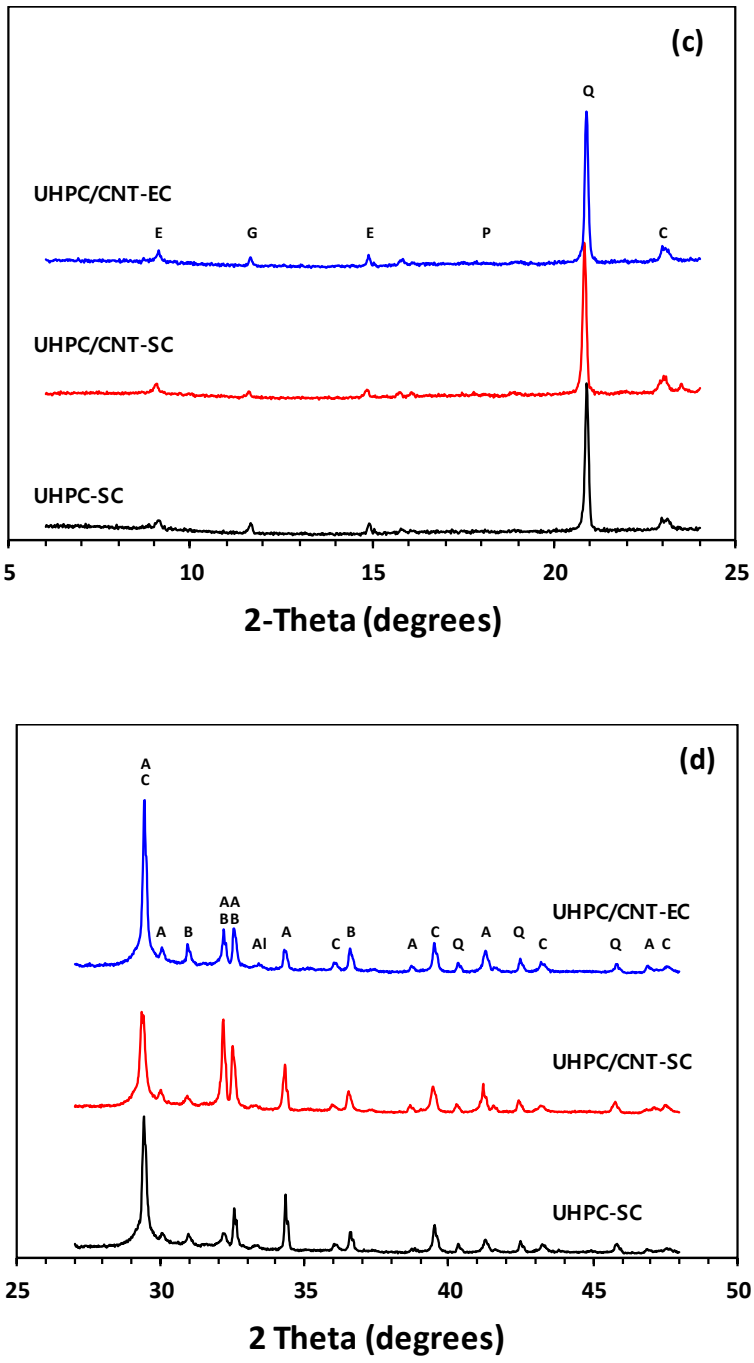

Fig. 7-2. *(Continued)* XRD patterns: (a) raw materials, (b–d) samples at 28 d (A: alite, Al: aluminate, B: belite, C: calcite, E: ettringite, F: ferrite, G: gypsum, P: portlandite, Q: quartz).

7.3.2 Thermogravimetric anlaysis

The results of TG for the samples cured for 28 d are presented in Fig. 7-3. The derivative thermogravimetric (DTG) curves (Fig. 7b) for all the samples showed weight losses at the temperature of around 100 ℃ due to the evaporations of free and physically bound water and the dehydrations of C-S-H and ettringite. The weight loss at this region can also result from the presence of third aluminate hydrate (TAH) species, which decompose at the temperature of 70–90 ℃. The weight loss at a temperature of 140 ℃ indicates the dehydration of the Al_2O_3–Fe_2O_3-mono (AFm) phase. The weight loss at the temperatures of around 360 ℃ was attributed to the dehydration of siliceous hydrogarnet (C_3ASH_4) [81]. This peak was only observed in the samples containing CNTs. The peaks centered at the temperature of 420 ℃ and 740 ℃ were associated with the dihydroxylation of portlandite and decarbonation of calcite, respectively.

Fig. 7-4 shows the calculated contents of portlandite and calcite using a stepwise method and normalization by the weight loss at 600 ℃ for quantitative comparison. The amount of portlandite in all the samples was calculated very low, in the range of 0.55–0.62%. This showed that most of the portlandite produced by the hydration of C_2S and C_3S was consumed by the pozzolanic reaction. The content of calcite for the reference sample was calculated as 12.44%, whereas it reduced in the range of 11.5–11.6 % in the samples with CNTs.

The total weight loss (Fig. 7-3a), and the peak corresponding to C-S-H and ettringite (Fig. 7-3b) and was relatively higher in the TG curves of the reference sample (UHPC-SC) in comparison to those of the samples containing CNTs. Therefore, the results confirmed that the DOH of the reference sample was the highest, which was consistent with the result of XRD analysis. For the samples containing CNTs, the UHPC/CNT-EC appeared to be slightly more hydrated than the UHPC/CNT-SC, but the difference was not significant.

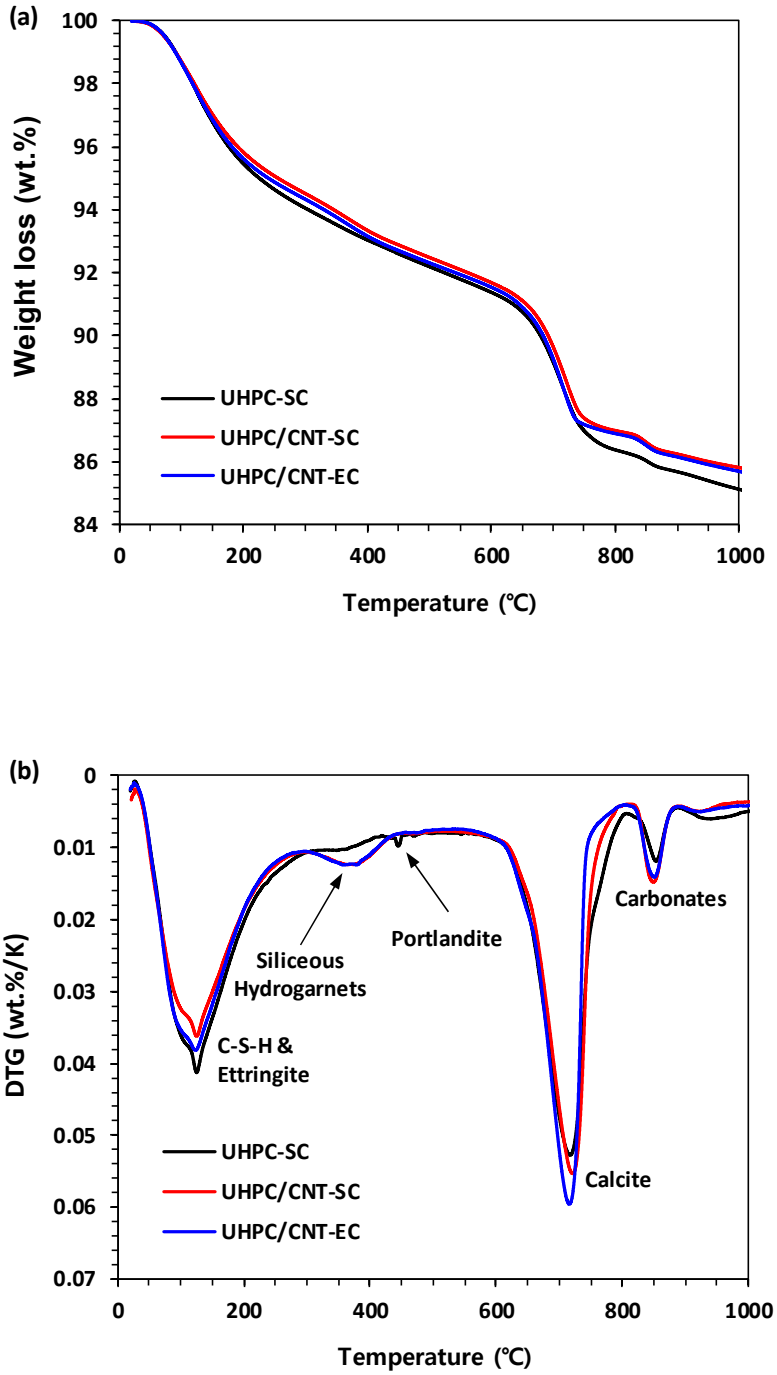

Fig. 7-3. Results of TG analysis for the samples at 28 d: (a) TG curves, (b) DTG curves.

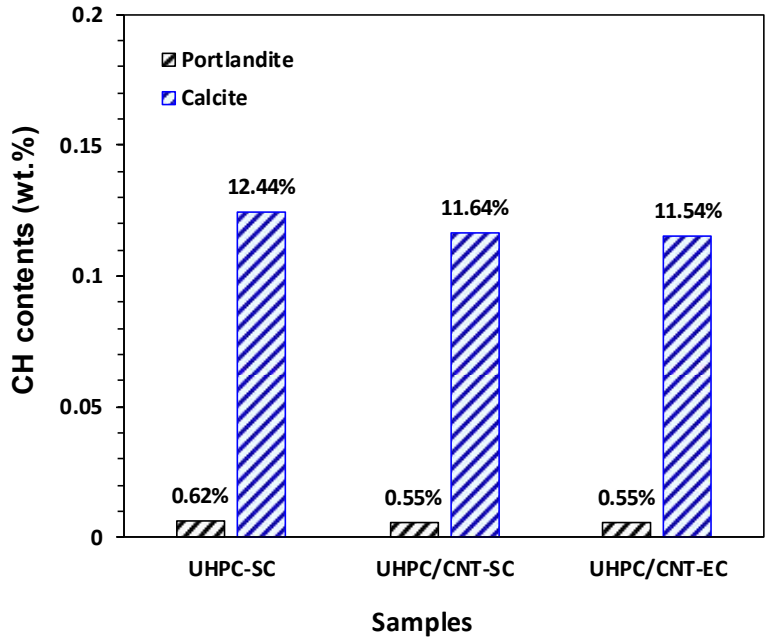

Fig. 7-4. Quantification of portlandite and calcite contents of the samples

7.3.3 ^{29}Si NMR spectroscopy

Fig. 7-5a shows the solid-state ^{29}Si NMR spectra of the raw material (i.e., the dry mixture of UHPC including silica sand). The spectra showed a narrow resonance at -71 ppm associated with the Q^0 site of C_2S and a broad resonance in the range between -66 and -80 ppm caused by C_3S [122]. A narrow resonance at -107 ppm and a broad resonance at around -112 ppm were the Q^4(0Al) site assigned from silica sand (marked as SS in the Fig. 8) [123] and amorphous SiO_2 which was originated from silica fume [124], respectively.

Generally, ^{29}Si NMR spectra of hydrated cement show resonances at -79 ppm and -85 ppm assigned to the chain-end (Q^1) and bridging sites (Q^2) of C-S-H, respectively. In addition, the resonance occurring at –81 ppm represents mid-groups (Q^2(1Al)) site, in which Al species substitute for Si in the bridging site of C-S-H [125]. However, cross-

linking (Q^3) and Q^3(1Al) sites of the silicate chains resonant at -95 and -89 ppm, respectively, are not typically observed due to the presence of the interlayer in the C-S-H [126].

The ^{29}Si NMR spectra for the samples in Fig. 7-5b showed almost identical intensity of signal at -107 ppm corresponding to the silica sand, which was the physical (non-reactive) filler. On the other hand, the resonance for all the samples at -71 ppm and -112 ppm corresponding to the anhydrous OPC and the unreacted silica fume, respectively, was lower than that of raw material owing to the hydration reaction. For the reference sample, the intensity at -112 ppm was significantly lower. In the same sample, the intensities at -79, -81, and -85 ppm in the spectra associated with Q^1, Q^2(1Al), and Q^2 (which indicated the presence of hydration product C-(A)-S-H) were remarkably higher than those of the samples containing CNTs. For quantitative comparisons among the samples, DOH of OPC and the degree of reaction (DOR) of silica fume were calculated as follows [127]:

$$\text{DOH or DOR} = 1 - \frac{I(t)}{I(t_0)}, \tag{7.1}$$

where $I(t_0)$ and $I(t)$ indicate the relative intensity for OPC or silica fume before and after 28 d of curing, respectively. As shown in Table 7-1, both the DOH of OPC and the DOR of silica fume for the reference sample were higher than those of the samples containing CNTs. Therefore, the reference sample was the mostly reacted in terms of DOH, which was consistent with results of XRD and TG analyses.

In the NMR spectra, the resonances at -95 and -89 ppm that assigned to Q^3 and Q^3(1Al), respectively, were observed for all samples. Additionally, the intensity peaks for the UHPC/CNT were much higher

than that of the reference sample regardless of the curing method. The deconvolution process was performed on all the NMR spectra for further analysis (Fig. 7-5c–f), and the mean chain length (MCL_C) and Al/Si_c ratio were calculated as follows [128]:

$$MCL_C = \frac{4\left[Q^1 + Q^2 + Q^2(1Al) + Q^3 + 2Q^3(1Al)\right]}{Q^1}. \quad (7.2)$$

$$Al/Si_C = \frac{Q^3(1Al)}{Q^1 + Q^2 + Q^2(1Al) + Q^3 + Q^3(1Al)}. \quad (7.3)$$

The results of deconvolution for the NMR spectra are listed in Table 7-2. For the reference sample, the DOH was the highest, which was consistent with the results of preceding analyses. In addition, the Al/Si_C ratio and MCL_C of C-(A)-S-H were calculated as 0.07 and 13.63, respectively. In contrast, for the UHPC/CNT, the DOH and DOR were lower, but cross-linking sites of the silicate chain, Al/Si_C ratio and MCL_C were calculated as much higher than those of the reference sample regardless of the curing method. Between the samples containing CNTs, the UHPC/CNT-EC showed higher values of DOH, DOR, Al/Si_C, and MCL_C than the UHPC/CNT-SC.

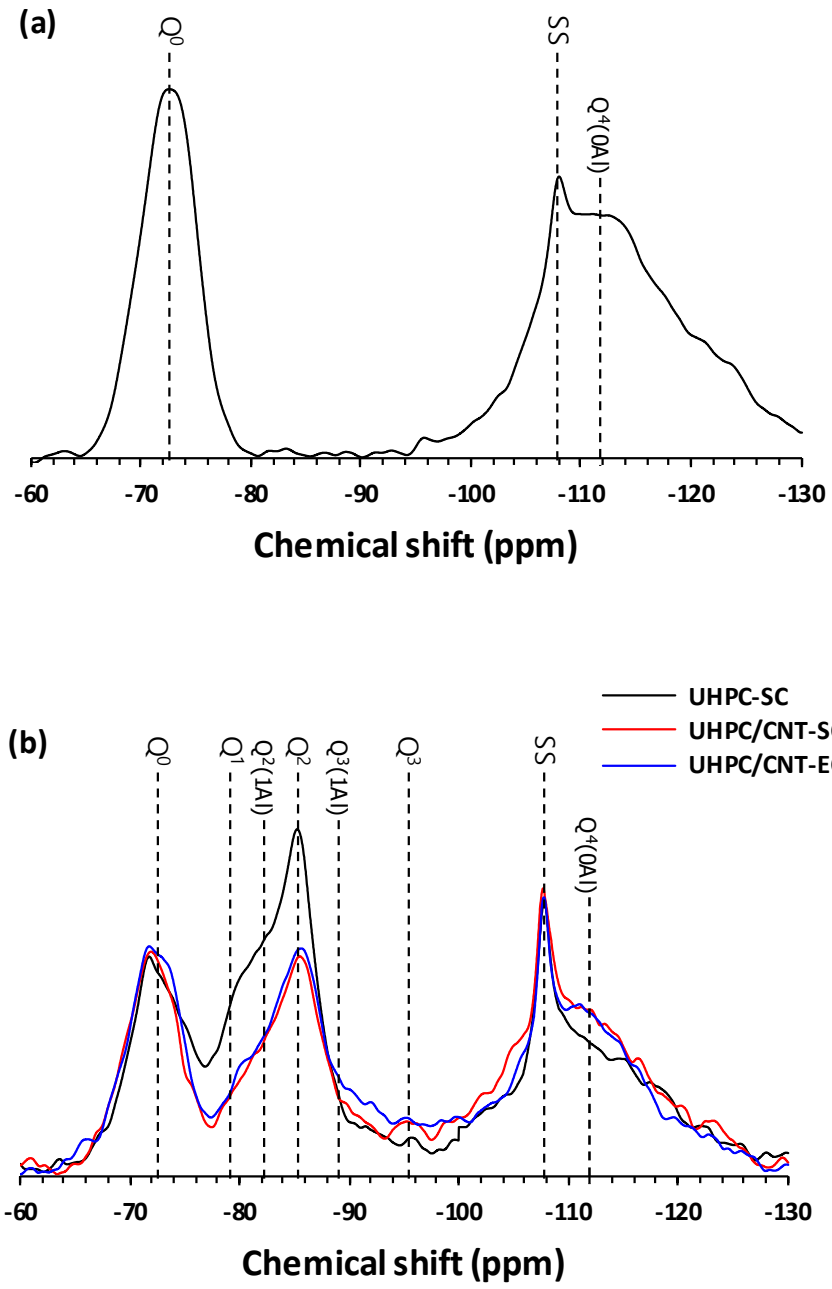

Fig. 7-5. ^{29}Si NMR spectra: (a) raw material (UHPC pre-mixture), (b) specimens, (c–e) spectral deconvolution for UHPC-SC, UHPC/CNT-SC, and UHPC/CNT-EC, and (f) deconvolution results.

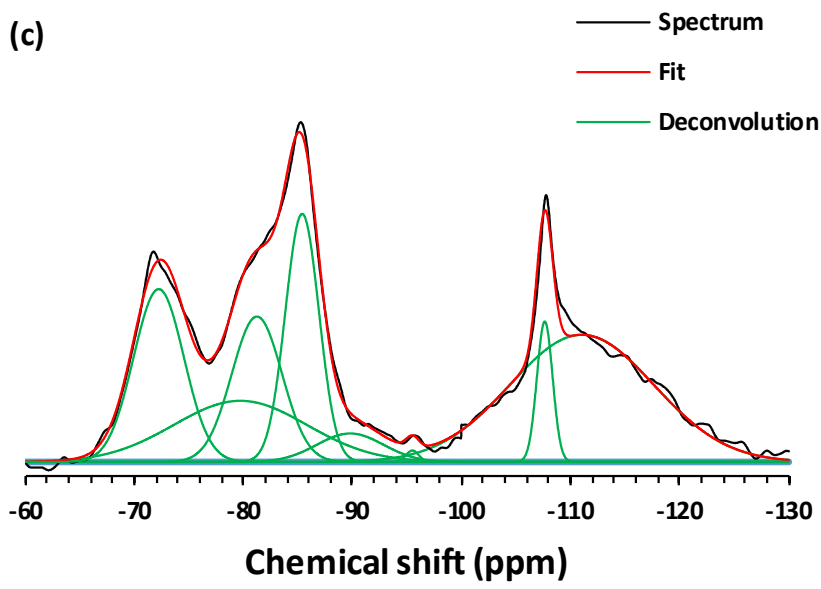

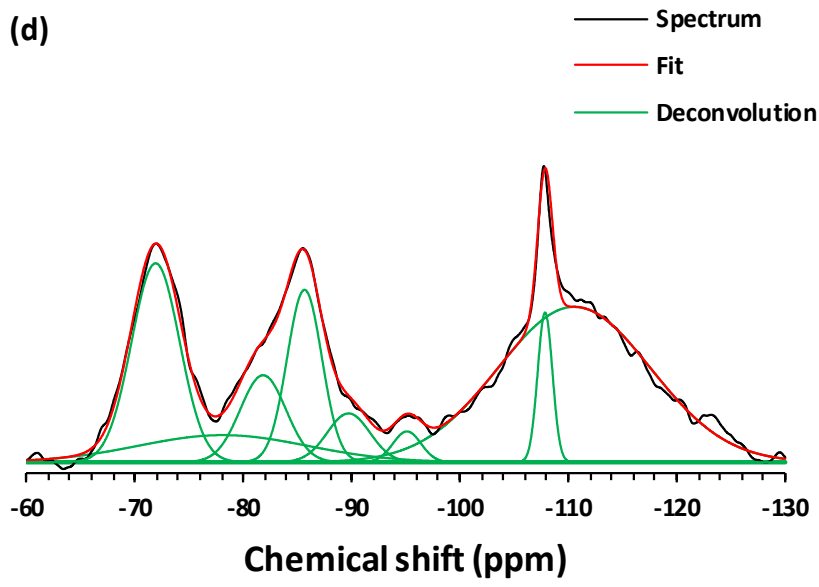

Fig. 7-5. *(Continued)* ^{29}Si NMR spectra: (a) raw material (UHPC pre-mixture), (b) specimens, (c–e) spectral deconvolution for UHPC-SC, UHPC/CNT-SC, and UHPC/CNT-EC, and (f) deconvolution results.

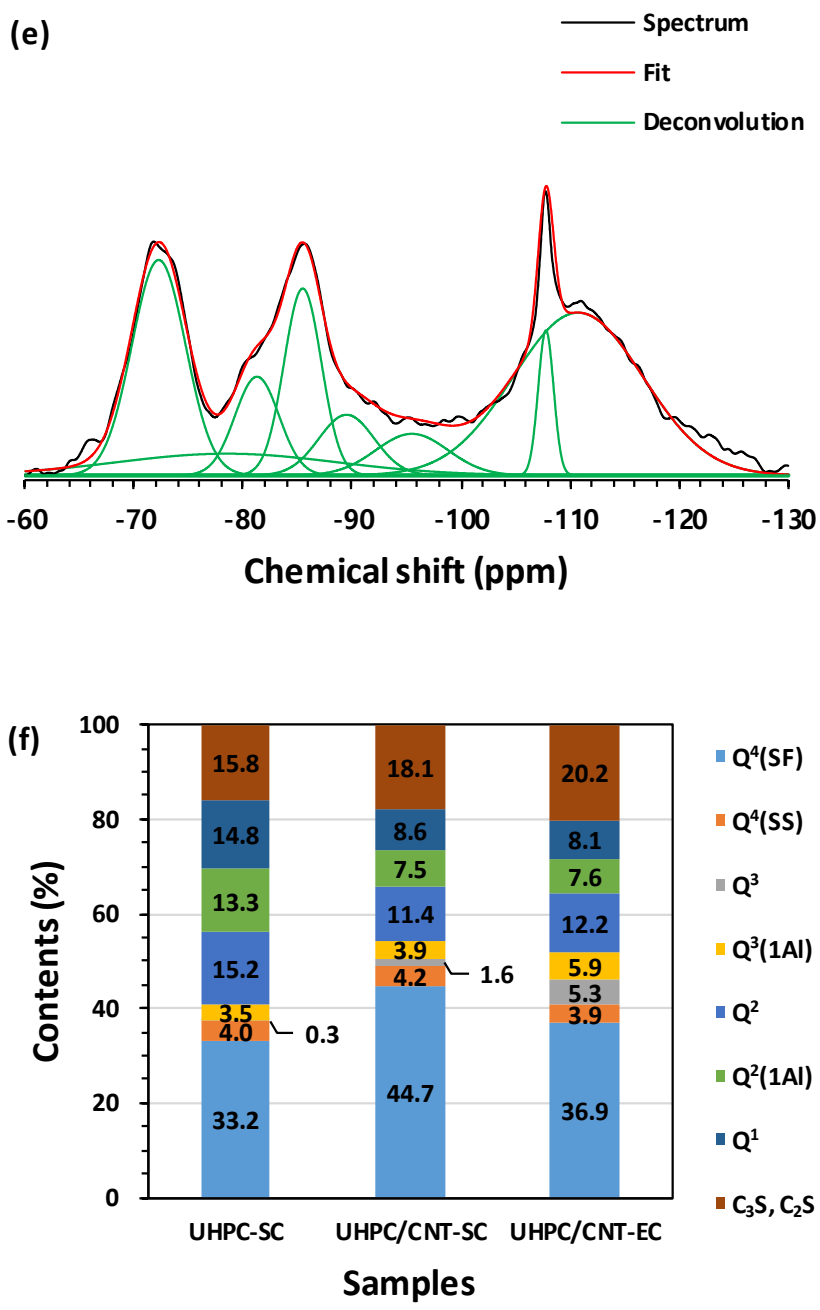

Fig. 7-5. *(Continued)* ^{29}Si NMR spectra: (a) raw material (UHPC pre-mixture), (b) specimens, (c–e) spectral deconvolution for UHPC-SC, UHPC/CNT-SC, and UHPC/CNT-EC, and (f) deconvolution results.

Table 7-1. DOH of OPC and DOR of silica fume.

Sample	DOH of OPC	DOR of silica fume
UHPC-SC	39.5	44.6
UHPC/CNT-SC	35.0	30.8
UHPC/CNT-EC	33.0	32.0

Table 7-2. Deconvolution results for the ^{29}Si NMR spectra (%).

Deconvolution	UHPC-SC	UHPC/CNT-SC	UHPC/CNT-EC
Q^0 (-71 ppm)	15.80	18.10	20.22
Q^1 (-79 ppm)	14.80	8.57	8.06
Q^2 (1Al) (-81 ppm)	13.30	7.53	7.60
Q^2 (-85 ppm)	15.16	11.35	12.20
Q^3 (1Al) (-89 ppm)	3.45	3.94	5.89
Q3 (-95 ppm)	0.26	1.63	5.26
Q4 (SS) (-107 ppm)	4.00	4.17	3.90
Q4 (SF) (-112 ppm)	33.23	44.70	36.89
Al/SI_C	0.07	0.12	0.15
MCL_C	13.63	17.25	22.27

7.3.4 Small angle X-ray scattering

A fractal is a structure, which appears the same at different scale levels, and can be observed in various materials such as materials with rough surfaces, gels, polymers, metals, aggregates, etc. Fractals allow an analytical representation of various geometrical parameters of the scattering intensity spectrum.

SAXS, along with small angle neutron scattering (SANS), is a well-established technique for investigating nano- and micro-scale structures in various materials with respect to fractals. This provides detailed structural analysis and physical information for a variety of 1–100 nm and beyond particle systems by characterizing average particle sizes and shapes. SAXS measurement experimentally can distinguish Porod and fractal regions through the value of the scattering exponent τ in each region where the scattering intensity $I(q)$ decays as a power-law (i.e., $I[q] \propto q^{-\tau}$). The $\tau > 4$ is associated to a Porod region, while the $\tau \sim < 4$ is assigned to a fractal region. In addition, a fractal region can be classified into volume fractal and surface fractal regions. If the τ is in the range of 2–3, the sample is a volume fractal (D_V) with fractal dimension τ (in the measured q range), and if the τ is between 3 and 4, the sample is a surface fractal (D_S) with fractal dimension $6 - \tau$ [129]. Fig. 7-6 shows the typical SAXS plot of the hydrated ordinary Portland cement paste. The absolute value of the slope (D) in the log-log plot for the SAXS pattern corresponds to the τ. Thus, the Porod and fractal regions can be classified by calculating the slope of the log-log SAXS plot. Generally, for the case of cementitious materials, information about particle or pore size distributions and geometric properties of C-S-H gel can be obtained in the Porod and fractal regions, respectively.

Fig. 7-7 shows the obtained 2D image data of the samples from the SAXS analysis. The electron density of the diffuse ring in the samples containing CNTs were much higher than that of the reference sample. This is because CNTs are strong field emitters with high

current density owing to extraordinary electrical properties, the intensity of the SAXS data in the samples incorporated with CNTs is much higher than that of the samples without CNTs.

Fig. 7-8a shows the SAXS patterns (log-log scale) of the samples converted from 2D image. It is clear that the SAXS pattern has changed with the addition of CNTs into the UHPC regardless of the curing method. The straight trend lines fitted to the SAXS patterns were derived and the slopes were calculated. In the SAXS plot for all the samples, two straight trend lines were derived, and the absolute values of their slopes were > 4 and $2 < D < 4$, respectively. Thus, the SAXS patterns were clearly divided into the Porod and fractal regions. In the current measurement, since the q range associated with the Porod region was too narrow (0.0028–0.02 nm^{-1}) and the measured data was not sufficient, only the analysis of fractal region was carried out.

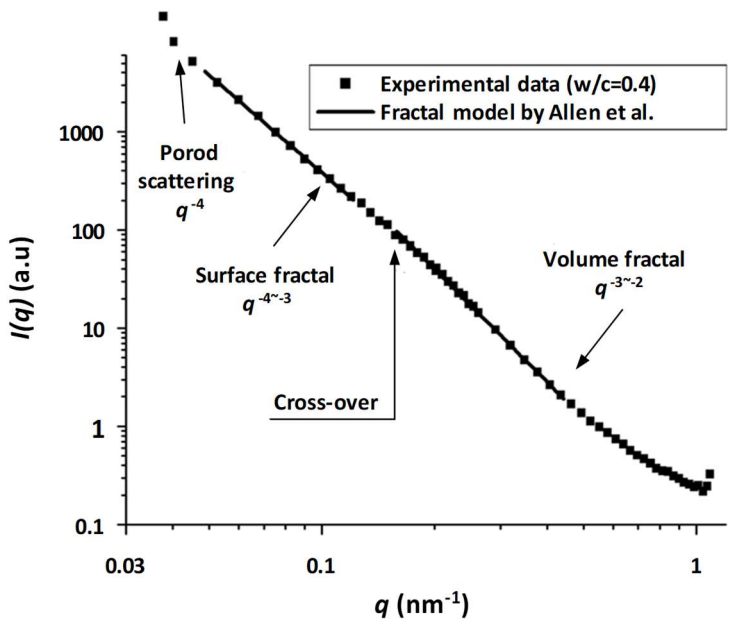

Fig. 7-6. Typical log-log plot of the SAXS curve for the hydrated cement paste (w/c = 0.4) with fitted curve based on fractal model (Allen et al.).

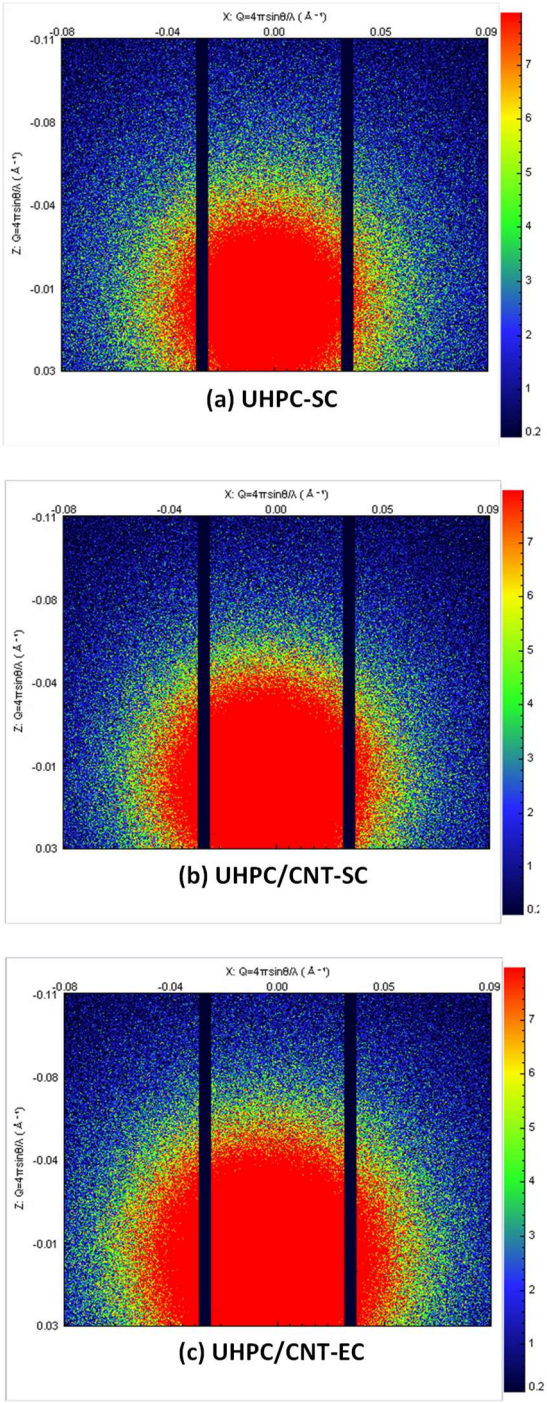

Fig. 7-7. Obtained 2D image of the samples from the SAXS analysis: (a) UHPC-SC, (b) UHPC/CNT-SC, and (c) UHPC/CNT-EC.

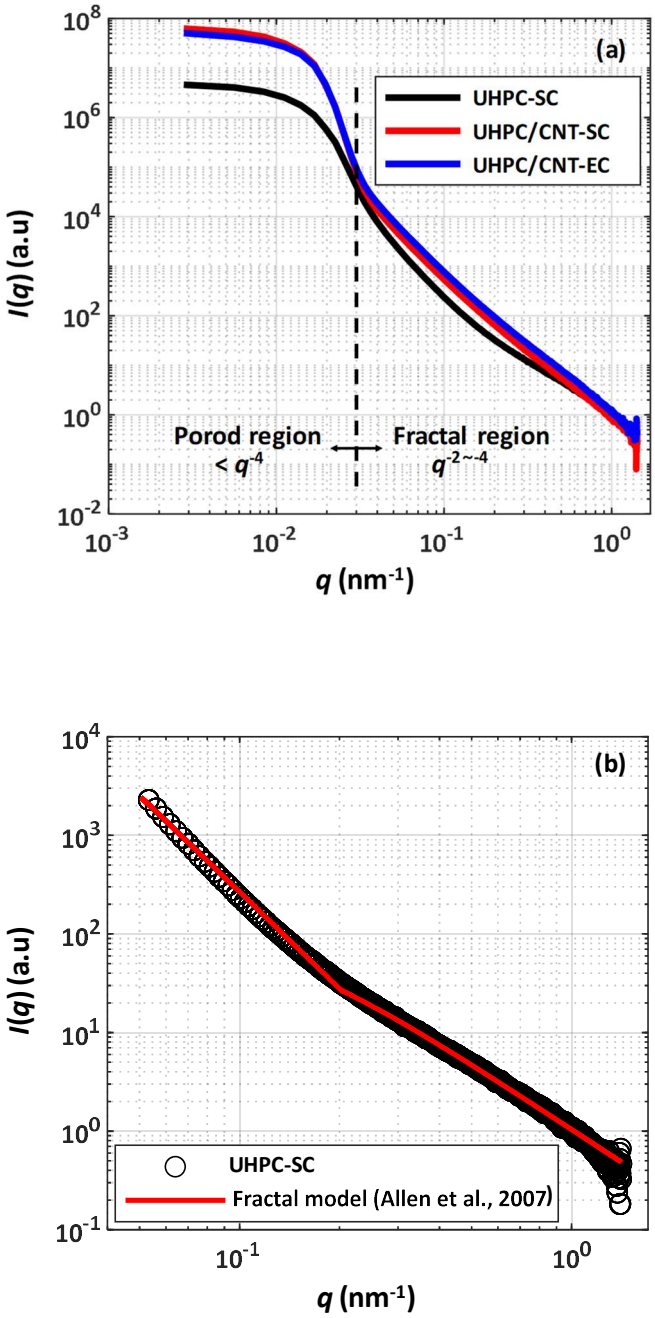

Fig. 7-8. SAXS (log-log) profiles (a) and the fitting results of the fractal model by Allen et al.: (b) UHPC-SC, (c) UHPC/CNT-SC, (d) UHPC/CNT-EC.

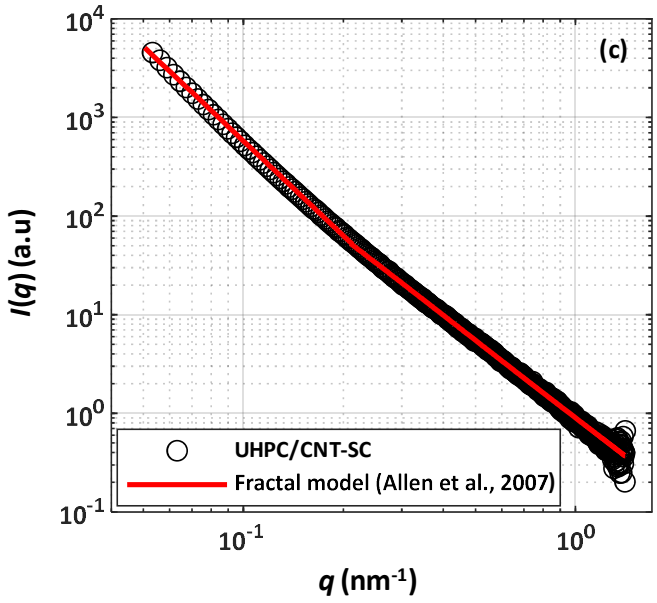

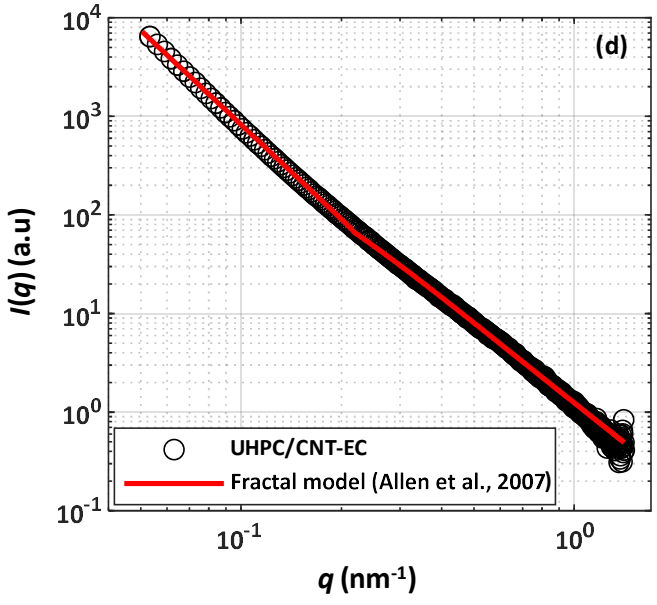

Fig. 7-8. *(Continued)* SAXS (log-log) profiles (a) and the fitting results of the fractal model by Allen et al.: (b) UHPC-SC, (c) UHPC/CNT-SC, (d) UHPC/CNT-EC.

In the fractal region, the effects of CNTs on meso-scale structure of UHPC were evaluated by employing a micro-structural model of C-S-H gel (called fractal model), introduced by Allen et al. [130] and Jennings [131]. Curves were fitted to experimental data as shown in Fig. 7-6 based on the fractal model.

The fractal model describes C-S-H gel as a fractal-like object formed by the packing of colloidal particles, called globules consisting of solid C-S-H layers and internal water layer between C-S-H layers [131] as illustrated in Fig. 7-9.

The fractal model consists of a volume fractal scattering term [$I_V(q)$] and a surface fractal scattering term [$I_S(q)$] as follows:

$$I(q) = I_V(q) + I_S(q) + BGD, \tag{7.4}$$

where *BGD* is the incoherent flat background scattering. The volume fractal term can be calculated as follows:

$$I_V(q) = f_{CSH} V_P \left|\Delta\rho\right|^2 F^2(q) \cdot \left[\frac{\eta}{\beta}\left(\frac{R_C}{R_0}\right)^3 \left(\frac{\xi_V}{R_C}\right)^{D_V} \frac{\sin\left[(D_V-1)\operatorname{atan}(q\xi_V)\right]}{(D_V-1)q\xi_V(1+(q\xi_V)^2)^{(D_V-1)/2}} + (1-\eta)^2\right], \tag{7.5}$$

where is f_{CSH} the volume fraction of solid C-S-H gel, V_P is the particle volume, $|\Delta\rho|^2$ is the scattering contrast, and $F^2(q)$ is the form factor for spheroidal particles with the size of R_0. In addition, η is the local packing fraction, β is the aspect ratio of the radii of the spheroid, R_C.is a basic building block size of globules (i.e., $R_C = 2R_0$), and ξ_V is the upper-limit length scale for volume fractal. The surface fractal term is given as follows:

$$I_S(q) = \pi \left|\Delta\rho\right|^2 \xi_S{}^4 \frac{S_0 \Gamma(5-D_S)\sin[(3-D_S)\tan^{-1}(q\xi_S)]}{q\xi_S[1+(q\xi_S)^2]^{(5-D_S)/2}}, \quad (7.6)$$

where S_0 is the smooth geometric surface area for the surface fractal microstructure, $\Gamma(x)$ is the Gamma function, and ξ_S is the upper-limit length scale for surface fractal.

To systematically fit the fractal model to the obtained SAXS plot, first, the magnitude of scattering vectors was divided into two ranges based on a weak peak or shoulder in the SAXS profile, i.e., low and high q ranges. This is because the surface fractal term is associated with a low q range, while the volume fractal term is attributed to a high q range [132]. Then, the coefficients of the volume and surface fractal term were calculated. For the calculation, both the value of $F^2(q)$ and β was selected as 1.0 [133], and $f_{CSH}V_P|\Delta\rho|^2$ in volume fractal term and $S_0|\Delta\rho|^2$ in surface fractal term were regarded as constants [134].

The comparison between the obtained SAXS data and fitted curves based on fractal model are presented in Fig. 7-8b–d with the fitted parameters in Table 7-3. The experimental data and fitted curves are in good correlation, and thus allows for further interpretation of the data using the parameters that were obtained from the modeling procedures. The R_C, D_V, and D_S of the reference sample were calculated as 8.73 nm, 2.19, and 2.71, respectively. These values significantly increased with the addition of CNTs into the UHPC regardless of the curing method, and calculated as 13.88 nm, 2.51, and 2.79 for the UHPC/CNT-SC, and 9.05 nm, 2.56, and 2.80 for the UHPC/CNT-EC, respectively. Between samples containing CNTs, the calculated fractal dimensions of volume and surface were similar, but the R_C was higher in UHPC/CNT-SC than that of UHPC/CNT-EC. Hence, it can be concluded that the degree of complexity of the meso-scale structure of the UHPC became higher with the incorporation of CNTs.

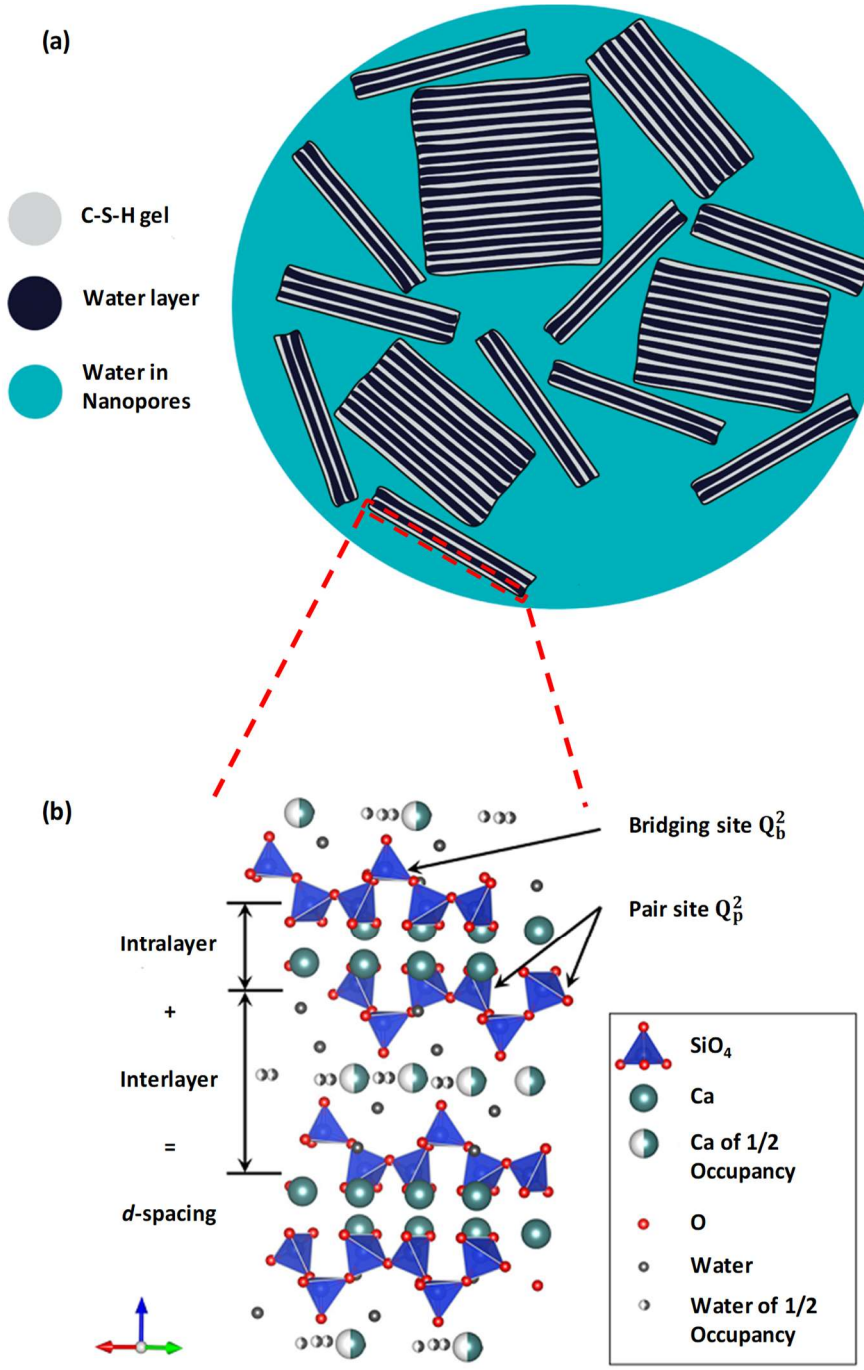

Fig. 7-9. Schematic illustration of C-S-H globule microstructure (a) [135] and nanostructure of C-S-H (b) [136].

Table 7-3. Volume and surface fractal parameters derived from SAXS fitting based on fractal model by Allen et al. (2007).

Sample	Volume fractal parameters					Surface fractal parameters		
	R_C (nm)	D_V	ξ_V (nm)	η	$f_{CSH}V_p\|\Delta\rho\|^2$ (nm)	D_S	ξ_S (nm)	$S_0\|\Delta\rho\|^2$ (nm)
UHPC-SC	8.73	2.19	7.78	0.99	17.23	2.71	191.80	2.1×10^{-4}
UHPC/CNT-SC	13.88	2.51	15.52	0.99	20.35	2.79	376.79	3.0×10^{-4}
UHPC/CNT-EC	9.05	2.56	8.91	0.99	43.47	2.80	425.44	3.9×10^{-4}

A weak peak or shoulder in the fractal region of the SAXS profile (log-log) indicates the presence of an interlayer periodic distance [137]. A shoulder was clearly shown in the SAXS profile of the reference sample in the fractal region, whereas it was not remarkably visible for the UHPC/CNT (Fig. 7-8a). Therefore, the SAXS patterns in the q range of 0.05–0.5 nm^{-1} were converted to log differential log (q)–log differential $I(q)$ plots. Then, a trend line with second degree of polynomial function was derived that fit the converted curves. In addition, the x-value was derived such that the slope of the trend lines became zero to find the point of q where the slope changed most dramatically. Thereafter, the q corresponding to the x-value was determined, and the d-spacing (d), which presents the lattice spacing or inter-atomic spacing as shown in Fig. 7-9b, was calculated using the Bragg equation ($d = 2\pi/q$).

The results of the preceding process are presented in Fig. 10. The d-spacing for the reference sample was calculated as 19.6 nm. However, the d-spacing of the samples significantly reduced with the addition of CNTs. The d-spacing of the UHPC/CNT-SC and UHPC/CNT-EC was calculated as 16.9 nm and 17.0 nm, respectively. Thus, the distance of interlayer in the hydration products in the UHPC reduced via incorporation of CNTs.

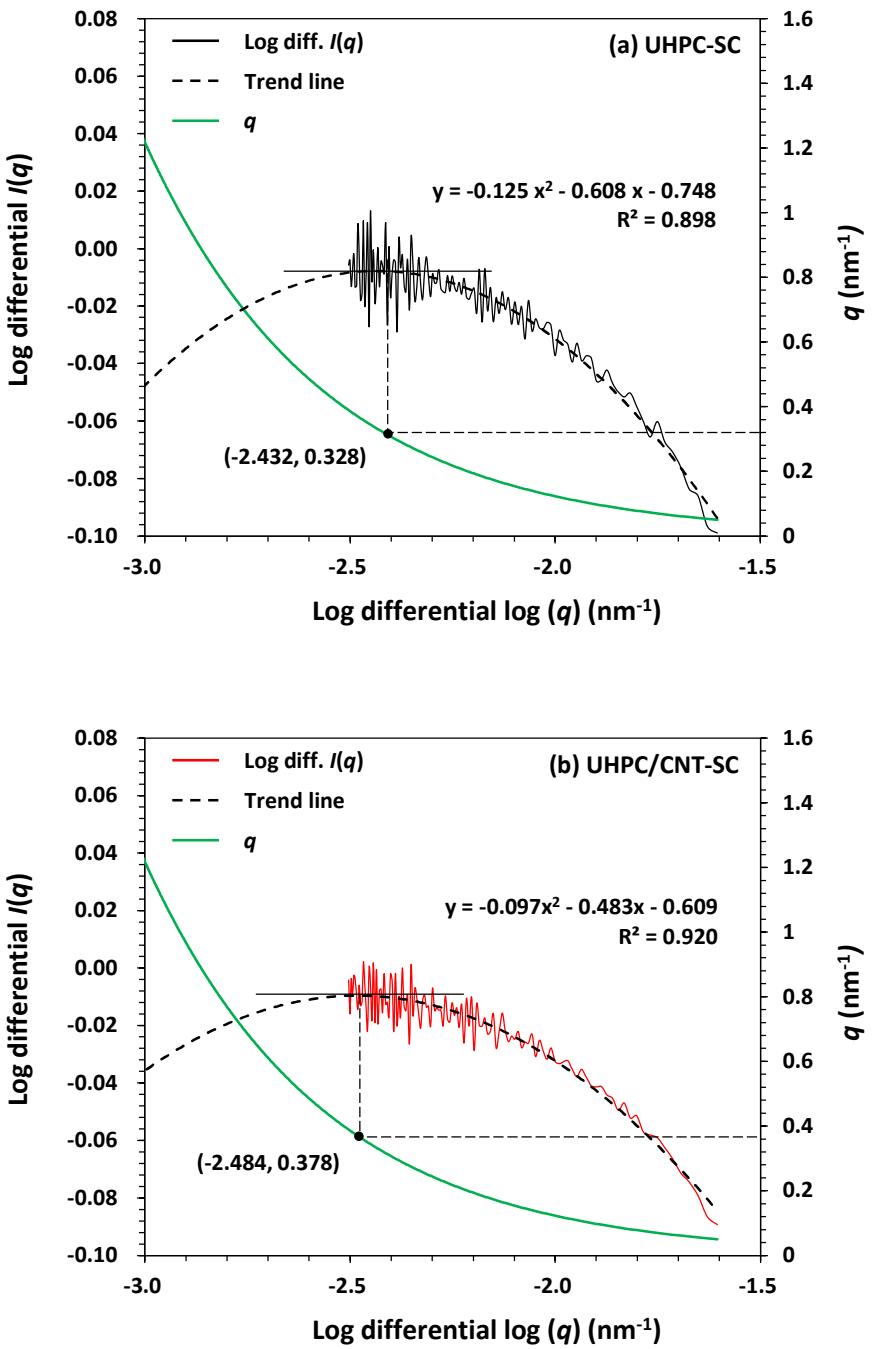

Fig. 7-10. Log differential log (q)–log differential intensity and q curves (a–c) and d-spacing of the samples (d).

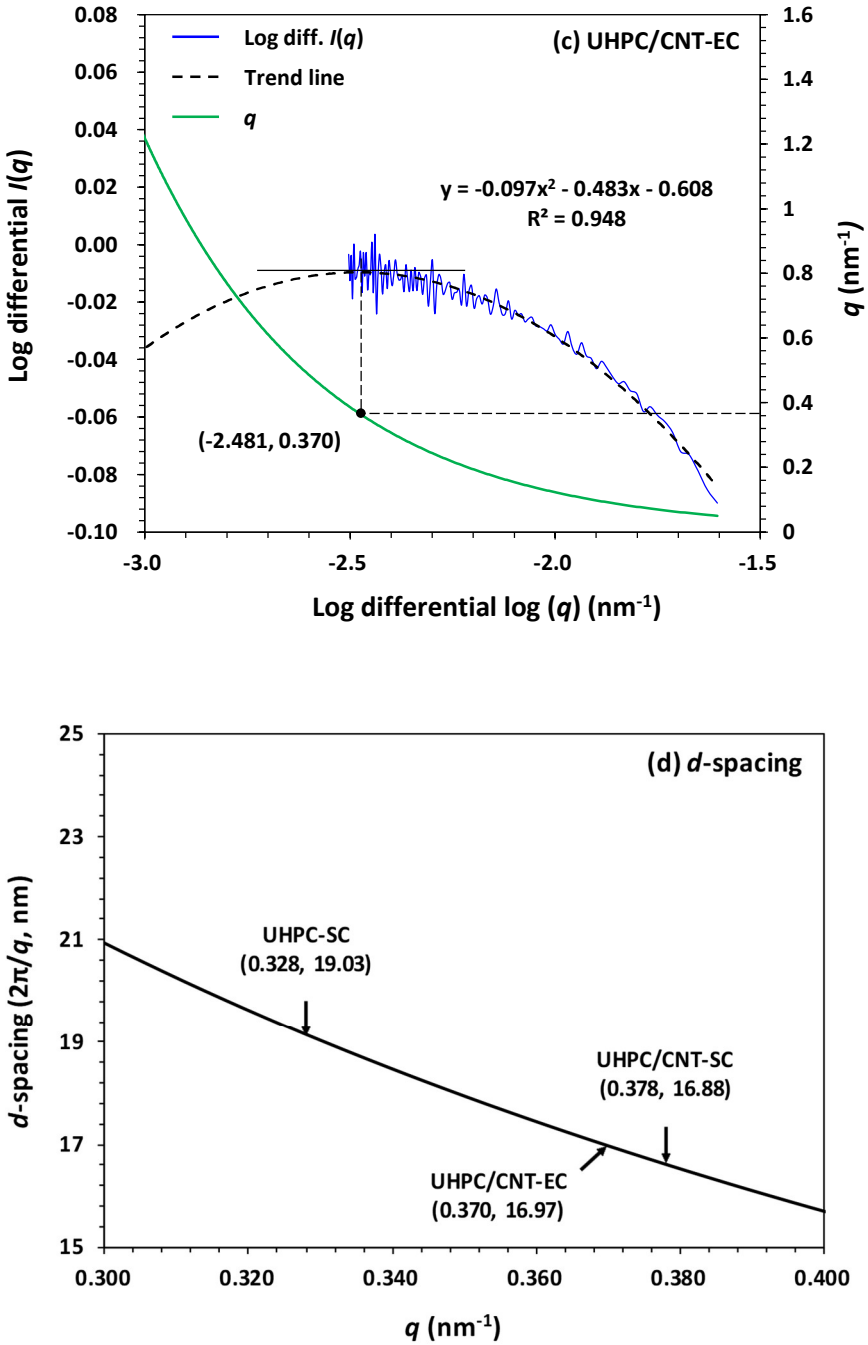

Fig. 7-10. *(Continued)* Log differential log (*q*)–log differential intensity and *q* curves (a–c) and *d*-spacing of the samples (d).

7.4 Discussion

It was proposed that the CNT content close to the critical incorporation concentration (CIC) tends to decrease the hydration of UHPC in chapter 5 [37]. For the samples containing CNTs, more cement clinkers (especially C_3S) remained unreacted, but the content of the portlandite was slightly lower than that of the reference sample based on the results of XRD and TG experiments. In addition, the result of ^{29}Si NMR analysis confirmed that the DOH of OPC and the DOR of silica fume were both lower in UHPC with CNTs. This was likely because the CNTs hindered the hydration of the cement and the reaction of the silica fume by reducing the contact area of the binders. Although the CNTs can act as nucleation seeds for promoting early hydration, its impact on the later ages was clearly turned around [138]. Specifically, for the UHPC, the spherical binders of cement and silica fume have a large contact area capable of reacting with water and portlandite. Therefore, both the acceleration of the hydration at early ages, and the pozzolanic reaction at later stages can be more active. In contrast, for cementitious materials with CNTs, nano-sized dispersed CNTs could act as nucleation sites for C_3S and C_3A hydration, resulting in acceleration of hydration at early ages [138, 139]. However, the DOH and DOR at later stages could be lower as observed in this study. The reason is that first, the needle shape of CNTs could cover the surface of the clinkers and reduce the contact area so that the hydration could be eventually hindered and the C-(A)-S-H could develop into complex shapes in the longitudinal direction along the CNTs. Second, the water had to penetrate the surface of the early hydrated product to hydrate with the inner clinkers. This led to less production of portlandite. Therefore, the silica fume reacted only with a lower amount of portlandite, resulting in a lower degree of pozzolanic reaction. In addition, accelerated hydration at early ages and lower DOH at later stages could cause an increase in the Al/Si ratio of C-(A)-S-H > 0.1

(Table 7-2), and probably produced siliceous hydrogarnet (Fig. 7-3b). Generally, it was reported that the siliceous hydrogarnet was produced when Al/Si ratio of C-(A)-S-H ≥ 0.1 [140]. In this study of UHPC/CNT hydration, the presence of siliceous hydrogarnet was suspected based on the result of TG experiment but, at the same time, it was not supported by XRD pattern, indicating that the sizable crystal of the hydrogarnet was not formulated [140].

There was a significant observation of cross-linking sites of C-(A)-S-H in the ^{29}Si NMR spectra. First, the frequency of cross-linking sites in the silicate chains was found to increase with increasing temperature [141]. However, the intensity peaks assigned to Q^3 and $Q^3(1Al)$ sites in the spectrum of the samples containing CNTs were much higher than those of the reference sample. This indicates that the interlayer of the C-(A)-S-H could be partially cross-linked by the hydration under the existence of CNTs. Although the overall DOH and DOR were lower, the structure of the C-(A)-S-H had more complex form which was evidenced by both the NMR and SAXS analyses as the hydration products had developed along the needle-shaped CNTs in a particular direction. Therefore, it can be possible that some of the CNTs affected the formation shape of C-(A)-S-H and caused the cross-linked interlayer structure between silicate chains. In addition, the carboxylic acid-based surfactant used to disperse the CNTs could have affected the interfacial interaction among the CNTs, portlandite, and C-(A)-S-H [139] . This meant that the high polarity of carboxylic and hydroxyl groups in the surface of the CNTs provided non-bridging oxygen (NBO) sites that accepted hydrogen bonds of interlayer water ions in the C-(A)-S-H [139]. Therefore, protons transferred from the carboxylic and hydroxyl groups to the NBO sites in C-(A)-S-H and improved the bonding with neighboring species (i.e., cross-linking sites of Q^3 and $Q^3(1Al)$ increased). For example, it was well reported that some chemical groups of carboxylic and hydroxyl were found to increase the interfacial bond strength between C-(A)-S-H and carbon material [142].

Furthermore, the Ca^{2+} and Al^{3+} ions in the C-(A)-S-H played a mediating role in bridging oxygen atoms in silicate chains under the contact with the carboxylic and hydroxyl groups on the CNTs, which increased the MCL_C (Table 7-2). A higher content of Q^3(1Al) presented in the ^{29}Si NMR spectra and the slightly lower contents of portlandite and calcite in the TG (Fig. 7-4) support this hypothesis [139, 143, 144].

The results of SAXS analysis also reinforced this abnormal structural modification. The CNT content close to the CIC lowered the DOH and DOR, which caused in a thicker water layer in the globules, increasing the R_C of the UHPC/CNT regardless of the curing method. Nevertheless, the dispersed CNTs increased the D_V and D_S which represents the more complicated shape (in terms of fractal dimension) of the C-(A)-S-H formulated in specific longitudinal direction due to the characteristic shape of CNTs. In addition, they shortened the *d*-spacing by cross-linking the interlayer of the C-(A)-S-H. Therefore, the shoulder was not significantly visible in the SAXS profile for the UHPC/CNT (Fig. 7-8a) and denser and stiffer structure explains the increase of the compressive strength and elastic modulus, even with the lower DOH in the UHPC/CNT (See Chapter 6.). The *d*-spacing of the samples was calculated to 16.88–19.03, which values were greater than that of C-S-H for OPC which was found to be about 1–2 nm. This is because the polycarboxylate superplasticizer was used to fabricate UHPC composites. Incorporating superplasticizer can allow different modes of steric arrangement of the copolymer in the interlayer of C-S-H due to the high polydispersity. as a result, a low and irregular stacking order of the layered double hydroxides can be expected, which result in increase in the *d*-spacing [137].

Between the samples containing CNTs, the UHPC/CNT-EC showed better results in most of the conducted tests compared to those of the UHPC/CNT-SC. These included a higher compressive strength and elastic modulus in the mechanical test, a higher DOH in TGA,

more existence of cross-linking sites of Q^3 and $Q^3(1Al)$ in ^{29}Si NMR, and higher D_V and D_S and smaller R_C in SAXS. This consistent result confirms more efficient hydration by the applied EC . Specifically, an electric field constructed by the applied voltage made the ionic polarization of various components active and the state of the ions unstable, resulting in a further accelerated chemical reaction for the hydration.

In summary, dispersed CNTs in UHPC slightly hindered the hydration reaction, but they contributed to the micro- and meso-structural modification of the C-(A)-S-H. This modification increased the fractal dimension and occurrence of partial cross-linking in the C-(A)-S-H along with reducing *d*-spacing of interlayer of C-S-H. such behavior was more significant when the EC was applied. This result well explained the enhanced mechanical performance of UHPC/CNT and the efficiency of the EC.

7.5 Conclusions

In this chapter, followed by chapter 6, effects of CNTs on micro- and meso-structural modifications of UHPC were investigated along with the feasibility for EC based on examinations of XRD, TG, solid-state ^{29}Si NMR, and SAXS analyses. Based on the experimental results and analyses, the following conclusions can be drawn:

1) The incorporation of dispersed CNTs close to CIC into UHPC slightly hindered the hydration reaction measured at 28 d by reducing the contact area of the binders due to their geometric shapes. In addition, hydration acceleration at early ages due to nucleation effect owing to incorporation of nano sized CNTs led to lower level of pozzolanic reaction which result in lower degree of DOH and DOR at later ages.

2) However, CNTs made the structure of the main hydration product of C-(A)-S-H more complex as the hydration products developed along the CNTs in the longitudinal direction. In addition, partial cross-linked the interlayer between silicate chains of the C-(A)-S-H was observed under the presence of the CNTs. As a result, the micro- and meso-structural modification of the C-(A)-S-H led the enhanced engineering properties of UHPC/CNT.

3) For the UHPC/CNT cured by EC showed even more structural changes compared to the case of UHPC/CNT cured by SC. The electrical field formed in the matrix during EC likely activated ionic polarization and accelerated the chemical reaction among ions, resulting in a higher DOH and DOR. This electrically-driven changes in the chemical reaction of UHPC made further modification of micro- and meso-scale structure of the C-(A)-S-H (i.e., more cross-linking sites and higher fractal dimensions) towards improved engineering properties of the UHPC/CNT composite.

Based on these results, it can be proposed that UHPC can be sufficiently manufactured in field construction by incorporating CNTs and applying EC. Along with the application of the UHPC, the reported curing method and CNTs based structural modification can be further implemented to enhance various properties such as mechanical and electrical performances of structural materials.

Chapter 8. Conclusions

Demand for hybrid concrete for multi-functional applications such as superb mechanical strength, EMI Shielding and SHM are increasing. UHPC exhibits excellent mechanical strength, but is insufficient for multi-functional applications and limited to produce on-site. Hence, for developing multi-functional UHPC with EMI SE and damage sensing capabilities for SHM and enabling production of UHPC on-site, CNTs, selected as a key material, were incorporated into UHPC. Then, UHPC embedded with CNTs was investigated with regard to dispersion, mechanical performance, EMI SE, crack sensing capabilities, electrical curing, and microstructural modifications. Based on the experimental results and analyses, the following conclusions can be drawn.

In chapter 3, ozone treatment was applied to CNTs for the first time as a dispersion method and its impact on dispersion of CNTs and hydration of UHPC were investigated. The results confirmed that ozone treatment is an effective method that can not only prevent CNT damaging, which is one of the weakness of sonication, but also simply disperse CNTs within aqueous solution and UHPC even without using specified equipment required for plasma oxidation. Oxygenic and carboxylic chemical groups, which are formulated by ozone treatment, functionalized the surface of the CNTs and enveloped the cementitious grains, which increasing the DOD of CNTs and interfacial interaction between CNTs and UHPC. Ozone treatment itself did not significantly modify the general hydration of UHPC. Instead, it provided multiple nucleation sites and double steric repulsion thorough the improved degree of dispersion of CNTs that resulted in accelerated hydration at early ages, as well as improved compressive strength at later ages.

In chapter 4, six different content of dispersed CNT suspensions were fabricated by sonication and shear mixing with superplasticizer, a

proposed method for dispersing high content of CNTs in UHPC. Then, UHPC/CNT composites were manufactured using the suspensions and their mechanical properties were investigated with respect to CNT content. The proposed dispersion method increased the flowability of the UHPC/CNT composites enough to mixing compared to that produced by just sonication. In addition, it was effective to disperse CNTs within both an aqueous solution and UHPC composite up to the CIC. Conducted experiments revealed that CNT content below the CIC improve the mechanical properties of UHPC through pore filling, bridging, and densification of C-S-H structure, whereas CNT content above CIC weakens the properties due to agglomeration of CNTs, suppression of hydration, and increase in air-voids.

In chapter 5, the role of CNTs on EMI Shielding of UHPC were examined. It was found that dispersed CNTs remarkably improved the electrical conductivity and resulting SE of UHPC up to the percolation threshold. Two testing methods for SE (ASTM D4935-18 and IEEE-STD-299) verified the result and suggested that ASTM D4935-18 can only be used to evaluate a rough trend of SE, and IEEE-STD-299 using the samples with sufficient incident area size at least 1200 × 1200 mm^2 should be considered to accurately evaluate the SE. According to the statistical analysis of the experimental results, a practical model to effectively estimate the SE of cementitious materials (especially UHPC) was proposed.

In chapter 6, effects of CNTs on UHPC were investigated in terms of EC, mechanical properties, and crack sensing. The addition of CNTs significantly decreased electrical resistivity of the UHPC, enabling EC at low voltages; improved mechanical properties via bridging, pore filling, and C-S-H stiffening effects; and influenced the deflection hardening behavior under flexural stress. Furthermore, the UHPC/CNT under compressive or flexural stress exhibited significant crack sensing capabilities due to the obtained low resistivity. A dramatic FCR value of

the UHPC/CNT can represent the failure under compression or first cracking under flexure. Therefore, it was verified that the UHPC/CNT can extend the applications of UHPC especially for on-site casting and structural crack sensors for UHPC-based structures.

In chapter 7, how CNTs modify the structure of the UHPC has been experimented at the micro- and meso-scale level. The dispersed CNTs slightly hindered the hydration reaction of the UHPC, however they significantly modified the structure of C-(A)-S-H to be denser, stiffer, and more complex which have been evidenced by observed partial cross-linking in the C-(A)-S-H, significantly reduced *d*-spacing and the higher fractal dimensions of solid system. Such behaviors were much more remarkable when EC was applied because the electrical field formed by EC activated ionic polarization and accelerated the chemical reaction among ions, resulting in a higher degree of hydration.

Based on the studies of chapters 3 and 4, comparison between the typical and proposed CNT dispersion methods are listed in Table 8-1. The proposed methods significantly improved the previous methods and overcame their major limitations in dispersing CNTs in UHPC. Ozone treatment improved the complex process to disperse CNTs, which is the key weakness of plasma oxidation. It can simply and promptly disperse CNTs within both aqueous solution and UHPC without damaging CNTs using a portable ozone generator. The other proposed CNT dispersion method, sonication and subsequent shear mixing with SP improve flow reduction of fresh cementitious materials, a key drawback of sonication with superplasticizer. The superplasticizer, added later and shear mixed with CNTs, not only improve the stability of dispersion by coating the CNTs, dispersed by sonication, but also is not adsorbed by CNTs, causing activation interfacial interaction to increase flow. Increase in fluidity allows dispersion of CNTs in UHPC that apply small w/c less than 0.25 even while maintaining appropriate workability.

Table 8-1. Comparison between typical and proposed CNT dispersion methods.

	Typical dispersion methods	Proposed dispersion methods
Method	Plasma oxidation	Ozone treatment
Strength	No damage	No damage, Simple process, No need for specific equipment, Eco-friendly
Weakness	Complex process, Need for specific equipment, Harmful for environment limited to small dosage of CNTs,	limited to small dosage of CNTs
Method	Sonication with superplasticizer (SP)	Sonication + Shear mixing with SP
Strength	Disperse high dosage of CNTs	Disperse high dosage of CNTs Increasing interfacial interaction, Increasing flowability
Weakness	Possibility of damaging of CNTs, Decreasing interfacial interaction, Decreasing flowability	Possibility of damaging of CNTs

Dispersed CNTs significantly improve the mechanical properties of the UHPC by filling pores, bridging adjacent UHPC particles and CNTs, and stiffening the C-(A)-S-H due to crosslinking of interlayer in C-(A)-S-H although they partially hinder the hydration of UHPC by absorbing water molecules, covering the surfaces of clinkers, and complexly developing the main hydration product C-(A)-S-H. However, excessive amount of CNTs, close to CIC or percolation threshold, increases the proportion of air-voids due to the decrease in the flow, hinders the hydration of UHPC, and acts as pores and cracks due to agglomeration leading to decrease in the mechanical properties.

Incorporation of dispersed CNTs into UHPC within percolation threshold remarkably decreases the electrical resistivity and improves the electrical conductivity of UHPC. Thus, a low level of resistivity enables EC at low voltages using heat generated by the joule effect and can realize the UHPC production with higher mechanical strength in the field. In addition, conductive UHPC can be used as a shield to protect the facilities from invasive EM waves. Furthermore, it can also be used as structural crack sensors for SHM by using FCR values that vary significantly when cracking.

In order to implement specific functions in UHPC by applying CNTs, the ideal mixture design according to CNT dispersion method and its properties focused on compressive strength are presented in the Tab based on the various mixture proportions used in this thesis. Incorporation of CNTs in UHPC increases compressive strength approximately 5–10%. CNTs are still expensive material, although mass production has made it much more realistic. Thus, applying CNTs to UHPC for the purpose of increasing this range of mechanical properties may be uneconomical. However, considering functions such as EMI shielding, crack self-sensing, and EC that are additionally obtained due to application of CNTs, it can be regarded to be more economical. For example, UHPC produced in the field by applying EC exhibits much higher compressive strength than that cured without high temperature curing, thus reducing the structural cross-section and therefore saving construction costs. In addition, compared to precast construction, it is possible to reduce the cost of equipment for SC, production at factory, and transportation while exerting the same or higher performance. Besides, UHPC with EMI shielding and crack self-sensing can save the cost of constructing separate facilities for these functions.

Table 8-2. Ideal mix design of UHPC/CNT composites for exhibiting specific performance, and its compressive strength.

Required performance	Mixture proportion (wt.% of cement)						Compressive strength (MPa)	Remark
	w/c	UHPC mixture	Super plasticizer	CNTs		Curing method		
				Content	Dispersion			
Mechanical #1	0.23	1	0.05	0.001	Ozone treatment	MC	**158.4 (9.8 % ↑)**	Ref. (144.2 MPa)
Mechanical #2	0.23	1	0.04	0.005	Sonication & Shear mixing	SC	**188.4 (5.5 % ↑)**	Ref. (178.6 MPa)
EMI SE	0.23	1	0.04	0.010	Sonication & Shear mixing	SC	**177.1 (0.8 % ↓)**	SE_{10kHz} : 17.2 dB SE_{1GHz} : 47.1 dB
Field casting or Crack sensing	0.24	1	0.05	0.012	Pre-dispersed suspension	SC or EC	**191.1–196.6 (5.5–8.6 % ↑)**	Ref. (181.1 MPa) Including 2 vol.% of steel fibers

[Note] MC : Moisture curing at 20 ℃ and RH of 60 %, SC : Steam curing at 90 ℃ and RH of 95 %, and EC : Electrical curing under low voltages of 19–23 V at 20 ℃ and RH of 95 % (initial condition)

In conclusion, incorporating appropriate amount of CNTs into UHPC using the proposed dispersion methods can overcome the limitation of UHPC and produce multi-functional UHPC with EMI SE and crack sensing capabilities on-site using EC.

Reference

[1] C. Beall, E. Delzell, P. Cole, I. Brill, Brain Tumors among Electronics Industry Workers, Epidemiology, 7 (1996) 125-130.

[2] J.K. Grayson, Radiation Exposure, Socioeconomic Status, and Brain Tumor Risk in the US Air Force: A Nested Case-Control Study, American Journal of Epidemiology, 143 (1996) 480-486.

[3] S. Szmigielski, Cancer morbidity in subjects occupationally exposed to high frequency (radiofrequency and microwave) electromagnetic radiation, Science of The Total Environment, 180 (1996) 9-17.

[4] T.L. Thomas, P.D. Stolley, A. Stemhagen, E.T.H. Fontham, M.L. Bleecker, P.A. Stewart, R.N. Hoover, Brain Tumor Mortality Risk Among Men With Electrical and Electronics Jobs: A Case-Control Study, JNCI: Journal of the National Cancer Institute, 79 (1987) 233-238.

[5] I. You, D.-Y. Yoo, S. Kim, M.-J. Kim, G. Zi, Electrical and Self-Sensing Properties of Ultra-High-Performance Fiber-Reinforced Concrete with Carbon Nanotubes, Sensors, 17 (2017).

[6] F. Naeem, H.K. Lee, H.K. Kim, I.W. Nam, Flexural stress and crack sensing capabilities of MWNT/cement composites, Composite Structures, 175 (2017) 86-100.

[7] P. Richard, M. Cheyrezy, Composition of reactive powder concretes, Cement and Concrete Research, 25 (1995) 1501-1511.

[8] Z. Hajar, D. Lecointre, A. Simon, J. Petitjean, Design and construction of the world first ultra-high performance concrete road

bridges, Proceedings of the Int. Symp. on UHPC, Kassel, Germany, 2004, pp. 39-48.

[9] D.-Y. Yoo, Y.-S. Yoon, A Review on Structural Behavior, Design, and Application of Ultra-High-Performance Fiber-Reinforced Concrete, International Journal of Concrete Structures and Materials, 10 (2016) 125-142.

[10] B. Han, L. Zhang, J. Ou, Smart and multifunctional concrete toward sustainable infrastructures, Springer, Singapore, 2017, pp. 247-400.

[11] D.D.L. Chung, Electromagnetic interference shielding effectiveness of carbon materials, Carbon, 39 (2001) 279-285.

[12] A.C. 239, ACI 239R-18 Ultra-High-Performance Concrete: An Emerging Technology Report, American Concrete Institute2018.

[13] Ultra High Performance Fibre-Reinforced Concretes, Interim Recommendation, (2002).

[14] S.-H. Kang, J.-H. Lee, S.-G. Hong, J. Moon, Microstructural Investigation of Heat-Treated Ultra-High Performance Concrete for Optimum Production, Materials, 10 (2017).

[15] D. Cecini, S.A. Austin, S. Cavalaro, A. Palmeri, Accelerated electric curing of steel-fibre reinforced concrete, Construction and Building Materials, 189 (2018) 192-204.

[16] T.K. Erdem, L. Turanli, T.Y. Erdogan, Setting time: An important criterion to determine the length of the delay period before steam curing of concrete, Cement and Concrete Research, 33 (2003) 741-745.

[17] J.D. McIntosh, Electrical curing of concrete, Magazine of Concrete Research, 1 (1949) 21-28.

[18] S. Bredenkamp, K. Kruger, G.L. Bredenkamp, Direct electric curing of concrete, Magazine of Concrete Research, 45 (1993) 71-

74.

[19] I. Heritage, Direct electric curing of mortar and concrete, Edinburgh Napier University, 2001.

[20] T.C. Madhavi, S. Annamalai, ELECTRICAL CONDUCTIVITY OF CONCRETE, ARPN Journal of Engineering and Applied Sciences, 11 (2016) 5979-5982.

[21] S. Iijima, T. Ichihashi, Single-shell carbon nanotubes of 1-nm diameter, Nature, 363 (1993) 603-605.

[22] D.S. Bethune, C.H. Kiang, M.S. de Vries, G. Gorman, R. Savoy, J. Vazquez, R. Beyers, Cobalt-catalysed growth of carbon nanotubes with single-atomic-layer walls, Nature, 363 (1993) 605-607.

[23] D.D.L. Chung, Carbon Composites, Butterworth-Heinemann, Cambridge, MA, 2017, pp. 333-386.

[24] I.W. Nam, S.M. Park, H.K. Lee, L. Zheng, Mechanical properties and piezoresistive sensing capabilities of FRP composites incorporating CNT fibers, Composite Structures, 178 (2017) 1-8.

[25] B. Han, K. Zhang, X. Yu, Enhance the Thermal Storage of Cement-Based Composites With Phase Change Materials and Carbon Nanotubes, Journal of Solar Energy Engineering, 135 (2013) 1-5.

[26] S.P. Shah, M.S. Konsta-Gdoutos, Uncoupling Modulus of Elasticity and Strength, Concrete International, 39 (2017) 37-42.

[27] M.S. Konsta-Gdoutos, Z.S. Metaxa, S.P. Shah, Highly dispersed carbon nanotube reinforced cement based materials, Cem. Concr. Res., 40 (2010) 1052-1059.

[28] S. Parveen, S. Rana, R. Fangueiro, M.C. Paiva, Microstructure and mechanical properties of carbon nanotube reinforced cementitious composites developed using a novel dispersion technique, Cem. Concr. Res., 73 (2015) 215-227.

[29] A.J.N. MacLeod, F.G. Collins, W. Duan, W.P. Gates, Quantitative microstructural characterisation of Portland cement-carbon nanotube composites using electron and x-ray microscopy, Cem. Concr. Res., 123 (2019) 105767.

[30] D.D.L. Chung, Carbon materials for structural self-sensing, electromagnetic shielding and thermal interfacing, Carbon, 50 (2012) 3342-3353.

[31] M. Jung, Y. Lee, S. Hong, Effect of Incident Area Size on Estimation of EMI Shielding Effectiveness for Ultra-High Performance Concrete With Carbon Nanotubes, IEEE Access, 7 (2019) 183105-183117.

[32] M.J. Jung, Y.S. Lee, S.G. Hong, Study on Improvement in Electromagnetic Interference Shielding Effectiveness of Ultra-High Performance Concrete (UHPC) / Carbon Nanotube (CNT) Composites, Journal of the Korea Concrete Institute, 31 (2019) 69-77.

[33] G.M. Kim, S.M. Park, G.U. Ryu, H.K. Lee, Electrical characteristics of hierarchical conductive pathways in cementitious composites incorporating CNT and carbon fiber, Cement and Concrete Composites, 82 (2017) 165-175.

[34] D.-Y. Yoo, I. You, S.-J. Lee, Electrical and piezoresistive sensing capacities of cement paste with multi-walled carbon nanotubes, Archives of Civil and Mechanical Engineering, 18 (2018) 371-384.

[35] J.G. Wilson, N.K. Gupta, Equipment for the investigation of the accelerated curing of concrete using direct electrical conduction, Measurement, 35 (2004) 243-250.

[36] H.K. Kim, I.W. Nam, H.K. Lee, Enhanced effect of carbon nanotube on mechanical and electrical properties of cement composites by incorporation of silica fume, Composite Structures, 107 (2014) 60-69.

[37] M. Jung, Y.-s. Lee, S.-G. Hong, J. Moon, Carbon nanotubes (CNTs) in ultra-high performance concrete (UHPC): Dispersion, mechanical properties, and electromagnetic interference (EMI) shielding effectiveness (SE), Cement and Concrete Research, 131 (2020) 106017.

[38] Z. Chen, J.L.G. Lim, E. Yang, Ultra high performance cement-based composites incorporating low dosage of plasma synthesized carbon nanotubes, Mater. Des., 108 (2016) 479-487.

[39] E. Dujardin, T.W. Ebbesen, H. Hiura, K. Tanigaki, Capillarity and Wetting of Carbon Nanotubes, Science, 265 (1994) 1850-1852.

[40] Y. Homma, S. Chiashi, T. Yamamoto, K. Kono, D. Matsumoto, J. Shitaba, S. Sato, Photoluminescence Measurements and Molecular Dynamics Simulations of Water Adsorption on the Hydrophobic Surface of a Carbon Nanotube in Water Vapor, Physical Review Letters, 110 (2013) 157402.

[41] S. Wen, D.D.L. Chung, Partial replacement of carbon fiber by carbon black in multifunctional cement–matrix composites, Carbon, 45 (2007) 505-513.

[42] W. Dong, W. Li, L. Shen, D. Sheng, Piezoresistive behaviours of carbon black cement-based sensors with layer-distributed conductive rubber fibres, Mater. Des., 182 (2019) 108012.

[43] M. Rupasinghe, P. Mendis, T. Ngo, T.N. Nguyen, M. Sofi, Compressive strength prediction of nano-silica incorporated cement systems based on a multiscale approach, Mater. Des., 115 (2017) 379-392.

[44] J. Cha, S. Jin, J.H. Shim, C.S. Park, H.J. Ryu, S.H. Hong, Functionalization of carbon nanotubes for fabrication of CNT/epoxy nanocomposites, Mater. Des., 95 (2016) 1-8.

[45] K. Yang, Z. Yi, Q. Jing, R. Yue, W. Jiang, D. Lin, Sonication-assisted dispersion of carbon nanotubes in aqueous solutions of the

anionic surfactant SDBS: The role of sonication energy, Chinese Science Bulletin, 58 (2013) 2082-2090.

[46] L.J. da Silva, T.H. Panzera, L.M.G. Vieira, J.G. Duduch, C.R. Bowen, J.C. Campos Rubio, Carbon nanotubes and superplasticizer reinforcing cementitious composite for aerostatic porous bearing, Proceedings of the Institution of Mechanical Engineers, Part J: Journal of Engineering Tribology, 231 (2017) 1397-1407.

[47] S. Alrekabi, A.B. Cundy, A. Lampropoulos, R.L.D. Whitby, I. Savina, Effect of high-intensity sonication on the dispersion of carbon-based nanofilaments in cementitious composites, and its impact on mechanical performance, Mater. Des., 136 (2017) 223-237.

[48] M.R. Irshidat, M.H. Al-Saleh, H. Almashagbeh, Effect of carbon nanotubes on strengthening of RC beams retrofitted with carbon fiber/epoxy composites, Mater. Des., 89 (2016) 225-234.

[49] K. Lu, R. Lago, Y. Chen, M. Green, P. Harris, S. Tsang, Mechanical damage of carbon nanotubes by ultrasound, Carbon, 34 (1996) 814-816.

[50] A. Sobolkina, V. Mechtcherine, V. Khavrus, D. Maier, M. Mende, M. Ritschel, A. Leonhardt, Dispersion of carbon nanotubes and its influence on the mechanical properties of the cement matrix, Cem. Concr. Comp., 34 (2012) 1104-1113.

[51] I.W. Nam, KIM, H. K., Lee, H. K., Investigation of high-strength and electromagnetic wave shielding properties of a mortar incorporating carbon nanotube (CNT), IV European conference on computational mechanics (ECCM IV)Paris, France, 2010.

[52] F. Sanchez, K. Sobolev, Nanotechnology in concrete – A review, Construction and Building Materials, 24 (2010) 2060-2071.

[53] C. Chen, B. Liang, A. Ogino, X. Wang, M. Nagatsu, Oxygen Functionalization of Multiwall Carbon Nanotubes by Microwave-

Excited Surface-Wave Plasma Treatment, The Journal of Physical Chemistry C, 113 (2009) 7659-7665.

[54] C. Chen, A. Ogino, X. Wang, M. Nagatsu, Plasma treatment of multiwall carbon nanotubes for dispersion improvement in water, Applied Physics Letters, 96 (2010) 131504.

[55] F. Morales-Lara, M.J. Pérez-Mendoza, D. Altmajer-Vaz, M. García-Román, M. Melguizo, F.J. López-Garzón, M. Domingo-García, Functionalization of Multiwall Carbon Nanotubes by Ozone at Basic pH. Comparison with Oxygen Plasma and Ozone in Gas Phase, The Journal of Physical Chemistry C, 117 (2013) 11647-11655.

[56] Q. Zhang, J. Wu, L. Gao, T. Liu, W. Zhong, G. Sui, G. Zheng, W. Fang, X. Yang, Dispersion stability of functionalized MWCNT in the epoxy–amine system and its effects on mechanical and interfacial properties of carbon fiber composites, Mater. Des., 94 (2016) 392-402.

[57] ASTM D4935-18 Standard Test Method for Measuring the Electromagnetic Shielding Effectiveness of Planar Materials, 2018.

[58] ASTM E1851-15 Standard Test Method for Electromagnetic Shielding Effectiveness of Durable Rigid Wall Relocatable Structures.

[59] MIL-STD-188-125-1 High-Altitude EMP Protection for Fixed Ground-Based Facilities, 2005.

[60] IEEE-STD-299 IEEE Standard Method for Measuring the Effectiveness of Electromagnetic Shielding Enclosures, 2007.

[61] I.W. Nam, H.K. Lee, J.B. Sim, S.M. Choi, Electromagnetic Characteristics of Cement Matrix Materials with Carbon Nanotubes, ACI Materials Journal, 109 (2012) 363-370.

[62] I.W. Nam, H.K. Kim, H.K. Lee, Influence of silica fume additions

on electromagnetic interference shielding effectiveness of multi-walled carbon nanotube/cement composites, Construction and Building Materials, 30 (2012) 480-487.

[63] A.P. Singh, B.K. Gupta, M. Mishra, Govind, A. Chandra, R.B. Mathur, S.K. Dhawan, Multiwalled carbon nanotube/cement composites with exceptional electromagnetic interference shielding properties, Carbon, 56 (2013) 86-96.

[64] B. Wang, Z. Guo, Y. Han, T. Zhang, Electromagnetic wave absorbing properties of multi-walled carbon nanotube/cement composites, Construction and Building Materials, 46 (2013) 98-103.

[65] D. Micheli, R. Pastore, A. Vricella, R.B. Morles, M. Marchetti, A. Delfini, F. Moglie, V.M. Primiani, Electromagnetic characterization and shielding effectiveness of concrete composite reinforced with carbon nanotubes in the mobile phones frequency band, Materials Science and Engineering: B, 188 (2014) 119-129.

[66] J. Chen, D. Zhao, H. Ge, J. Wang, Graphene oxide-deposited carbon fiber/cement composites for electromagnetic interference shielding application, Construction and Building Materials, 84 (2015) 66-72.

[67] J.M. Chiou, Q. Zheng, D.D.L. Chung, Electromagnetic interference shielding by carbon fibre reinforced cement, Composites, 20 (1989) 379-381.

[68] Y. Dai, M. Sun, C. Liu, Z. Li, Electromagnetic wave absorbing characteristics of carbon black cement-based composites, Cem. Concr. Comp., 32 (2010) 508-513.

[69] X. Fu, D.D.L. Chung, Submicron carbon filament cement-matrix composites for electromagnetic interference shielding, Cem. Concr. Res., 26 (1996) 1467-1472.

[70] H. Guan, S. Liu, Y. Duan, J. Cheng, Cement based electromagnetic shielding and absorbing building materials, Cem. Concr. Comp., 28

(2006) 468-474.

[71] F. Azhari, N. Banthia, Cement-based sensors with carbon fibers and carbon nanotubes for piezoresistive sensing, Cement and Concrete Composites, 34 (2012) 866-873.

[72] I.W. Nam, H. Souri, H.K. Lee, Percolation threshold and piezoresistive response of multi-wall carbon nanotube/cement composites, Smart Structures and Systems, 18 (2016) 217-231.

[73] S.-J. Lee, I. You, G. Zi, D.-Y. Yoo, Experimental Investigation of the Piezoresistive Properties of Cement Composites with Hybrid Carbon Fibers and Nanotubes, Sensors, 17 (2017).

[74] M. Saafi, Wireless and embedded carbon nanotube networks for damage detection in concrete structures, Nanotechnology, 20 (2009) 395502.

[75] X. Yu, E. Kwon, A carbon nanotube/cement composite with piezoresistive properties, Smart Materials and Structures, 18 (2009) 055010.

[76] B. Han, X. Yu, E. Kwon, J. Ou, Effects of CNT concentration level and water/cement ratio on the piezoresistivity of CNT/cement composites, Journal of Composite Materials, 46 (2011) 19-25.

[77] S.H. Lee, S.H. Kim, D.Y. Yoo, Hybrid effects of steel fiber and carbon nanotube on self-sensing capability of ultra-high-performance concrete, Construction and Building Materials, 185 (2018) 530-544.

[78] G.M. Kim, B.J. Yang, G.U. Ryu, H.K. Lee, The electrically conductive carbon nanotube (CNT)/cement composites for accelerated curing and thermal cracking reduction, Composite Structures, 158 (2016) 20-29.

[79] J.G. Wilson, N.K. Gupta, Analysis of power distribution in reinforced concrete during accelerated curing using electroheat, IEE

Proceedings - Electric Power Applications, 143 (1996) 172-176.

[80] Y. Jeong, C.W. Hargis, S.-C. Chun, J. Moon, The effect of water and gypsum content on strätlingite formation in calcium sulfoaluminate-belite cement pastes, Construction and Building Materials, 166 (2018) 712-722.

[81] K. Scrivener, R. Snellings, B. Lothenbach, A Practical Guide to Microstructural Analysis of Cementitious Materials, Taylor & Francis, 2016.

[82] P. Bernadó, D.I. Svergun, Structural analysis of intrinsically disordered proteins by small-angle X-ray scattering, Molecular BioSystems, 8 (2012) 151-167.

[83] ASTM C1856, Standard Practice for Fabricating and Testing Specimens of Ultra-High Performance Concrete, 2017.

[84] H. von Daake, D. Stephan, Setting of cement with controlled superplasticizer addition monitored by ultrasonic measurements and calorimetry, Cem. Concr. Comp., 66 (2016) 24-37.

[85] A. Zingg, F. Winnefeld, L. Holzer, J. Pakusch, S. Becker, R. Figi, L. Gauckler, Interaction of polycarboxylate-based superplasticizers with cements containing different C3A amounts, Cem. Concr. Comp., 31 (2009) 153-162.

[86] P.K. Mehta, P.J.M. Monteiro, Concrete: Microstructure, Properties, and Materials, McGraw-Hill Education, 2013.

[87] B. Han, K. Zhang, X. Yu, E. Kwon, J. Ou, Fabrication of piezoresistive CNT/CNF cementitious composites with superplasticizer as dispersant, Journal of Materials in Civil Engineering, 24 (2012) 658-665.

[88] B. Lothenbach, K. Scrivener, R.D. Hooton, Supplementary cementitious materials, Cem. Concr. Res., 41 (2011) 1244-1256.

[89] J.M. Makar, G.W. Chan, Growth of Cement Hydration Products on

Single-Walled Carbon Nanotubes, Journal of the American Ceramic Society, 92 (2009) 1303-1310.

[90] T. Manzur, N. Yazdani, M.A.B. Emon, Potential of Carbon Nanotube Reinforced Cement Composites as Concrete Repair Material, Journal of Nanomaterials, 2016 (2016) 10.

[91] B.Z. Dilnesa, B. Lothenbach, G. Renaudin, A. Wichser, E. Wieland, Stability of Monosulfate in the Presence of Iron, Journal of the American Ceramic Society, 95 (2012) 3305-3316.

[92] S. Mindess, J.F. Young, Concrete, Prentice-Hall, 1981.

[93] B. Zou, S.J. Chen, A.H. Korayem, F. Collins, C.M. Wang, W.H. Duan, Effect of ultrasonication energy on engineering properties of carbon nanotube reinforced cement pastes, Carbon, 85 (2015) 212-220.

[94] A.H. Korayem, N. Tourani, M. Zakertabrizi, A.M. Sabziparvar, W.H. Duan, A review of dispersion of nanoparticles in cementitious matrices: Nanoparticle geometry perspective, Construction and Building Materials, 153 (2017) 346-357.

[95] S. Mondal, L. Nayak, M. Rahaman, A. Aldalbahi, T.K. Chaki, D. Khastgir, N.C. Das, An effective strategy to enhance mechanical, electrical, and electromagnetic shielding effectiveness of chlorinated polyethylene-carbon nanofiber nanocomposites, Composites Part B: Engineering, 109 (2017) 155-169.

[96] R. Perez, Handbook of Electromagnetic Compatibility, Academic Press, San Diego, 1995, pp. 401-443.

[97] S. Loya, Analysis of Shielding Effectiveness in the Electric Field and Magnetic Field and Plane Wave for Infinite Sheet Metals, 2016.

[98] L. Sandrolini, U. Reggiani, A. Ogunsola, Modelling the electrical properties of concrete for shielding effectiveness prediction, Journal of Physics D: Applied Physics, 40 (2007) 5366-5372.

[99] T. Bourdi, J.E. Rhazi, F. Boone, G. Ballivy, Modelling dielectric-constant values of concrete: an aid to shielding effectiveness prediction and ground-penetrating radar wave technique interpretation, Journal of Physics D: Applied Physics, 45 (2012) 405401.

[100] Polar molecules. By P. Debye, Ph.D., Pp. 172. New York: Chemical Catalog Co., Inc., 1929. $ 3.50, Journal of the Society of Chemical Industry, 48 (1929) 1036-1037.

[101] T. Bourdi, J.E. Rhazi, F. Boone, G. Ballivy, Application of Jonscher model for the characterization of the dielectric permittivity of concrete, Journal of Physics D: Applied Physics, 41 (2008) 205410.

[102] H. Xu, B. Li, S. Xu, H. Feng, The Measurement of Dielectric Constant of the Concrete Using Single-Frequency CW Radar, 2008 First International Conference on Intelligent Networks and Intelligent Systems, 2008, pp. 588-591.

[103] S.K. Yee, M.Z.M. Jenu, Shielding effectiveness of concrete with graphite fine powder in between 50MHz to 400MHz, 2013 Asia-Pacific Symposium on Electromagnetic Compatibility (APEMC), 2013, pp. 1-4.

[104] K.L. Kaiser, Electromagnetic Compatibility Handbook, Taylor & Francis2004.

[105] H.W. Ott, Electromagnetic Compatibility Engineering, Wiley2009.

[106] A. D'Alessandro, M. Rallini, F. Ubertini, A.L. Materazzi, J.M. Kenny, Investigations on scalable fabrication procedures for self-sensing carbon nanotube cement-matrix composites for SHM applications, Cement and Concrete Composites, 65 (2016) 200-213.

[107] D.D.L. Chung, Self-heating structural materials, Smart Materials and Structures, 13 (2004) 562-565.

[108] S. Vaidya, E.N. Allouche, Strain sensing of carbon fiber reinforced geopolymer concrete, Materials and Structures, 44 (2011) 1467-1475.

[109] S. Wang, S. Wen, D.D.L. Chung, Resistance heating using electrically conductive cements, Advances in Cement Research, 16 (2004) 161-166.

[110] F. Reza, J.A. Yamamuro, G.B. Batson, Electrical resistance change in compact tension specimens of carbon fiber cement composites, Cem. Concr. Comp., 26 (2004) 873-881.

[111] Standard Test Method for Flow of Hydraulic Cement Mortar, 2015.

[112] Standard Practice for Fabricating and Testing Specimens of Ultra-High Performance Concrete, 2017.

[113] F.-C. Chiu, A Review on Conduction Mechanisms in Dielectric Films, Advances in Materials Science and Engineering, 2014 (2014) 18.

[114] J.J. Barron, C. Ashton, The effect of temperature on conductivity measurement, TSP, 7 (2005) 1-5.

[115] Y.-H. Kwon, S.-H. Kang, S.-G. Hong, J. Moon, Intensified Pozzolanic Reaction on Kaolinite Clay-Based Mortar, Applied Sciences, 7 (2017).

[116] Y.-H. Kwon, S.-H. Kang, S.-G. Hong, J. Moon, Acceleration of Intended Pozzolanic Reaction under Initial Thermal Treatment for Developing Cementless Fly Ash Based Mortar, Materials, 10 (2017).

[117] D.K. Hardy, M.F. Fadden, M.J. Khattak, A. Khattab, Development and characterization of self-sensing CNF HPFRCC, Materials and Structures, 49 (2016) 5327-5342.

[118] K. Millrath, Modefying Concrete Matrices with Beneficiated Dredged Material Or Other Clayey Constituents, Columbia

University, 2003.

[119] D.-Y. Yoo, N. Banthia, Mechanical properties of ultra-high-performance fiber-reinforced concrete: A review, Cement and Concrete Composites, 73 (2016) 267-280.

[120] S.H. Park, D.J. Kim, G.S. Ryu, K.T. Koh, Tensile behavior of Ultra High Performance Hybrid Fiber Reinforced Concrete, Cement and Concrete Composites, 34 (2012) 172-184.

[121] H. Zanni, M. Cheyrezy, V. Maret, S. Philippot, P. Nieto, Investigation of hydration and pozzolanic reaction in Reactive Powder Concrete (RPC) using 29Si NMR, Cement and Concrete Research, 26 (1996) 93-100.

[122] J. Skibsted, H.J. Jakobsen, C. Hall, Quantification of calcium silicate phases in Portland cements by 29Si MAS NMR spectroscopy, Journal of the Chemical Society, Faraday Transactions, 91 (1995) 4423-4430.

[123] A. Peyvandi, I. Harsini, D. Holmes, A.M. Balachandra, P. Soroushian, Characterization of ASR in Concrete by Si29 MAS NMR Spectroscopy, Journal of Materials in Civil Engineering, 28 (2016) 04015096.

[124] N.K. Lee, K.T. Koh, M.O. Kim, G.S. Ryu, Uncovering the role of micro silica in hydration of ultra-high performance concrete (UHPC), Cement and Concrete Research, 104 (2018) 68-79.

[125] F. Brunet, P. Bertani, T. Charpentier, A. Nonat, J. Virlet, Application of 29Si Homonuclear and 1H−29Si Heteronuclear NMR Correlation to Structural Studies of Calcium Silicate Hydrates, The Journal of Physical Chemistry B, 108 (2004) 15494-15502.

[126] B. Wu, G. Ye, Carbonation mechanism of different kind of CSH: rate and products, Int. RILEM Conference on Materials, Systems and Structures in Civil Engineering 2016-Segment on Concrete

with Supplementary Cementitious Materials, RILEM, 2016, pp. 163-272.

[127] F. Brunet, T. Charpentier, C.N. Chao, H. Peycelon, A. Nonat, Characterization by solid-state NMR and selective dissolution techniques of anhydrous and hydrated CEM V cement pastes, Cement and Concrete Research, 40 (2010) 208-219.

[128] R.J. Myers, S.A. Bernal, R. San Nicolas, J.L. Provis, Generalized Structural Description of Calcium–Sodium Aluminosilicate Hydrate Gels: The Cross-Linked Substituted Tobermorite Model, Langmuir, 29 (2013) 5294-5306.

[129] E. Anitas, Small-Angle Scattering from Mass and Surface Fractals, 2018.

[130] A.J. Allen, J.J. Thomas, H.M. Jennings, Composition and density of nanoscale calcium–silicate–hydrate in cement, Nature Materials, 6 (2007) 311-316.

[131] H.M. Jennings, Refinements to colloid model of C-S-H in cement: CM-II, Cement and Concrete Research, 38 (2008) 275-289.

[132] A.J. Allen, J.J. Thomas, Analysis of C–S–H gel and cement paste by small-angle neutron scattering, Cement and Concrete Research, 37 (2007) 319-324.

[133] A.J. Allen, R.C. Oberthur, D. Pearson, P. Schofield, C.R. Wilding, Development of the fine porosity and gel structure of hydrating cement systems, Philosophical Magazine B, 56 (1987) 263-288.

[134] D.R. Vollet, W.A.T. de Sousa, D.A. Donatti, A. Ibañez Ruiz, Mass fractal characteristics of sonogels prepared from sonohydrolysis of tetraethoxysilane with additions of dimethylformamide, Journal of Non-Crystalline Solids, 353 (2007) 143-150.

[135] W.-S. Chiang, E. Fratini, P. Baglioni, D. Liu, S.-H. Chen,

Microstructure Determination of Calcium-Silicate-Hydrate Globules by Small-Angle Neutron Scattering, The Journal of Physical Chemistry C, 116 (2012) 5055-5061.

[136] G. Geng, R.J. Myers, M.J.A. Qomi, P.J.M. Monteiro, Densification of the interlayer spacing governs the nanomechanical properties of calcium-silicate-hydrate, Scientific Reports, 7 (2017) 10986.

[137] S. Ng, E. Metwalli, P. Müller-Buschbaum, J. Plank, Occurrence of intercalation of PCE superplasticizers in calcium aluminate cement under actual application conditions, as evidenced by SAXS analysis, Cement and Concrete Research, 54 (2013) 191-198.

[138] M. Jung, S. Hong, J. Moon, Positve Effect of Ozone Treatment on the Dispersion of Carbon Nanotubes and the Mechanical Performance of Ultra-High Performance Concrete, Mater. Des., Accepted (2020).

[139] D. Hou, Z. Lu, X. Li, H. Ma, Z. Li, Reactive molecular dynamics and experimental study of graphene-cement composites: Structure, dynamics and reinforcement mechanisms, Carbon, 115 (2017) 188-208.

[140] R.J. Myers, E. L'Hôpital, J.L. Provis, B. Lothenbach, Effect of temperature and aluminium on calcium (alumino)silicate hydrate chemistry under equilibrium conditions, Cement and Concrete Research, 68 (2015) 83-93.

[141] T.T.H. Bach, C.C.D. Coumes, I. Pochard, C. Mercier, B. Revel, A. Nonat, Influence of temperature on the hydration products of low pH cements, Cement and Concrete Research, 42 (2012) 805-817.

[142] H. Alkhateb, A. Al-Ostaz, H.D. Cheng Alexander, X. Li, Materials Genome for Graphene-Cement Nanocomposites, Journal of Nanomechanics and Micromechanics, 3 (2013) 67-77.

[143] G.Y. Li, P.M. Wang, X. Zhao, Mechanical behavior and

microstructure of cement composites incorporating surface-treated multi-walled carbon nanotubes, Carbon, 43 (2005) 1239-1245.

[144] M. Wang, R. Wang, H. Yao, S. Farhan, S. Zheng, C. Du, Study on the three dimensional mechanism of graphene oxide nanosheets modified cement, Construction and Building Materials, 126 (2016) 730-739.

Appendix

Appendix. A-1 Compressive stress-strain curves of the samples.

Samples	Mechanical properties		Experimental data						
			Average[a]	#1	#2	#3	#4	#5	#6
CNT0 (Ref.)	Compressive Strength (MPa)		178.61	164.83	177.66	183.24	179.72	178.44	179.08
	Elastic Modulus (GPa)	ASTM C469	49.1	50.79	44.43	47.37	54.78	49.14	51.96
		BS-1881-121	52.05	56.76	47.30	48.49	62.76	50.91	56.83
CNT0.2	Compressive Strength (MPa)		176.82	180.57	173.24	167.43	188.46	176.19	177.27
	Elastic Modulus (GPa)	ASTM C469	49.77	54.05	43.51	53.23	48.08	50.09	47.69
		BS-1881-121	50.49	57.34	45.67	58.04	46.42	51.28	46.94
CNT0.5	Compressive Strength (MPa)		188.37	184.93	179.07	189.43	201.34	192.73	186.40
	Elastic Modulus (GPa)	ASTM C469	54.96	55.86	59.71	54.93	55.26	52.26	53.78
		BS-1881-121	58.41	58.04	64.02	62.66	57.82	53.01	55.14
CNT0.8	Compressive Strength (MPa)		177.13	182.90	177.94	187.62	175.38	172.32	164.51
	Elastic Modulus (GPa)	ASTM C469	52.24	48.14	55.98	46.98	60.39	57.87	42.32
		BS-1881-121	55.69	49.64	60.95	48.05	64.13	67.03	46.66
CNT1.0	Compressive Strength (MPa)		169.78	172.92	170.24	168.52	167.43	178.03	162.22
	Elastic Modulus (GPa)	ASTM C469	50.25	50.13	55.32	45.70	49.84	40.35	55.43
		BS-1881-121	53.53	57.42	58.05	46.61	52.03	42.97	62.31

[a] Average = [Sum of experimental values - (Max. value + Min. value)] / No.of data

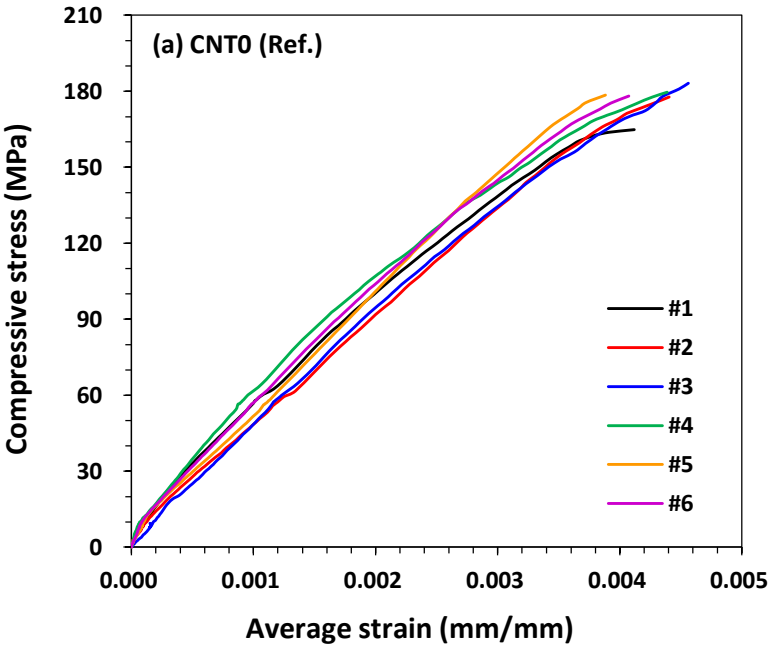
(a) CNT0 (Ref.)
Compressive stress (MPa)
Average strain (mm/mm)
0
30
60
90
120
150
180
210
0.000
0.001
0.002
0.003
0.004
0.005
#1
#2
#3
#4
#5
#6

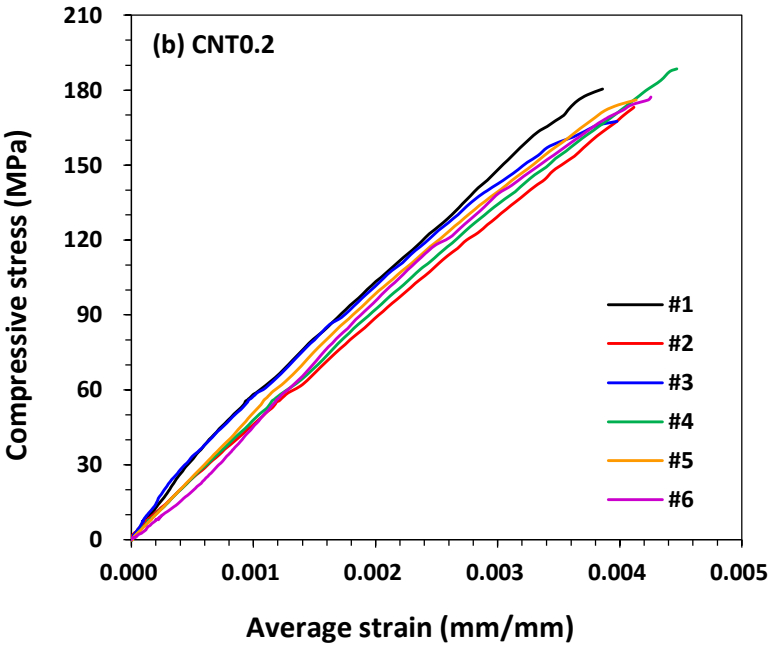
(b) CNT0.2
Compressive stress (MPa)
Average strain (mm/mm)
0
30
60
90
120
150
180
210
0.000
0.001
0.002
0.003
0.004
0.005
#1
#2
#3
#4
#5
#6

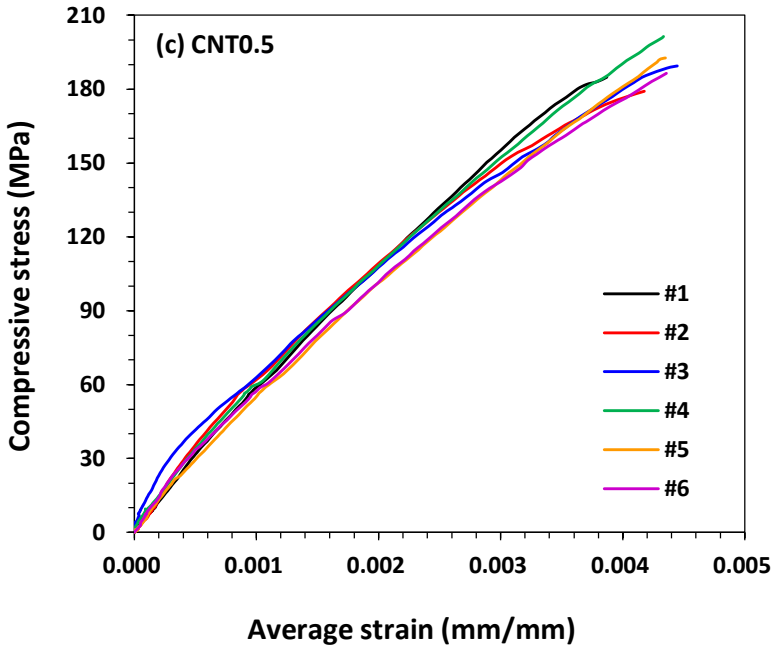
(c) CNT0.5
Compressive stress (MPa)
Average strain (mm/mm)
0
30
60
90
120
150
180
210
0.000
0.001
0.002
0.003
0.004
0.005
#1
#2
#3
#4
#5
#6

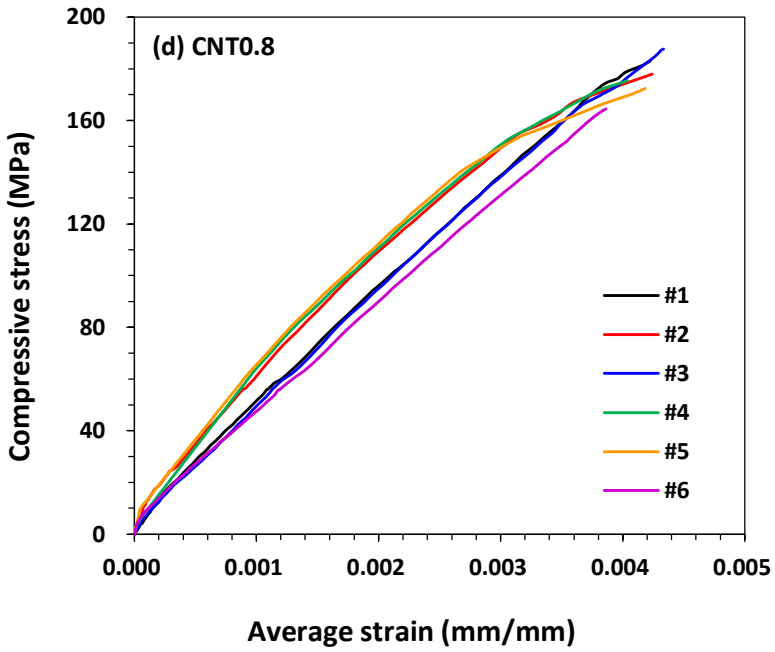
(d) CNT0.8
Compressive stress (MPa)
Average strain (mm/mm)
0
40
80
120
160
200
0.000
0.001
0.002
0.003
0.004
0.005
#1
#2
#3
#4
#5
#6

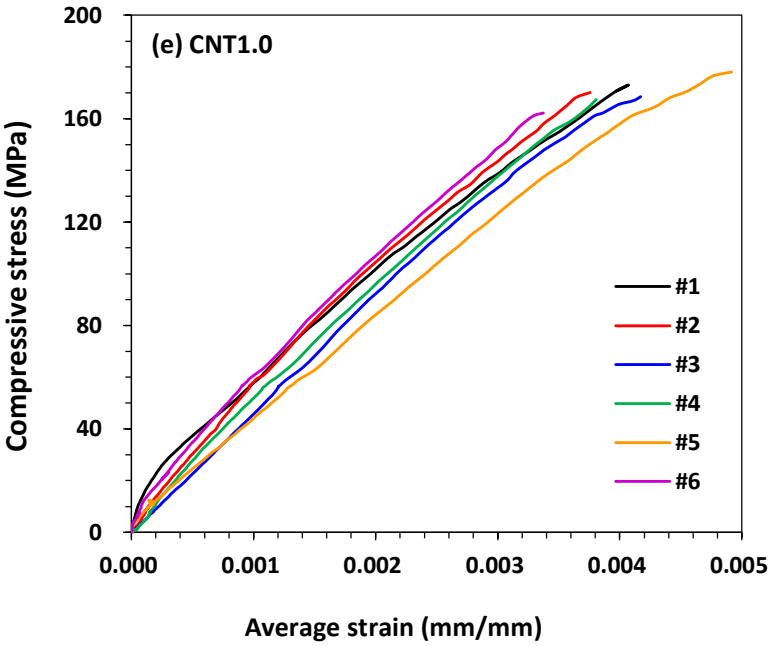
(e) CNT1.0
Compressive stress (MPa)
200
160
120
80
40
0
0.000
0.001
0.002
0.003
0.004
0.005
Average strain (mm/mm)
#1
#2
#3
#4
#5
#6

Appendix. A-2 Electrical resistance of the samples.

CNT0 (Ref.)_1 (5.39 MΩ)

CNT0 (Ref.)_2 (6.03 MΩ)

CNT0 (Ref.)_3 (6.75 MΩ)

CNT0.2_1 (394.43 kΩ)

CNT0.2_2 (385.56 kΩ)

CNT0.2_3 (474.54 kΩ)

CNT0.5_1 (11.89 kΩ)

CNT0.5_2 (12.05 kΩ)

CNT0.5_3 (12.35 kΩ)

CNT0.8_1 (1.34 kΩ)

CNT0.8_2 (1.33 kΩ)

CNT0.8_3 (1.44 kΩ)

CNT1.0_1 (250.71 Ω)

CNT1.0_2 (226.87 Ω)

CNT1.0_3 (238.68 Ω)

CNT2.0_1 (239.97 Ω)

CNT2.0_2 (225.36 Ω)

CNT2.0_3 (206.16 Ω)

초 록

이 논문은 뛰어난 기계적 특성 (Mechanical properties)을 보유했을 뿐만 아니라 전자파 간섭 (Electromagnetic interference, EMI)에 대한 차폐 효과 (Shielding effectiveness, SE), 구조 헬스 모니터링 (Structural health monitoring, SHM) 적용을 위한 균열 자기 감지 (Crack self-sensing) 등 다양한 기능 발휘로 복합 응용이 가능한 초고성능 콘크리트 (Ultra-high performance concrete, UHPC)를 개발하고 현장 시공이 가능토록 하는 것을 목적으로 하였다.

이 연구의 목적을 달성하기 위해 탄소나노튜브 (Carbon Nanotubes, CNTs)를 핵심 재료로 선정하여 UHPC에 혼입하고 분산 방법 (dispersion methods), 기계적 특성, 전자파 차폐, 균열 자기 감지, 전기 경화 (Electrical curing, EC), 그리고 미세구조 변형 (Microstructural modifications) 관점에서 논의 하였다.

CNT를 UHPC에 효과적으로 분산시키기 위한 방법 중 하나로 오존 처리 (Ozone treatment)를 적용하고 이에 따른 UHPC의 수화 반응 (Hydration reaction)을 조사하였다. 오존 처리는 산소 및 카르복실기 (Oxygenic and Carboxylic chemical group)를 CNT 표면과 UHPC 입자 주위에 형성하여 효과적으로 CNT를 분산시키고 UHPC의 계면활성작용 (Interfacial interaction)을 개선하였다. 오존 처리는 UHPC 수화 반응에 큰 영향을 미치지는 않았지만 CNT의 효과적인 분산을 통해 다중 핵 형성 반응을 (Multiple nucleation)을 촉진하여 UHPC의 초기 수화 반응을 가속화 할

뿐만 아니라 필러 효과 (Filler effect)로 인해 더욱 더 향상된 압축강도를 발현하는데 기여하였다.

대용량의 CNT를 UHPC에 균일하게 분산시키기 위하여 초음파 처리 (Sonication) 및 초고성능 감수제 (Super plasticizer)를 활용한 전단 혼합 (Shear mixing) 방법을 제안하였다. 그리고 제안된 분산 방법을 통해 제조된 CNT 분산액을 UHPC와 혼합하고 CNT 혼입 중량에 따른 기계적 특성을 조사하였다. 제안된 분산 방법은 혼입 임계점 (Critical incorporation concentration, CIC) 미만에서 CNT를 효과적으로 분산시킬 수 있었으며 공극 충전 (Pore filling), 가교 효과 (Bridging effect), C-S-H (Calcium-silicate-hydrates) 치밀화 (Densification) 등을 통해 압축강도 (Compressive strength) 및 탄성계수 (Elastic modulus)를 향상시켰다. 하지만, 혼입 임계점 이상의 CNT가 혼입된 경우에는 분산된 CNT가 일부 응집되어 (Agglomeration) UHPC의 수화반응을 방해하고 공극 또는 균열로 작용하여 기계적 특성을 약화시켰다.

분산된 CNT는 침투 임계점 (Percolation threshold) 범위 내에서 UHPC의 전기전도도 (Electrical conductivity) 및 전자파 차폐 효과를 극대화 시켰다. 전자파 차폐 효과를 측정하는 두 가지 표준 시험 (ASTM D4935-18, IEEE-STD-299)을 적용한 결과 ASTM D4935-18은 재료 수준에서 차폐 효과의 대략적인 추세를 평가하는데 사용될 수 있으나 실제 구조 수준에서 정확하게 차폐 효과를 측정하기 위해서는 최소 1200 × 1200 mm^2 이상의 충분한 입사 면적 (Incident area)을 가지는 실험체로 IEEE-STD-299에 의거 실험해야 함이 입증되었다.

UHPC내에 균일하게 분산된 CNT는 UHPC의 전기저항률을 현저히 낮추어 약 19–23 V 범위의 저전압 하에서도 증기 양생과 동등 이상의 효과를 발현하는 전기 경화를 가능하게 하였으며 그 결과 압축강도, 탄성계수, 휨 변형 경화 (Deflection hardening)

등의 기계적 특성이 눈에 띄게 향상되었다. 또한, UHPC/CNT 복합재료는 낮은 전기저항률로 인해 압축 및 휨 응력 하에서 탁월한 균열 자기 감지 능력을 발현하여 구조체의 균열 및 안정성 여부를 판단할 수 근거를 제시하였다.

미세구조 분석 결과, CNT는 UHPC의 중장기 수화 반응을 다소 억제하였지만 C-(A)-S-H의 중간층 (Interlayer) 간격을 줄이고 일부를 연결함으로써 UHPC의 미세구조를 더욱 치밀하게 하고 강성을 강화할 뿐만 아니라 복잡하게 하였다. 이러한 현상은 전기 경화를 적용했을 때 더욱 심화되었는데 이는 전기 경화에 의해 UHPC 매트릭스 내에 형성된 전기장으로 인해 이온 분극 및 화학반응이 가속화되어 수화도가 향상되었기 때문이다.

결론적으로 이 연구에서 제안한 분산 방법을 적용하여 목적에 맞게 적절한 양의 CNT를 UHPC에 혼입하면 UHPC의 한계점을 극복하고 뛰어난 기계적 특성을 발현하는 가운데 전기 경화를 통해 현장 타설이 가능하며 전자파 차폐, 균열 자기 감지 등 다기능 복합 응용이 가능한 UHPC 개발이 가능하다.

주요어: 균열 자기 감지, 분산, 전기 경화, 전자파 차폐 효과,
초고성능 콘크리트, 탄소나노튜브,

학 번: 2017-39383